THE BEHAVIOR OF SWIRLING FLAMES UNDER VARIABLE FUEL COMPOSITION

A THESIS SUBMITTED IN PARTIAL FULFILLMENT
OF THE REQUIREMENTS FOR THE DEGREE OF

DOCTOR OF PHILOSOPHY
IN
MECHANICAL ENGINEERING

AT THE
SCHOOL OF ENGINEERING
CARDIFF UNIVERSITY

JONATHAN LEWIS

2014

DECLARATION AND STATEMENTS

Declaration

This work has not been submitted in substance for any other degree or award at this or any other university or place of learning, nor is being submitted concurrently in candidature for any degree other award.

Signed: .... (Candidate)
Date: ....

Statement 1

This thesis is being submitted in partial fulfilment of the requirements for the degree of PhD in Mechanical Engineering.

Signed: .... (Candidate)
Date: ....

Statement 2

This thesis is the result of my own independent work/investigation, except where otherwise stated. Other sources are acknowledged by explicit references. The views expressed are my own.

Signed: .... (Candidate)
Date: ....

Statement 3

I hereby give consent for my thesis, if accepted, to be available for photocopying and for inter-library loan, and for the title and summary to be made available to outside organisations.

Signed: .... (Candidate)
Date: ....

SUMMARY

This thesis is concerned with the swirl stabilised combustion of gases with variable composition, primarily those derived from the gasification of carbonaceous material, and secondarily those that occur naturally, such as shale gas.

During the course of this research the temporal composition of producer gas, derived from the gasification of biomass, was studied in order to ascertain the effect its variable fuel composition had on its combustion properties. Its variation was highly dependent on gasifier operation, and despite the stoichiometric air-to-fuel ratio and Wobbe Index of the fuel being consistent, high throat temperatures resulted in high hydrogen content and laminar flame speeds.

Alterations in flame speed are linked to thermo-acoustic instabilities, flame extinction and damaging flame propagation. Acoustic response under combustion conditions was investigated, to determine how it altered over a flames stability range. Indicators of impending flame flashback and blowoff were found, which could be utilised to prevent such events from occurring in an appropriate control system, without the need for real time gas analysis.

Flames with high hydrogen content display a propensity for flashback, especially in high turbulence burners, such as those found in gas turbines, where thermo-acoustics are also a significant problem. Variation in fuel composition, particularly in the proportion on hydrogen, exacerbates these problems. The diffusive injection effects of three gases on reacting flow structures were investigated as a method of improving the stability of pre-mixed flames. Carbon dioxide was found to improve flame stability, whilst reducing emissions during the combustion of syngas mixtures in a development gas turbine combustor.

Monitoring acoustic response and diffusive injection are thus suggested as additional stabilisation methods for the combustion of gases with variable composition.

ACKNOWLEDGEMENT

Firstly I would like to thank my supervisors; particularly Dr. Richard Marsh, who over the past three and a half years has provided me with support, encouragement and pragmatic advice whenever it was required, and Professor Anthony Griffiths, whose input has significantly improved the quality of this thesis. My thanks also go to Refgas UK, who part funded my research, in chiefly George and Paul Willacy.

I would also express my gratitude to Steve Morris, who has challenged my perceptions of both life, and swirl combustion. Yura Sevcenco, who, with little reward, put up with me and my taste in music on our many exciting, combustion related, escapades. Agustin Valera-Medina, who provided insight and impetus to my research, and to all the other staff at the GTRC and Cardiff University who have been influential, for varying reasons over the past three years, including; Professor Philip Bowen, Malcolm Seaborne, Terry Treherne, James Lyons, Sally Hewlett, Jack Thomas, Gina Goddard-Bell, Professor Nick Syred, Dr. Tony Giles and Dr. Andrew Crayford.

My final thanks go to my family and friends, particularly my mother and father, who have never wavered in their love and support.

CONTENTS

REFERENCES

APPENDICES

INDEX OF FIGURES

INDEX OF TABLES

NOMENCLATURE

$\bar{a}$ = mean amplitude (-)
A = cross sectional area of tube (m^2)
A_{CRZ} = cross sectional area of the CRZ (m^2)
A_e = area of burner nozzle exit (m^2)
A_{HMFR} = cross sectional area of the HMFR (m^2)
A_{mp} = area represented by each measurement point (m^2)
A_s = cross sectional area of structure (m^2)
A_t = area of tangential Inlet (m^2)
A_{th} = throat area (m^2)
c = speed of sound (m/s)
c_c = correlation coefficient
C_p = specific heat (kJ/kg·K)
CV = calorific value of the fuel (various)
d_c = the characteristic dimension of an obstacle (m)
d_d = diameter of the particle (m)
d_{max} = maximum distance between particles (m)
d_{pixel} = diameter of pixels (m)
E = shear number
F = focal ratio
f = frequency of oscillations (Hz)
ft = frequency to analyse
G = pressure gain (-)
G_x = axial momentum flux (kg/m·s)
G_θ = axial flux of tangential momentum (kg·m/s)
H_P = sensible heat in products (kJ)
H_R = sensible heat in reactants (kJ)
H_R = sensible heat in reactants (kJ)
H_T = sensible heat (kJ)
I = turbulent intensity (%)
$J_0(E)$ = 0th order Bessel function with argument E, BesselJ(0,E)
$J_0(W)$ = 0th order Bessel function with argument W, BesselJ(0,W)
$J_1(E)$ = 1st order Bessel function with argument E, BesselJ(1,E)
$J_1(W)$ = 1st order Bessel function with argument W, BesselJ(1,W)
ke = turbulent kinetic energy (m^2/s^2)
L = characteristic length of exit (m)
L_{ct} = length of tube between chamber and transducer (m)

L_t = throat effective length (m)
L_{te} = length of tube between transducer and end (m)
m = mass (kg)
M_f = magnification of the lens
N_{int} = number of pixels (-)
n_{mp} = number of measurement points in structure (-)
Ø = equivalence ratio (-)
P = pressure
P_1 = pressure at condition 1 (Pa)
P_2 = pressure at condition 2 (Pa)
P_c = combustion chamber pressure
Pr = Prandtl number (ν / α)
P_t = pressure at transducer
Q = volumetric flow rate (m^3/s)
Q_L = heat loss to burner (various)
Q_{ta} = tangential flow rate (m^3/s)
Q_{to} = total flow rate (m^3/s)
r = radius (m)
R = universal gas constant (J/K·kg)
r_c = radius of centroid (m)
r_e = characteristic radius or radius of burner nozzle exit (m)
R_M = momemtum ratio (-)
Ro = Roshko number (Re·St)
r_t = effective radius of tangential Inlet (m)
S = swirl number ($G_\theta/(G_x \cdot re)$)
sg = specific gravity (-)
S_L = laminar flame speed (cm/s)
S_T = turbulent flame speed (cm/s)
St = Strouhal number (f·L/U)
Stk = Stokes number ($\tau \cdot U/d_c$)
T = absolute temperature (K)
t = time (s)
T_1 = temperature at condition 1 (K)
T_2 = temperature at condition 2 (K)
T_f = temperature of flame (K)
T_p = temperature of product gases (K)
T_r = temperature of reactant gases (K)
$\bar{U}$ = mean velocity (m/s)
U = velocity (m/s)

U_a = axial velocity (m/s)
u_a' = root-mean-square of turbulent velocity fluctuations in the axial direction (m/s)
$\bar{U}_{CRZ}$ = mean velocity of the CRZ (m^2)
$\bar{U}_{HMFR}$ = mean velocity of the HMFR (m^2)
U_{max} = maximum velocity (m/s)
u_{mp} = velocity at measurement point (m/s)
U_r = radial velocity (m/s)
u_r' = root-mean-square of turbulent velocity fluctuations in the radial direction (m/s)
U_t = tangential velocity (m/s)
u_t' = fluctuating tangential velocity (m/s)
V = volume of pressure transducer cavity (m^3)
V_1 = volume at condition 1 (m^3)
V_2 = volume at condition 2 (m^3)
V_c = volume of Cavity (m^3)
v_{max} = maximum velocity (m/s)
V_s = volume of structure (m^3)
W = wave number
WI = Wobbe Index ($CV/\rho_r^{0.5}$)
X = reflection coefficient
$X(f)$ = the FFT
$x(t)$ = the time domain signal
X_{mp} = x-coordinate of measurement point (m)
y = propgation constant
α = thermal diffusivity (m^2/s)
γ = ratio of specific heats (-)
δ = depth of field (mm)
θ = phase shift (°)
λ = frequency of the laser (Hz)
μ_f = dynamic viscosity of the fluid (m^2/s)
ν = kinematic viscosity (m^2/s)
ρ = density (kg/m^3)
ρ_r = relative density
ρ_d = particle density (kg/m^3)
τ = particle relaxation time (s)
ω = angular frequency (rad/s)

ABBREVIATIONS

AFR	Air to Fuel Ratio
AGSB	Atmospheric Generic Swirl Burner
BFG	Blast Furnace Gas
BIG-GT	Biomass Integrated Gasification-Gas Turbine
CB	Cyclone Burner
CCHP	Combined Cooling, Heat and Power
CHP	Combined Heat and Power
CI	Compression Ignition
CIVB	Combustion Induced Vortex Breakdown
CRZ	Central Recirculation Zone
CV	Calorific Value
DIGCCC	Development Integrated Gasification Combined Cycle Combustor
ERZ	Edge Recirculation Zone
FFT	Fast Fourier Transform
GC	Gas Chromatograph
GCV	Gross Calorific Value
GTCC	Gas Turbine Combined Cycle
GTRC	Gas Turbine Research Centre
HHV	Higher Heating Value
HMFR	High Momentum Flow Region
HPCR	High Pressure Combustion Rig
HPOC	High Pressure Optical Casing
IGCC	Integrated Gasification Combined Cycle
LHV	Lower Heating Value
NCV	Net Calorific Value
PFM	Positive Flow Momentum
PIV	Particle Image Velocimetry
PLIF	Planar Laser Induced Fluorescence
PPQ	Pora Plot Q
PVC	Precessing Vortex Core
RDF	Refuse Derived Fuels
RFM	Reverse Flow Momentum
RGA	Residual Gas Analyser
S50/50	Syngas blend: 50% Hydrogen and 50% Carbon Monoxide by volume
S85/15	Syngas blend: 85% Hydrogen and 15% Nitrogen by volume
SAFR	Stoichiometric Air to Fuel Ratio
SI	Spark Ignition
TCD	Thermal Conductivity Detector

Chapter 1: Introduction

1.1 Background

As the issue of climate change becomes increasingly prevalent in modern society, new renewable energy markets have developed as both the public and private sector strive to reduce emissions of greenhouse gases and the dependence on potentially unsecured resources (Liao et al., 2011). With the decommissioning and dismantling of many outdated generation plants, and few new installations to take their place, the UK is in special need of these new technologies to meet the increasing demand for power (Cockroft and Kelly, 2006).

One such technology, the gasification of biomass or biowaste to produce electrical and/or thermal energy may be very important as a decentralised power source of the future (Melvin G.R, 2003). A significant advantage of using this method is that the producer gas, derived from an industrial gasification process can be used to generate power with existing equipment, such as internal combustion engines (Stassen and Koele, 1997) and potentially gas turbines (Fiaschi and Carta, 2007), allowing previously fossil fuelled systems to be converted. There are many examples of research into the firing of internal combustion engines with producer gas (Stassen and Koele, 1997, Tinaut et al., 2006, Mohon Roy et al., 2009, Sridhar et al., 2001), dating back to the second world war, where automobiles across Europe were equipped with gasifiers so they could be run on wood, as typically shown in Figure 1. The process has been used commercially in Combined Heat and Power Systems.

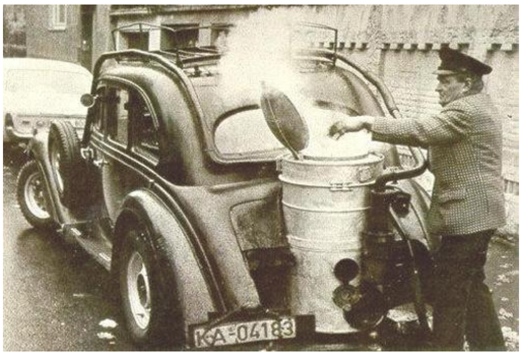

Figure 1: Converted car during WWII

The comparatively low Calorific Value (CV) of producer gas, typically in the range 3-7 MJ/kg, means the conversion of equipment designed for use with fuels with high calorific values, such as gasoline or natural gas, often results in a significant de-rating of the maximum power and reduced efficiency (Sridhar et al., 2001). A more pressing issue when using existing technologies such as internal combustion engines or gas turbines is the content of high molecular mass volatile organic compounds, often known as tar, in the producer gas. These organic compounds readily condense (Anis and Zainal, 2011) on working surfaces which can foul turbines, engines or other auxiliary equipment such as turbochargers. To minimise the detrimental effect of these tars, the producer gas could be used to produce thermal rather than electrical energy. Ultimately, this would allow the gas to be used 'hot' and without interaction with moving parts, avoiding the issue of tar condensation. Due to high gasification temperatures, the temperature of the producer gas leaving the gasifier is also high, typically 700-1000°C for a down-draft gasifier (Son et al., 2011) as used in this study. Extensive cooling and gas clean up is required for use with internal combustion engines, however this thermal energy could be utilised by firing in boiler systems, including systems originally designed for use with fossil fuels. Regardless of the combustion system, there is a compromise to be found between the added cost of ancillary equipment and flow meters capable of withstanding high temperatures, the condensation of organic compounds and wasted thermal energy.

On a practical level direct combustion of producer gas is complicated by both its low CV and variable composition, notably its hydrogen content which has been shown to play a major factor in defining flame stability limits (Syred et al., 2012). To address these issues a swirl combustor can be utilised. Swirling flows occur in most forms of modern combustion equipment, from swirl induced by chamber geometry in internal combustion engines (Prasad et al., 2011), to high intensity combustion processes which utilise swirling flows to stabilise flames and reduce combustion length whilst increasing mixing rates (Syred and Beér, 1974). Swirl combustion has also been shown to be an effective method to burn producer gas (Syred et al., 2004, Kalisz et al., 2008).

Syngas can be produced from the gasification of any carbonaceous material, historically coal is the most significant source of gasifier feedstock (Beychok, 1974).

In 1959 it was demonstrated by the British Gas Council that Liquid Natural Gas (LNG) could be successfully imported, when the Methane Pioneer delivered 5000 m^3 from Louisiana to Canvey Island (Tusiani and Shearer, 2007), and in 1965 the first North Sea gas reserves were discovered. However, prior to North Sea gas being brought ashore in 1967 the United Kingdom's centralised gas supply was Town Gas. Derived from gasified coal, a technology dating back to the 1790's when used by William Murdoch as an illumination gas (Griffiths, 2004).

Coal gas was also used extensively used in America and Germany; during the Second World War Germany became leaders in the field of coal gas research and carbon chemistry, with petroleum shortages being the spark that ignited the development of Fischer-Tropsch synthesis to produce fuel.

The use of coal as a fuel subsided significantly during the second half of the 20th century, with the majority of energy suppliers using oil and natural gas, which are cleaner burning fuels. However, unrest in the Middle East, amongst other factors, has resulted in a steep rise in oil prices, from being 20-30 US$/bbl in the 20 years prior to 2003, to over 60 US$/bbl since 2005 (Williams, 2011). A similarly high price rise has also been seen in the price of natural gas due to the rapid industrialisation and huge increase in energy requirement in countries of expanding economies, such as China and India, with prices increasing from 5-6 US$/MBtu (0.005-0.006 US$/MJ) to over 10 US$/MBtu (0.01 US$/MJ) in the same period (Williams, 2011). This price rise has driven an increase in coal use and improvement in technology to make its use less of an environmental burden. The discovery of vast shale gas reserves in the United States has again prompted their coal use to be stunted; this has simply caused import prices to the UK to be reduced.

Despite the discovery of other, cleaner fuel sources and the increasing push to use renewable technology, in the UK, where there is a capitalist economy and a private power generation industry; profit will always be of primary importance to the generators themselves. As such coal is still an exceptionally widely used fuel, and is likely to stay that way for a considerable time as fossil fuel power generation will be required to fulfil base load capacity whilst renewable markets continue to develop, and overall demand increases. Figure 2 (a) (Simbeck, 2007), shows how the worlds gasification capacity has increased since 1970, and how major developments are planned in the very near future. There are multiple uses of Syngas other than power generation, with the various possibilities to manufacture chemicals and fuels. Indeed Sasol in South Africa use Lurgi gasifiers and the Fischer-Tropsch process to produce a variety of synthetic fuels and polymers, including kerosene that conforms to the strict standards of Jet A-1 fuel. Figure 2 (b) shows how the current and planned global gasification capacity will be utilised, what is immediately obvious is the 450% increase in power generation capacity.

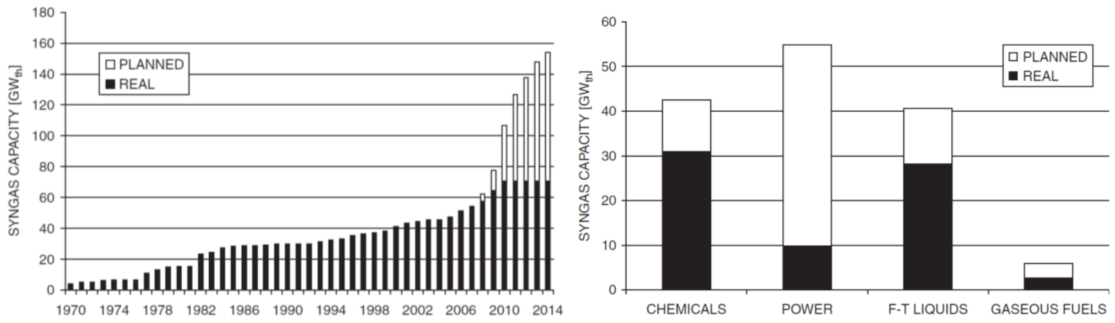

(a) *(b)*

Figure 2:(a) World gasification capacity and (b) in what market area from Simbeck (2007)

The utilisation of gasification in power generation in Integrated Gasification Combined Cycle (IGCC) enhances the environmental acceptability of coal. Coal derived Syngas is of 'better' quality than that of biomass, with higher energy and reduced moisture content. However, significant fuel processing is required before it can be fired in gas turbines. Typical fuel processing and preparation steps are shown in a typical IGCC plant layout in Figure 3 (Kunze et al., 2011). In order to improve gas calorific value pure oxygen is typically used as the gasifier oxidant, which requires an air separation unit.

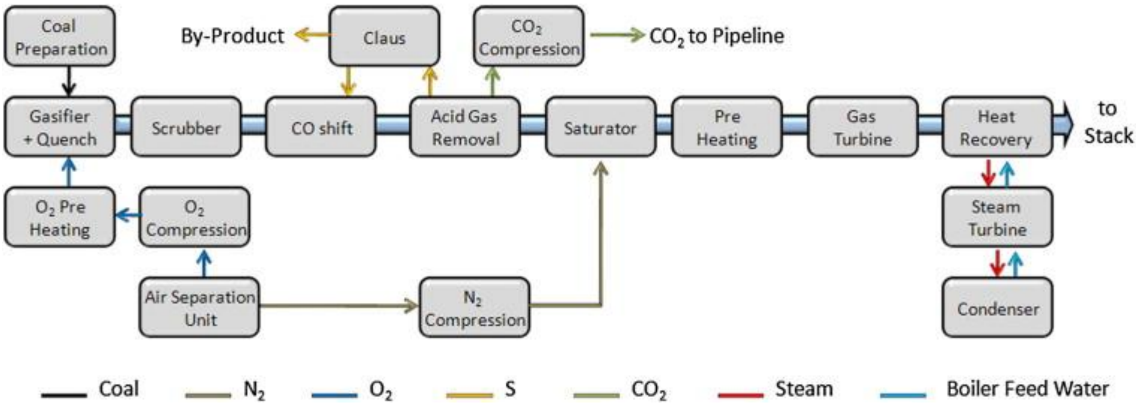

Figure 3: Simplified scheme of a typical case IGCC concept, from Kunze et.al. (2011)

The syngas is then scrubbed, to remove particulate matter and tars, before the water gas shift reaction is utilised to increase the hydrogen quantity. The multi-step Claus process, first patented by Carl Friedrich Claus in 1883 (Gary and Handwerk, 1984), is used to remove sulphur from gaseous hydrogen sulphide. Acid gas removal, via amine gas treating, is then employed to remove hydrogen sulphide and carbon dioxide (Baker, 2002). Prior to combustion, nitrogen previously separated from oxygen in the air separation unit, is used to dilute the fuel so it is acceptable for gas turbine combustion. Despite this significant gas processing, the final composition of the fuel is still subject to variations in compositions, of which gas turbines are very sensitive.

The fuel that has been predominantly used for power generation in centralised plants, which utilise gas turbine systems, is natural gas. Nevertheless, it is also prone to variations in composition capable of impacting upon gas turbine operation (Abbott et al., 2012).

Natural gas is a naturally occurring, hydrocarbon based, fuel that consists mainly of methane, but also contains varying quantities of higher alkanes, nitrogen, hydrogen sulphide and carbon dioxide. It is found in underground rock formations associated with coal beds and oil deposits, and is produced in the same way, as a combination of biogenic and thermogenic reactions (naturalgas.org, 2010).

The first well specifically intended to extract natural gas was dug in 1821 in Fredonia, New York, and was used to produce light, as town gas had been in the UK and Baltimore previously (naturalgas.org, 2010). Natural gas was not extensively utilised prior to the technical advances in welding and pipe forming that resulted from WWII. This lack of transportability and ultimately the lack of end-use meant it was not economic to be utilised, and despite being the by-product of oil drilling was often flared or released to the atmosphere at the drilling site.

Globally, there are still huge reserves of natural gas available, and whilst they provide an economic source of energy they will continue to be utilised. Russia, as shown in Table 1, has the largest reserves, and they export a great deal to neighbouring countries, including the United Kingdom, in the form of Liquid Natural Gas (LNG). The largest single reserve of natural gas in the world is Qatar’s North Field, which is a non-associated offshore field containing all of Qatar’s estimated 25 trillion cubic meters. At the current level of extraction (Central Intellegence Agency, 2013) this would last 216 years. Despite a drive to reduce reliance on fossil fuels, global production is actually increasing, with the world’s two economic super powers, the United States and China, being two of the five countries worldwide that produce in excess of 100 billion cubic meters of natural gas per year, as shown in Figure 4.

Table 1: Proved natural gas reserves of the World and top ten countries (Central Intellegence Agency, 2013)

-	World	208,400,000,000,000	m^3	1 January 2011 est.
1	Russia	47,570,000,000,000	m^3	1 January 2012 est.
2	Iran	33,070,000,000,000	m^3	1 January 2012 est.
3	Qatar	25,200,000,000,000	m^3	1 January 2012 est.
4	Turkmenistan	24,300,000,000,000	m^3	1 June 2012 est.
5	Saudi Arabia	8,028,000,000,000	m^3	1 January 2012 est.
6	United States	7,716,000,000,000	m^3	1 January 2009 est.
7	United Arab Emirates	6,089,000,000,000	m^3	1 January 2012 est.
8	Venezuela	5,524,000,000,000	m^3	1 January 2012 est.
9	Nigeria	5,110,000,000,000	m^3	1 January 2012 est.
10	Algeria	4,502,000,000,000	m^3	1 January 2012 est.

Aside from the increased demand for power, the discovery, and technology to extract, Shale gas has caused this increase in production, and further increases are predicted. The U.S. was gearing up to increase the use of coal for energy production in IGCC plants, whilst the use of natural gas was maintained or slightly reduced. However, the discovery of huge reserves of shale gas has changed that. Figure 5 shows the annual production of natural gas, including that extracted from shale seams.

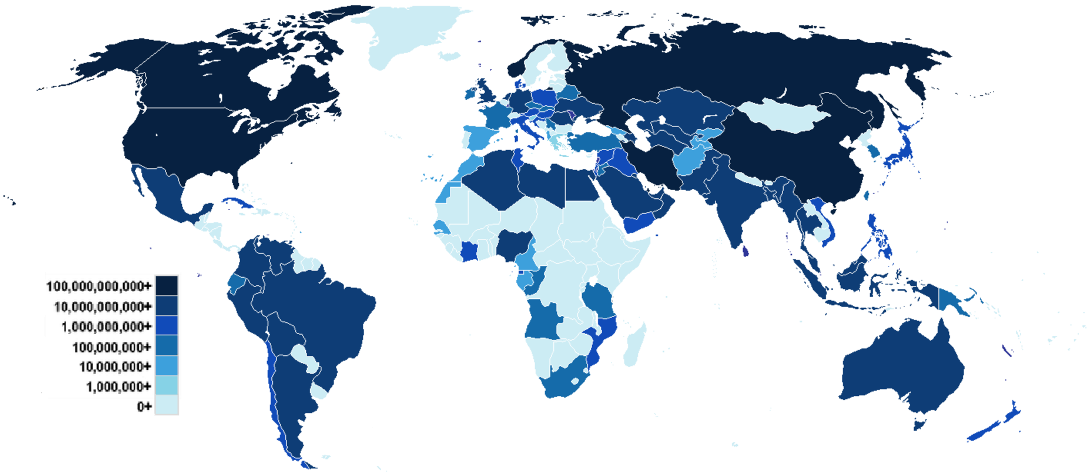

Figure 4: Annual production of cubic meters of natural gas per year by country (Central Intellegence Agency, 2013)

The United States, China and Russia, three of the world’s major economies, all produce in excess of 100 Mm^3 each year, as do Canada and Iran. While the U.K. produces in excess of 10 Mm^3 per year. With production levels so high, and increasing, it is highly probably that natural gas, which can be used relatively cleanly and efficiently, will still play a major role in future energy production.

Gas which is found in conjunction with an oil field is called 'associated' natural gas, whereas that found isolated is referred to as 'non-associated'. These accumulations are the result of natural gas migration from gas rich shale, through sandstone formations, and is trapped by and impermeable formations known as the seal. Coal bed methane is also found deposited in coal seams, relatively close to the earth's surface. Shale gas is that which is extracted directly from the gas-rich shale. The advances in horizontal drilling technology, and 'fracking', have been crucial in facilitating this extraction. A schematic demonstrating the geographical positions of natural sources is shown in Figure 6. The requirement of deeper drilling, that can penetrate horizontally into the shale seam; to extract shale rather than 'associated' gas is indicated.

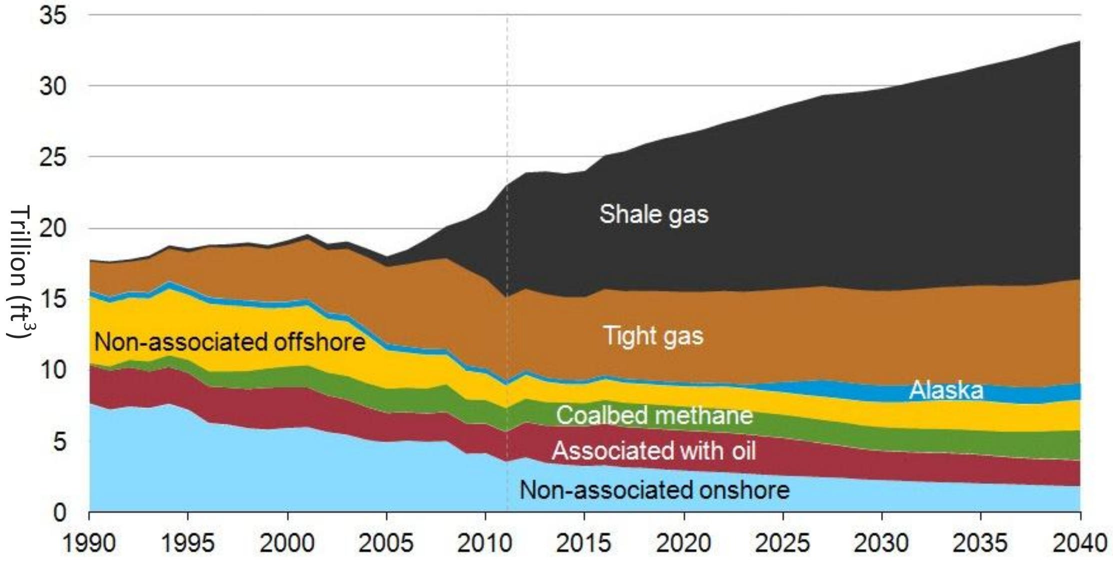

Figure 5: History and prediction of U.S. natural gas production (U.S. Energy Information Administration, 2010)

The technique of hydraulic fracturing, often referred to as fracking, was invented in 1947. It uses the injection of high-pressure fluids, typically fresh water mixed with chemicals and sand, to induce fractures in shale rock. After the initial fracturing, the fluid is removed and a path is created for gases, including natural gas, to pass through to the well head.

As of 2010 it was estimated 60% of new wells, for both oil and gas, were hydraulically fractured, and as of 2012, 2.5 million fracturing jobs had been performed, over one million of which were in the U.S. (King, 2012). However, fracking has many critics, and due to the perceived risks has been suspended or banned in many countries. The reasons for the suspension of fracking in the United Kingdom included; the environmental and health risks due to potential ground water contamination, and geological risks due to induced seismicity when the artificial fractures coincide with pre-existing faults.

With the aim of becoming a part of, what Prime Minister David Cameron in December 2012 called, 'the shale gas revolution', the U.K. government opted for a new approach (Wright et al., 2012). Cuadrilla Resources Ltd., were granted permission to continue work, when a ban on hydraulic fracturing was lifted, despite causing earthquakes whilst fracking in 2011. The blanket ban was replaced by new controls and regulations, which were set up reduce the risks of induced quakes. Energy Secretary Ed Davey believed, 'Shale gas could have potential to help the U.K. to diversify its energy mix and provide an indigenous source of gas to support the move to the low-carbon economy.' (Bakewell, 2012)

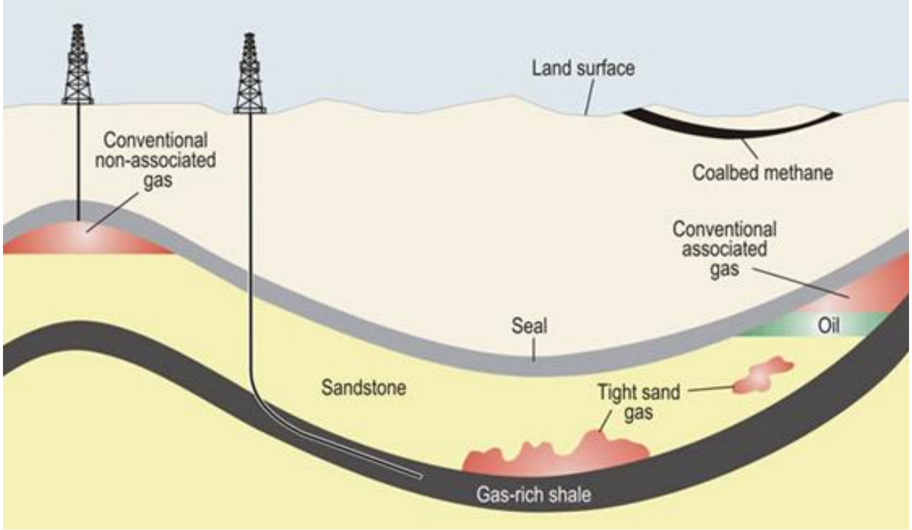

Figure 6: Schematic geology of natural gas sources (U.S. Energy Information Administration, 2010)

Syngas, whether derived from biomass or coal, and natural gas, whether extracted from conventional fields or shale seams, are very different in composition and production. What they do have in common is that they will all have their part to play in future energy production, whether it is in distributed or centralised networks, and like other alternative fuels, such as biogas, they all have variable compositions.

1.2 Centralised and Distributed Power Generation

In order to achieve maximum potential for efficiency in future electricity generation it has been heavily argued that current centralised model must be abolished in favour of a decentralised system (Greenpeace, 2005). The UK pioneered the centralised system, with sixteen low voltage networks, developed in the 1940's to deliver electricity from thermal power plants to end users around the country. This type of system was adopted worldwide, to the extent that as of 2003, 93% of electricity supplied globally was via a centralised system (Brown, 2002). When it was initially developed coal was the primary fuel source for power generation, with large plants utilising the large and locally available reserves to produce heat and drive steam cycles. These coal fired steam turbine plants typically operated at an efficiency of only 33%, on a Higher Heating Value (HHV) basis, whilst producing 965 g/kWh of carbon dioxide (Strachan and Farrell, 2006). These figures include transmission losses, which in the UK have been recorded as high as 9.8% over a period of one year (OFGEM, 2003). The picture is largely the same worldwide; with the US power industry delivering 33% efficiency in 2003, the same figure as 1960 (Casten, 2003). Since the development of Closed Cycle Gas Turbine power stations operating on natural gas, potential efficiency has increased markedly, reaching 50%, whilst producing a comparatively low 363 grams of carbon dioxide per kilowatt hour of electricity generated.

Decentralised energy is that which is generated close to the point of end use, and is defined by the Office of Gas and Electricity Markets (OFGEM) (2001) as being produced by a plant rated at under 50 MW and connected to a local distribution network. However, plants of significantly higher power output are considered distributed if all of its output is consumed by the generator, and is therefore not connected to public networks.

Just as the current and previous generation of coal-fired power stations were built close to coal seams, in order to reduce the emissions and costs associated with transportation, decentralised generation helps increase the viability and commercial attractiveness of renewable fuel sources, namely biomass and Refuse Derived Fuel (RDF). Unlike fossil fuels, the energy density in renewable fuels such as biomass and municipal waste is very low, which significantly increases the cost per kilowatt of transportation. As the production of these sources is decentralised, it occurs on a small scale at sites connected to small distributed networks. They are not an attractive fuel for centralised generation. However if energy production occurred on the same scale, large amounts of this waste becomes an economically viable fuel source

Another significant advantage of using a decentralised model is the ability to make use of 'waste heat' that is the by-product of electricity generation in co-generation systems. Co-generation refers to a system, often defined as Combined Heat and Power (CHP), which produces both useful electricity and useful heat. A further development is Tri-generation, or Combined Cooling, Heat and Power (CCHP) systems, which are those that also utilise absorption chillers to produce cooling, as and when required. A typical tri-generation model is capable of delivering 85% efficiency, with 45% of the energy input converted to electricity, 40% converted to heating or cooling, and the remaining 15% making up heat and line losses (13% and 2% respectively) (San Martin et al., 2008).

1.3 Types of Gasifiers

In simple terms, the process of gasification transforms a solid fuel into a gaseous one, allowing it to use in a variety of applications. In reality there are liquid and solid products of the process, of which the composition and quantity is dependent on the fuel type and the operation of the gasifier. There are many designs of gasifiers in operation all over the world, the overwhelming majority of which can be placed into one of three categories (Basu, 2010).

1. Entrained Flow Gasifiers use a dry-pulverised fuel, unlike other types of gasifier, with the pulverised feedstock entrained in the oxidant flow, which is often pure oxygen. This type of gasifier requires a high level of energy intensive fuel preparation, particularly if pure oxygen is used. They operate at very high temperatures that inhibit the formation of ash and particulates, and throughput of the fuel is also high, but as the gas requires cooling before using in most applications thermal efficiency is very low.
2. Fixed Bed Gasifiers pass the gasification agent, typically air, oxygen, or steam, through a bed of carbonaceous material. There are two configurations of fixed

bed gasifiers, up and down draft, also known as counter-current or co-current respectively. The exit temperature of the producer gas is lower than that of an entrained flow gasifier; this leads to a higher overall thermal efficiency but higher particulate levels, which require extensive cleaning of the gas. Heat is required for the reaction to take place; this can be from external sources or by the combustion of a small amount of the fuel.

3. Fluidised Bed Gasifiers suspend the fluidised fuel in the stream of the gasification agent. This is very beneficial when the fuel is biomass or RDF, whose ash, which is often high in corrosive material does not come into contact with the walls as would be the case in a slagging gasifier. However, the high level of oxidant required to maintain the structure of the bed means that temperatures are low, so a highly reactive fuel to achieve an efficient conversion from solid to gaseous fuel is required.

1.4 Combined Heat and Power (CHP) Systems

In a CHP system, the initial process uses fuel to produce electrical energy as the result of a combustion process. Obviously, this leads to the production of significant heat. Rather than allow this heat to be wasted, the thermal energy is extracted and utilised. The most useful form of heat is in the exhaust gases, which are at high temperature, although there are other sources of heat available from cooling systems.

Combined heat and power systems are perfectly suited to distributed power generation, as the waste heat from the electricity production can be recycled and used to supply buildings heating demands. Using this waste heat allows the overall efficiency of a plant to reach extremely high levels compared to separate production of heat and power (Martens, 1998), the thermal efficiency of a plant is as dependant on the way heat is extracted as the amount available.

Having the plant in close proximity to the end user allows effective use of the extracted heat; it is not practical or efficient to distribute over large distances. This close proximity is also ideally suited for the use of biomass, or waste derived fuels, resulting in a reduction in both the economic and environmental costs of transportation. The low calorific value, coupled with the high water and ash content of these fuels (Faaij et al., 1997) means that transportation costs per unit energy are very high compared to fossil fuels. The combustion of producer gas in CHP systems has predominately been achieved using internal combustion engines, however there is significant work to utilise swirl flows in burner-furnace configurations and gas turbines, in order to increase plant sizes. The output power of a plant is dependent on the combustion apparatus, and the use of internal combustion engines practically limits the scale of these plants to 100kW$_{el}$ (Baratieri et al., 2009), a significant cause of this is the de-rating that occurs when low CV gas is used as the fuel (Stassen and Koele, 1997). The size and capacity of the engines and auxiliary equipment, compared to the power output is also a factor when considering increasing potential output, hence largely distributed use of this technology, rather than centralised power source.

A practice that is exceptionally uncommon in the United Kingdom, but widely used in Denmark is the use of thermal stores. A significant factor in the increased use in Denmark is not down to the design of CHP systems, but more down to the fluctuating availability of electricity from wind turbines. In 2005 Denmark generated 29.3% of its electrical energy from renewable energy, of which 62.1% was from wind (European Commision, 2008). In 2010 the installed wind capacity was 3545 MW, with a further 720 MW under construction (Danish Energy Agency, 2011). This high capacity means that low wind speeds can result in a large energy shortfall, one way to make up for this lack of electricity is to use highly efficient CHP plants.

A CHP system, which does not have a heat store, is designed to meet a given electrical and heat demand. Should the electrical demand be significantly reduced, i.e. if wind turbines are operating to full capacity, then the CHP plant is required to operate simply to produce heat energy, meaning the electrical energy is effectively lost, significantly reducing the efficiency of the plant. This reduced efficiency will also occur when the electrical demand exceeds the thermal demand.

1.4.1 Internal Combustion Engines

Figure 7, shows the cycle of a four-stroke engine. The first part of the cycle involves the intake of air and fuel, and the second involves compression of the gases. The gases are then ignited, by either a spark, as shown in Figure 7, or by the compression. The final stage of the process is for the combustion products to be exhausted from the chamber. The second and third stages can be effected by variations in fuel compositions, hydrogen content in particular, as auto-ignition can occur (Sridhar et al., 2001).

The standard approach, when using an internal combustion engine to fire producer gas is to add a Spark Ignition (SI) system to a Compression Ignition (CI) engine, benefiting from the robust construction of the CI engine with the spark used to ignite the low CV gas. Another approach is to co-fire the producer gas with diesel, or similar fuel, in a CI engine. Co-firing a diesel engine in dual fuel mode has been shown to have positive results due to the presence of hydrogen (Sahoo et al., 2011). The addition of the diesel provokes the ignition of all the fuel in the chamber; however, this approach remains dependant on external, non-renewable, fuel sources and therefore is not ideal.

(a) (b) (c) (d)

Figure 7: Stages of Four stroke IC engine (Colorado State University, 2007);
(a) Intake, (b) compression, (c) spark ignited combustion and expansion, (d) exhaust

The efficiency of firing producer gas in reciprocating engines has been reduced by restricting the compression ratio to around 12:1 to prevent auto-ignition early in the compression stroke and inducing a knock in the engine, however studies have shown that a compression ratio of 17:1 is achievable (Sridhar et al., 2001).

Another issue is the for mentioned overheating and the further reduction of rated power that occurs when introducing high temperature, reduced CV, producer gas. Therefore the gas must be cooled prior to entering the combustion apparatus, rather than waste the heat it is possible preheat gasification air or use as a heat source in a CHP system by passing it through a heat exchanger.

A significant increase in the long-term efficiency of a plant could be achieved by the installation of a thermal store (Fragaki and Andersen, 2011). Thermal stores use large water tanks to accumulate heat energy, when electrical demands exceed heat demands the excess heat energy is transferred to the tank, effectively charging it, discharging of the heat energy happens when heat demands exceed electrical demands. The methods used to charge and discharge depend on the designs of each system; Figure 8 shows a simple schematic of a heat store. Excess heat is utilised in a heat exchanging heater, which heats the water in closed system. The water is stored in an insulated tank, and due to the effects of fluid dynamics, hot water is kept at the top. The heat can then be used when required. The example system in Figure 8 has a space heating as an extension of the closed water system, while mains water can be heated via a heat exchanger in an open system.

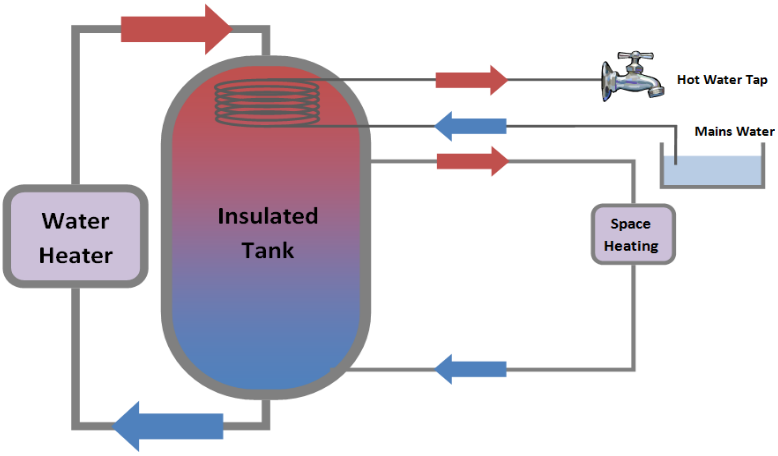

Figure 8: Indication of idealised thermal store schematic

1.5 Gasification of Biomass and Refuse Derived Fuel

Biomass, in the form of wood, has been the fuel of choice for the majority of human history, until the advent of fossil fuels began the industrial revolution, and continues to be in many parts of the world (Lewis, 1981). The direct combustion of biomass is inefficient and produces high levels of pollutants which have a negative impact on human health (Johansson et al., 2003), the gasification of biomass produces a Syngas variant called Producer gas, the components of which include (Marsh et al., 2010):

- Carbon Monoxide
- Carbon Dioxide
- Hydrogen
- Methane, and higher hydrocarbons
- Nitrogen (if air is used as oxidant)

Contaminated fuel streams such as RDF may also result in other gases, often sulphuric or hydrochloric acid, being present.

The feedstock, and equally importantly, the design and operation of the gasifier will have an effect on the composition of the producer gas (Narvaez et al., 1996) which in turn may have significant effects on flame stability. In order for plants to operate economically and at higher efficiencies the processing of feedstock is kept to a minimum, this being the case composition of the feedstock will vary, obviously this will induce a variation in producer gas composition. Conditions inside the gasifier will also have an effect, at start up, when the gasifier is not at running temperature the composition, including particulate levels will vary, stabilising over time, during this stabilising process the gas would normally be flared. Commercially available fuels, such as Gasoline and Natural Gas, have a composition that does not vary greatly due to regulation by Standards, such as ASTM D975-14 (ASTM), the international standard for diesel. This steady composition greatly simplifies the design of combustion equipment.

With regards to swirl combustion, hydrogen content of a gas is very important, studies have shown that a small variation in the percentage hydrogen content can have a significant effect on flashback limits (Syred et al., 2011). Flashback occurs when turbulent flame speed is greater than local fluid velocity, allowing the flame to propagate back into the burner. Two types of flashback were defined (Valera-Medina, 2009), of which one, where the flame propagates to the premixed region of a burner was shown to have the potential to cause significant damage (Coghe et al., 2004).

Similarly, for internal combustion engines hydrogen content of a fuel has impact on auto-ignition limits (Thiessen et al., 2010), this misfiring can cause damage to engines as well as effecting output power.

Gas temperature, which is a result of gasifier operation and processing also has an effect on the stability of the gas, aside from any changes in composition the density of the gas is decreased. An accurate estimate of the expansion is achievable using the ideal gas law in Equation 1.1:

$$\frac{P_1.V_1}{T_1} = \frac{P_2.V_2}{T_2} \qquad \text{Eq (1.1)}$$

Where: P_1 = Pressure at condition 1 (Pa)^{i}

V_1 = Volume at condition 1 (m^3)^{ii}

T_1 = Temperature at condition 1 (K)

P_2 = Pressure at condition 2 (Pa)^{i}

V_2 = Volume at condition 2 (m)^{ii}

T_2 = Temperature at condition 2 (K)

[i] applicable to any unit of pressure, SI units shown

[ii] applicable to any unit of volume, SI units shown

The results is a reduced amount of energy per unit volume of the producer gas, therefore cooling producer gas that leaves a gasifier at 400°C, 2 MJ/m^3 to 40°C will increase the energy per unit volume to 4.6 MJ/m^3. The effects of this temperature change, which will in turn affect the flow rates entering, mixing rates, and preheat temperature, must be assessed for each individual burner.

When designing or modifying combustion apparatus to run on producer gas that is almost directly fed from a gasifier, the constantly changing composition and temperature of the gas must be accommodated to achieve safe operation. Changes in geometry or installation of additional control systems have the potential to solve the problems caused by variable composition.

Due to the nature of the fuel, the producer gas tends to have relatively high levels of tar and particulates; these have impact on the design of combustion and pre-combustion components in a power generation system. Pyrolysis and torrefaction, which occur to a limited degree in the majority of gasifiers (Basu, 2010), lead to the production of ash and tars. A case study by Marsh et al. (2010) recorded particulates levels, equal to 1.7% of the feedstock by mass, entrained in the gaseous stream exiting the gasifier, prior to gas processing.

Many plants employ a scrubbing system that will remove high levels of these particulates, to avoid the impact that they may have on equipment further down the line and the effect they have on emission levels. The downsides of scrubbing the producer gas, which is at a high temperature when it leaves the gasifier, is the cooling effect that it has, which significantly reduces the thermal efficiency of the plant (Wu et al., 2009), this may be desired due to the concentrating effect it has on energy density.

It also generates another waste stream of potentially hazardous wastes that must be disposed of, at a cost to the operator.

1.6 Integrated Gasification Combined Cycle Power Plants

Utility companies continue to mix evolution with revolution and maintain varied portfolios of generating plants, as such, the established and profitable fossil fuel technologies will continue to be developed and implemented in order to meet the rising global energy demands. During the transition between the centralised, fossil-fuelled system and a partially decentralised, renewable based system, fossil fuels must be used as efficiently and cleanly as possible, whilst remaining commercially viable.

On a large scale, coal remains a major contributor to global energy production, despite the high levels and greenhouse gases and pollution produced. This is down to simple economy; large accessible reserves mean the cost of producing electrical energy via the oxidation of coal remains relatively low. IGCC plants offer a cleaner method of extracting electrical energy from coal than traditional coal fired, steam cycle plants. Despite this, they are still opposed by many who feel that rather than continuing to invest in improved coal technology, the money and effort should be directed toward renewable technologies (Whaley, 2007).

A standard IGCC plant has five major components; an Oxygen Production Unit (OPU), a gasification system, a gas cleaning system, a Gas Turbine (GT) based primary generator, and a steam cycle based secondary generator, a new plant is likely to be specified with Carbon Capture and Storage (CCS) capabilities.

1.6.1 Oxygen Production

In order to yield a Syngas with a higher calorific value, ‘pure’ oxygen is used as the oxidiser. Due to the large quantities required, the oxidiser is produced on-site in the OPU, which is one of the most expensive components in an IGCC plant. The basis of OPU is an Air Separation Unit (ASU), of which there are several types, including ion and oxygen transport membranes, pressure swing absorption, and vacuum pressure swing absorption. However, the most cost effective, and therefore the most utilised, technology for oxygen production continues to be cryogenic distillation. The cryogenic distillation of air is a very energy intensive process that has been around for over 100 years, recent advantages in train size, structured packing in distillation columns and more complex cycle designs have reduced the power consumption (IEA., 2007), improving overall plant efficiency.

1.6.2 Gas Cleaning and Processing

The Syngas produced from the gasifier is not suitable for gas turbine combustion; the impurities in the gas would cause damage and blockages in the engine. Conventionally the Syngas is first cooled, so water vapour and semi-volatile matter condensates. The gas is then passed through an absorber to remove any soluble contaminants in the stream, producing a dry gas stream purified of water, ammonia and halides.

The prime issue with firing producer gas instead of coal derived Syngas is the presence of tars entrained in the gas stream, whereas internal combustion engines are very tolerant gas turbines can be heavily affected. The turbine section is not sensitive to tars due to the very high temperatures, at which they are usually in vapour form, however the compressor section, or heat exchangers and piping before the GT may become blocked or fouled by the tars (Baratieri et al., 2009). This makes the firing of coal derived Syngas significantly less problematic.

When derivation of the feedstock for the gasification process is from waste streams, the producer gas may become even less suitable for use in a gas turbine due to the potential hydrochloric or sulphuric acid components of the gas, which can react with and cause damage to the many parts, primarily the blades that are present in a gas turbine.

The dry gas stream contains many impurities that must be removed before it enters the gas turbine; they are listed in Table 2. They are removed by using a number of techniques, including:

- Absorption into a liquid
- Absorption on a solid
- Membrane permeation
- Chemical conversion
- Condensation

Once the gas has been cleaned shift reactors are used to convert carbon monoxide to carbon dioxide, producing hydrogen as a result. Prior to entering the gas turbine some of the carbon dioxide is removed and the gas is saturated with nitrogen from the ASU.

Table 2: Impurities in the dry gas phase (Kohl and Neilson, 1997)

1	Hydrogen Sulphide
2	Carbon Dioxide
3	Sulphur Dioxide
4	Nitrogen Oxides
5	Volatile Organic Compounds
6	Volatile Chlorine Compounds
7	Volatile Fluorine Compounds
8	Nitrogen Compounds
9	Carbon Monoxide
10	Carbonyl Sulphide
11	Carbon Disulphide
12	Organic Sulphur Compounds
13	Hydrogen Cyanide

1.6.3 Gas Turbines

The stages in a gas turbine, as shown in Figure 9, are very similar to a conventional 4-stroke reciprocating engine; compression, combustion and expansion through the turbine, providing work energy and exhaustion. Gas turbines rely heavily on the effect of swirl to allow a compact combustion chamber design whilst providing good mixing of the fuel with the primary combustion air. Designs vary for power generating and aviation derivatives to accommodate the difference in fuels, in power generation the fuel is normally gaseous, allowing a premix of fuel and air. In an aviation engine, where the liquid jet fuel is used, the air is swirled prior to the addition of atomised fuel to the flow.

Since the discovery of natural gas in abundance, and a change in regulations in many countries allowed its use in electricity generation, gas turbines have become one of the most important technologies in thermal power conversion. For long periods gas turbines were an unattractive option due to their low efficiency, a problem caused primarily by the low temperature permitted in the turbine section. Figure 10 demonstrates how significant improvements in the materials used for the turbine blades, firstly in metallic's, and latterly in ceramics, coupled with advances in blade cooling allowed the maximum Turbine Inlet Temperature (TIT) to increase. This temperature increase, coupled with larger pressure ratios in the compressor section, has resulted in the thermal efficiency of the turbine to increase from 15 to 45 % (Boyce, 2006). When used in a Combined Cycle Gas Turbine (CCGT) plant gas turbine systems are capable of reaching global electrical efficiencies of 60%, and with a significantly higher electrical efficiency than a typical CHP plant, which uses an internal combustion engine. This increased efficiency means a higher output for a given input and reducing emissions of greenhouse gases.

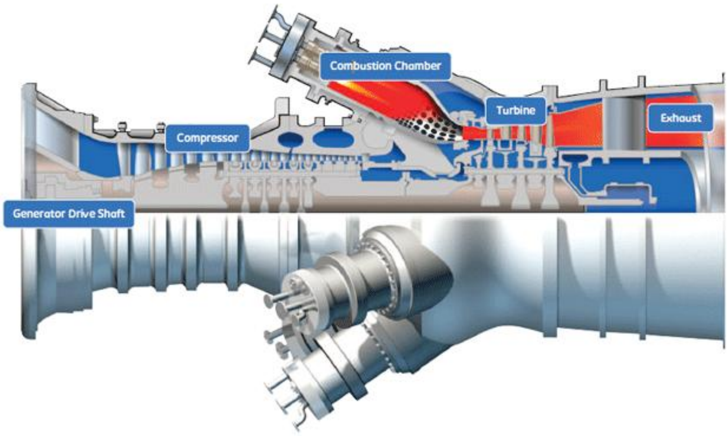

Figure 9: Diagram of Gas Turbine (GE Energy, 2011)

Biomass Integrated Gasification/Gas Turbine (BIG-GT) plants have the potential to significantly increase the electrical efficiency of a producer gas fired plants, with the obvious use in an IGCC plant, which is essentially a BIG-GT plant integrated into a combined cycle.

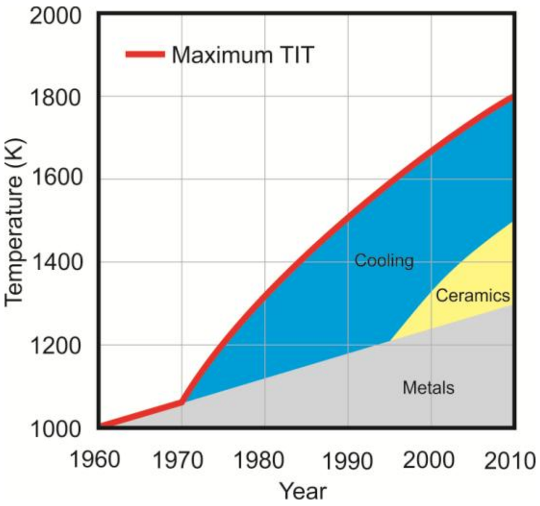

Figure 10: Increase in permissible turbine temperature and the technological drivers, adapted from Assadi and Ohlsson (2008)

The power rating of the turbine may suffer as a result of using producer gas, with its low energy content per unit volume. However co-firing with natural gas can compensate for this, firing with upward of 35% natural gas, on an energy basis, will allow for the full power rating of the turbine to be realised (Rodrigues et al., 2003). This co-firing may be an important step in realising the potential of BIG-GT plants in the short term, but using natural gas means there is still a reliance on externally supplied fossil fuels.

1.7 Summary and Thesis Aims

Energy requirement is increasing, and as a result, so is its production. This is true of the United Kingdom and the world as a whole. Despite this, there is both a moral and legislative drive to significantly reduce the emission of greenhouse gases, including carbon dioxide. To achieve this, new technologies must be developed and deployed, whilst the efficiency and capabilities of existing technologies must be increased.

The use of gas turbines, boilers, and internal combustion engines, all well developed technologies, fired on alternative fuels, are viable methods for producing energy in the short to medium term. Alternative fuels range from those based on highly enriched hydrogenated blends, to those that are produced from bio-materials, and those that occur naturally.

A property shared by many alternative fuels is a composition that is prone to variation. The initial aim of this thesis is to assess how changes in composition, with biomass derived producer gas and natural shale gas of particular interest, alter combustion properties. The potential effect of alterations in combustion properties on flame stability are then considered to assess whether current fuel classification techniques are sufficient.

Gas turbine technology in particular is evolving to cope with the use of these new fuels. However, operators are still finding problems with fuels that vary in composition. They are prevented from consistently operating under optimal conditions, posing a new challenge to produce more flexible equipment or operating procedures.

Methods to aid in the stabilisation of alternative fuel combustion will increase their viability for energy production, whilst facilitating combustion under leaner conditions, which will reduce emissions. This thesis aims to offer potential for additional stabilisation of flames in order to compensate for variations that occur in fuel composition. The monitoring of acoustic response, and diffusive dilution of fuels, particularly those with high hydrogen content, are the methods researched.

1.8 Thesis Structure

Chapter 1-	Provides a background into natural gas, the history of gasification, the sources of gasifier feedstock and the end use of the gaseous fuel produced. It also provides background information regarding the combustion processes used to extract thermal energy from the fuels, and the systems in which they are utilised.
Chapter 2-	Reviews literature relating to swirl combustion, thermo-acoustic phenomena and the variable nature of the fuel sources discussed in chapter 1.
Chapter 3-	Reviews the techniques used to investigate flame flow fields, acoustic oscillations, and the test rigs with which they were used.
Chapter 4-	Details experiments in producer gas variability, and assesses how the variability in producer gas and natural gas composition affect combustion properties.
Chapter 5-	Details experiments in burner acoustic response under isothermal conditions.
Chapter 6-	Details experiments in burner acoustic response under combustion conditions.
Chapter 7-	Details experiments into reactive and proactive structure augmentation using diffusive injection.
Chapter 8-	Discusses the conclusions of this work, and the direction of future research.
Chapter 9-	A bibliography of studies referenced in this work.
Chapter 10-	Additional material relating to this thesis

Chapter 2: Swirling Flows, Thermo-acoustics and Fuel Composition

2.1 Introduction

Swirl combustion is a practice that has been heavily investigated for over half a century in many institutions all over the world, and is a hugely applied technology. Despite this activity there are still many unknowns and unexplained phenomena associated with the combustion of swirling flows. Due to their exceptional ignition, burnout and mixing characteristics they can be found in almost all industrial combustion processes, including refineries, furnaces, reciprocating engines and gas turbines (Hoffmann et al., 1994) where they are capable of stabilising the high intensity flames that these operations warrant (Froud. D, 1996).

The primary reason for using swirl combustion is flame stabilisation. A stable flame is one that will not propagate beyond the design limits of the combustor, will not extinguish, and thus will not spontaneously re-ignite (Schefer, 1998). It is by no means the only method of flame stabilisation; others include the use of baffles, bluff bodies, or pilot flames, with different methods suiting different applications. The similarity between swirlers, baffles and bluff bodies is that they create low flow velocity or recirculation zones which in which the fluid velocity of the unburned mixture is less than, or equal to, its flame speed, which prevents the flame from blowing off. For a flame to be blown off, and extinguished, the local and global velocity of the flow must exceed the flame speed of the mixture. In swirling flows, velocity should be at its greatest when it is at the exit nozzle of the swirler, from that point an axial decay of the tangential velocity and radial pressure occurs (Syred, 2006). Ideally, the turbulent flame speed and fluid velocity are such that the flame will be stabilised at the point it exits the nozzle. If the flame speed drops then the flame will stabilise at a point further downstream. If the flame speed drops sufficiently, relative to local and global flow velocities, the flame will be unable to stabilise and ignite the unburned mixture, thus the flame will go out.

Thermo-acoustics are the pressure fluctuations that result from a combustion process, most work in the field deals with the instabilities that develop as a result. The onset of these instabilities was first theorised by Lord Rayleigh (1896), who defined a criterion for their positive coupling. Thermo-acoustic oscillations always exist, however, without positive coupling they may not actually develop into instabilities capable of having a negative effect on the combustion process. Indeed there are combustion systems that depend on sustained instabilities to achieve increased performance levels, including pulse combustors, ramjets and scramjets (Hathout, 2012, Lieuwen and McManus, 2003).

Given a suitable phase relationship, acoustic oscillations and heat release pressure fluctuations within the combustion chamber can amplify to the extent that the flame can flashback or blowoff. There have been many passive techniques employed to prevent this, like Helmholtz resonators or acoustic dampers. These techniques are still widely used in practical applications, however research now tends to focus on active techniques (Stone and Menon, 2002), which are extremely varied, but are capable to reacting dynamically to system changes and can target a wide range of frequencies.

Syngas, has a great number of definitions, in this context it is a synthetically produced fuel, with usually two of its main constituents being hydrogen and carbon monoxide, derived from the gasification of a carbonaceous material, including:

- Biomass, which is classed as a renewable energy source. Its greatest potential is in distributed power generation, most likely in CHP systems utilising a boiler or internal combustion engine, with a fuel source located close to the plant.
- Coal, which will be important in the future to supply base load power. Gasification prior to the combustion process makes coal more environmentally acceptable, and the Syngas is of far higher calorific value than that of biomass. This allows it to be used successfully in centralised power stations with and IGCC configuration, where a significantly higher electrical efficiency can be achieved.

One issue relating to fuels derived from gasification are variations in composition, which define combustion properties. A successful burner design is capable of producing a stable manageable flame despite fuel variability; this may be achieved using burner geometry or a flow control system. Normally a burner is designed for use with a specific fuel, if another fuel is used the Wobbe Index is used to assess the interchange ability. The Wobbe Index is calculated by dividing the Gross Calorific Value (GCV) of the gas by the square root of its specific gravity, the higher the Wobbe Index the greater the calorific value of the quantity of gas that will flow through a hole of a given size in a given amount of time (American Gas Association, 1946). Producer gas has a naturally variable composition, as gasifier operation and feedstock vary (Yan et al., 2010, Lewis et al., 2012), so even though the fuel source is seemingly constant the same considerations of the Wobbe index must be applied.

2.2 Swirl Flow Characteristics

Swirling flows are defined as a flow that simultaneously experiences axial and tangential vortex motions (Syred et al., 2012). These motions and inherent momentum on the flow may are caused by burner geometry and the introduction of flow in some cases, and are affected by the combustion process. The primary definition of a swirling flow and the most predominantly used parameter for characterisation is swirl number (Abdulsada et al., 2011).

2.2.1 Swirl Number

Swirl number (S) is a similarity criterion that specifies the intensity of swirl that is imparted on the flow (Syred and Beér, 1974), and is defined by the ratio of axial flux of the tangential momentum to the product of axial momentum flux and characteristic radius (Beér and Chigier, 1972), as shown below in Equations 2.1, 2.2 and 2.3:

$$S = \frac{G_\theta}{G_x \cdot r_e} \qquad \text{Eq (2.1)}$$

Given that:

$$G_\theta = \int_0^x (\rho \cdot U_a \cdot U_t + \rho \cdot u_a' \cdot u_t') r^2 \, dr \qquad \text{Eq (2.2)}$$

$$G_x = \int_0^x \left[\rho \cdot {U_a}^2 + \rho \cdot {u_a}'^2 + (\rho - \rho_\infty \cdot r^2)\right] dr \qquad \text{Eq (2.3)}$$

Where: G_θ = axial flux of tangential momentum (kg·m/s)

G_x = axial momentum flux (kg/m·s)

U_a = axial velocity (m/s)

u_a' = fluctuating axial velocity (m/s)

U_t = tangential velocity (m/s)

u_t' = fluctuating tangential velocity (m/s)

ρ = density (kg/m^3)

r = radius (m)

r_e = characteristic radius (m)

Combustor geometry and the profile of the flow strongly influence the expression of swirl number (Huang and Yang, 2009). Although the geometry is fixed, during combustion the flow pattern is subject to the influence of changing temperatures within the combustion zone, and the existence of coherent structures which can have significant effects upon the flow field (Valera-Medina, 2009). Due to these potential changes, the estimation of the preceding integrals is exceptionally complex, as is specifying a single swirl number without the use of velocity measurements.

A more practical and easily obtained characterisation of swirl imparted on the flow is obtained by calculating the Geometric Swirl number, (S_g). It is calculated using only inlet conditions and combustor geometry, allowing variations in flow pressure to be neglected (Syred and Beér, 1974). It is defined below for isothermal conditions, where density is constant, in radial type burner:

$$S_g = \frac{A_e \cdot r_t}{A_t \cdot r_e} \cdot \left(\frac{Q_{ta}}{Q_{to}}\right)^2 \qquad \text{Eq (2.4)}$$

Where: A_e = Area of Burner Nozzle Exit (m^2)

r_t = Effective Radius of Tangential Inlet (m)

A_t = Area of Tangential Inlet (m^2)

r_e = Radius of Burner Nozzle Exit (m)

Q_{ta} = Tangential Flow Rate (m^3/s)

Q_{to} = Total Flow Rate (m^3/s)

To simplify for situations where all flow is fed either tangentially or diffusively, the geometric swirl number can be broken down to its Geometric Coefficient (C_g) and Flow Coefficient (C_f), so:

$$C_g = \frac{A_e \cdot r_t}{A_t \cdot r_e} \quad \text{Eq (2.5)}$$

$$C_f = \left(\frac{Q_{ta}}{Q_{to}}\right) \quad \text{Eq (2.6)}$$

$$S_g = C_g \cdot C_f^2 \quad \text{Eq (2.7)}$$

The temperature of the gases leaving a combustor nozzle is increased by the combustion process. Due to the nature of the geometry of a swirl combustor this occurs after tangential momentum has been applied to the flow, as such the increase in temperature and subsequent expansion of product gases increases the axial momentum of the flow with respect to tangential momentum, reducing the level of swirl. To account for combustion S_g may expressed thus:

$$S_g = C_g \cdot C_f^2 \cdot \left(\frac{T_r}{T_p}\right) \quad \text{Eq (2.8)}$$

Where: T_r = Temperature of reactant gases (K)
T_p = Temperature of product gases (K)

Geometric swirl number is not an estimation of swirl number, which is a property of the flow exiting the nozzle, but of the burner geometry and the flow entering.

2.2.2 Types of Swirl Burners

The majority of swirl burners, especially those commissioned for industrial applications can be split in to two categories, axial swirlers and radial swirlers.

Radial swirlers use inlets that are perpendicular to the central axis of the burner to generate the swirling flow, as depicted in Figure 11, as such the geometric swirl number of these types of burners can be de easily defined. They are easily adapted to operate over a range of geometric swirl numbers and have been the focus of a large amount of research studies into swirl combustion (Syred et al., 2004, Syred et al., 2012, Valera-Medina, 2009, Valera-Medina et al., 2009, Valera-Medina et al., 2011b, Abdulsada et al., 2011, Bagdananvicius et al., 2010, Claypole and Syred, 1983, Claypole and Syred, 1985, Fick, 1998, Fick et al., 1998, Froud, 1995, Froud et al., 1995, Froud. D, 1996, Lewis et al., 2012, O'Doherty et al., 1999).

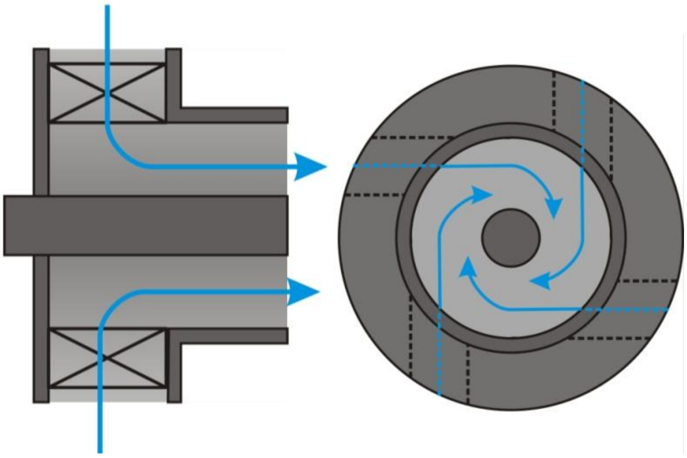

Figure 11: Schematic of a radial swirler

The schematic shown in Figure 11 is of a simple radial swirler in which air enters through tangential inlets which do not intersect with the burner axis, resulting in a flow that circulates around an axial injector. Fuel can either be injected axially or premixed with the combustion air. Many variations on this design have been developed over the years, two of which are shown in Figure 12, however the principle remains the same. The burner in Figure 12 (a) has two sets of air inlets; those combined with a honeycomb and mesh assembly near the base providing air with axial momentum, and those providing air with tangential (and some axial) momentum. Fuel is injected at the centre of a large, annular bluff body, which aids in the formation of a recirculation zone. The burner in Figure 12 (b) also has tangential and axial inlets, in this case air with tangential momentum mixes with air and gas with axial momentum in the swirl pipe. Axial swirlers generate swirl using an array of vanes to redirect the flow and apply a tangential momentum, and as such are not applicable to the geometric swirl number, a schematic of a simple axial swirler is shown in Figure 13.

Gas turbine combustors utilise axial swirlers, however they often utilise two concentric sets of vanes.

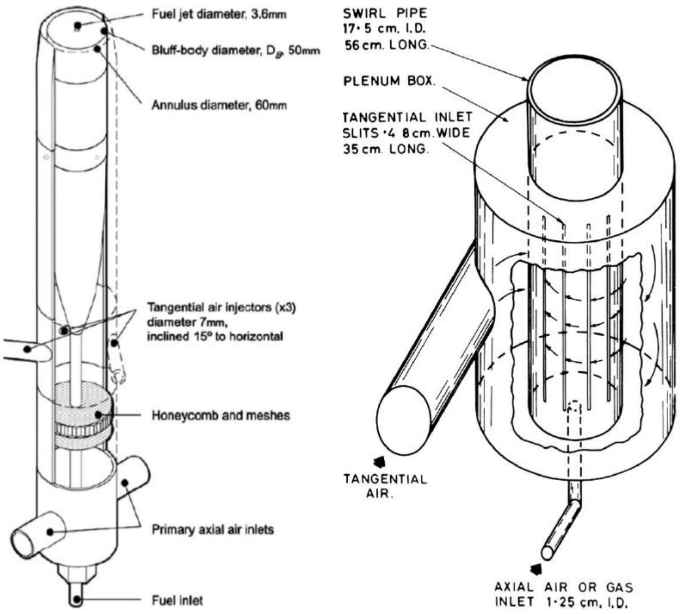

(a) *(b)*

Figure 12: Examples of radial swirl burners of varying design (a) developed by the Sydney university group (Guo B, 2003, Masri AR, 2004, Al-Abdeli YM, 2003, Al-Abedi YM, 2003) (b) as documented by Syred and Beer (1974)

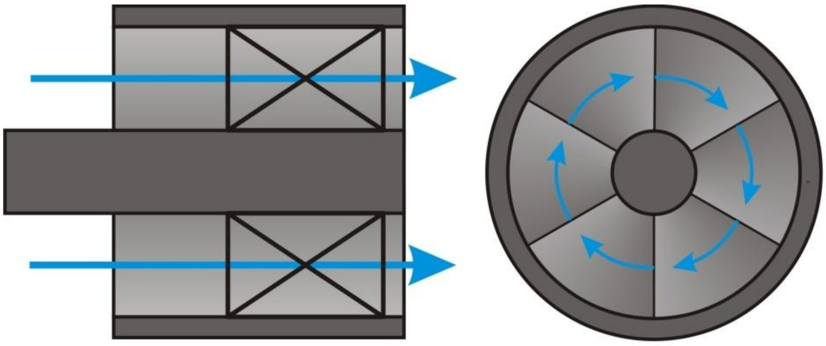

Figure 13: Schematic of an axial swirler

2.2.3 Vortex Breakdown

Vortex breakdown is a recognised phenomenon that is essential to swirl combustion as it results in the formation of a centralised recirculation zone, which will be discussed in detail later. Below the critical swirl number, believed to be around S = 0.6 (Luca-Negro and O’Doherty, 2001). The flow forms a structure resembling those observed naturally in tornadoes or typhoons, and like these structures there is a low velocity region that is encircled by a high velocity region. If the critical swirl number is exceeded then vortex breakdown or vortex bursting occurs. Faler and Leibovich (1978) used a liquid dye tracer in swirling water flows to identify seven modes of vortex breakdown, the three most distinct of which were also identified as being double helix, spiral and axis symmetric (Sarpkaya, 1971a, Sarpkaya, 1971b). Similar structures have been identified under conditions of swirl combustion (Syred, 2006), a double Precessing Vortex Core (PVC), a single PVC and a Central Recirculation Zone (CRZ) respectively. However, in swirl combustion it is established that a PVC cannot be formed without a CRZ; therefore an axis symmetric breakdown is the type of most significance. The schematic in Figure 14 (Gupta et al., 1984) demonstrates the process leading to an axis symmetric vortex breakdown, where P represents pressure, U_t represents tangential velocity and U_a represents axial velocity.

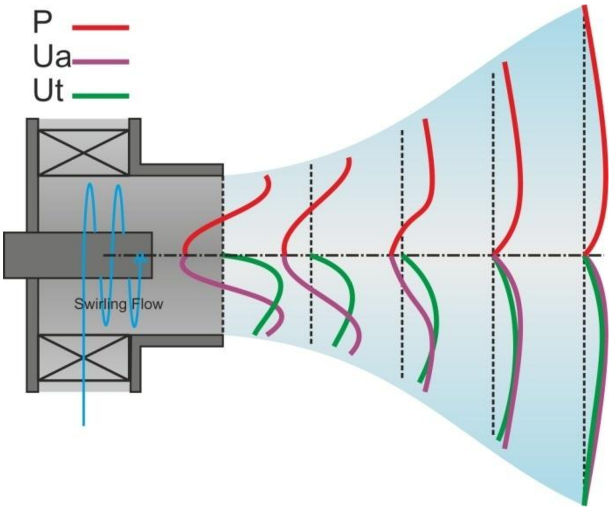

Figure 14: Schematic of the process leading to vortex breakdown, adapted from Gupta et. al. (1984)

It can be seen that there is no tangential velocity along the axis of the burner. As axial distance from the nozzle increases, the flow expands in the tangential and radial directions. This results in a reduction in velocity and an area of low or negative pressure along the central axis of the burner. When swirl number reaches its critical value the low or negative pressure exerts a force sufficient to suck fluid back toward the nozzle, creating a recirculation zone, the CRZ.

2.2.4 Flow Structures

Once vortex breakdown has occurred coherent flow structures are formed downstream of swirler, these structures have significant effect on the stability of the burner in both positive and negative ways. There has been significant work into the characterisation of structures that occur within swirling flows (Gupta et al., 1984, Valera-Medina, 2009, Syred and Beér, 1974, Syred et al., 1997, Lee et al., 2000, Froud et al., 1995). These structures have been shown to stabilise the flame, in the form of a Central Recirculation Zone (Syred et al., 1971), or be a cause of instabilities, in the form of Precessing Vortex Core.

2.2.4.1 Central Recirculation Zone

The CRZ is so named because it re-circulates both thermal energy and active chemical species in a low pressure, low velocity zone that occurs at the burner exit, also allowing turbulent flame speed to match the flow velocity. This re-circulation allows a flame to be established and stabilised (Syred and Beér, 1974, Gupta et al., 1984). Figure 15 (Beér and Chigier, 1972) shows lines of constant stream functions in a typical swirling flame, on a plane that intersects the central axis of the burner.

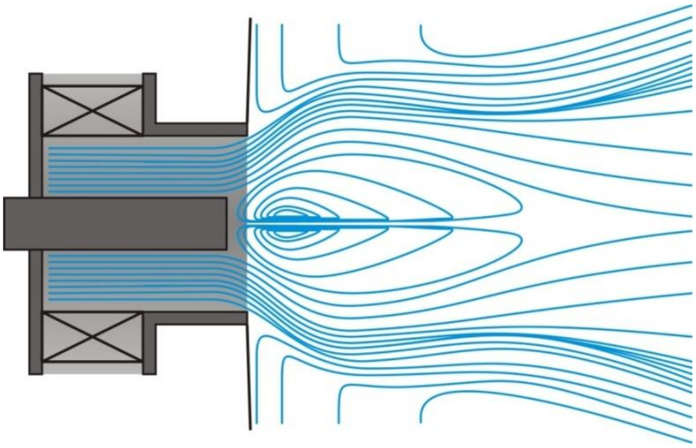

Figure 15: Stream function distribution showing a typical recirculation zone of a swirl burner, adapted from Beér and Chigier (1972)

As the swirling flow exits the burner it expands due to its tangential velocity, and in this case, together with the fuel injector, creates an area of low pressure into which low velocity swirling air is drawn, this air is then re-circulated around the central axis of the burner. It is possible to introduce fuel on the central axis of the burner in diffusion mode, or to premix the fuel into the swirling flow, where the fuel is introduced has a marked effect on the strength of the CRZ and the shape of the flame, as is shown in Figure 16.

Figure 16 (a), where all fuel is premixed into the swirling airflow, shows that upon leaving the burner exit the flame is of the same diameter. As the fuel is evenly mixed with the swirling air a relatively low percentage is entrained into the CRZ, so it does not have a strong structure, which is in complete contrast to the flame in Figure 16 (b). The axially introduced fuel does not effectively mix and produce a combustible mixture with and the swirling airflow until noticeably downstream of the burner exit, with the majority of it initially retained in the strong recirculation zone, which reaches down to the burner exit. This gives the flame the distinctive tulip shape seen in Figure 16 (b).

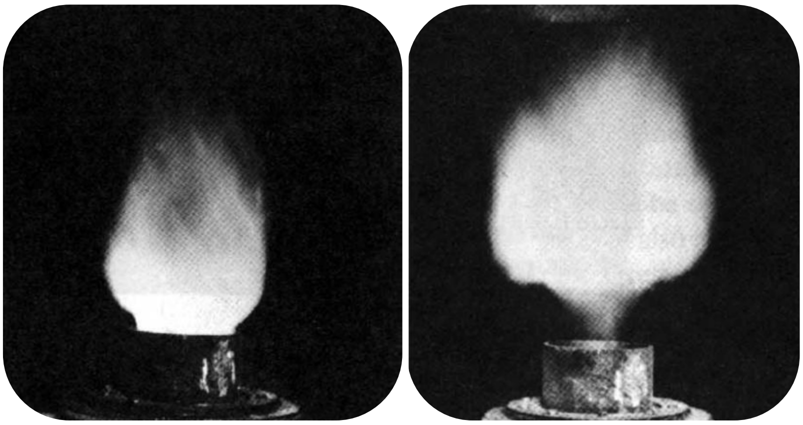

(a) *(b)*

Figure 16: The effect of fuel introduction on the shape of a flame with S = 1.8, 5% excess air with fuel (a) fully premixed and (b) injected on central axis (Syred and Beér, 1974)

2.2.4.2 Precessing Vortex Core

The PVC is a three dimensional, time dependant, rotating hydrodynamic instability that occurs as soon as a swirl generated CRZ is formed (O'Doherty et al., 1999), developing when the CRZ starts to precess around the central axis of the burner at a well defined frequency (Huang and Yang, 2009). The presence of a PVC distorts the shape of the CRZ so that its profile becomes that of a crescent, rather than annular. The two structures then rotate around the burner exits central axis in the direction of the prominent swirl, as shown in Figure 17. The axial loss of tangential momentum and velocity causes the structure of the PVC to become helical about the central axis of the exit nozzle, this helical structure is shown in Figure 18 (a). When compared with an image of a PVC in a premixed flame in Figure 18 (b) its helical nature is visible, but is not as prominent as the exaggerated visualisation in (a).

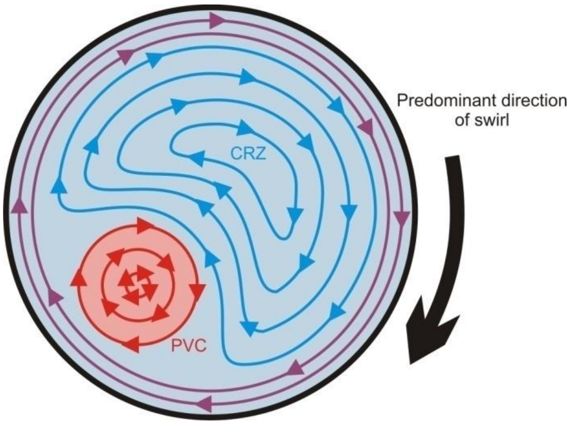

Figure 17: Flow patterns of a PVC and CRZ pairing, adapted from Syred (2006)

The mechanisms that result in the manifestation of the PVC are not known conclusively, however theories do exits. Yang and Lieuwen (2005) believed it to be a series of small eddies that are generated by the CRZ, similarly Paschereit and Gutmark (2006) claimed that Kelvin-Helmholtz vortices, produced by inequalities in momentum and density, found a common path energized by the CRZ. Aleseenko (1999) gave ideas it was a manifestation of the compressing-expanding mechanism in the inner part of the structure. Despite the mechanism of its manifestation being unclear, as is its influence on the combustion system as a whole, it is known to provide a route of rapid transport of fluid through the flame's recirculation zone (Valera-Medina, 2009) and has a fundamental role in flame stability (Syred, 2006).

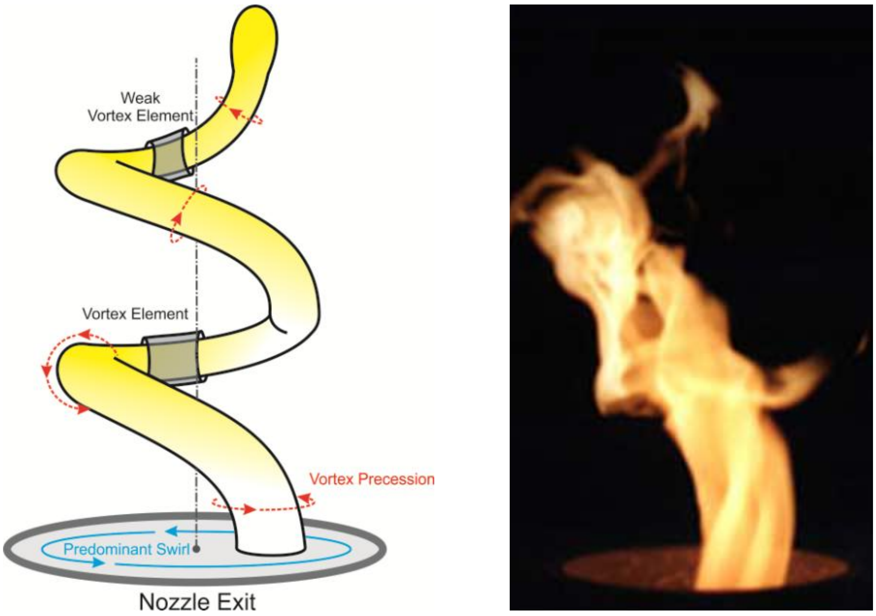

(a) *(b)*

Figure 18: Visualisations of the PVC (a) its helical nature (b) with axial injection into a premixed flame adapted from Fick (1998)

With regards to the current studies, the effect the PVC has on pressure fluctuations inside the burner is very important as they can have a significant effect on burner stability as they couple with other oscillations within the system. The frequency of the PVC can be characterised by Strouhal and swirl numbers (Gupta et al., 1984, Syred and Beér, 1974, O'Doherty T, 1994, Syred N, 1994, Sprruyt, 1972, Chanaud, 1962), the Strouhal number being a weak function of Reynolds number. Fick (1998) showed, using a pressure transducer mounted in the burner nozzle, that the PVC would create pressure fluctuations at the same frequency that it rotates around it.

The PVC may be severely dampened under combustion conditions, having a significant effect on the resulting pressure fluctuations. Work using a radial swirl burner (Claypole, 1980b, Claypole, 1980a, Claypole and Syred, 1980) showed how fuel injection played a crucial role in defining the strength of a PVC by comparing the resulting pressure fluctuations under isothermal and combustion conditions. Figure 19 (a) shows that when fuel is injected axially the amplitude of pressure fluctuations of the PVC are reduced significantly, by up to a factor of 15. However, premixing the fuel is shown to have a minimal effect on its strength, Figure 19 (b) showing under most conditions actually increasing it.

The frequency recorded may also be affected by the presence of a second precessing vortex as was also investigated by Claypole and Syred (1980). A double PVC is the result of a type of vortex breakdown similar to that identified as double helix breakdown, but does not necessarily occur at the initial breakdown phase (Sarpkaya, 1971a, Sarpkaya, 1971b, Faler and Leibovich, 1978).

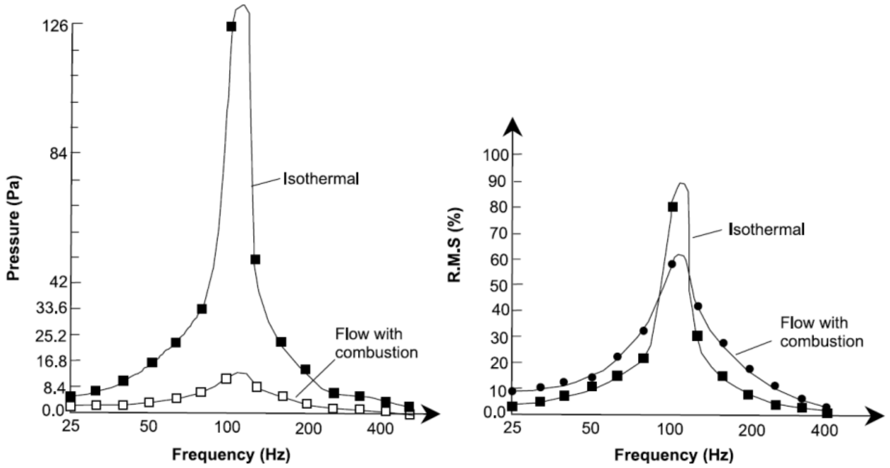

(a) *(b)*

Figure 19: Effect of combustion on the PVC (a) diffusive fuel (b) premixed fuel (Claypole, 1980b, Claypole, 1980a, Claypole and Syred, 1980)

Figure 20 (a) shows that vortex breakdown and the presence of a PVC only occurs above the critical geometric swirl number of 0.3 and critical flow rate of 0.6 m^3/min, which is equivalent to a Reynolds number of 40,000. When S_g is in the range 0.8 to 1.8, and when flow rate is sufficient, a second PVC is developed of equal intensity. Images of a double PVC formation were captured using a high speed camera. A reflective surface allowed axial and radial views to be taken simultaneously; they are shown in Figure 20 (b). They show the symmetrical nature of the formation which results in a second harmonic in the acoustic response.

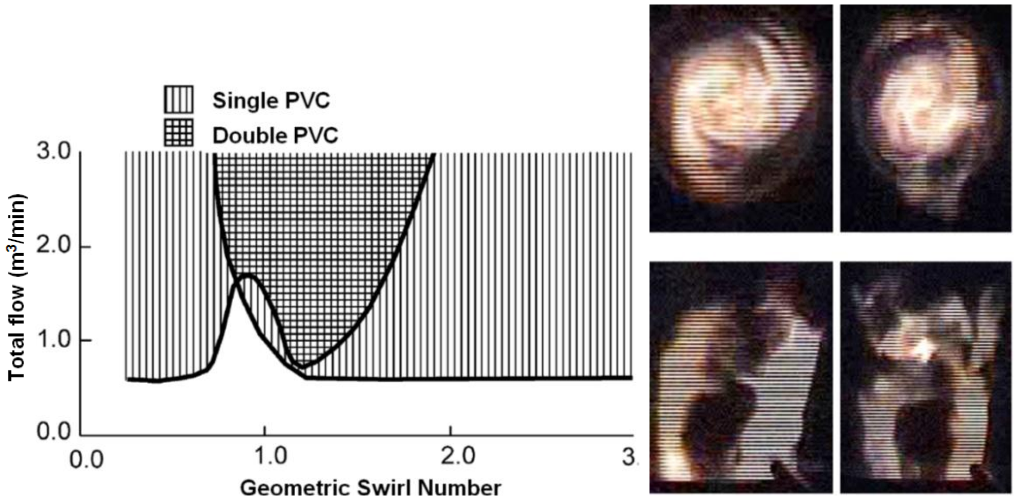

(a) *(b)*

Figure 20: The presence of a double PVC as identified by Claypole (Claypole and Syred, 1980, Claypole, 1980b, Claypole, 1980a) (a) occurrence for a range of swirl numbers and flow rates (b) image pairs simultaneously taken axially and radially

2.2.4.3 Edge Recirculation Zone

An Edge Recirculation Zone (ERZ), sometimes referred to as the corner recirculation zone, is former by the sudden expansion of flow when the burner nozzle terminates in a combustion chamber of greater diameter. Like the central recirculation zone it is formed by areas of low pressure causing the direction of the flow to change, it is also annular; the flow patterns for both recirculation zones are shown on the left hand side of Figure 21.

Although it is not crucial for stability like the CRZ, the ERZ also re-circulates hot unburned gases into the reactant mixture (Coghe et al., 2004). The presence of an ERZ can be eliminated via combustor design, as shown on the right hand side of Figure 21, where the lack of a corner prevents a low-pressure zone forming.

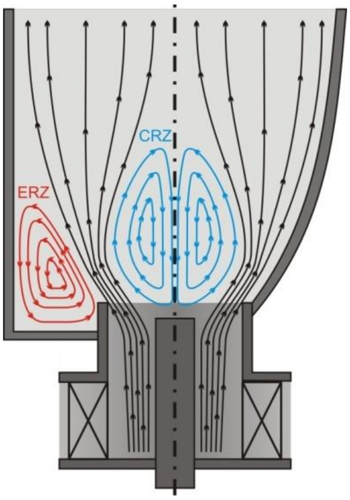

Figure 21: Indication of flow patterns of Central and Edge Recirculation Zones

2.2.4.4 Mixing and Shear Layers

The mixing layer in a flame defines where the un-ignited mixture meets the flame front and the ignited mixture, a velocity gradient exists across it which is related to the stability of the flame (Dhanuka et al., 2009). The position of the mixing layer is shown in Figure 22 (b).

Strong shear layers develop where the high velocity swirling flow meets the relatively stagnant fluid in the combustion chamber. This shear layer produces regions of low velocity flow, and can allow the flame to propagate back to the combustor nozzle. The further downstream, the greater the fluid velocity is reduced, increasing the thickness of the shear layer; evidence of this is shown in Figure 22 (a), its position shown more clearly in Figure 22 (b). The diameter of the low velocity region in the centre of the flow also increases as the distance from the combustor nozzle increases, this can been seen in Particle Image Velocimetry (PIV) data taken from a gas turbine combustor in Figure 23. The radial magnitude, which is indicative of overall magnitude, is highest in Figure 23 (a), at a distance from the burner exit which is equal to 0.045 of its diameter. The scalar plots indicated radial velocities reaching 65 m/s, the shear layer where the swirling flow mixes with the air and products in the combustion chamber is very thin. Progressing downstream in (b) and (c) the peak velocities reduces and the shear layer thickness increases. At 0.45 diameters downstream, shown in (d), the peak radial velocity has reduced to 56 m/s.

The result being that the annulus where overall flow velocity is too great for the flame to propagate into reduces in thickness the further downstream the fluid is. For the flame in Figure 22 (a) the conditions are such that the low velocity flammable regions of the flames main body and shear layer meet up allowing the flame to propagate.

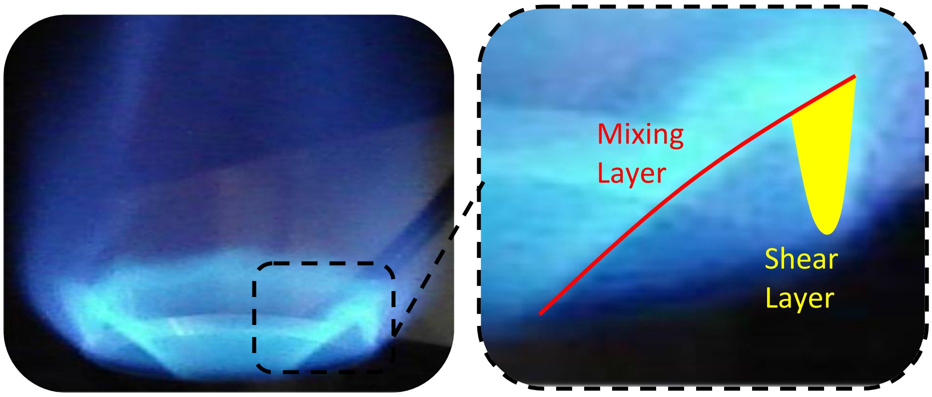

(a) *(b)*

Figure 22: Shear layer propagation in a swirling flame as seen by Syred et.al. (2012). (a) shows the full flame and (b) shows an indication of the mixing and shear layers

Once propagation through the shear layer has been established, flashback can occur via the further propagation through the outer wall boundary layer of the combustor nozzle, being controlled by critical velocity gradient (Bagdananvicius et al., 2010) as defined by Lewis and von Elbe (1987).

The mixing layer that exists between the pilot flame and the main fuel mixture (Dhanuka et al., 2009) ensures that equivalence ratio in the shear layers is not affected by that of the pilot.

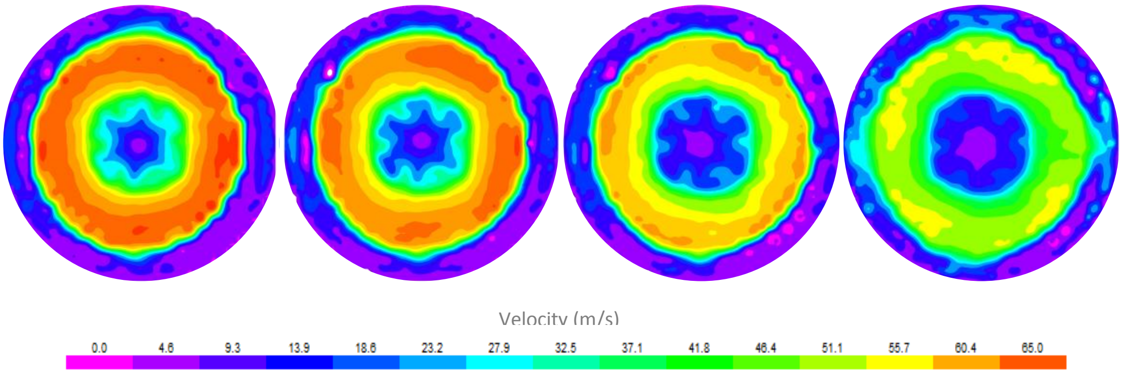

(a) *(b)* *(c)* *(d)*

Figure 23: Radial magnitude plots of combustor at (a) 0.045D (b) 0.09D (c) 0.23D (d) 0.45D from nozzle exit (Morris, 2012)

Where these layers occur so does the Kelvin-Helmholtz instability, which results in eddies appearing in the flow. These instabilities are the result of either a velocity shear in a single continuous fluid or when two fluids of different velocities pass over each other. The result is a wave like formation caused by friction and fluid tension; both examples are seen frequently in nature. Velocity shear in a single fluid is shown in Figure 24 , where shearing winds result in this particular type of turbulence, with cloud entrainment acting as an indicator.

(a)

Figure 24: Kelvin-Helmholtz instabilities occurring in nature caused by shearing winds (customhouse, 2012)

These instabilities can lead to structures forming in the flow, as previously mentioned. Paschereit and Gutmark (2006) believe that they are the fundamental source of the PVC. These development and breakdown of these structures may lead to periodic heat release capable of driving pressure fluctuations (Schadow and Gutmark, 1992). The shear driven instability and the modulations in the mixture result in distinct modes over a wide frequency range (Fritsche, 2005).

2.2.5 Combustion Induced Vortex Breakdown

Combustion Induced Vortex Breakdown (CIVB) is a phenomena that can be, but should not be, confused with Vortex Breakdown. Whereas, as it was earlier established, vortex breakdown is the fundamental cause for the induction of a central recirculation zone, CIVB is the cause of its destruction. Some researchers (Valera-Medina, 2009, Valera-Medina et al., 2009, Valera-Medina et al., 2011a, Valera-Medina et al., 2011b, Valera-Medina et al., 2012, Stöhr et al., 2012) have observed that the CRZ has a close connection to the stability of the system, with its shape, strength and curvature being of high importance to its resistance to flashback and blowoff (Valera-Medina et al., 2012, Kedia and Ghoniem, 2012). Therefore it stands to reason that in the interest of flame stability CIVB should be avoided. Indeed CIVB has been identified, in a series of papers (Lieuwen et al., 2008, Fritz et al., 2004, Kroner, 2002, Kroner et al., 2003) as being one of the four causes of flashback, namely (i) boundary layer flame propagation, (ii) turbulent flame propagation in the core flow, (iii) thermo acoustics and (iv) upstream flame propagation of coherent vortical structures via CIVB. Although it could be argued that CIVB also plays its part in boundary layer and turbulent flame propagation by augmenting the position of the flame in a way that makes them happen more readily (Lewis et al., 2014).

Dam et al. (2011a) demonstrated combustion induced breakdown of vortices as a result of the high velocity zones of a flame squeezing the recirculation zone, causing the CRZ to propagate upstream and vortex breakdown to continue until the flame becomes attached to swirl injector. This squeezing of the recirculation zone is shown in Figure 25, where equivalence ratio in the images increased left to right, then top to bottom. The flame was initially stabilised downstream of the tip of the burner’s centre body, two high velocity flame zones are visible, there are also visible vortices, V_1, V_2, W_1 and W_2, propagating through the recirculation zones. As the equivalence ratio increased, the recirculation zone visibly increased in size. Once the equivalence reached a critical level the recirculation zone became squeezed and ultimately broke down, inducing a flashback.

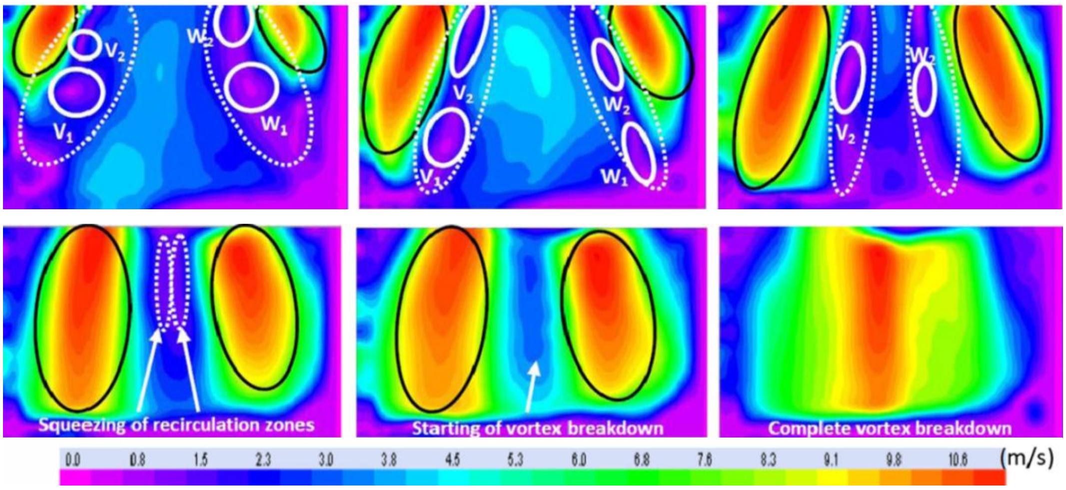

Figure 25: Sequence of a CIVB flashback for a fuel mixture of 10% H_2 and 90% CO with S = 0.97; areas enclosed by solid black, dotted white, and solid white lines represent the approximate location of flames, recirculation zones, and vortices, respectively (Dam et al., 2011a)

2.3 Thermo-acoustic Instabilities

There is a significant challenge posed by the large variety of thermo-acoustic responses that may appear in a combustion system, resulting from equally varied dynamic properties, even in static systems. Inside the scope of this project thermo-acoustic instabilities are unwanted effects of a combustion process that can lead to the extinction of flames and damage to combustion systems, the mechanisms of initiation and the detrimental effects of which will be discussed. However, there are several applications where these sustained instabilities are utilised to achieve a greater level of performance, including pulse combustors, ramjets and scramjets (Hathout, 2012, Lieuwen and McManus, 2003)

When compared with steady combustion, pulse combustors have the potential to deliver higher efficiency and combustion intensity whilst keeping pollutant emissions very low (Dec et al., 1990). There are three fundamental pulse combustor types, each being applicable to a certain fuel type. Schmidt combustors and Rijke tubes are used with liquid and solid fuels respectively, whilst Helmholtz resonators are used where the fuel is gaseous. As the name suggests the combustion process is intermittent, resulting in a pulsing pressure and heat release, utilising the thermo-acoustic coupling that can be so destructive in a swirl combustion system. Thermo-acoustic instabilities refer to large amplitude oscillations of pressure, heat release, velocity and other variables inside the combustion chamber, which often occur at discrete frequencies associated with the natural acoustic modes of the combustor (Lieuwen, 2012a). They represent a major challenge with regard to the design of combustion systems as their occurrence is incredibly difficult, or even impossible to predict as they are the result of a spontaneous excitation of a feedback mechanism that exists between unsteady heat release and a natural acoustic mode of the system itself (Mohammad et al., 2012, Lieuwen, 2012a).

The high pressure fluctuations that can result are capable of causing flame extinction, through either flashback or blowoff, or, for gas turbines in particular, oscillatory mechanical loads that lead to high cycle fatigue in system components and an uneven thermal distribution in the exhaust gases. Impending flame extinction events, as well as potentially being caused by fluctuations in pressure, are also the result of changes in the equivalence ratio of the reactant mixture, whether it is caused by a change in fuel composition or air-to-fuel ratio. The consequential effect on flame speed is another one of many factors that have the potential to induce thermo-acoustic instabilities (Lieuwen et al., 2008). Other factors are vibration phenomena, wall thermal stresses and reduced combustion efficiency. All contribute to compromise the structural integrity and performance of the combustor (Fichera et al. 2001). Regardless of combustion conditions, be they stable or not, in any practical combustion system, oscillations will always exist, a theory prescribed to by Putnam as far back as 1971 (Putman, 1971). The type of oscillations can be grouped into three rough categories:

- Stable combustion produces small amplitude pressure oscillations; they are typically less 5% of the chamber pressure.
- Rough combustion produces large amplitude pressure fluctuations with no distinct pattern.
- Unstable combustion produces large amplitude pressure oscillations with a well defined frequency.

2.3.1 Mechanisms and Saturation

The onset of thermo-acoustic instabilities was first theorised by Lord Rayleigh, who defined a criterion for positive coupling based on a phenomenological, heuristic description of said instabilities (Hathout, 2012, Fritsche, 2005). It is established that there are always unsteady combustion process' present in a combustion system with turbulent flows, the mechanism of coupling between these heat release oscillations and perturbations in the flow and mixture is what leads to acoustic oscillations in the combustion process, as shown in Figure 26.

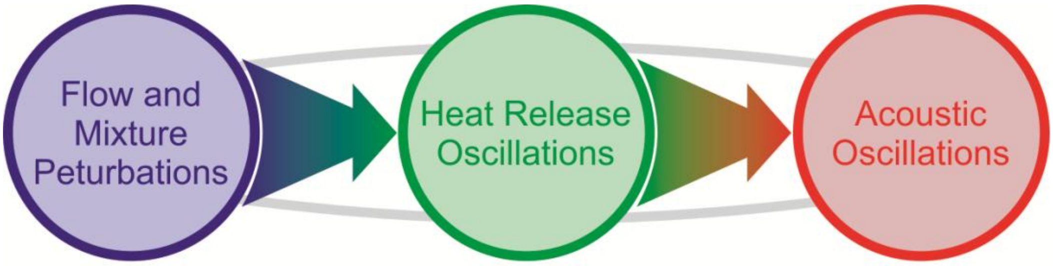

Figure 26: Heat release and flow perturbations causing acoustic oscillations, adapted from Lieuwen (2012a)

As was previously discussed, acoustic oscillations do exist under stable combustion conditions; as such, their presence does not necessarily indicate a present or impending instability. In order for an instability to develop a feedback mechanism must exist, depicted in Figure 27. This consists of a generic sequence of events (Lieuwen, 1999, Lieuwen, 2012a).

- Fluctuations in some flow or thermodynamic variable e.g. velocity, pressure, Air-to Fuel Ratio (AFR) etc. excites a fluctuation in heat release.
- The unsteady heat release triggers acoustic oscillations that propagate away from the combustion region.
- The acoustic oscillations generate the flow and thermodynamic disturbances.

The effect of coupling is amplified by the Rayleigh criterion (Syred, 2006, Lefebvre and Ballal, 2010), which emphasises the importance of phase relation in driving the oscillations to the point of instability and describes the mechanism responsible for limit-cycle heat driven oscillations in addition to the relationship between the pressure wave and heat release (Lord Rayleigh, 1896).

The phase relationship between the heat release oscillations and the acoustic oscillations is fundamental to the feedback process resulting in an instability (Fritsche, 2005). The energy added to the acoustic pressure wave by the heat release must be in phase, so the instantaneous peak in acoustic pressure in the combustion zone must coincide with the instantaneous peak in heat release, regardless of frequency. Actually the instantaneous peaks do not need to be perfectly aligned, with feedback mechanism occurring if the magnitude of the phase between the unsteady acoustic oscillations and the unsteady heat release oscillations is less than 90 degrees (Farhat and Mohamed, 2010, Lieuwen, 1999).

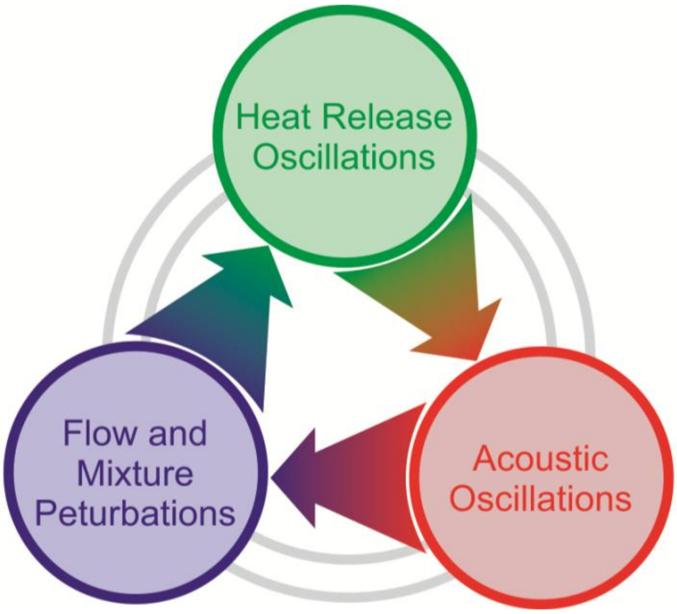

Figure 27: Feedback mechanism for thermo-acoustic instabilities, adapted from Lieuwen (2012a)

Conversely, energy is removed from the acoustic pressure oscillations when the heat release oscillations in the combustion zone are in the range of 90 to 180 degrees out of phase. Without an acceptable phase relation, the interactions between perturbations in the flow and mixture, and oscillations of heat release or acoustics will destructively interfere with each other, as a result thermo-acoustic instability will not occur (Lieuwen, 1999).

When the amplitude of the acoustic pressure oscillations reach their maximum value the instability is said to be saturated, at this point the time average of energy addition is equal to the time average of energy dissipation by the process of damping. When understanding thermo-acoustic instabilities knowledge of the saturation mechanism is just as important as that of the initiation and amplification (Fritsche, 2005), the time evolution of the acoustic oscillations is shown in Figure 28.

When the oscillations reach their peak amplitude they are termed limit cycle oscillations (Lieuwen, 2012a), the characterisation of which are influenced heavily by the non-linear processes that saturate the unstable amplitude (Fichera et al., 2001).

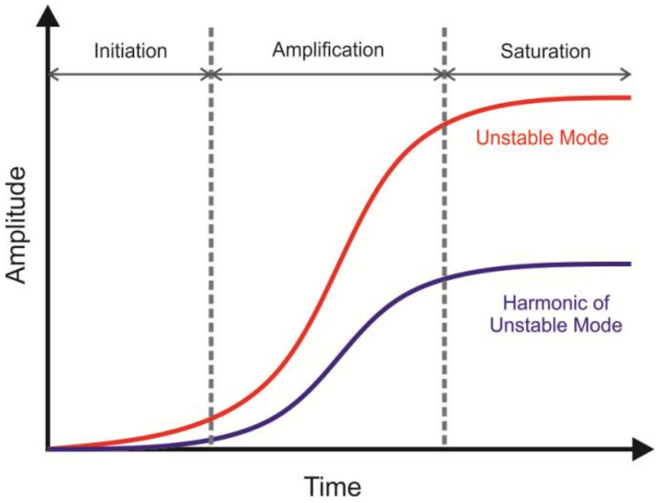

Figure 28: Initiation, amplification and saturation of unstable mode over time, adapted from Lieuwen (2012a)

2.3.2 Control

Sustained instabilities are the result of a maintained presence of the feedback mechanism outlined in Figure 27. During the design and development of a burner the onset and effect of these instabilities is exceptionally hard to predict, the potential problems posed by these instabilities has warranted the advancement of solutions to try and suppress these oscillations (Noiray and Schuermans, 2012). The suppression of the oscillations, and effective elimination of the thermo-acoustic instabilities, involves interrupting the feedback loop between the interaction of the heat release and acoustic oscillations (Huang and Yang, 2009). Two approaches have been adopted in developing systems to prevent this feedback occurring; passive methods and active control systems (Lefebvre and Ballal, 2010, Farhat and Mohamed, 2010, Stone and Menon, 2002).

2.3.2.1 Passive Techniques

Passive techniques are those which work to prevent the formation of instabilities independently of time, their form is fixed, and as such they do not offer a dynamic response to changes that may occur during the combustion process (Farhat and Mohamed, 2010). Passive techniques have been widely adopted in industrial burners for decades, as well as other fields, to increase a systems acoustic dampening by modifying hardware components, effectively reducing the amplitude of pressure oscillations (Lefebvre and Ballal, 2010). This reduces the rate at which energy is transferred to unsteady motions, preventing the acoustic oscillations contributing to the feedback mechanism and opening the feedback loop, preventing instabilities developing.

Acoustic dampers are widely used, in various forms. Helmholtz resonators are used in many architectural type systems, like internal combustion engines in the exhaust and induction system. They are the acoustic equivalent of a mass damper system, tuned to a specific frequency, as such they can effectively target a narrow band of noise, working most effectively at their particular tuned frequency, and as such act a band reject filter.

Quarter wave tubes are also narrow band reject filters, working most effectively at their tuned frequency. They are used in induction and exhaust systems as well as being used in pump pulsation abatement and other applications. The tubes are cylindrical, with one end open to the acoustic environment, the length of which is one quarter the length of the wavelength of noise that is being damped. In travelling the length of the tube twice the waves experience a 180 degree phase shift, abating the target noise.

Perforated acoustic liners are used in industrial mufflers and in the nacelle of aircraft engines. They consist of a solid backing separated from a perforated lining, as such they act like a large number of Helmholtz resonators, covering and providing acoustic damping over a large area. Perforated liners are well suited to high temperature applications as cooling flows can be passed between the perforated sheet and the solid backing.

Acoustic damping methods such as Helmholtz dampers have been researched by Noiray and Schuermans (2012), whilst Tran et. al. (2008) have investigated perforated sheets and Gysling et. al. (2000) Helmholtz resonators. However, the majority of researchers now prefer to avoid passive techniques, as they cannot adapt to dynamic system changes, and are effective over a narrow frequency band, preferring to focus on active control (Stone and Menon, 2002).

2.3.2.2 Active Techniques

All active control systems dynamically detect and correct for insipient instabilities. However the techniques employed to do this vary in regard to the their theoretical basis and the hardware employed (Lefebvre and Ballal, 2010). The goal of the systems is to reduce the instantaneous error between desired and actual behaviour of the system. A sensor detects present or impending instabilities in the combustion process, the closed loop control system then modifies one or more of the input parameters to introduce external excitations, such as acoustic forcing or fuel/air flow modulations. The aim is to interrupt the coupling between acoustic pressure oscillations and unsteady heat release and prevent the instability occurring (Huang and Yang, 2009).

Varying success has been achieved using active control mechanisms. Candel (2002) reported that research has focused on sensors, actuators, and control algorithms, with limited success being achieved in scaling from laboratory experiments to practical devices. Laboratory scale studies have shown that it is possible to reduce the amplitude of thermo-acoustic instabilities via active control, with application to full-scale gas turbines resulting in an increased stability margin.

Active control is applied using a closed loop control system, as shown in Figure 29. A sensor, whether it is a remote pressure transducer or external microphone, detects oscillations in the combustion zone. A control unit then uses an actuator to influence the input parameters to the system in order to reduce the amplitude of the perturbations and oscillations in the system.

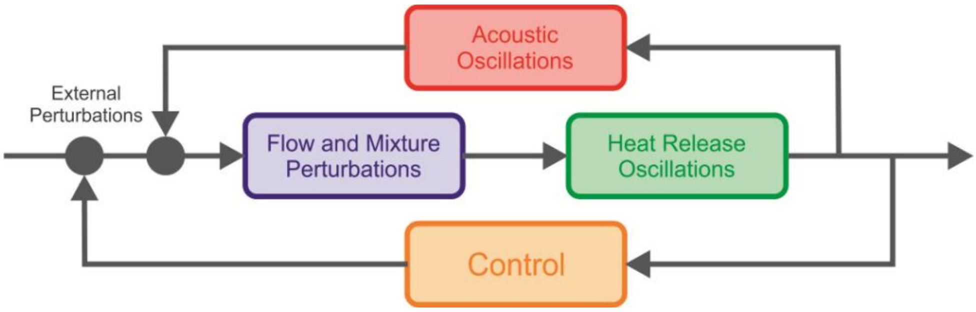

Figure 29: Schematic of thermo-acoustic feedback mechanism with active control loop, adapted from Candel (2002)

The strategies, sensors and actuators used can have a great deal of variety, Tachibana et.al (2007) used secondary fuel injection in order suppress combustion oscillations in a model lean premixed combustor. Similarly Yi and Gutmark (2008) found that sinusoidal or steady air forcing of the swirling air shear layer or fuel line could reduce the pressure oscillations. Paschereit et al. (1998) employed a closed loop method of altering acoustic boundary conditions which dampened pressure oscillations and reduced NO_X emissions in an experimental low-emission swirl-stabilised combustor.

2.3.3 Gas Turbine Thermo-acoustics

Gas turbine combustors, operating with a lean premixed flame, are highly susceptible to thermo-acoustic oscillations, significantly more so than systems that use a diffusion flames, due to several characteristic features (Lieuwen and McManus, 2003, Kelsall and Troger, 2003, Delaat and Paxson, 2008). Three significant characteristics are equivalence ratio, system damping and combustor length:

- In order to reduce the combustion temperature, and thus NO_X emissions, the combustors operate close to the flames lean blowoff limit (Bender, 2012, Nair et al., 2002), so small perturbations in heat release are capable of causing large pressure oscillations.
- There is also the absence of dilution air and cooling liners, which suppress resonant amplifications (Huang and Yang, 2009) and act as efficient acoustic dampers. This results in a reduction of system damping (Delaat and Paxson, 2008). The lack of an inherent damping mechanism makes the flame more

prone to both static and dynamic instabilities and allows small perturbations to escalate to large pressure oscillations. The flames are also more sensitive to acoustic excitations from sound waves, with flame response dependant on the nature of the acoustic waves, as well as its frequency, amplitude and phase (Syred, 2006).

- The length of lean pre-mixed combustors is relatively short, reducing the likelihood of blowoff, this results in a flame that is short when compared to the longitudinal acoustic wavelength of the chamber (Huang and Yang, 2009), helping interaction between the motion of the flow and the heat release of the flame.

Injector design is also a potential cause of increased thermo-acoustics. In gas turbines they promote intense turbulence levels and a uniform temperature distribution, the result of which is an acoustically homogenous system (Delaat and Paxson, 2008).

Two coupled processes have been identified as being responsible for the propensity of combustors to thermo acoustic instabilities (Culick and Yang, 1995, Lieuwen and McManus, 2003). The fundamental reasoning being the coupled process is the same as that previously described, the flames are very sensitive to acoustic perturbations due to their proximity to the lean blowoff limit, and as such only a small fraction of the energy released by the combustion process is required to drive unsteady motions in the flame. The combustion chambers are also acoustically closed, so any sounds generated inside the chamber are reflected rather than dispersed. The resulting fluctuations in pressure disturb the flame and its rate of heat release by introducing oscillations. These waves generate acoustic waves, which are reflected and re-impinge in the flame, which, given an adequate phase alignment will result in an increase in the amplitude of the oscillations, in other words the system is inherently lacking in damping.

The initial cause of the instabilities, which could derive from either pressure or heat release oscillations according to Huang and Yang (2009), can come from various sources. Some are caused by fluctuations in the air supply to the combustion system. Some by aerodynamic disturbances that are formed inside the combustion chamber itself, the rest are due to poor fuel distribution throughout the combustion chamber which results in local extinction and re-ignition in the flame zone (Lefebvre and Ballal, 2010). Variations in these causes identified by Candel (2002), Fritsche (2005) and Lieuwen (1999) include a non-uniform flame front area, caused by fuel-air oscillations, acoustic coupling between the combustion zone and the fuel line, varying turbulence intensity, mixing rate fluctuations and a periodic change in fuel composition.

2.3.3.1 Predicting Instabilities

According to Lieuwen (2005) it would be highly desirable for a gas turbine operator to have a quantitative description of stability margins of a system, or a how it would react to variable operating conditions, without having to operate in an unstable mode. Similarly, a major obstacle preventing the implementation of advanced flame optimisation strategies is the risk that unstable operation or blow out may occur (Ballester and Garcia-Armingol, 2010).

There has been a great deal of research aimed at investigating instabilities at various operating conditions and parameters. The prevalence of high amplitude and low frequency oscillations is repeatedly identified, as is the fact that predicting their onset is still a great challenge (Lieuwen, 2012a, Abbott et al., 2012, Bender, 2012, Candel, 2002, Farhat and Mohamed, 2010, Fichera et al., 2001, Fritsche et al., 2007, Gysling et al., 2000, Hathout, 2012, Huang, 2003, Huang and Yang, 2009, Lieuwen, 2012b, Lieuwen and McManus, 2003).

There are many complexities that prevent this prediction, including; interactions between the flame, present acoustics and vortices or structures, all of which may affect the mixing of the air and the fuel and chemical kinetics (Yi and Gutmark, 2008). This being the case, there is a lack of reliable flame models capable of predicting relevant combustion parameters whilst accounting for operating conditions, burner settings or the transient response to other variables (Ballester and Garcia-Armingol, 2010). Various approaches have been applied to predict and control instabilities, Lieuwen (2005) proposed an original approach in which processing the autocorrelation of the signal from pressure waves could be used to assess the damping coefficient of a system. When the damping coefficient is positive then the system is stable, as it approaches zero the system approaches its stability limit, and if negative, it is unstable. Yi and Gutmark (2008) calculated damping ratios in the frequency domain using the excited acoustic modes and a weighted least square algorithm. Nair et al. (2002) used spectral, statistical and wavelet data analysis techniques to predict blow out in a piloted premixed flame by detecting its precursors.

2.3.3.2 Classification

One classification of combustion instabilities relates to the primary driving factor behind the instability, system, chamber and intrinsic instabilities (Valera-Medina, 2009, Huang, 2003);

- System instabilities are when system effects interact with combustion dynamics.
- Chamber instabilities are triggered by hydrodynamic instabilities, shock dynamics, or acoustic disturbances, and relate to the acoustic character of the combustion chamber which is a function of its geometry.
- Intrinsic instabilities are wholly dependent on combustion kinetics. They can be triggered without external influence and exist irrespective of confinement (Candel, 1992).

With regard to gas turbine combustion thermo-acoustic instabilities can be classified by the frequency of their oscillations, and this is the prevailing general approach. Frequency bands exist to categorise them as low frequency, intermediate frequency and high frequency (Huang, 2003, Huang and Yang, 2009).

The precise ranges of these bands is open to debate and will have a certain degree of variance depending on the combustion system. As a general rule, low frequency instabilities are those which occur below 30 Hz. They are likely to be related to the blowoff phenomena when equivalence ratio is low. The low frequency heat release fluctuations that are the result of extinction and re-ignition that occurs and tend to be of high amplitude.

The frequency range of intermediate instabilities is 100 to 1000 Hz; they are caused by a coupling of the air-to-fuel ratio and acoustic oscillations, corresponding to the combustors longitudinal acoustic modes. Any instabilities above 1000 Hz are termed high frequency and are the result of the flame's evolution and acoustic disturbances. They are related to the tangential acoustic modes of the combustor, and with the potential to cause swift engine hardware failure are of a great concern.

2.4 Fuel Compositions

2.4.1 Natural Gas

When first extracted, natural gas contains oil and water, both of which require removal. After this, the composition of the dry natural gas is highly variable, as shown in Table 3. Post drying the gas goes through the processes of acid gas removal, dehydration, mercury removal and nitrogen rejection. A turbo-expander and de-methaniser are employed prior to the gas being sent to the sales gas pipeline in order to keep the percentage of methane in the gas as high as possible. This potential for differing compositions, along with differing operations in the gas processing facilities gives potential for composition changes in the composition of gas in the supply pipelines.

This being the case, countries have produced regulations to specify the requirements of the natural gas supply by providing upper and lower limits for Wobbe Index (WI). The WI considers the energy density of the fuel under normalised pressure and temperature conditions (Ranga Dinesh et al., 2014), and is calculated as stated in Equation 2.9, where relative density equals the density of the fuel divided by the density of air:

$$WI = \frac{CV}{\sqrt{\rho_r}} \qquad \text{Eq. (2.9)}$$

Where: CV = Calorific Value (MJ/m^3)

ρ_r = relative density (-)

The upper and lower Wobbe Index limits of eight European Union member countries are shown in Figure 30. It shows that the range of composition allowed is greater than typically observed variations (Abbott et al., 2012), and due to the sources of natural gas utilised by different countries has resulted in the large variance in the regulatory limits, with the Dutch upper limit only slightly exceeding the Danish lower limit. There is now a large amount of international trade in natural gas, in the UK North Sea gas production is in decline, whilst the import of LNG from Russia has increased significantly, and will continue to do so (National Grid, 2011). This being the case there has been an effort made to standardise regulations for natural gas supply within Europe by the European Commission.

Table 3: Typical composition of unrefined natural gas (naturalgas.org, 2010)

Methane	CH_4	70-90%
Ethane	C_2H_6	0-20%
Propane	C_3H_8	
Butane	C_4H_{10}	
Carbon Dioxide	CO_2	0-8%
Oxygen	O_2	0-0.2%
Nitrogen	N_2	0-5%
Hydrogen sulphide	H_2S	0-5%
Rare gases	A, He, Ne, Xe	trace

The European Association for Streamlining of Energy Exchange (EASEE) established a sub-group, EASEE-Gas, to “develop and promote the simplification and streamlining of both the physical transfer and the trading of gas across Europe” (EASEE-Gas, 2005). The limits set out by EASEE-Gas, shown in Figure 30, are still very wide, with the potential for 15% variance in Wobbe Index, this is sufficient to cause significant problems for gas turbine operators and manufacturers.

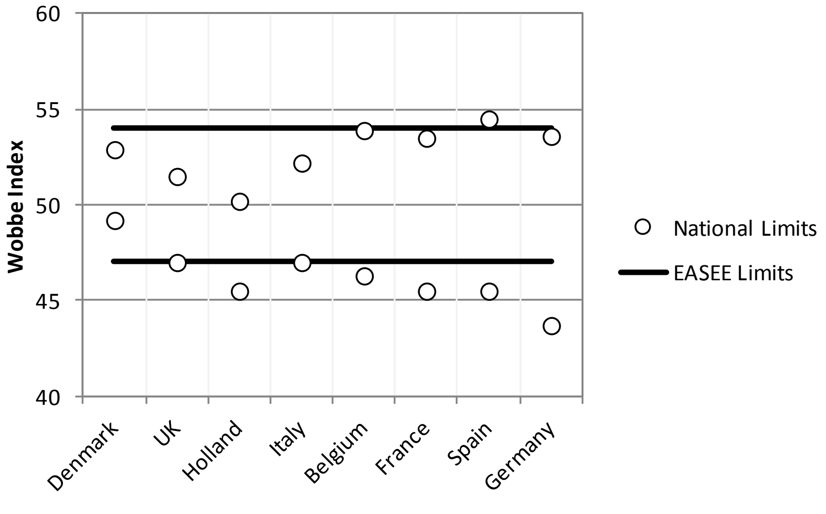

Figure 30: European regulations for Wobbe Index limits, at 15°C, 1atm (Groenendijk. W, 2006, EASEE-Gas, 2005)

Gas turbines in general can be run on a great variety of fuels, with markedly different specifications; however a specific turbine has a very limited acceptable range for fuels. Before the regulation of emissions gas turbines used to use diffusive injectors, which is a very stable method of combustion, capable of supporting large changes in fuel composition. However, regions of particularly intense heat cause high a high emission of nitrous oxides, to avoid this, modern gas turbines utilise lean pre-mixed combustion. Premixed combustion is susceptible to flashback and blowoff, and both of these more likely to occur when high levels of combustion dynamics or thermo-acoustic instabilities occur. Because of this combustors tend to be tuned to quite a specific operating range. Manufacturers also specify limits in terms of heating value and other bulk fuel properties, and typically specify an operating range that is in excess of ± 10% of mid range values. In order to achieve such a broad range the gas turbine may require re-tuning, including some hardware changes. A typical, tuned, installation range would be ± 5%, and some may be as low as ± 2% of the specified fuel properties (Abbott et al., 2012).

Data published by Abbott et. al. (2012), taken directly from an E.ON UK gas turbine site, demonstrates not only how natural gas supply composition in the U.K. varies, but also how the changes in composition effect operation of gas turbines. This data is taken from a gas turbine that was tuned with a relatively high WI fuel in mind. During periods when the WI of the fuel was low, shown in Figure 31, the alarm system detected increased combustion dynamics. The explanation given for this was the reduction in power of the pilot fuel, which allowed flame lifting and quasi-stabilisation deeper in the combustion chamber and an increase in airflow due to lower chamber pressures. This agrees with work that will be presented later in this thesis where flames approaching lean blowoff limits resulted in significant heat release and pressure fluctuations.

The change in WI observed in Figure 31, between approximately 51 and 48, was significant enough to cause operational problems; however, this is well within the regulatory limits of the UK and the EASEE, 51.5 – 47 and 54 – 47 respectively. An increase from 51 – 54 is likely to cause similar problems with respect to rich limits and combustor dynamics, so regulation of gas composition in this manner is not sufficient to prevent it effecting the operability of gas turbines.

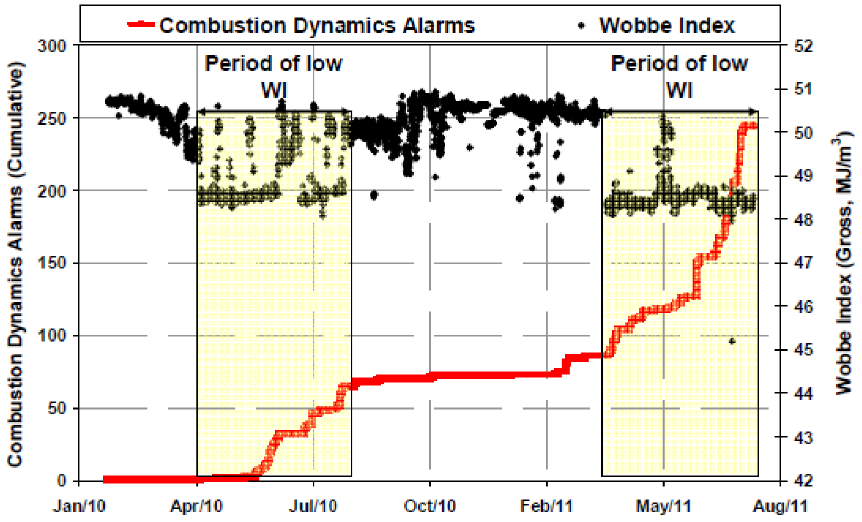

Figure 31: The influence of fuel composition on combustor dynamics alarms at an E.ON UK site (Abbott et al., 2012)

2.4.2 Biomass

Producer gas is the result of the gasification of biomass. Composition changes in producer gas are likely to have a significant effect on its combustion properties, including its stoichiometric air to fuel ratio and its flame speed. The producer gas composition will be directly affected by the type of biomass, and any variations in its own composition.

The properties of different sources of biomass can vary quite considerably, as shown by the proximate analysis of several types in Table 4 (García et al., 2013). M represents moisture content of the biomass source. A, VM and FC represent ash content, volatile matter and fixed carbon respectively, once moisture content has been removed. The lower heating value of the biomasses have also been estimated using an empirical equation derived by Erol (2010). These properties will affect both the operation of the gasifier and the overall composition of the fuel, increased moisture content will reduce the operating temperature of the gasifier, which has been shown to have a significant effect on hydrogen content of the producer gas (Lewis et al., 2012, Bal´aˇs et al., 2012).

The chemical composition of the biomass feedstock, with a number shown on a dry basis in Table 5 (Demirbaş, 1997, Demirbaş, 1998) also shows a significant variance, which again will directly affect the composition of the producer gas leaving the gasifier.

Table 4: Proximate analyses of different biomass sources (García et al., 2013)

Source	% M	% A (dry)	% VM (dry)	% FC (dry)	LHV (kJ/kg)
Apple tree leaves	9.3	12.0	71.9	16.1	14.9
Beetroot pellets	12.5	9.0	76.0	15.0	15.7
Chestnut tree leaves	8.2	4.9	72.4	22.7	18.6
Hazelnut shell	8.7	2.2	77.0	20.8	20.9
Miscanthus	7.5	9.6	79.0	11.4	14.8
Nectarine stone	8.2	1.1	76.0	22.9	21.6
Peach stone	8.6	0.5	75.6	23.9	21.4
Pine leaf pellets	8.3	3.2	74.5	22.3	20.0
Pistachio shell	8.8	1.3	82.5	16.2	21.2
Soya grain	10.4	4.8	77.0	18.2	18.6
Wheat grain	10.3	2.8	80.0	17.2	20.2
Wood pellets 1	8.0	1.3	82.0	16.7	21.3
Wood pellets 2	7.5	0.7	84.0	15.3	21.2

The examples shown in Table 4 and Table 5 represent a uniform sample of the particular variety of biomass. In reality, the properties and composition of the biomass will vary due to a variety of reasons. These reasons include location of growth, seasonality, which can in turn vary year upon year, and method of harvesting. Different sources display a differing level of variance. The dynamic nature of the biomass composition results in a non-steady operation with a non-steady feedstock, causing the composition of the producer gas to vary.

Table 5: Ultimate analyses of different biomass sources (Demirbaş, 1997, Demirbaş, 1998)

Source	C	H	N	S	Cl	O(diff.)
Red oak wood	50	6	0.3	-	-	42.4
Wheat straw	41.8	5.5	0.7	-	1.5	35.5
Olive husk	49.9	6.2	1.6	0.05	0.2	42
Beech wood	49.5	6.2	0.4	-	-	41.2
Spruce wood	51.9	6.1	0.3	-	-	40.9
Corncob	49	5.4	0.5	0.2	-	44.5
Tea waste	48	5.5	0.5	0.06	0.1	44
Walnut shell	53.5	6.6	1.5	0.1	0.1	45.4
Almond shell	47.8	6	1.1	0.06	0.1	41.5
Sunflower shell	47.4	5.8	1.4	0.05	0.1	41.3

2.4.3 Coal and Coal Derived Syngas

Coal is formed through the application of pressure and heat to dead biotic material over time. The precursor to coal is Peat; this has been widely used as a conditioner for soil, but in places where it is found in abundance, such as Ireland and Finland it is also used as a fuel source. Peat is transformed into lignite, or brown coal, which is the lowest rank of coal and is used almost exclusively for power generation. After lignite, the coal is transformed into sub-bituminous, used primarily as a fuel for steam generation but also in the chemical synthesis industries. The next stage is bituminous coal, a dense sedimentary rock used for power generation and the production of coke for the steel industry. The final rank of coal used for power generation is anthracite, although it is primarily used for residential and commercial space heating. The highest rank of coal is graphite, which is very difficult to ignite, due largely to its low percentage of volatiles. It is instead used in production industries or as a lubricant when powdered. The classification of coal according to American regulations (ASTM, 1998) is shown in Figure 32. It demonstrates that once transformation has caused the formation of what is classed as coal, continued exposure to high temperature and high pressure increases the percentage of fixed carbon and reduces the gross calorific value of the fuel until it reaches the rank of low-volatile bituminous. After that, continued transformation causes both fixed carbon percentage to and gross calorific value to increase.

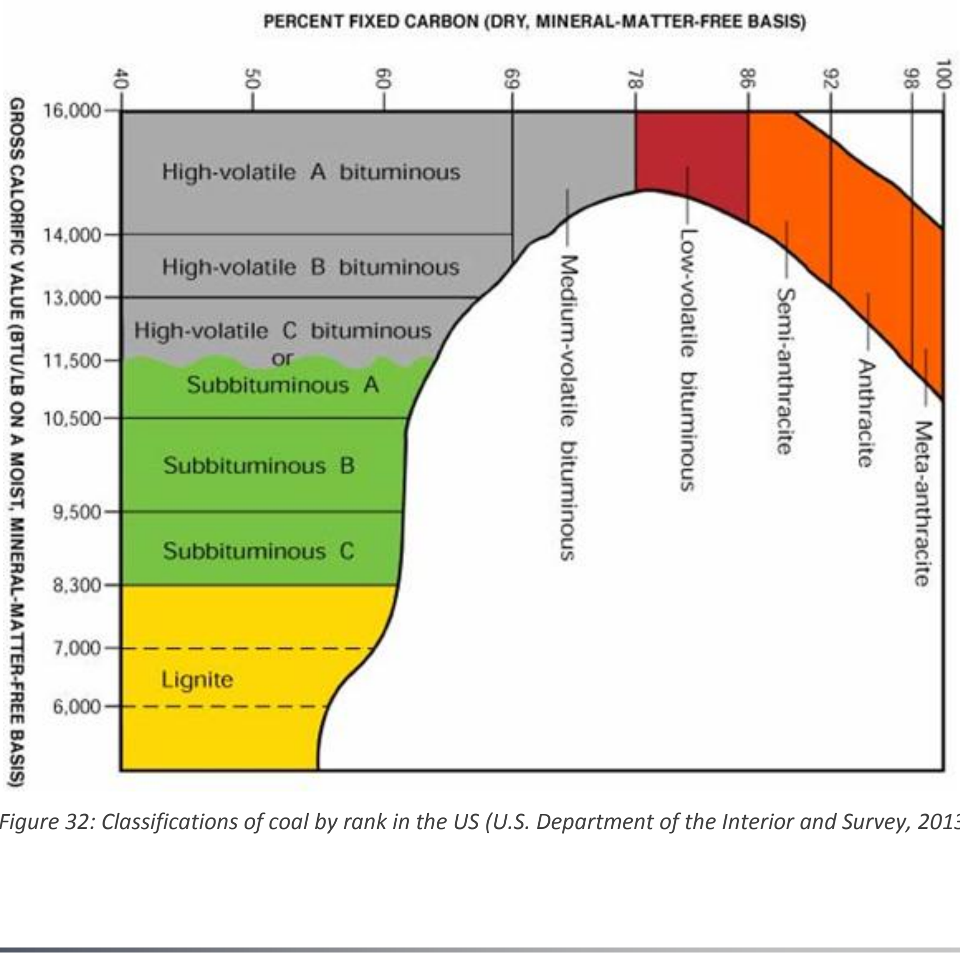

Figure 32: Classifications of coal by rank in the US (U.S. Department of the Interior and Survey, 2013)

The classification of coal according to German regulations is show in Table 6, where the ranks from flame to non-baking coal represent the transition from sub-bituminous to bituminous coal. There is a large variability between, and within, different ranks of coal.

Although there are not large variations in the coal from a single source, small variations do exists, and will have an effect on the composition of the Syngas produced; however the main cause of any composition changes will be the design and operating conditions of the gasifier.

Table 6: Classification of coal according to German regulations (Hoinkins and Lindner)

Designation	Volatiles %	Carbon %	Hydrogen %	Oxygen %	Sulphur %	LHV (kJ/kg)
Lignite	45–65	60–75	6.0–5.8	34-17	0.5-3	<28,470
Flame coal	40-45	75-82	6.0-5.8	>9.8	~1	<32,870
Gas flame coal	35-40	82-85	5.8-5.6	9.8-7.3	~1	<33,910
Gas coal	28-35	85-87.5	5.6-5.0	7.3-4.5	~1	<34,960
Fat coal	19-28	87.5-89.5	5.0-4.5	4.5-3.2	~1	<35,380
Forge coal	14-19	89.5-90.5	4.5-4.0	3.2-2.8	~1	<35,380
Non-baking coal	10-14	90.5-91.5	4.0-3.75	2.8-3.5	~1	35,380
Anthracite	7-12	>91.5	<3.75	<2.5	~1	<35,300

The composition of Syngas' produced and utilised in five major IGCC plants worldwide are shown in Table 7 (Ansaldo Energia, 2010, Kehlhofer et al., 1999).

Table 7: Composition of Syngas produced in current generation IGCC gasifiers (Ansaldo Energia, 2010, Kehlhofer et al., 1999)

Plant % Volume of Syngas	Buggenum	Puertollano	Wabash	Nakoso	Tampa Polk -Sub-Bituminous	Tampa Polk -Bituminous
Hydrogen	12.3	10.7	34.4	10.5	38.0	34.0
Carbon Monoxide	24.8	29.2	45.3	30.5	44.0	48.3
Water/Steam	19.1	4.2	-	-	-	-
Nitrogen	42.0	53.1	1.9	55.5	2.4	3.1
Argon	0.6	0.6	0.6	-	0.9	1
Carbon Dioxide	0.8	1.9	15.8	2.8	14.7	13.6
Methane	0	0.1	1.9	0.1	-	-
Oxygen	0.4	0.3	-	-	-	-

There are significant differences between there make-up, noticeably that Tampa Polk, in Florida, has a hydrogen content of almost 400% of Puertollano, in southern Spain, or Nakoso in Japan. The plant in Tampa is capable of using different coal sources, and data taken from the plant operating on both bituminous and sub-bituminous coal shows how the feedstock effects the Syngas compositions. The behaviour of these fuels in a combustor will be very different, which highlights the difficulty in specifying gas turbine combustor designs.

2.5 Chapter Summary

This chapter has reviewed previous studies relating to swirl combustion, thermo-acoustics, and variation in the composition in natural and shale gas, biomass and coal. To summarise the following conclusions are drawn:

- Swirl combustion is a technique which involves applying tangential momentum to reactants prior to combustion.
- The level of tangential and axial momentum in flow can be compared by the application of the Swirl number (S) to the flow leaving the combustor. Alternatively, in a radial burner, it may be compared via the application of geometric swirl number (S_g) to the flow entering the combustion zone.
- Upon leaving the combustor exit, expansion of the swirling flow creates a region of low pressure. This acts to stabilise the flame via the recirculation of hot combustion products.
- The formation of a recirculation zone also results in the development of additional flow structures. Together with thermo-acoustic effects these may act to destabilise the flame.
- After the initiation of pressure oscillations, a feedback mechanism exists, that with sufficient phase relation will develop into thermo-acoustic instabilities.
- Perforated combustion chambers aside, passive control techniques have largely been disregarded due to the narrow frequency band at which they can be targeted. Active control, where insipient instabilities are detected and corrected for, is a preferred technique.

- Natural gas composition is prone to variations, which has been shown to effect gas turbine operation. Regulations actually allow for a significant range of Wobbe Index, which is a standard measurement of the fuels energy density.
- With regard to gaseous fuels derived from the gasification of carbonaceous material, biomass and coal both come in varying forms, and as such have a variety of compositions and energy density. These will directly affect the composition and properties of fuels derived from them.

Chapter 3: Experimental Rigs and Methodology

3.1 Introduction

Experimentation in this research was performed with several experimental rigs, and using a variety of diagnostic techniques. At the metaphorical centre of each of rigs used was a swirl burner; each with a different exit diameter. The thermal power range that this collection of burners is capable of achieving is very large, ranging from 30 kW at ambient conditions in a generic swirl burner up to a full 500 kW in a development gas turbine combustor, each with a particular feature that made it the most suitable for use in the particular trial.

Initial experimentation was performed using an industrial biomass gasification plant, where fuel variability was investigated, and its potential effects on flame stability were assessed. The response of a cyclone swirl burner, with both reacting and non-reacting flows, was then investigated to try and determine acoustic indicators of a flame approaching its stability limits. Dynamic pressure indicators were further investigated using a development gas turbine combustor. A radial swirl burner, with a generic design was then used to investigate how flow structures could be augmented using the diffusive injection of different gases. The potential benefits of diffusive injection on emissions were also investigated using the gas turbine combustor.

Detailed information on all the swirl burners and diagnostic techniques used in to complete this thesis is provided in proceeding chapter.

3.2 Diagnostic Techniques

Several different diagnostic techniques were used to assess changes in combustion conditions and flame structures. The techniques varied from the monitoring of exhaust gas temperatures with thermocouples, to more advanced techniques such as stereo Particle Image Velocimetry (PIV) and dynamic monitoring of pressure oscillations.

3.2.1 High Speed Photography

High Speed Photography (HSP) may refer to either of two things; capturing a series of images at a high sampling frequency, or, recording an image with an exceptionally short exposure time, which acts to reduce motion blur and appears to freeze the motion. In this case it refers to the former, where the photography is deemed to be high speed when frame rate exceeds 128 frames per second (fps) and a minimum of 3 frames are captured.

The applications of high speed photography have change considerably since its inception. Its first practical application was to investigate whether all of a horse's hooves were simultaneously off the ground when galloping or running. A 1,000 fps camera developed by Eastman Kodak in the 1930's was used by Bell Telephone Laboratories (BTL) to study relay bounce. The camera was further developed by BTL to achieve 5,000 fps, and after the design was sold to the Wollensak Optical Company via Western Electric it was improved to the extent that 10,000 fps could be captured.

In 1940 a patent was filed for the rotating mirror camera, which was theoretically capable of capturing 1,000,000 frames per second. The first known rotating mirror camera was built by Berlin Brixner for use during the Manhattan Project to photograph early prototypes of the first nuclear bomb.

Film based photography has now been replaced for almost all applications, by digital photography, using Charge Coupled Devices (CCD) or Complementary Metal-Oxide Semiconductor (CMOS) sensors. Whereas film based HSP depended on a mechanical device quickly moving film through the camera, or in the case of a rotating mirror camera altering the exposure point. Digital HSP is dependent on the fast capture and storage of information on CCD's.

A typical CCD HSP resolution would be in the single Mega Pixel (MP) range, whereas even CMOS sensors in mobile phones now have a resolution that exceeds 40 MP, despite this, the use of CCD's allows a higher resolution than film based techniques. It also results in a high quantity of data being produced. When digitilisation perceives a fairly limited 256 colours or tones (8-bit), recording an image stream at 3000 frames per second with a resolution of 1.3 MP, the data rate is in excess of 6 gigabytes per second. Requiring high speed data transfer equipment and devices with a large storage capacity.

3.2.2 Particle Image Velocimetry

Particle Image Velocimetry (PIV) is a method of flow visualisation based on the tracking of particles in successive images to analyse velocities in a flowing fluid. Its great benefit is that it is almost entirely unobtrusive and does not cause any changes to the flow being analysed. Although the flow may be altered by particles that are added to the flow, choosing the correct seed results in the alterations being negligible.

3.2.2.1 Fluid Seeding

In air the flow is typically seeded with smoke, water droplets or metal oxides, with the choice of particles playing a critical role in the accuracy of the overall results. It must be assumed that the movement of particles exactly matches that of the fluid in which they are entrained. In actuality the degree to which the particles follow the flow dynamic is not perfect, and is defined by the Stokes number (Stk), a dimensionless number corresponding to the behaviour of particles suspended in a fluid flow, as defined by Equation 3.1 (Brennan, 2005):

$$Stk = \frac{\tau \cdot U}{d_c} \qquad \text{Eq (3.1)}$$

Where: d_c = the characteristic dimension of an obstacle (m)

U = velocity (m/s)

And: τ = particle relaxation time (s), which is calculated thus:

$$\tau = \frac{\rho_d \cdot d_d^2}{18 \cdot \mu_f} \qquad \text{Eq (3.2)}$$

Where: ρ_d = particle density (kg/m^3)

d_d = diameter of the particle (m)

μ_f = dynamic viscosity of the fluid (m^2/s)

The smaller the Stokes number the better the accuracy of the trace. When Stk is greater than 1 the particles will detach from the flow, particularly under heavy acceleration, whereas when Stk is less than 1 the particles will follow streamlines very closely. An Stk of less than 0.1 corresponds to a tracing accuracy of greater than 99% (Tropea and Yarin, 2007).

In order for the particles to be clearly visible they must be illuminated in some way. In the vast majority of systems this is achieved by a laser pulse, often Neodymium-doped Yttrium Aluminium Garnet (Nd:YAG), which is converted into sheet form by optics. Using a sheet means that only particles on a particular plane are illuminated, this is important to attain legible results. A laser pulse is emitted, and a camera aligned perpendicular to the laser sheet captures an image, as a second laser pulse is emitted a second image is captured by the camera. A schematic of a typical PIV setup is shown Figure 33.

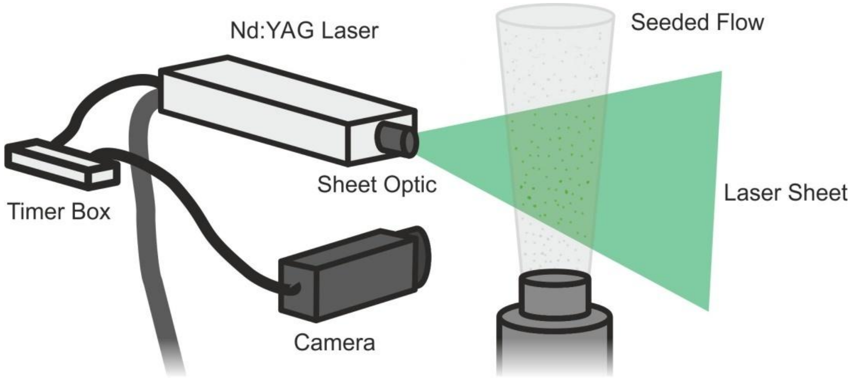

Figure 33: Single camera PIV technique

Powerful lasers are also required for high quality results, and the use of solid state, double cavity Nd:Yag lasers is standard procedure in air. Q-switches are also used to increase the power of the emitted laser sheets. Q-switches quickly open the exit of the laser cavity, allowing a build up of lasing energy before the high powered, short duration beam is produced, lighting up the seeding particles almost instantaneously. In order to produce the two laser sheets required for PIV, Double-Q-Switches are utilised, these allow a single laser lamp to be used to produce both sheets. The measurement area should also be kept as close as possible to the laser, as the power to distance relationship follows the inverse square law. This means that doubling the distance between the laser and the measurement area reduces the laser power to a quarter (DANTEC, 2013).

3.2.2.2 Optics and Interference Filters

In order to improve quality of the images recorded, which are directly related to the quality of the results, various optics and interference filters are used. Optical lenses are used to select the volume of the study, whilst insuring that the particles are clearly visible and that the PIV software is able to differentiate between them. When selecting optics the focal length, focal ratio and depth of field must be considered. The focal length is a parameter defined by lens shape and describes how strongly light is forced to converge or diverge, and is the distance between the focal point and then centre of the lens. In a PIV system, where light is directed onto a digital sensor, it is converged, and the correct focal length is critical to achieving sharp images. A lens with variable focus is preferred as it allows easy adjustment to ensure that the particles illuminated by the laser sheet are at optimal focus. The focus ratio, or F-number is the ratio between the focal length and the aperture diameter. It is a measure of lens speed, and as well as affecting the image intensity by restricting the amount of light that sensor is exposed to, is fundamental to defining the depth of field.

The depth of field describes the portion of the image that is in focus; as only a specific distance from the lens can be in perfect focus, the depth of field (δ) describes the gradual decrease in sharpness either side of this distance, and for a PIV system is calculated thus (Valera-Medina, 2009):

$$\delta = 4 \cdot (1 + \frac{1}{M_f}) \cdot F^2 \cdot \lambda \qquad \text{Eq (3.3)}$$

Where: M_f = magnification of the lens (-)
F = focal ratio (-)
λ = frequency of the laser (Hz)

Interference filters are used to prevent unwanted light sources causing noise in the image by only allowing the camera to detect the light at the frequency of the laser, which has been scattered by the seed particles. The filters are made of multiple layers of dielectric material, each of which has a different refractive index. If two semi-reflective coatings are applied to either side of a transparent spacer, and the width of the spacer is half that of the desired wavelength, reflections and interference will result in only light in of a specific wavelength being emitted. Other wavelengths will be attenuated by destructive interference. The desired wavelength is that of the laser, so the vast majority of light that reaches the camera sensor is that scattered by the particles in the laser sheet (Bass, 1995).

3.2.2.3 Image Processing

The basic theory behind PIV is that if a particle is identifiable on two images, and if it's relative position on the two images and the time between the two images is known, then its displacement and velocity can be calculated. In order to translate changes in image position to actual velocity then the system must be calibrated in order for the system to calculate scale factor between pixel position and actual position.

A method for calculating this scale factor is to calibrate dimensions against a known quantity in the measurement plane, which can be achieved using a calibration target. Images of a calibration target positioned above the burner exit taken with two cameras in a stereo PIV set up are shown in Figure 34; user input defines the position of the origin, which is the large central white dot. Two further positions and the distance between them are also user defined, the software then recognises the position of the grid and determines the scale factor.

Early systems attempted to analyse flow in the whole frame. Modern systems however divide the frames into smaller, more easily manageable areas, called interrogation regions. In each region the pixular, and in turn the actual displacement of the detected particles is calculated to obtain the velocity vectors. This is repeated for all regions, until the entire field of view has been built up. It is highly probable that particles make the transition from one interrogation region to the neighbouring one in the time between laser pulses, in order to maximise the amount of data available it is commonplace to overlap interrogation areas (DANTEC, 2013).

The in order to calculate displacement, a process called cross correlation is applied to the two frames that are captured in quick succession. A mathematical algorithm based on a Fourier Transform is applied to corresponding interrogation regions on both frames, this makes the seeded particles appear as bright spots in a dark, grey scale background. A number of peaks are identified in both the frames, and the relative displacement is then calculated and a velocity vector is displayed.

The number of vectors produced is important to produce a coherent picture, and the number produced is dependent on the number of pixels in the camera array and the size of the interrogation region (DANTEC, 2013).

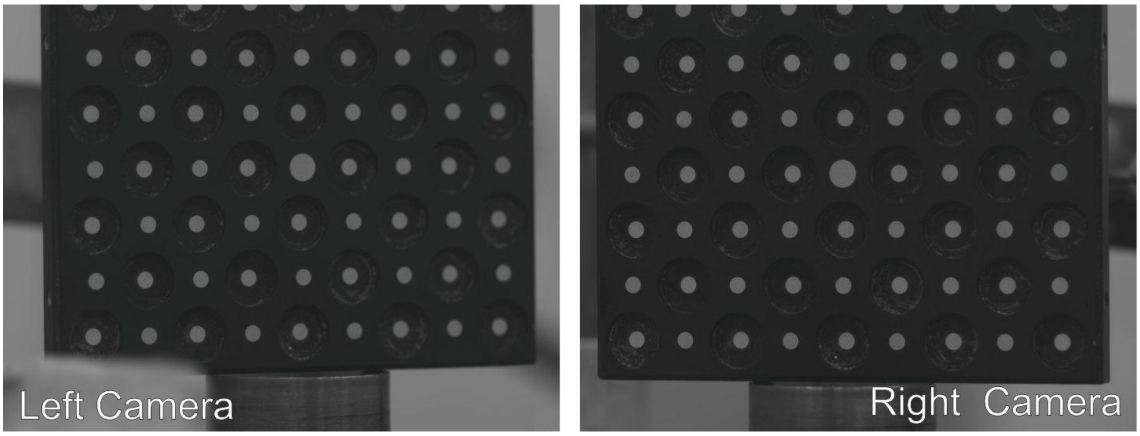

Figure 34: Images taken calibration target positioned at burner exit, from two cameras, during stereo PIV setup

The resolution of the PIV image, which refers to the smallest velocity structure which can be captured within the flow field, is dependant not just on the resolution of the camera, but the amount of time between laser pulse, which is particularly important as short times between pulses allows an 'instantaneous' velocity to be calculated rather than and average. The maximum distance (d_{max}) that can be measured with a particular PIV system can be calculated thus (DANTEC, 2006):

$$d_{max} = M_f \cdot v_{max} \cdot t \ \leq 0.25 \cdot N_{int} \cdot d_{pixel} \qquad \text{Eq (3.4)}$$

Where: d_{max} = maximum distance between particles (m)

M_f = magnification of the lens (-)

v_{max} = maximum velocity (m/s)

t = time (s)

N_{int} = number of pixels (-)

d_{pixel} = diameter of pixels (m)

3.2.2.4 Stereo PIV

Single camera PIV is limited to producing results in a single plane, i.e. with two components of velocity. The use of two cameras, viewing the measurement area from different angles, allows a third component of velocity to be derived from the particle movement. Figure 35 demonstrates, in an exaggerated fashion how results from two cameras cause the velocity of a single particle to be calculated completely differently, neither of which providing a particularly accurate interpretation of its actual displacement. Neighbourhood validation and other processing techniques are used to reduce the likelihood and magnitude of these errors. However, combining two velocity maps, along with calibration data, allows the true displacement to be calculated. In an actual PIV system this means that displacement can be resolved in three dimensions, so total particle velocity can be calculated.

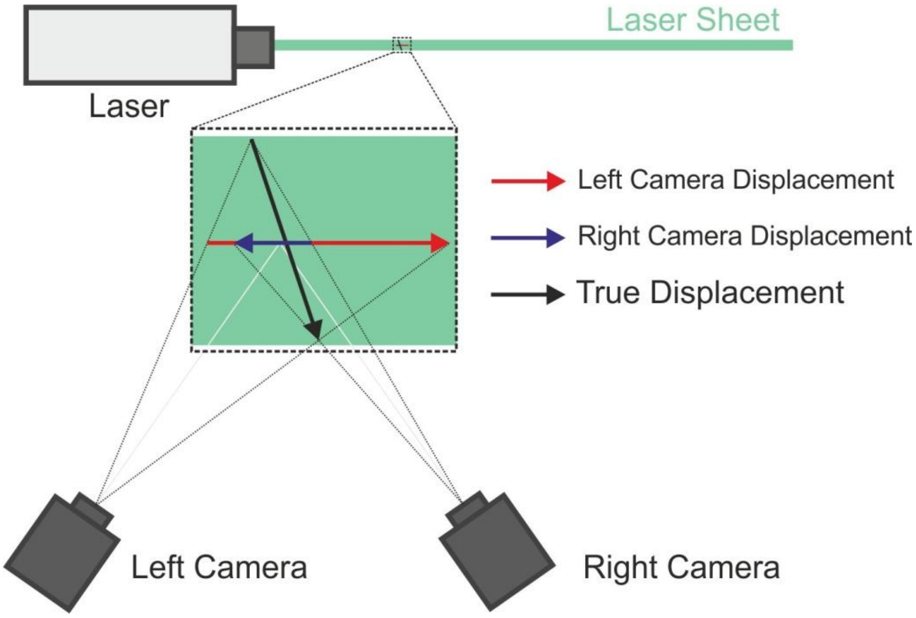

Figure 35: Principles of stereo PIV

3.2.3 Dynamic Frequency Response

The combustion systems in gas turbines have evolved to operate within exceptionally stringent emissions targets using lean pre-mixed combustion (LPM). The emission of NO_x is of particular importance. In order to reduce NO_x emissions combustion temperature is kept relatively low by using as a high level of excess air as possible. This however requires the combustion system to be operated on the verge of flame stability, which induces a high level of combustion pressure dynamics. If these are able to couple with the natural characteristic of the rig, damage and flame extinction can occur. Under atmospheric conditions and when there are no moving parts and background noise is low it is possible to detect acoustic instabilities and large oscillations in pressure with a microphone positioned near the rig, this is not the case where gas turbines are concerned. In order to monitor these pressure dynamics inside the combustor section of a gas turbine one would ideally place a pressure transducer inside the combustion lining, however due to the extreme temperatures this is not a reasonable solution. A commonly used approach to achieve dynamic pressure measurements under these conditions is to mount a pressure transducer, perpendicularly, on a length of tubing (Stuttaford et al., 2003, Ferrara et al., 2005, England and Richards, 1984). This method is often referred to as the semi-infinite line pressure transducer technique. A relatively short length of tube connects an orifice in the combustion chamber to a T-section, perpendicularly housing the pressure transducer; it is then connected to very long length of tube of the same diameter.

The theory behind this is that the pressure transducer will experience fluctuations equal to the those at the opening to the combustion chamber, and that pressure waves will dissipate along the length of the tube and will not affect results by being reflected back, i.e. as if the line length was infinite. In reality the visco-thermal effects on the sound attenuation are capable of causing errors between the actual and the recorded dynamic pressure measurements.

One method used to account for these errors, considered to be the best method by others (Van Ommen et al., 1999, Samuelson, 1967), is to use the segmented line equation model of Bergh and Tijdeman (1965), which is an extension of the work originally performed by Iberall (1950). The segmented line model defines the pressure experienced by the transducer (P_t) compared to the actual combustion chamber pressure (P_c) as defined below:

$$\frac{P_t}{P_c}(i\omega) = \frac{1}{\cosh(y \cdot L_{ct}) + X \cdot \sinh(y \cdot L_{ct}) + (\sinh(y \cdot L_{ct}) \tanh(y \cdot L_{te}))} \quad \text{Eq (3.5)}$$

This equation incorporates the lengths of the tubing, as well as the reflection coefficient (X), and the propagation constant (y). These in turn incorporate the shear number (E), and wave number (W), all of which are defined below:

$$W = \sqrt{r^2\left(-\frac{i\omega}{v}\right)} \qquad \text{Eq (3.6)}$$

$$E = Pr.W \qquad \text{Eq (3.7)}$$

$$y = \frac{\omega}{c}\left[\frac{1+\frac{2(\gamma-1)\cdot J_1(E)}{E\cdot J_0(E)}}{\frac{2\cdot J_1(W)}{W\cdot J_0(W)}-1}\right]^{\frac{1}{2}} \qquad \text{Eq (3.8)}$$

$$X = \frac{\omega V}{cA}\left[\frac{1}{\left[1+\frac{2(\gamma-1)\cdot J_1(E)}{E\cdot J_0(E)}\right]\cdot\left[\frac{2\cdot J_1(W)}{W\cdot J_0(W)}-1\right]}\right]^{\frac{1}{2}} \qquad \text{Eq (3.9)}$$

Where: P_c = Combustion chamber pressure (bar)

P_t = Pressure at transducer (bar)

A = Cross sectional area of tube (m^2)

c = Speed of sound (m/s)

$J_0(E)$ = 0th order Bessel function with argument E, BesselJ(0,E)

$J_1(E)$ = 1st order Bessel function with argument E, BesselJ(1,E)

$J_0(W)$ = 0th order Bessel function with argument W, BesselJ(0,W)

$J_1(W)$ = 1st order Bessel function with argument W, BesselJ(1,W)

L_{ct} = Length of tube between chamber and transducer (m)

L_{te} = Length of tube between transducer and end (m)

r = Radius of tube (m)

V = Volume of pressure transducer cavity (m^3)

Pr = Prandtl number (-)

γ = Ratio of specific heats (-)

ν = Kinematic viscosity (m^2/s)

ω = Angular frequency (rad/s)

Certain assumptions are made, for example that the cross section of the tube is identical both before and after the insertion of the transducer and is homogenous along its entire length.

Using the values of P_t/P_c over the desired range of frequencies it is possible to evaluate the pressure gain (G), and phase shift (θ), between the two transducer and the chamber using Equations 3.10 and 3.11:

$$G = \sqrt{Re\left(\frac{P_t}{P_c}\right)^2 + Im\left(\frac{P_t}{P_c}\right)^2} \qquad \text{Eq (3.10)}$$

$$\vartheta = tan^{-1}\left(\frac{Im\left(\frac{P_t}{P_c}\right)}{Re\left(\frac{P_t}{P_c}\right)}\right) \qquad \text{Eq (3.11)}$$

Examples of the pressure gain and phase change expected, for a typical semi-infinite line transducer system, are shown in Figure 36. The potential for errors in the magnitude of the pressure waves recorded is clearly demonstrated in Figure 36 (a), at 800 Hz this corresponds to a 6.5% error.

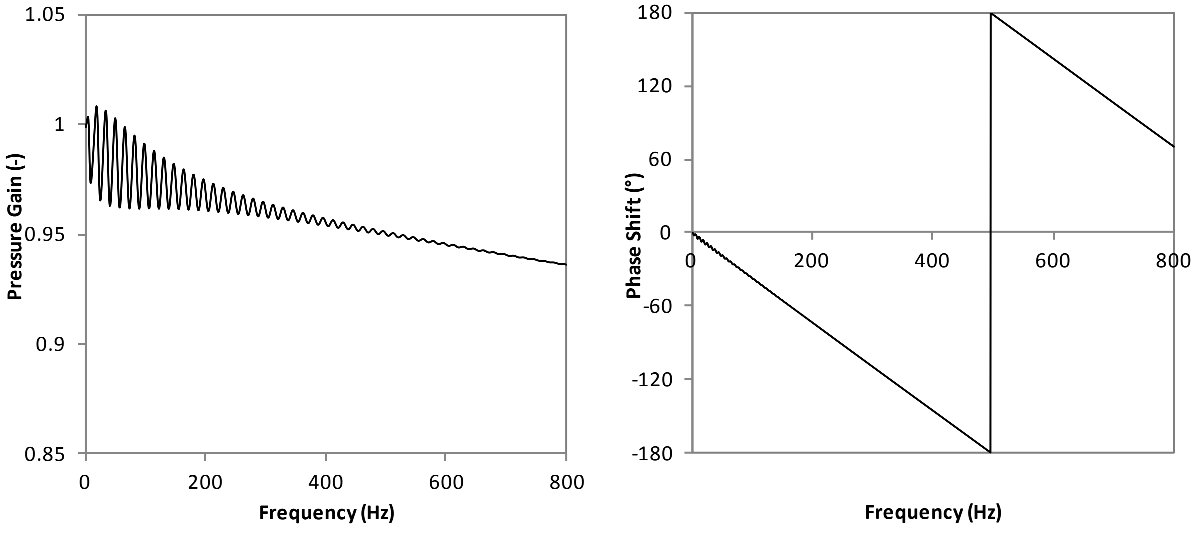

(a) *(b)*

Figure 36: The (a) pressure gain and (b) phase shift expected using a semi-infinite line under normalised conditions with: $v = 10^{-7}$ m^3, $l_{ct} = 0.5$ m, $l_{te} = 13.0$ m, r = 0.0019

3.3 Swirl Burners

As discussed in Chapter 2, swirl combustion has been used extensively in a large range of applications. Swirl burners vary markedly in design and size, depending on the application for which they are intended. The experimentation performed in the completion of this thesis used several different burners, some of which were restricted to atmospheric combustion in stand-alone systems, and some which required installation in the High Pressure Combustor Rig (HPCR), all are summarised in Table 8.

Small atmospheric rigs were best suited to experimentation where frequent extinction events occurred due to the short start up times. They also provide a level of access that simply cannot be achieved with systems capable of operating under conditions of elevated pressure. The elevated pressure capable burner was installed in the HPCR, which can deliver input air at elevated and temperature pressure conditions that are representative of those in a power derivative gas turbine engine. As well as using a variety of burners, a range of fuels were used in different tests. The majority of the experimentation was performed with conventional fuels; pure methane and mains supplied natural gas.

Tests with these fuels were directed toward fundamental effects on and affects of the flame, such as assessing how the characteristics of flame could be purposefully altered in order to improve the combustion process, determining how both planned and unplanned changes in inlet conditions would augment the flame, and how such augmentation could be detected and, if necessary, avoided.

Table 8: Summary of burners used

Name	Abbreviation	Type		Exit Diameter	Nominal Rated Power^
		Swirler	System		
Cyclone Burner	CB	Radial	Standalone	80 mm	100 kW
Development IGCC Combustor	IGCCC	Co-Axial	HPCR Integrated	110 mm	500 kW
Atmospheric Generic Swirl Burner	AGSB	Radial	Standalone	28 mm	30 kW

^ with methane as fuel, under atmospheric conditions

3.3.1 High Pressure Combustor Rig

The compressor and heater systems are capable of delivering 5 kg/s of air at 900K and 16 barA, thus allowing combustors to be operated at inlet conditions applicable to use in a power generation derivative gas turbine engine. At the core of the high pressure optical rig is the High Pressure Optical Casing (HPOC); this is a stainless steel casing capable of withstanding the high heat and pressure developed within, whilst offering optical access to the combustion zone via two large quartz windows. Downstream of the HPOC the exhaust ducts are water-cooled, in order to withstand the temperature of the combustion products, another quartz window is located at the back of the exhaust section, allowing optical access down the central axis of the burner. The high pressure optical rig is shown in Figure 37, with the visible quartz windows highlighted in blue. In order to get a sense of scale, the length of the assembly shown is 2660 mm. In the configuration demonstrated the air is delivered via twelve hoses to a plenum chamber inside the rig, as this best represents the installation of a gas turbine combustor. It can however, if required, be altered so fuel is delivered straight to the installed burner.

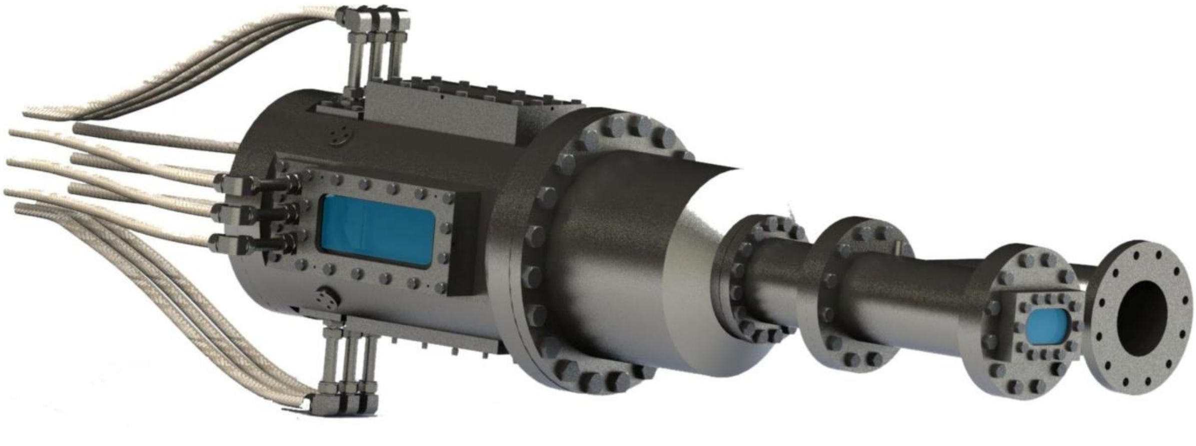

Figure 37: View of high pressure combustor rig assembly

3.3.2 Cyclone Burner

The laboratory-scale rig comprised of a 100 kW rated burner that could be fed by both air and fuel through a single axial inlet, as well as two tangential inlets. The burner is a geometrically scaled version of a 1.5 MW industrial scale burner that was designed for the combustion of low calorific value fuels (Fick et al., 1998). The burner consists of a combustion chamber and a cylindrical furnace section with a conicular constriction. An external view and the dimensions of the burner are shown in Figure 38 (a) and (c) respectively. The ignition of the burner was controlled by a Satronic DKG 972 atmospheric burner control box, which also maintained a pilot light, detected by an ionisation probe, above the burner to ensure no unburned fuel is released.

Circular tangential air inlets, denoted by (a) in Figure 38 (b), which have fuel inlets extending across the horizontal traverse (b), 300mm upstream of the swirl chamber, are used to ensure air and fuel are fully mixed when entering the swirl chamber (c). Air or fuel can also be injected through the diffusive injector on the burner's central axis (d). The air-fuel then passes through the swirl chamber exit nozzle and into the combustion chamber before exiting via the constriction orifice (e). Natural gas is supplied at a mains pressure of approximately 37 mbarG, air from a centrifugal fan producing approximately 20 mbarG. Fuel can be delivered up to a maximum of about 120 litres per minute, and is measured via rotameters. The fan is capable of delivering 3500 litres per minute of air, which is also measured by rotameters.

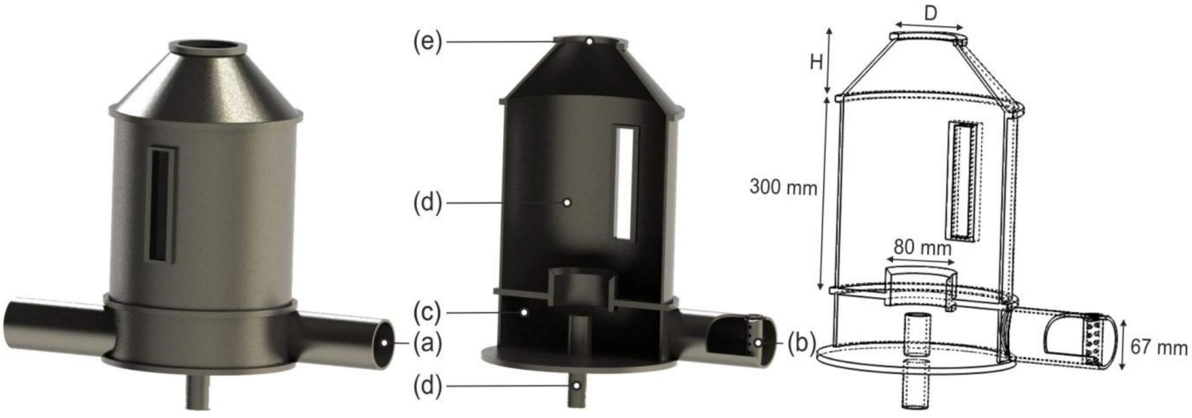

(a) *(b)* *(c)*

Figure 38: (a) External view, (b) sectioned view and (c) wireframe of the laboratory-scale 100 kW burner

There are two conical confinements that can be attached to the burner, as shown in Figure 38 (c), one of which height (H) is 120 mm and diameter (D) is 80 mm, this is confinement A, confinement B has dimensions H = 230 mm and D = 50 mm. The different confinement configurations alter the backpressure in the system, the result of which is a change in stability limits. The geometric coefficient of geometric swirl number can be altered using a variety of inserts, which alter the area and effective radius of the tangential inlets. By blocking the air inlets with inserts with widths that correspond to 10, 25, 50 and 75 percent of the inlet diameter, as indicated in Figure 39, it is possible to alter the geometric coefficient, and consequentially the S_g, of the burner from 0.74 to 4.46. A combination of inserts can be used to produce intermediate values of C_g, however previous work that this creates an imbalance which can result in two recirculation zones (Valera-Medina, 2009).

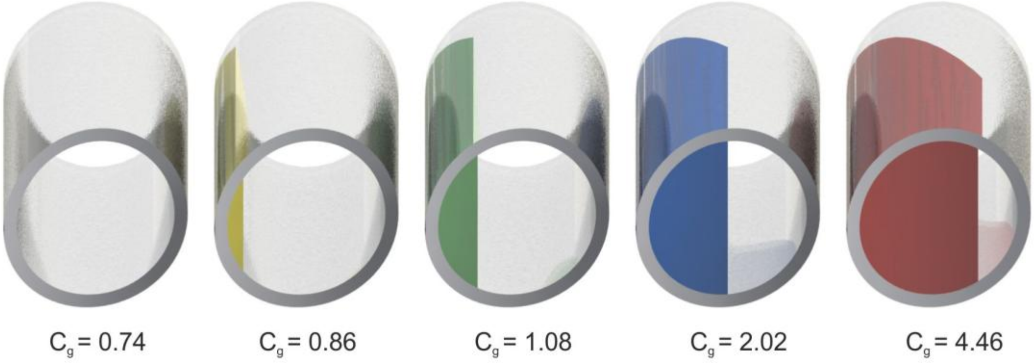

Figure 39: Visualisation of the inserts used to vary geometric coefficient in the cyclone burner

3.3.2.1 Experimental Methodology

Oscillations were monitored using a PCB Piezotronics 378B02 condenser microphone, positioned outside of the combustion chamber. The data acquisition system used LabView to record and process the raw data, with the sensors connected via signal conditioning unit and a National Instruments cDAQ-9178 PCI card. The free-field microphone and fitted preamplifier have a flat frequency response up to 1000HZ.

At each test point under isothermal conditions the desired flow rate of air was set, 4000 samples were then taken at a rate of 2000 Hz using the data acquisition system. Three data sets were taken per test point. The second and third data sets were used to verify the first data set. Verification involved ensuring that for any frequency where amplitude exceeded 10% of the dominant frequency in the first data set, amplitude was with 5% of that in the second and third data sets.

Prior to combustion testing the burner was fired under approximately 100 kW stoichiometric conditions for 5 minutes to overcome it’s the thermal inertia. At each test point under combustion conditions a lean, low powered, main flame was lit using the pilot flame as an ignition source. Air and fuel flow rates were then adjusted to the desired power conditions and, as per isothermal test points, three data sets of 4000 samples were taken at a rate of 2000 Hz.

3.3.2.2 Measurement Error

The accuracy of rotameter readings are dependent on the accuracy of pressure, temperature and flow control during calibration and operation (Cole-Parmer, 2006). As such, a deviation of ambient conditions from calibration conditions will result in an inaccuracy of measurement. The flow rates were measured by air and natural gas rotameters, with a degree of accuracy of ±5%. This means that the calculated equivalence ratios have a potential accuracy of ±10 %. Equivalence ratios may also be affected by small changes in gas composition, although this is unlikely in the experimental time frame.

The positioning of a microphone outside of the combustion chamber is a method of analysing thermo-acoustic emissions reported by Farhat and Mohamed (2010). However, this method means that pressure fluctuations inside the chamber are not directly monitored. As such amplitude comparisons can only be made with other results taken in this set-up. The external position of the microphone also means that it is susceptible to sensing noise from other sources, for example the fan in the extraction system. A band stop filter was applied to the data between 24 and 25 Hz which successfully removed noise from the extraction fan, unfortunately this means that any oscillations within the combustion chamber in this frequency range would be filtered out. The same is true between 34.5 and 35.5 Hz, which was the frequency of noise produced by the centrifugal fan.

3.3.3 Development IGCC Combustor

The development combustor is fundamentally different to the other burners as it uses angled vanes rather than radial passages to impart tangential momentum of the flow. As this is the preferred type of swirler used practical combustion systems, it provides a way to assess the fundamental flow characteristics observed in the radial burners in a practical situation. The combustor, which was designed for use as part of an IGCC turbine configuration, was installed in the high pressure optical rig. An outer view of the pressure casing assembly and a sectioned view are shown in Figure 40. Air enters the rig at (a) and passes into the burner assembly, represented by (b), via the rig plenum (c). Fuel enters the burner assembly at (d) and combustion occurs inside a quartz confinement (e), with the combustion zone visible from (f) and (g). Exhaust gases leave via a tee in the cooled exhaust duct (h).

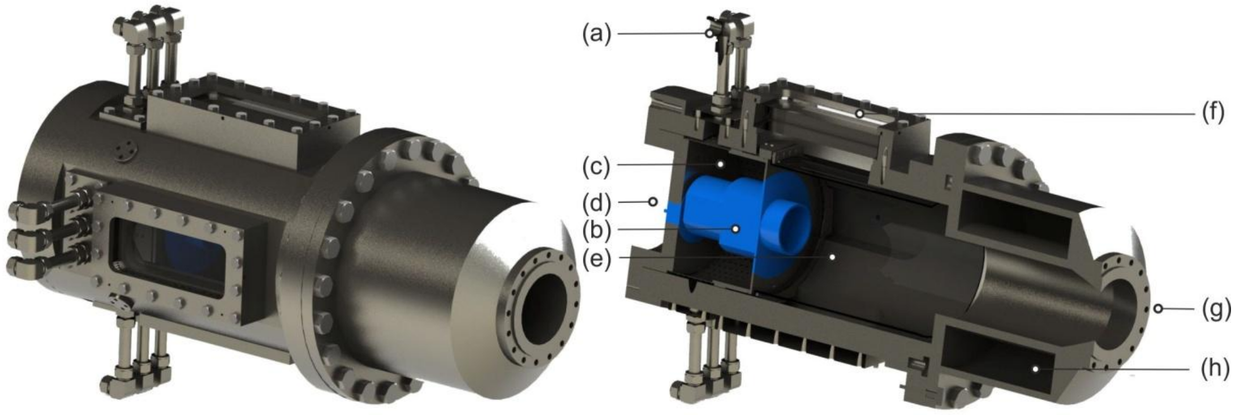

(a) *(b)*

Figure 40: (a) External and (b) sectioned views of the HPOC assembly with development burner

The volumetric flow rate and temperature of the air passing through the combustor are defined by its designated compressor, and the majority of testing was performed at these conditions as they have the greatest practical relevance. There are two available flow paths for combustion air and fuel, the first path is through the combustor pilot and the second through the main axial swirler. The pilot injector, which is also an axial swirler, is positioned on the central axis of the combustor, through which pilot fuel, and approximately ten percent of the combustion air are fed. The main, annular, axial, swirler, which surrounds the pilot swirler, is fed by the main fuel supply and the remaining combustion air.

3.3.3.1 Experimental Methodology

The Development Integrated Gasification Combined Cycle Combustor (DIGCCC) was operated in a continuous fashion, with data recorded as stream. All three diagnostic techniques described in section 3.2 were performed on this rig. During operation of the HPCR, fuel and air flow rates, as well as multiple rig parameters, including exhaust gas and burner tip temperatures, are recorded at a rate of 1 Hz. Data sets containing 4000 samples, taken at a rate of 2000 Hz from the pressure transducers are recorded at a rate of 0.5 Hz. The raw data and a graph of power spectral density are recorded for each transducer. The frequency and amplitude of the dominant oscillations for each transducer are also logged, in a separate file, at a rate of 0.5 Hz.

The HPOC rig was fitted with three PCB Piezotronics 102M206 pressure transducers. The transducers permissible operating conditions fall well below those in the rig, for that reason they are located on semi-infinite lines, a technique detailed in section 3.2.3. The inlets to these lines are located at different points in the combustion system, namely the air inlet plenum, the combustor face, and the exhaust, as shown in Figure 41. This allows the effect of oscillations on different sections, and the position of their source to be analysed.

Similar to the atmospheric burner, the data acquisition system utilises LabView to record and process the raw data, with the sensors connected via a signal conditioning unit and a National Instruments PCI-6013 DAQ card.

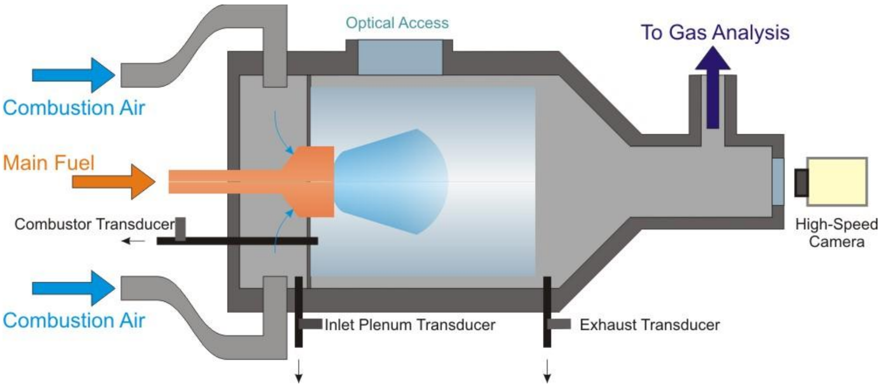

Figure 41: Schematic of the HPCR rig with proprietary gas turbine combustor

The calibration factors determined for the three measurement points are dependent on the response of the pressure transducers, where a certain change in pressure will result in a specified change in voltage output, and the semi-finite line assemblies. The minutiae of the three semi-infinite lines and pressure transducer responses are detailed in Table 9.

Table 9: Semi-Infinite line assembly details

	Inlet Plenum	Combustor Face	Exhaust
Response (mV/psi)	98.27	95.40	98.35
r (m)	0.0015875	0.0015875	0.0015875
L_{ct} (m)	0.15	0.40	0.25
L_{te} (m)	9	9	8.4
V (m^3)	5.143×10^{-8}	5.143×10^{-8}	5.935×10^{-8}

Using Equations 3.5 to 3.11 combined calibration factors and scaling factors, which are dependent on frequency of response, were calculated for each of the three pressure transducers. The calibration factors are shown in Figure 42 over the range of 0 to 1000 Hz and turn the voltage output of the transducers into millibars of pressure.

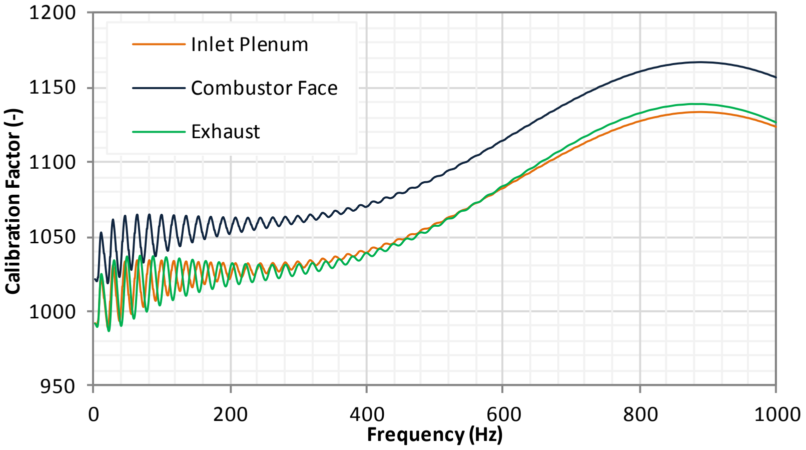

Figure 42: Calibration factors for the three pressure transducer and semi-infinite line assemblies

3.3.3.2 PIV Set-up

The Dantec PIV system used on the DIGCCC consisted of a dual cavity Nd:YAG Litron Laser of 532 nm capable of operating at 15 Hz. A Dantec Dynamics laser sheet optics (9080X0651) was used to convert the laser beam into a 1 mm thick sheet. Two sheet orientations were used to capture velocity data on a radial plane, as shown in Figure 43 (a), and on an axial plane, as shown in Figure 43 (b). The laser was installed on a traverse, so radial planes could be captured at varying distances downstream of the burner exit nozzle. To record the images a Hi Sense MkII Camera model C8484-52-05CP was used, with 1.3 megapixel resolution at 8 bits. The inlet air was seeded with aluminium oxide (Al_2O_3) by a perforated ring positioned behind the main axial swirler of the DIGCCC.

After acquisition of the PIV data, a frame-to-frame adaptive correlation technique was then carried out with a minimum interrogation area of 32x32 pixels and a maximum of 64x64, with an adaptivity to particle density and velocity gradients. 500 pairs of frames per plane were used to create an average phase locked velocity. In order to reduce the parallax error, the line of view of the camera was positioned exactly in the middle of the nozzle using a calibration grid provided by the system manufacturer. The grid was used to correct, via software, any positioning issue. The field of view was calibrated with the central line of the burner in the centre of the grid, thus ensuring that the position of the system would not affect the results.

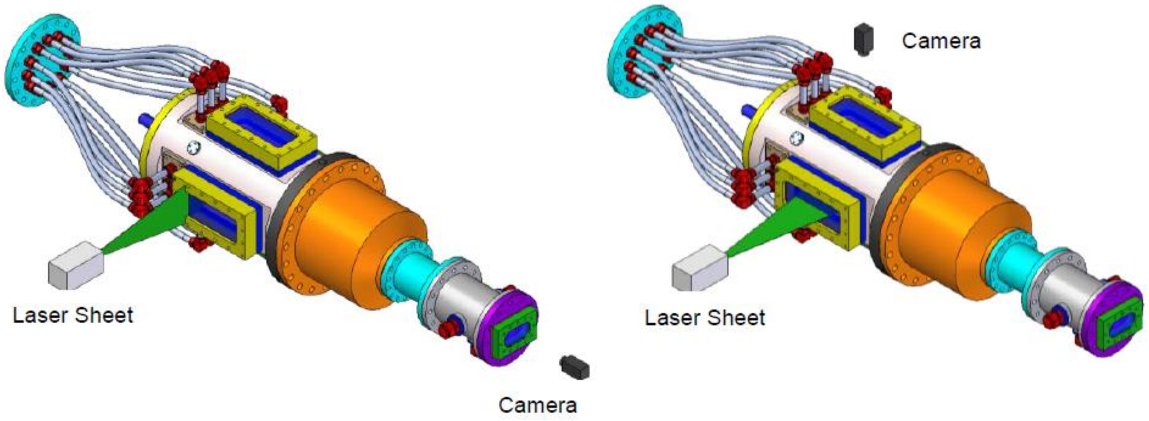

(a) (b)

Figure 43: PIV system orientation during analysis of the development IGCC combustor, (a) on a radial plane and (b) on an axial plane

3.3.3.3 Gas Analysis

The gas analysis line, the position of which is indicated in Figure 41, is constructed of stainless steel and is maintained at a temperature of 463K ±10K which is used to convey the gas sample to a suite of Signal brand, gas analysers. Analysers are included for the detection of CO_2, CO, NO, NO_2, UHC and O_2, as is a high pressure back purge which is used to stop fuel entering the sample line during ignition and also to clear the probe if necessary (Wedlock et al., 2008).

The sample line splits to form two channels. One sample line leads to the smoke analysis equipment, both filter stain and an optical measuring technique being applied. The second line leads to a filter oven to remove any particulate matter before passing to the analysis suite (Wedlock et al., 2008).

The gas analysis suite is described in detail by Brundish K. D et al. (2002) and similar analysers and methods were used for this study. One significant difference was that the NO/NO_X analyser used was no longer a dual channel system and therefore sequential measurements had to be made.

The analysis of the NO/NO_x and total hydrocarbons was performed using a wet sample, while for the other measurements the sample is dried. In order to calculate the concentration of the ambient water in the inlet air the dew point is measured. The dew point of the dried sample is also measured to allow volume corrections to be applied (Wedlock et al., 2008). The raw data is processed to ARP 1533 (Aerospace Recommended Practice, 1996). This accounts for the required corrections for inlet air humidity, cross interference effects and dried sample correction.

3.3.3.4 Measurement Error

The flow rates of fuel and air into the rig are monitored by coriolis meters with accuracies between ± 0.1 % and ± 0.2 % of total flow rate (Emerson Process Management, 2014). Temperatures are monitored by k-type thermocouples, which have an accuracy which is equal to ± 0.75 % at the temperatures in question (Reotemp Instruments, 2011).

The main source of potential errors is the semi-infinite lines which connect the pressure transducers. As discussed in section 3.2.3 the lines can be the source of pressure gains and phase shift, by amounts which vary depending on the frequency of oscillations. A method for predicting the pressure gains and phase shift, as defined and described by other researchers (Iberall, 1950, England and Richards, 1984, Rohrssen, 2007, Straub and Ferguson, 2007), was used to derive correction factors in the range of 0-1000 Hz for each semi-infinite line assembly. These correction factors were applied to the raw data to achieve the highest accuracy of results possible. The accuracy of the pressure transducers is with ± 1.0 % (PCB Piezotronics, 2003).

Due to electrical interference band stop filters were used in the ranges 49.5-50.5 Hz and 149.5-150.5 Hz. This means that any oscillations within the combustion chamber in this frequency range would be filtered out.

3.3.4 Atmospheric Generic Swirl Burner

The generic swirl burner, constructed from stainless steel, was used to examine the flame structure at atmospheric conditions (1bar, 293K). External, sectioned and wireframe images of the generic burner are presented in Figure 44.

A single tangential inlet, denoted by (a) in Figure 44 (b), feeds the premixed air and fuel to an outer plenum chamber (b) which uniformly distributes the gas to the slot type radial tangential inlets (c). Swirling premixed air and fuel then passes into the swirl chamber (d), then into the exit nozzle (e). The central diffusion fuel injector (f) extends centrally through the combustor body to the exhaust. This burner has been used extensively, and as such is well represented in published literature (Abdulsada et al., 2011, Abdulsada et al., 2013, Syred et al., 2012, Syred et al., 2013b). The burner can be fitted with a number of swirl heads and exhaust, with varying geometry, in order to change its characteristics.

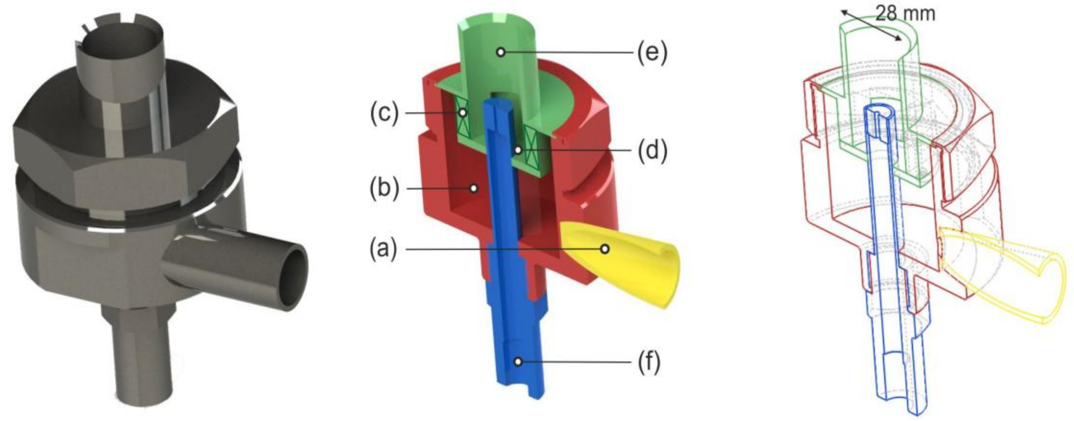

(a) *(b)* *(c)*

Figure 44: (a) External view, (b) sectioned view and (c) wireframe of the generic burner

3.3.4.1 Experimental Methodology

Prior to combustion testing the burner was fired under approximately 10 kW stoichiometric conditions for 2 minutes to overcome it's the thermal inertia. At each test point under combustion conditions a lean, low powered, main flame was lit using the pilot flame as an ignition source. Air and fuel flow rates were then adjusted to the desired power conditions and PIV data was taken.

3.3.4.2 PIV Set-up

AGSB PIV data taken was on an axial-radial plane that intersected the central axis of the burner exit, with both stereo and single camera PIV analysis being performed.

The Dantec PIV system used consisted of a dual cavity Nd:YAG Litron Laser of 532 nm capable of operating at 15 Hz, a Dantec Dynamics laser sheet optics (9080X0651) was used to convert the laser beam into a 1 mm thick sheet. The sheet, and therefore, the measurement plane, intersected the central axis of the burner exit nozzle. To record the images a Hi Sense MkII Camera model C8484-52-05CP was used, with 1.3 megapixel resolution at 8 bits. For stereo PIV two Hi Sense cameras were used. 60mm

Nikon lenses were used for resolution purposes, which allowed a field of view of approximately 75x75 mm, with a resolution of 5.35 pixels per mm and a depth of view of 1.5 mm. The inlet air was seeded with aluminium oxide (Al_2O_3) by an accumulator positioned 2.0m upstream of the burner inlets. The accumulator is fed by the main compressed air.

After acquisition of the PIV data, a frame-to-frame adaptive correlation technique was then carried out with a minimum interrogation area of 32x32 pixels and a maximum of 64x64, with an adaptivity to particle density and velocity gradients. 150 (150 pairs for stereo PIV) frames per plane were used to create an average phase locked velocity map after tests showed 150 pair of frames produced results almost identical to those obtained using 500 frames. Adaptivity in the analysis allowed very coherent images, with just a mask refinement of ~15-20% of the entire field of view. In order to reduce the parallax error, the line of view of the camera was positioned exactly in the middle of the nozzle using a calibration grid provided by the system manufacturer. The grid was used to correct, via software, any positioning issue. The field of view was calibrated with the central line of the burner in the centre of the grid, thus ensuring that the position of the system would not affect the results.

3.3.4.3 Measurement Error

The system was fed using compressed air through flexible hoses and methane from cylinders was used as main fuel. The flow rates of fuel and air into the rig are monitored by coriolis meters with accuracies between ± 0.1 % and ± 0.2 % of total flow rate (Emerson Process Management, 2014).

There will also be an element of error in the PIV data as the result of the image masking and neighbourhood validation employed during the image processing. Masking is used to remove noise, which can cause anomalous results, from the captured and unprocessed images. As a result, areas where a mask is applied will have no velocity. When the flow fields are calculated neighbourhood validation is employed in order to produce coherent results. This causes an element of averaging between neighbouring measurement points.

This means that where masked areas are next to high velocity regions, for example at the burner exit, the velocity of the flow will be underestimated. The level of underestimation will vary based on the size of the neighbourhood used for validation. The percentage error of the measurement point adjacent to the masked area will equal approximately the width of the neighbourhood (in terms of measurement points) divided by the width of the neighbourhood minus one. So with neighbourhood validation of 3x3 and 5x5, the reported velocity at measurement point adjacent to the masked area would be approximately 66% and 80% of the actual velocity.

3.4 Industrial Gasification Plant Composition Analysis

Data relating to the composition was taken at a proprietary gasification plant. The plant consists of a top fed, downdraft gasifier, an extensive gas cooling and cleaning system and a flare stack. With Grade-A wood chip (The Wood Recyclers Association, 2009) as a feedstock and operating at a typical, but not maximum 0.7 MW, it develops producer gas with an approximate calorific value of 6 MJ/Nm^3 at a rate of 420 Nm^3/h.

During the trials, the composition of the producer gas was analysed at regular intervals using a Gas Chromatograph (GC). Other conditions in the plant, including gasification throat temperature, were monitored and recorded using the plants control and logging system.

The producer gas was sampled during trials to assess the feasibility for its combustion in situ. The producer gas sampling point was directly before it entered the burner. It was treated using two impinger bottles, one of which contained a solution of isopropanol, the other silica gel, in order to protect the GC from any organic compounds or moisture that may have remained in the stream (Marsh et al., 2010).

The gas analysis GC system was a Varian CP-4900 micro gas GC, operating two channels enabling the simultaneous measurement of oxygen, nitrogen, light hydrocarbons, carbon monoxide, carbon dioxide and hydrogen. Channel 1 was a Thermal Conductivity Detector (TCD) column, running at 105°C for retention times up to 2 minutes with a balance gas of argon; this channel was used to detect hydrogen, oxygen and nitrogen. Channel 2 was a Pora Plot Q (PPQ) column, running at 105°C for retention times up to 2 minutes with a balance gas of helium; this channel was used to detect light hydrocarbons, carbon monoxide and carbon dioxide. To calibrate the system in situ a calibration standard was prepared with the concentration as shown in Table 10.

Table 10: Calibration Gas Composition

Volume (%)							
N_2	CO	CO_2	CH_4	C_2H_6	C_3H_8	C_4H_{10}	H_2
45	15	15	5	2	2	1	15

Additional composition gas analysis was performed using an HAL 201 RC Residual Gas Analyser (RGA). The measurement point used for the RGA was the same as used for the gas chromatograph. The RGA was set-up to detect the percentage volume of nitrogen, carbon monoxide, carbon dioxide, hydrogen, oxygen and methane.

The detection of hydrogen, which is of particular interest in this study, using thermal conducivity instruments is problematic due to cross-interference from other gas species. This can lead to errors in quantitive analysis. The use of a gas chromatograph, allows seperation of gas species, allowing the elimination of cross-interference, and improving the accuracy of results (Sluder. C et al., 2004). This work is concerned with how composition alters temporaly, this can be assessed despite any errors, as long as they are consistent.

3.5 Chapter Summary

This chapter provides details of the diagnostic techniques used during experimentation, and the swirl burners on which experimentation is performed. It also provides background on a proprietary gasification plant, where testing of producer gas composition took place, and the gas sampling system employed to do so. To summarise the following points are highlighted:

- High speed photography is used to visualise temporal flame evolution detect light emissions from flame under steady conditions.
- Particle image velocimetry is used to assess the velocity profiles of flame flow structures.
- A free field microphone and semi-infinite line, dynamic response pressure transducer assemblies are used to determine remote and external frequency response of swirling flows.
- A cyclone burner, of radial swirl type, is used to perform acoustic analysis of flows under isothermal and combusting conditions.

- A gas turbine combustor, of axial swirl type, is used to perform acoustic, chemical and light emission analysis using methane and syngas. Isothermal flow field analysis is also performed.
- A generic swirl burner, of radial swirl type is used to perform flow field analysis of atmospheric, unconfined flames.
- During trials at a proprietary gasification plant as a gas chromatograph and residual gas analyser were used to asses changes in producer gas composition.

Chapter 4: Variable Composition and Combustion Characteristics of Producer and Natural Gas

4.1 Introduction

As discussed previously, producer gas can be highly variable in composition. This is caused by variations in both gasifier operation and feedstock. Hydrogen content in particular has been shown to have a significant influence on flame stability (Syred et al., 2012, Mohon Roy et al., 2009), due to its high burning rates and extinction strain rates (Jackson et al., 2003).

Different feedstocks will result in different producer gas compositions. However, changes in the conditions of gasification and non-uniformity of feedstock also have the potential to cause composition fluctuations. The non-uniformity of feedstock is dependent on the nature of its source and how it is processed prior to gasification.

The work in this chapter aims to assess how changes in fuel composition affect the combustion properties of the fuel, with Wobbe Index and laminar flame speed of particular focus. Trials, as detailed in section 3.4, were performed in a proprietary, combined heat and power, gasification plant. Grade-A woodchip (The Wood Recyclers Association, 2009), which is expected to be comparatively homogeneous, was used as a fuel source, and gas chromatography was used to determine producer gas composition. The effect of the variable composition of producer gas focused on how flame speed was affected. The relationship between laminar flame speed and Wobbe Index is also assessed for a number of fuel sources.

The preferred practice of gas turbine manufacturers is to a qualify fuel suitability and interchange ability in terms of Wobbe Index (WI) (Abbott et al., 2012, Coyle et al., 2007), which is easily calculable using online gas chromatography. Wobbe Index will accurately determine the thermal energy of the fuel, but is not necessarily linked to flame stability. Consideration of flame speed, a characteristic often overlooked where fuel interchange ability is concerned (Loubar et al., 2007, Zachariah-Wolff et al., 2007), may be required when fuel variations are assessed.

4.2 The Effect of Variable Producer Gas Composition

4.2.1 Variation in Composition

On a commercially viable scale, fluctuations cannot be predicted to a high degree of accuracy. Figure 45, which displays the throat temperature of the gasifier as recorded by the proprietary plant’s control system, and the hydrogen content of the producer gas from gas chromatograph results, shows a relationship exists between the throat temperature of the gasifier and the hydrogen content of the producer gas. Peaks and troughs in throat temperature have corresponding peaks and troughs in Hydrogen content, which is offset by two minutes to account for the transit time of the producer gas from the gasifier to the sampling point. The first 20 minutes after the gasification has been initiated sees both hydrogen content and throat temperature increase, with peaks of 15.8% and 711°C observed respectively. The temperature then steadily declines as does hydrogen content, toward optimum operating temperature defined by the manufacturer, which is between 500 and 550°C. Sudden increases in throat temperature occur at 40 and 50 minutes which are matched by increases in hydrogen content. Similar relationships between temperature and hydrogen content have been reported by other researchers with regard to biomass gasification, experimentally (Bal´aˇs et al., 2012) and using models (Mhilu, 2012). It has also been reported for the gasification of coal (Haji-Sulaiman et al., 1986) and municipal solid waste (He et al., 2009).

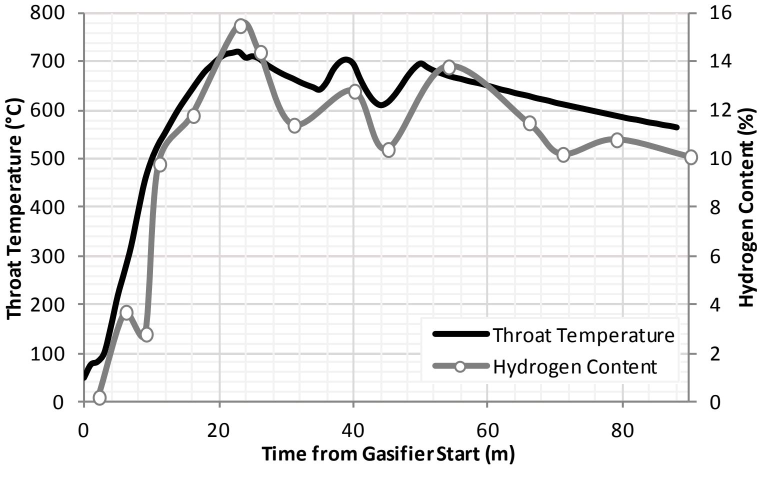

Figure 45: Gasifier Throat Temperature vs. Hydrogen Content (Lewis et al., 2012)

Monitoring the gas composition of the output of a plant under continuous operation is less than ideal due to the high expense of the equipment required. However monitoring certain operating conditions, such as throat temperature is straight forward. Therefore, derivation of a relationship between gas composition and gasifier throat temperature allows optimisation of combustion conditions, such as air-to-fuel ratio, to be effectively estimated. This information can then be used as the input in an open loop burner control system to improve flame stability and combustion efficiency by maintaining optimum conditions (Snyder et al., 2010). For the fuel used in these trials, a strong relationship was determined and was applied to a gasifier trial to determine how the properties of the producer gas were affected.

4.2.2 Calorific Value and Stoichiometric Air-to-Fuel Ratio

Based on gas samples from the proprietary pilot plant an empirical model was developed to predict composition based on certain criteria of the gasifiers performance, and for a given fuel, in this case Grade-A wood chip. The model was developed by defining a relationship between the percentage volume of seven gases present in the producer gas and gasifier throat temperature. The relationship was derived from the plants operating logs and composition data taken over a series of trials, all using the same batch of gasifier feedstock. The relationships, which are the best fit between the throat temperature and recorded concentration, are listed in Table 11.

Table 11: Composition and Temperature Relationships

Carbon Monoxide	$0.2138 \times T^{0.6844}$
Carbon Dioxide	$0.0789 \times T^{0.7976}$
Oxygen	$16.731 \times e^{(-0.006 \times T)}$
Methane	$0.0029 \times T^{1.013}$
Ethane	$T \times 0.0046 + 0.0484$
Propane	$T \times 0.0035+0.0625$
Nitrogen	difference

Using throat temperature measurements from the gasifier, the model was used to predict the composition of the producer gas. The predicted constitutional volumes were then compared against the recorded composition over time, as shown in Figure

46 (a). Three constituents of the producer gas, nitrogen, hydrogen and oxygen are shown, and the model appears to predict their respective volumetric concentrations accurately. There is a large change in general composition during the first 1000 seconds of the run, as gasification is initiated and the gasifier reaches its operating temperature. The changes in hydrogen and nitrogen volume over this period are well predicted by the model, although there is a significant underestimation in terms of the oxygen concentration. This is because the feedstock is not yet being gasified, so the output is essentially air. After 1000 seconds there is good accuracy in the prediction of all three gases, with mean errors equalling 10.9%, 4.3% and 7.1% of predicted values for hydrogen, nitrogen and oxygen respectively. To further assess the accuracy of the model, recorded and predicted compositions were plotted against each other and the coefficient of determination was found. The recorded and predicted results for nitrogen, hydrogen and oxygen are plotted in Figure 46 (b). The coefficients of determination are 0.88, 0.93 and 0.82 respectively indicating good accuracy. The results for carbon monoxide, carbon dioxide and methane are not shown, but the calculated coefficients of determination were found to be 0.69, 0.92 and 0.65 respectively. The model was then used to predict the composition over a separate 5-hour trial, the predicted composition was then compared to results recorded using the GC as means of validation.

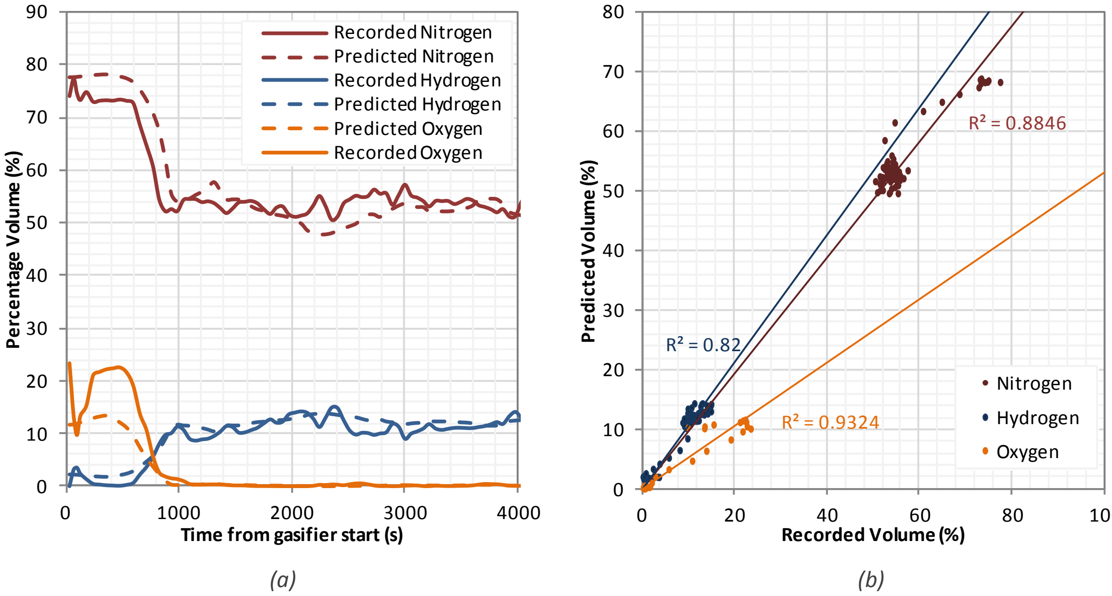

(a) (b)

Figure 46: Verification of the empirical model (a) predicted and actual results over time and (b) actual results against predicted results to find coefficient of determination

Figure 47 shows four properties of the producer gas over a gasification run, based on the empirically derived model and the recorded performance of the gasifier. It includes the percentage volume of hydrogen and hydrocarbons in the producer gas, as they have the greatest effect on two of its most important properties, Lower Heating Value (LHV), and stoichiometric air-to-fuel ratio. After approximately twenty minutes, the performance of the gasifier begins to stabilise, however post stabilisation significant fluctuations in the percentage volume of hydrogen remain; there are also fluctuations in the level of hydrocarbons, although they are not as obvious. Despite these fluctuations, the LHV remains steady, as does the stoichiometric AFR.

This is very important from a combustion point of view, as although the composition of the gas may vary over a run, the requirements of combustion air stay very stable, as should the thermal output of the burner. Hydrogen content has a marked effect on the stability limits of the combustion equipment, caused by the significant way it affects flame speed (Monteiro et al., 2010). In swirl burners it has also been shown that regardless of hydrogen content, reduction in mass flow rate (Syred et al., 2012) increases the stable operating range of equivalence ratios.

With producer gas as the fuel there is greater potential for blowoff occurring, where the flame detaches from the burner, rather than flashback, where the flame retreats inside the burner. This is due to its low laminar flame speed, if the flame starts to detach reduction in mass flow rate and fluid velocity may allow the flame to stabilise near the burner exit.

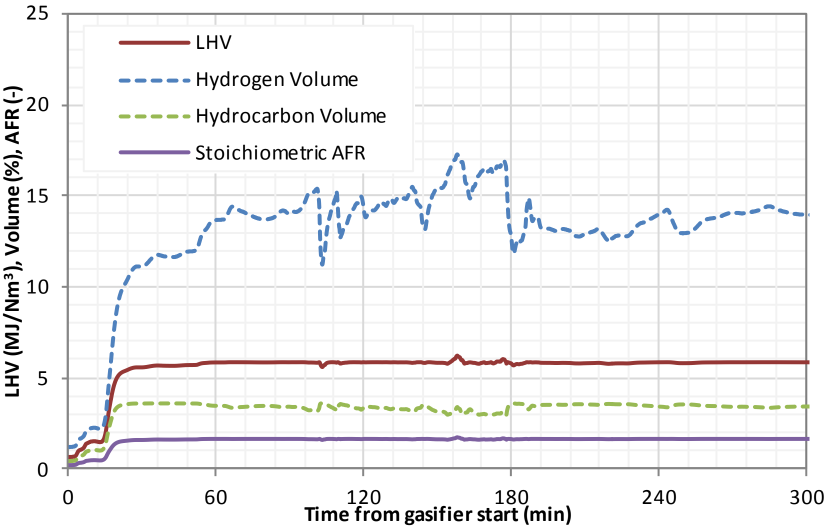

Figure 47: Producer Gas Properties based on model (Lewis et al., 2012)

4.2.3 Laminar Flame Speed

As stated, the hydrogen content of the fuel has a significant effect on the flame speed of a fuel, and thus a significant effect on its stability (Abdulsada, 2012, Syred et al., 2012). Both Figure 45 and Figure 47 demonstrate that hydrogen content can significantly vary, even during steady gasifier operation, with percentage of hydrogen varying from 11 to 17% without a noticeable change in the CV of the gas. The laminar flame speed (S_L) of a producer gas with varying levels of hydrogen was simulated using CHEMKIN, which previous studies have shown to provide a good approximation (Pareja et al., 2011). The gas compositions simulated had a hydrogen content varying from 5 - 15%, with the remaining volume made up as shown in

Table 12. The composition of the make-up gas is defined by the average composition of the producer gas, sans hydrogen.

In contrast to air blown producer gas there is a plethora of experimental data available into the flame speeds of Blast Furnace Gas (BFG). As a by-product the quality of the gas is of secondary concern to the iron-making process, resulting in a variable composition much like producer gas. The main constituents of dry BFG are; H_2 in the range of 0-7%, 20-30% CO and 16-25% CO_2, with N_2 (and possibly small quantities of H_20) making up the balance (Chu et al., 2004, Lampert et al., 2010, Ziebik et al., 2008, Lui et al., 2009). Where lower hydrogen levels are present, the Li et al. (2007) mechanism provides a very good estimation of the flame speed (Pugh et al., 2012), particularly at higher equivalence ratios, hence its use when flame speed was simulated over a variety of hydrogen compositions and equivalence ratios. Atmospheric pressure and ambient temperature initial conditions were used, with a mixture pressure of 1 bar and temperature of 20°C, the simulated flame speeds are displayed over a range of equivalence ratios in Figure 48.

Between the range of equivalence ratios simulated, for a given hydrogen content the lowest laminar flame speed occurred when equivalence ratio (Ø) was 2.0. As Ø decreases, S_L increases until a peak value is reached.

Regardless of hydrogen content, peak flame speed occurred when Ø was 1.2; with an increase in hydrogen content from 5% to 15% caused the peak flame speed to increase by 225%. Flame speed then decreases as Ø continues to decrease. Increasing the percentage volume of hydrogen from 11 – 17%, as was observed in Figure 47, would increase the peak flame speed from 17.8 cm/s to 27.1 cm/s.

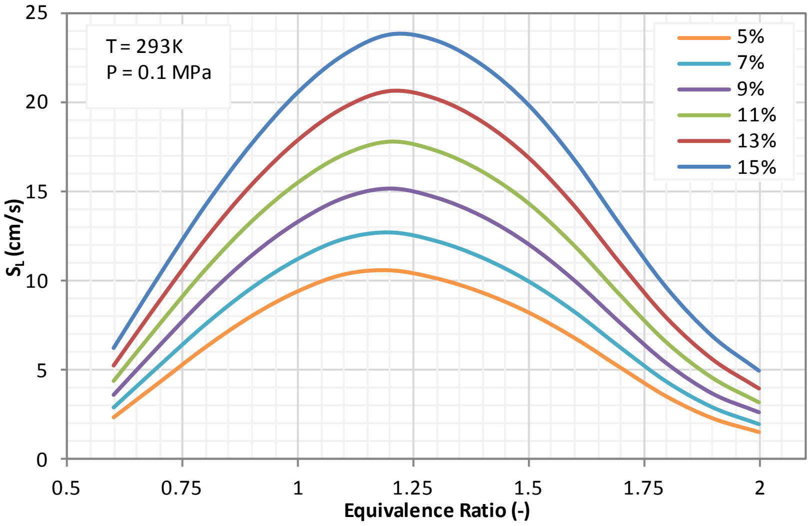

Figure 48: Effect of Hydrogen on Flame Speed modelled using the Li et al. (2007) mechanism

Table 12: Composition of Make-Up Gas

% Volume					
N_2	CO	CO_2	CH_4	C_2H_6	C_3H_8
64	18	14.5	2.3	0.7	0.5

This would have a significant effect on the stability limits of a burner, which, ignoring other factors would see the flashback and blowoff limits in terms of volumetric flow rate increase by a ratio of 1.52 as hydrogen content increases from 11% to 17%. The results were verified by comparison with the third iteration of the Gas Research Institute chemical mechanism (GRI Mech 3.0)(Bowman et al., 1999), as shown in Figure 49. Although there is a significant disagreement between the two mechanisms, especially in richer mixtures, both demonstrate the effect of hydrogen content on flame speed.

There is little published experimental data on the flame speeds of producer gas. However, a previous study into the flame speeds of oxygen blown producer gas by Vu et al. (2011) compared experimental data against a prediction using GRI Mech 3.0. In Vu's study GRI Mech 3.0 estimated flame speeds when equivalence ratio (Ø) equals 0.6 very closely, but as equivalence ratio increased so did its underestimation. As oxygen rather than air is used as the oxidant there is very little nitrogen diluting the gas, unlike the composition in

Table 12, resulting in a gas with a far higher LHV, as can be seen in Table 13.

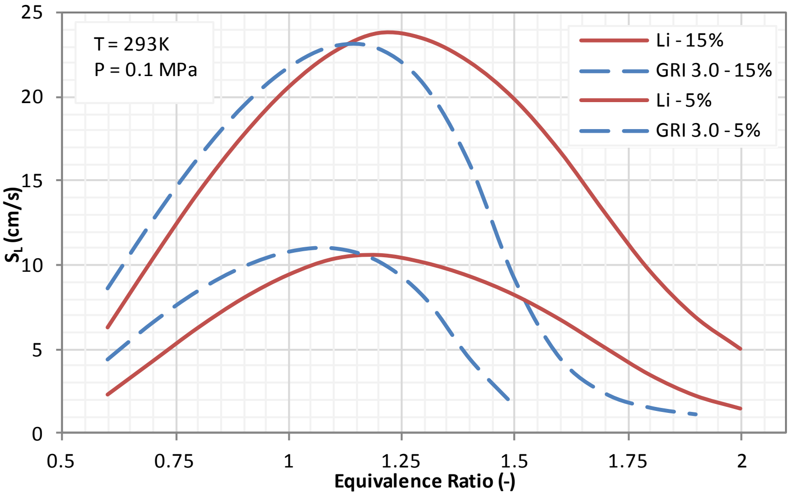

Figure 49: Comparison between Li et al. (2007) and GRI Mech 3.0 (Bowman et al., 1999) mechanisms

Comparison of Vu's experimental data with that predicted by the GRI Mech 3.0 (Bowman et al., 1999) and Li et al. (2007) mechanisms, as detailed in Figure 50, shows that both mechanisms underestimate the recorded flame speeds. Both make similar predictions, with the GRI Mech 3.0 seeming closer to the experimental data over in the entire range of equivalence ratios. The Li et al. Mechanism is however more accurate under lean conditions, which are preferred.

Table 13: Composition of Gas used by Vu (2011)

LHV (MJ/kg)	% Volume				
	N_2	CO	CO_2	CH_4	H_2
9.2	2.3	35.5	27	6.5	28.7

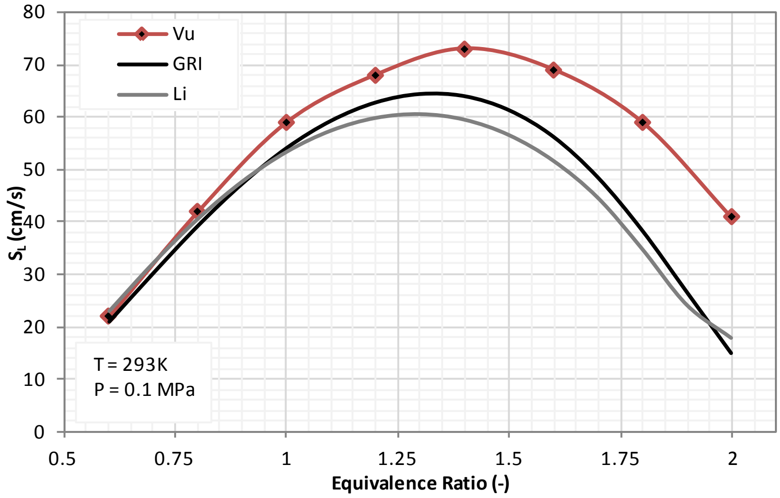

Figure 50: Comparing Experimental Data of Vu (2011), with Li et al. (2007) and GRI Mech 3.0 (Bowman et al., 1999)

Using the Li et al. mechanism and Equation 2.9, the laminar flame speed, and the Wobbe Index (WI), of the producer gas can be estimated. For the producer gas estimations in Figure 47, progressive changes in S_L and WI were plotted against time in Figure 51. Wobbe index is fairly constant, as was observed with LHV. Only significant increases or decreases in volumetric hydrogen content, caused sudden alterations in WI. The effect of these increases or decreases in hydrogen content is considerably greater in laminar flame speed. In Figure 47 a large decrease in hydrogen content occurs at around 180 minutes after gasifier start.

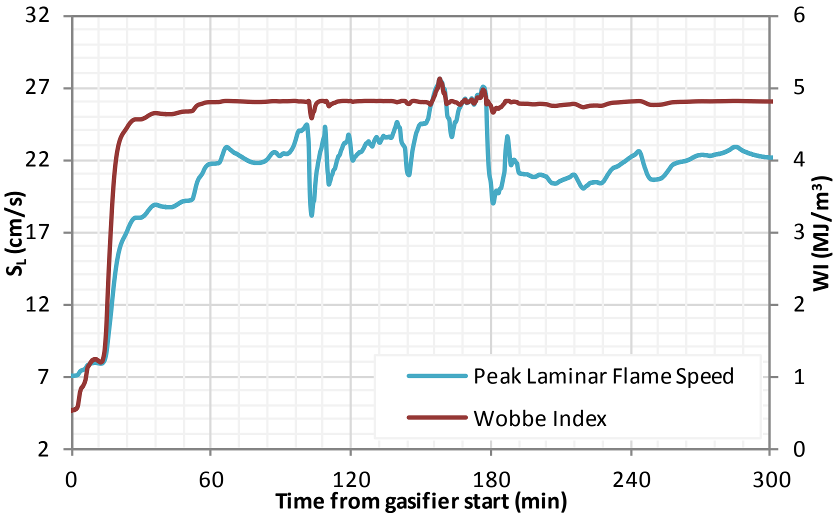

Figure 51: Fluctuations in Wobbe index and laminar flame speed based on the composition from Figure 47

This results in WI dropping from 5.45 MJ/m^3 to 5.11 MJ/m^3, a 6.7% decrease. The reduction in flame speed is larger, with S_L dropping from 26.97 cm/s to 18.92 cm/s, a 42.5% decrease. The disparity in these reductions is of concern to burner or engine manufacturers, who often define acceptable fuels based upon their Wobbe index.

4.2.4 The Effect of Initial Combustion Temperature

In all combustion design, knowledge of flame temperatures is exceptionally important to specify materials capable of withstanding the conditions immediately downstream of the flame, whilst avoiding over specification to minimise costs. When burning a fuel that is derived from waste sources it is especially important that flame temperatures can be predicted as regulations specify minimum flame temperatures and residence times. In the European Union the incineration of waste is regulated by Directive 2000/76/EC (The European Parliment, 2000). When calculating the adiabatic flame temperature of a given fuel, one must start by considering the energy balance across the entire combustion system, which is simplified in Equation 4.1, where; CV is the calorific value of the reactants, H_R is the sensible heat in the reactants, H_P is the sensible heat in the products, and Q_L is the heat loss to the burner.

$$CV + H_R = H_P + Q_L \qquad \text{Eq (4.1)}$$

Since adiabatic conditions are of concern, no heat transfer occurs across the systems boundary, heat losses to surroundings are not considered, and therefore the heat in the products can be calculated as described in Equation 4.2:

$$H_P = CV + H_R \qquad \text{Eq (4.2)}$$

To calculate the energy present on either side a mass must be know, using one kilogram simplifies matters as the most common way to express the calorific value of a gas is in J/kg, kJ/kg or MJ/kg. Calculation of sensible heat requires knowing the composition of the gas, and the specific heat of each component, at temperature *T,* where *m* is mass and C_P is specific heat. Sensible heat is calculated as shown in Equation 4.3:

$$H_T = T.\sum\left(m.C_p\right)_T \qquad \text{Eq (4.3)}$$

Therefore, calculating flame temperature, T_f, where the temperature of the reactants is, T_r, is possible using the Equation 4.4:

$$T_f.\sum\left(m,C_p\right)_{P@Tf} = CV + T_r\ .\sum\left(m,C_p\right)_{R@Ti} \qquad \text{Eq (4.4)}$$

After finding the energy value of the right hand side, iteration will be required to calculate the flame temperature. The mass and components of the products would not be the same as the reactants. When producer gas leaves a gasifier it is at high temperatures, upwards of 500°C when biomass is the feedstock (Brammer and Bridgwater, 2002). Heat is naturally lost when the gas is treated, but when the gas is fed into internal combustion engines significant gas cooling is also required (Makartchouk, 2002), wasting thermal energy. Therefore it would be more energy efficient to use the gas in way that allows this thermal energy to be retained. In gas turbine combustion, where air and fuel are preheated, increasing the heat of the combustion products by a degree Kelvin increases the adiabatic flame temperature by approximately half a degree Kelvin (Lefebvre, 1999). However, there is not a perfect linear relationship between reactant temperature and flame temperature, caused, fundamentally, by a non-linear relationship between temperature and specific heat capacity.

Figure 52 shows the adiabatic flame temperature of three air and fuel mixtures, with adiabatic flame temperatures normalised against those under normalised conditions of temperature and pressure. The blue line shows a stoichiometric mixture of methane and air, with both fuel and combustion air preheated; there is a significant increase in flame temperature as preheat temperature increases, and thus the extraction of more thermal energy is possible. When, in a stoichiometric mixture, only the methane is preheated, as indicated by the red line, there is only a minor increase in flame temperature, the high stoichiometric air-to-fuel ratio meaning the initial temperature of the mixture as a whole is only raised slightly.

For the producer gas observed from then proprietary plant, which has a typical stoichiometric AFR of 1.2, as opposed to approximately 17.2 for methane, the effects of preheated fuel are far more obvious. The green line in Figure 52 shows the adiabatic flame temperature of a stoichiometric mixture of producer gas and air. By increasing the preheat temperature to 400°C, the adiabatic flame temperature, and approximately the thermal energy in the product gas, has increased by 7%.

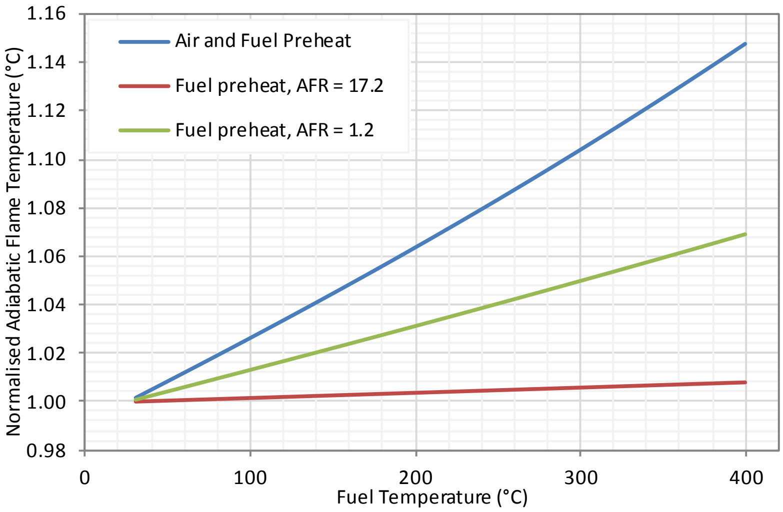

Figure 52: Adiabatic flame temperatures with varying preheat, AFR is calculated by mass

This shows that for gasification to thermal energy applications it would be beneficial to retain the heat in the producer gas, however there are other factors to consider, such as particulates that may exist in gas stream at this temperature and whether auxiliary equipment, such as valves or flame arrestors, remain operable.

4.2.5 Simulation with Natural Gas

The potential to use diluted methane as a simulated producer gas was investigated, initially with the calorific value of the overall mixture defining an equivalent composition. However, as previously discussed the relationship between laminar flame speed and local velocity of mixture is of great importance to flame stability. CHEMKIN was again used to simulate the flame speeds of mixtures of producer gas (with the Li mechanism) and natural gas with air as the oxidant (with the preferred GRI Mech 3.0 mechanism), which are shown in Figure 53.

There is a difference between the flame speeds of producer and natural gas mixtures with the same overall CV. Flame speeds are equal at a CV of 2.6 MJ/Nm^3. At this point, the equivalence ratios of producer gas and air diluted natural gas are 1.21 and 0.68 respectively.

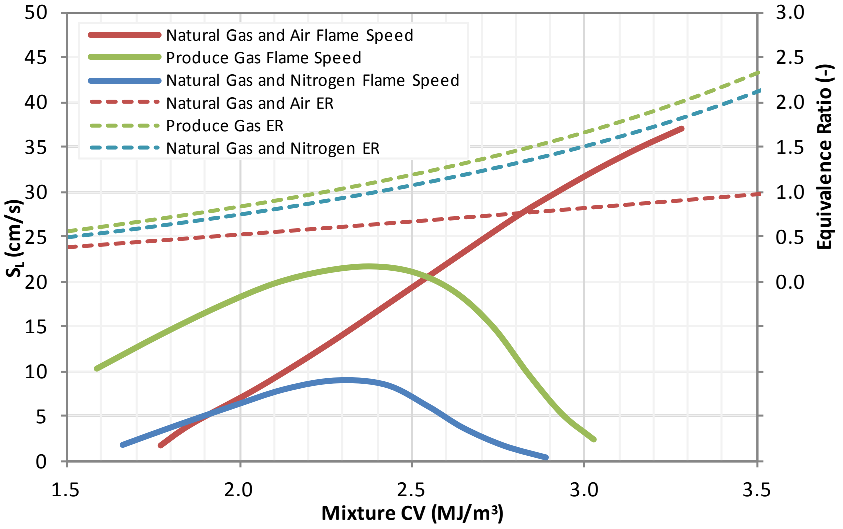

Figure 53: Producer and Natural Gas Flame Speeds (Lewis et al., 2012)

At an equivalence ratio of 1, the flame speed of producer gas is 21.6 cm/s, at an equivalent mixture CV the flame speed of natural gas is 13.2 cm/s. This means that simulating combustion of a stoichiometric AFR Producer gas mixture with natural gas would underestimate blowoff limits and overestimate flashback limits (in terms of mass flow rate). Indeed, this would be the case for producer gas equivalence ratios below 1.21, above which the opposite becomes true. Although there are differences between flame speeds, they are not so considerable that potential laboratory experimentation with diluted natural gas should be disregarded, especially when the majority of the fuel is introduced tangentially or experimentation is not focussed on stability limits.

A better simulation may be achieved by diluting natural gas with nitrogen, which could reduce the overall mixture CV without the addition of an oxidant. As Figure 53 indicates, this results in a equivalence ratio that is much closer to that of producer gas across the range of CV's, as such the flame speed profile across the range is a very similar shape, with both having a peak flame speed when the CV of the mixture is between 2.3-2.4 MJ/Nm^3. However, in producer gas equivalence ratios in the range 0.79 to 1.41, within which combustion equipment would be expected to operate, the flame speed of air diluted natural gas is closer to that of producer gas than nitrogen diluted natural gas. When stability is being investigated, it is preferable to equate flame speeds. This can be achieved by using a lean mixture of natural gas and air. Figure 54 shows the natural gas equivalence ratio required to reproduce the same flame speed as producer gas mixtures over the equivalence ratio range of 0.5 to 1.7. For example, producer gas with an equivalence ratio of 1.00 will have the same laminar flame speed as a natural gas mixture with an equivalence ratio of 0.68. The methane equivalence ratios required to simulate the mixture CV of producer gas are also shown in Figure 54. Only when producer gas Ø and natural gas Ø are 1.16 and 0.66 respectively, do flame speed and mixture CV equate.

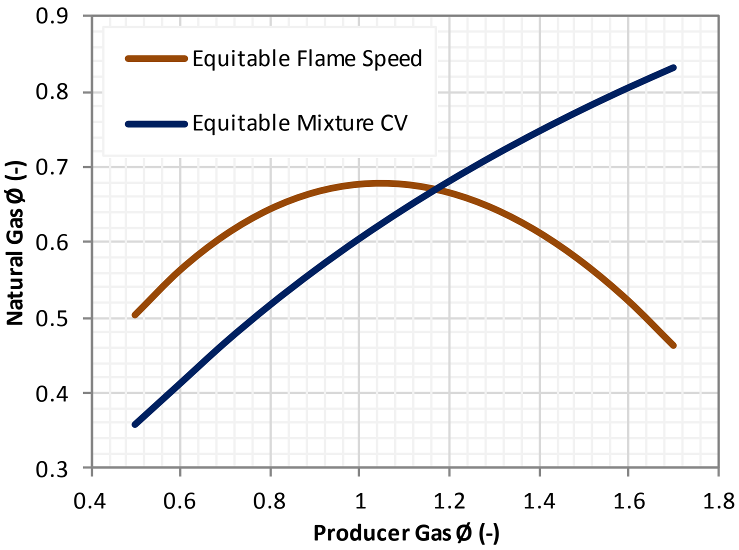

Figure 54: Producer and Natural Gas Mixtures with the same Flame Speed and/or Mixture CV

Diluted methane combustion could be used to assess the how changes in composition effect a combustion system. The laminar flame speed and WI ranges of the producer gas from the proprietary plant can be matched with natural gas and air mixtures. Varying the AFR of air and methane mixtures could replicate the changes in S_L or WI seen in Figure 51 (Lewis et al., 2012).

4.3 Wobbe Index and Flame Speed

Laminar flame speed (S_L) itself is not of direct relevance in gas turbine combustors, where the flow of the combustible mixture will be, in almost all cases, highly turbulent. There is a direct relationship between laminar and turbulent flame speeds. With increased turbulence, the fluctuating velocity in the flow increases (Cheng et al., 2009), which promotes flame propagation. With turbulent flame speed (S_T) equalling the laminar flame speed plus the product of a gas dependant constant and root mean square of fluctuating velocity (Syred et al., 2014), .

CHEMKIN, in conjunction with the GRI Mech 3.0 chemical mechanism (Bowman et al., 1999), was used to assess how the a change in gasl composition may affect the relationship between Wobbe Index and laminar flame speed. Propane has a significantly higher WI than methane, 69.1 MJ/m^3 compared to 45.4 MJ/m^3 at 1 barA and 293 K, and a higher laminar flame speed. Figure 55 (a) shows the addition of propane, representing higher hydrocarbons, to methane changes the WI of the fuel and S_L of mixture, at conditions representative of a gas turbine combustor. The most notable observation is the strong, but not perfect linear relationship that exists between WI and S_L that exists across all equivalence ratios.

What must also be considered is that as WI changes, so does the Stoichiometric Air-to-Fuel Ratio (SAFR). The way a gas turbine operates results in a constant mass flow of air, so changes in SAFR cause similar changes in equivalence ratio, further altering the laminar flame speed. Figure 55 (b) takes this further change into account, comparing the calculated average (Φ =0.5..1.0) and stoichiometric laminar flame speeds with those corrected for the changes in equivalence ratio. An air mass flow rate for the maximum WI is assumed, and it can be seen that the relationship between WI and S_L remains linear and that discrepancy in flame speeds is very small, the maximum being 0.83%. This linear relationship is retained, largely due to the two gases involved being flammable and having similar stoichiometric air-to-fuel ratios. When there is a variation in the balance between flammable and non-flammable there is a deviation from this linearity.

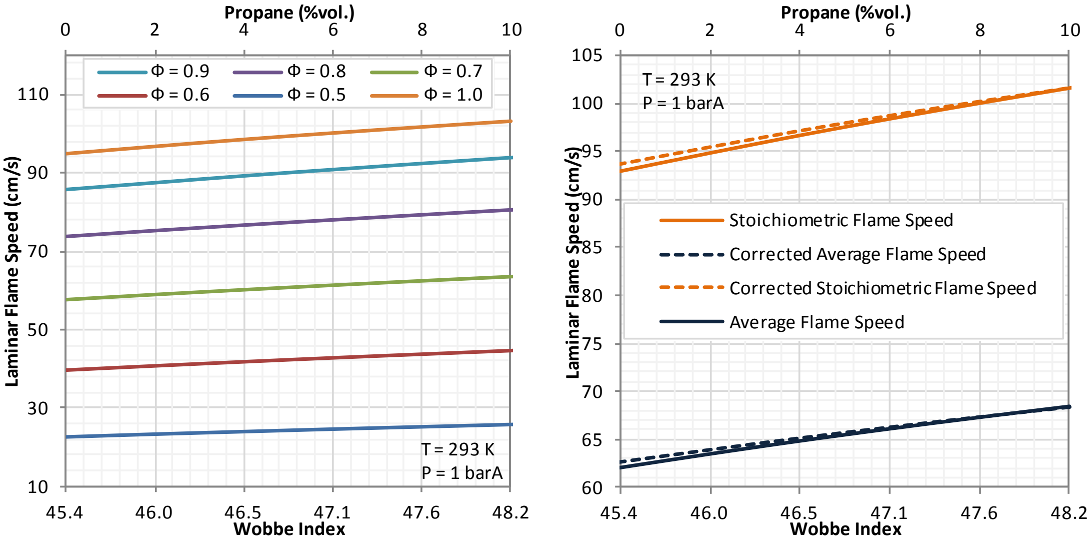

(a) (b)

Figure 55: A comparison between Wobbe Index and laminar flame speed for (a) different equivalence ratios and (b) correcting for change in equivalence ratio with Wobbe Index

Figure 56 (a) shows the relationship between WI and S_L for the producer gas variations detailed previously. Looking at how the relationship changes for a stoichiometric mixture this deviation is apparent, but what is more apparent is the combined effect of the change in WI and equivalence ratio on the flame speed, with small changes in composition having a significantly more pronounced effect on flame speed.

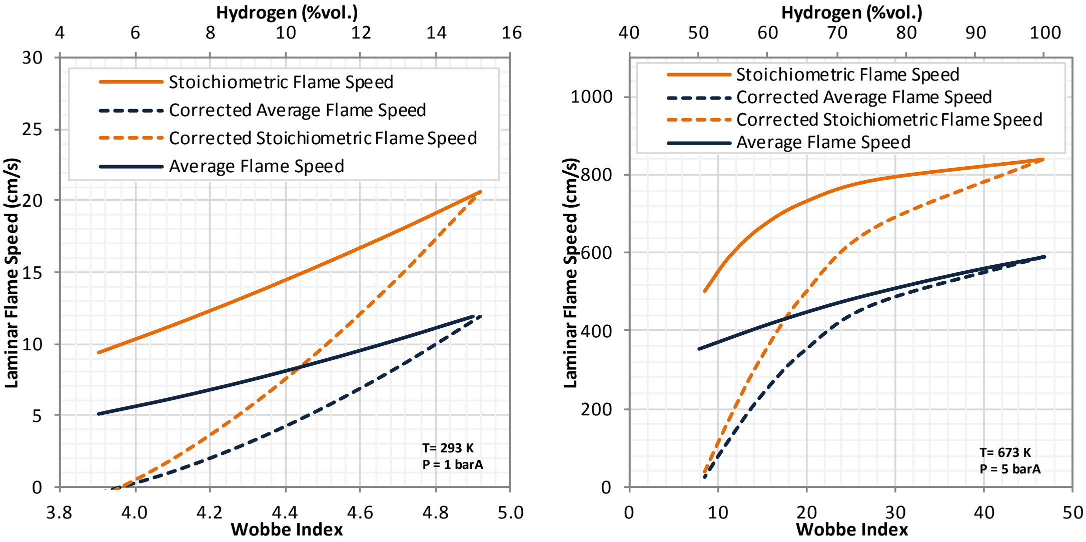

(a) (b)

Figure 56: A comparison between Wobbe Index and laminar flame speed for (a) producer gas with variable hydrogen and (b) hydrogen nitrogen mixtures

The same is true of pure hydrogen-nitrogen blends, which are shown in Figure 56 (b).

The work by Abbott et. al. (2012) demonstrated that WI has significant impact upon gas turbine operation in a practical application. The work suggested that WI alone is not a sufficient method of fuel characterisation, and the results in Figure 56 are in agreement with that. Fuel blends containing inert gases, including natural gas in practical situations, display non-linear relationships between WI and S_L, with small changes in WI having significant implications on laminar flame speed. Perhaps more significantly where interchangeability of fuels is concerned significant variations were observed in the S_L of methane/propane and hydrogen/nitrogen blends of equal WI. When WI was 46 MJ/m^3 and equivalence ratio was 1, the laminar flame speeds of the methane/propane and hydrogen/nitrogen blends were 94.8 cm/s and 837.6 cm/s.

As previously stated laminar flame speed is not directly relevant in gas turbine combustion due the high turbulence present. Therefore it is unlikely to be the second parameter of fuel characterisation that Abbott et. al. Suggest is required, however it does indicate how fundamental flame characteristics may vary within prescribed WI limits. Parameters directly related to turbulent combustion, such as turbulent flame speed, Markstein number or critical stretch are likely to be more appropriate.

4.4 Chapter Summary

The consistency of producer gas composition from a proprietary gasification plant was investigated using gas analysis. The gasifier used grade-A woodchip (The Wood Recyclers Association, 2009), which is a fairly homogenous biomass source.

A relationship between throat temperature and hydrogen content was established, where hydrogen content increased as gasification temperature increased (Lewis et al., 2012), an effect that has been reported by other researchers (Bal´aˇs et al., 2012). The stoichiometric equivalence ratio of the fuel remained very steady, this was due to the opposing effect of temperature on hydrocarbon content of the producer gas, which reduced as gasification temperature increased. This reduction was observed in methane by Bal´aˇs et al. (2012), and is in agreement with modelled results for biomass over the same temperature range produced by Mhilu (2012). Temperature dependent composition, with hydrogen content increasing relative to hydrocarbon content as temperature rises, has also been reported with regard to the gasification of coal by Haji-Sulaiman et al. (1986), and the gasification of municipal solid waste by He et al. (2009).

An empirical model was derived for this particular gasifier and feedstock combination to predict producer gas composition based on gasifier throat temperature. Comparison over a short gasification run showed good agreement between predicted and recorded results. The model was applied to a longer gasification run and the variation in stoichiometric air to fuel ratio and lower heating value of the producer gas were assessed over time. As gasifier temperature is the main factor in defining composition (Bal´aˇs et al., 2012), and it has a competing effect on the main combustible constituents of the gasifier, the SAFR and LHV remain very steady despite large fluctuations in composition. The most significant fluctuations predicted were in hydrogen content, which can have a major effect on flame stability (Dam et al., 2011b, Mohon Roy et al., 2009, Syred et al., 2012, Thornton et al., 2007) due to its impact upon flame speed (Monteiro et al., 2010).

CHEMKIN was used to simulate how the flame speed of the producer gas would be affected by the fluctuations in hydrogen content. The Li (2007) chemical mechanism was used after Pugh (2012) determined its suitability for simulating blast furnace gas flame speeds, which has a similar composition and hydrogen content to the producer gas in question. The accuracy of the Li mechanism was assessed against both experimental data (Vu et al., 2011) and another CHEMKIN integrated chemical mechanism (Bowman et al., 1999). Simulations, at ambient temperature and atmospheric pressure, showed the marked effect that hydrogen content has on laminar flame speed. At a typical lean premix equivalence ratio of 0.91, equal to 10% excess air, as hydrogen content increases from 5% to 15%, laminar flame speed increases from 8.0 cm/s to 17.7 cm/s (Lewis et al., 2012).

The predicted range of hydrogen volume in the producer gas, (once the gasifier operation was stable), was 11–17%. Although this had little impact upon SAFR or LHV this would cause peak flame speed to vary between 17.8 cm/s and 27.1 cm/s. A sudden drop from 17 to 12 % in hydrogen content was predicted. This is a significant difference, and would result in a sudden drop from 17.0 cm/s to 8.0 cm/s at an equivalence ratio of 0.91. A drop in S_L of that degree is likely to cause flame detachment, whereas a sudden increase of that nature is likely to cause to flashback (Syred et al., 2012).

Producer gas leaves the gasifier at high temperature (Brammer and Bridgwater, 2002), for use in an internal combustion engine the gas must be extensively cooled, in order to achieve reasonable levels of efficiency (Makartchouk, 2002). When the gas is to be utilised in a continuous combustion system, like a boiler or gas turbine, maintaining the thermal energy in the gas is beneficial. The efficiency of energy production is improved, as increasing reactant temperature by a degree equates to approximately half a degree gained in flame temperature (Lefebvre, 1999). The effect of fuel temperature on the adiabatic flame temperatures of a stoichiometric producer gas and air mixture was assessed. By purely retaining temperature, maintaining a gas stream temperature of 400°C rather than 40°C increased adiabatic flame temperature and energy output by 7%.

The potential to use diluted natural gas as a simulated producer gas was investigated, with air and nitrogen as the diluents. Although diluted natural gas has the potential to yield flame speeds exceeding the range of a producer gas and air mixtures, at equitable flame speeds the calorific value of the mixtures were appreciably different (Lewis et al., 2012). Therefore, depending on what conditions are being assessed, simulation with natural gas would require a choice between thermal or velocimetric equilibrium.

Manufacturers prefer to specify fuels in terms of their energy density, with this parameter defined by Wobbe Index (WI) (Abbott et al., 2012). WI, is also used to assess interchange ability between fuels (Coyle et al., 2007). Changes in WI and laminar flame speed (S_L) were compared for methane and propane variations. An almost linear response was seen, which suggested that WI is a reasonable method of assessment for fuel sources without inert components. This suggests that the range of acceptable WI of 48.96 to 56.62 MJ/Nm^3 proposed by EASEE-gas (2005) is too large for lean combustions. With a linear response this equates to a 15.6% range of flame speeds, significant enough to cause instability. This is supported by Slim (2011) who reported stability issues with low NO_x industrial burners over this range of WI.

Potential changes in flame speed are often disregarded when natural gas composition variations are assessed (Loubar et al., 2007), or hydrogen addition is suggested as a method of fuel doping (Zachariah-Wolff et al., 2007). These results show that where interchange ability between fuel sources is concerned, flame speed must be considered, with Wobbe Index alone not sufficient. There should also be a regard for the temperature of the fuel supply (Abbott et al., 2012), as increasing temperature will increase flame speed (Zhao et al., 2004) but reduce WI.

Chapter 5: Mechanisms of Isothermal Acoustic Response

5.1 Introduction

With an ultimate aim of identifying how acoustic response changes with fuel-air mixtures, which will occur if fuel composition varies, the initial aim of this chapter is to gain understanding into the acoustic response of a combustion system with non-reacting flows. This will determine the aerodynamic effects on acoustic response.

Uncontrolled or unmonitored acoustic resonances have the potential to cause severe damage to the combustion systems in which they prevail. There are many sources of pressure oscillations in a combustion system and the potential of these to cause large amplitude, destructive, instabilities, depends on a complete feedback mechanism being present. Acoustic oscillations can be the result of heat release oscillations, or perturbations in the flow or mixture air-to-fuel ratio (Lieuwen, 1999, Lieuwen, 2012a). If the resulting acoustic oscillations are sufficiently in phase with the preceding oscillations or perturbations, then the feedback mechanism promotes amplification of the resulting oscillations (Farhat and Mohamed, 2010).

Whenever there is a steady flow of gas passing through a combustion system some oscillations will be present. This is true whether there is a combustion process occurring or not. This being the case, it stands to reason that the presence of acoustic oscillations does not necessarily indicate that a system is unstable.

As such, combustion free, system acoustic responses are analysed, to identify the acoustic oscillations that exist independently of the combustion process; thus making them identifiable as the source of oscillations when combustion is introduced. A series of isothermal experiments were performed in order to characterise the acoustic signature of burners under different flow conditions in order to determine natural resonance within the system, whilst detecting coherent structures and establish their temporal evolution. Thus allowing the isothermal effect of swirl and flow rate on cold flow structures to be compared to the effect under combustion conditions.

Isothermal experimentation was performed using the cyclone burner and methodology described in section 3.3.2. Oscillations from two sources were present during testing; those which resulted from natural resonance of the rig, excited by the flow of fluid through the system, and those that were the direct result of the fluid flow.

5.2 Predicting Resonance

The natural frequency of the system is defined largely by the geometry of the combustion and swirl chambers, which act similarly to Helmholtz resonators. The natural frequency of the various system components can be estimated using equation 5.1, and the method described by Putman (1971):

$$f = \frac{c}{2\pi} \cdot \sqrt{\frac{A_{th}}{V_c \cdot L_t}} \qquad \text{Eq (5.1)}$$

Where: A_{th} = Throat Area (m^2)

V_c = Volume of Cavity (m^3)

L_t = Throat Effective Length (m)

And c = Speed of sound (m/s), defined for an ideal gas thus:

$$c = \sqrt{\gamma \cdot R \cdot T} \qquad \text{Eq (5.2)}$$

Where: γ = Ratio of Specific Heats (-)

R = Universal Gas Constant (J/K·kg)

T = Absolute Temperature (K)

The flow of gas through the cavities means that they do not behave exactly like a Helmholtz resonator, therefore the speed of sound in the Eq. (5.1) is adjusted thus:

$$c = \sqrt{\gamma \cdot R \cdot T} - \frac{Q}{A_t} \qquad \text{Eq (5.3)}$$

Where: Q = Volumetric Flow rate (m^3/s)

For the cyclone burner the predicted Helmholtz frequencies for an ambient air temperature of 295 K, and with no flow, were 218 Hz, 117 Hz and 162 Hz for the combustion chamber with confinement A fitted, the combustion chamber with confinement B fitted, and the swirl chamber respectively. The temperature of gas in the respective throats is affected by combustion. This will change natural frequency by a factor equal to the square root of the ratio of absolute actual temperature and absolute ambient temperature. This assumes that the speed of sound of the gaseous products of the combustion process is the same as that of air. In actuality the ratio of specific heats for the product gases of a stoichiometric mixture is 1.375, approaching 1.4 as equivalence ratio increases. When predicting natural frequency, this would contribute a maximum percentage error of 1.33%.

5.3 Cold Coherent Structures

There are several factors that contribute to combustion driven instabilities, heat release oscillations have been well documented (Lieuwen, 1999, Lieuwen, 2012a, Putman, 1971, Huang and Yang, 2009). Large-scale coherent structures have also been shown to be a source of thermo acoustic instabilities (Yazdabadi, 1995, Fick, 1998, Froud et al., 1995, O'Doherty et al., 1999, Syred, 2006). These structures include Central Recirculation Zone (CRZ) (Coghe et al., 2004), a Precessing Vortex Core (PVC) that occurs when a CRZ is formed (O'Doherty et al., 1999, Syred, 2006), and vortex shedding mechanisms. Previous work performed on this burner documented the presence of pressure fluctuations caused by the presence of a PVC (Valera-Medina, 2009). Vortical structures distort the shape of the flame, leaving it asymmetric, therefore, the surface oscillates and causes heat release oscillations (Schadow and Gutmark, 1992). The pressure fluctuations caused by structures in the flow are difficult to detect using an external microphone; to prevent combustion noise distorting the potential influence of coherent structures on the acoustic behaviour of a burner isothermal experimentation was used.

The PVC is seen as major driver for combustion instabilities (Moeck et al., 2012), and the oscillations it induces are particularly likely to cause damage to a combustion system if they couple with the combustions chamber's natural frequency, which will result in higher amplitude fluctuations in pressure. Experiments determined the dominant frequency over a range of flow rates, with four burner inlet configurations, as demonstrated in Figure 39, used to deliver geometric swirl numbers of 0.74, 1.08, 2.02 and 4.46, for both confined and unconfined conditions.

5.3.1 Structure Strength

The Fast Fourier Transform (FFT) analysis and autocorrelation plot of the acoustic response for three instances are shown in Figure 57 (a). The instances are isothermal flows with geometric swirl numbers of 0.74, 1.08 and 2.02, with an exit nozzle Reynolds number of 48200; the combustion chamber was fitted with confinement A, as shown in Figure 38. The power spectrum produced from the FFT analysis of S_g = 2.02 shows a very strong frequency response at 98 Hz, with significantly reduced responses at 154 and 208 Hz. The weak responses around 154 and 208 Hz are also visible in the power spectrum from S_g = 0.74 and 1.08. The weak, yet consistent, responses are caused by the flow of air exciting the natural frequencies of the combustion chamber fitted with confinement A and the swirl chamber, which were estimated to be 212 and 158 Hz respectively. S_g = 1.08 also shows a strong response at 75 Hz. The strong peaks at 98 and 75 Hz indicate a defined oscillation occurring at these frequencies, consistent with a coherent structure. The autocorrelation plots in Figure 57 (b) show the presence of a periodic repetitive signal, which increases dramatically in amplitude and correlation time as swirl number increased.

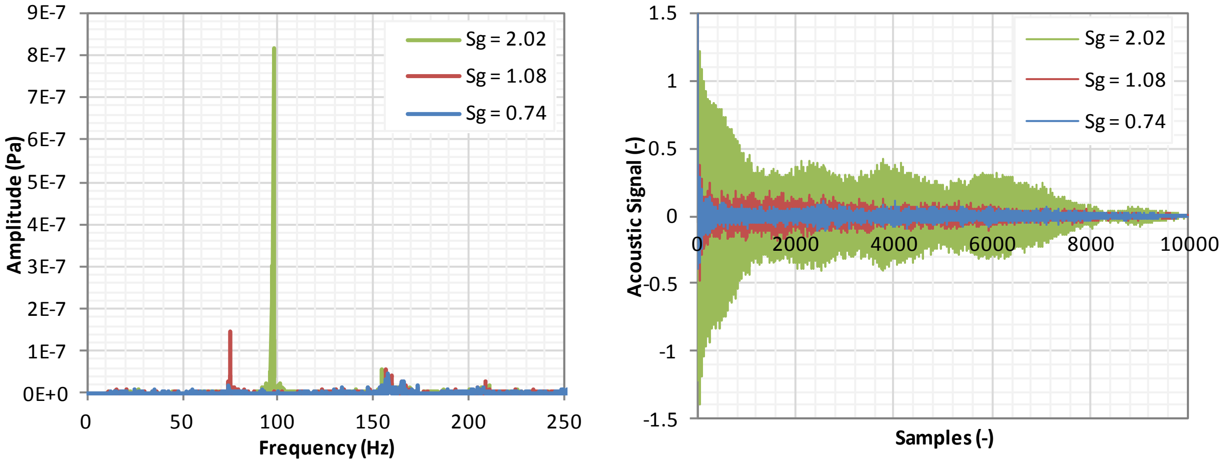

(a) *(b)*

Figure 57: (a) FFT analysis and (b) Autocorrelation of an isothermal flow with Sg= 2.02,1.08 and 0.74, with confinement A (Exit Nozzle Re = 48200, Tangential Inlet Re = 68700, 39500 and 34400 respectively)

As the only variation is in swirl number, it is concluded that vortex breakdown, which is dependent on swirl strength and Reynolds number (Luca-Negro and O'Doherty, 2001) has occurred when S_g = 1.08 and 2.02. As a result structures have formed in the flow, and that strength and rotational frequency of the structures increases with the level of swirl. Previous work using this particular burner has confirmed the existence of an isothermal CRZ-PVC pairing under these conditions (Froud, 1995, Valera-Medina, 2009), although only its presence and appearance was investigated.

There is no definite peak in the spectrum of the case where $S_g = 0.74$, this is caused by one of two reasons. That the level of swirl is not great enough to have induced vortex breakdown, or as suggested by the results shown later in Figure 58, where a peak is detected for $S_g = 0.74$ and Re = 48200, the strength of the structures are not great enough to cause a detectable resonance of the burner.

The results in Figure 57 demonstrate that for a given burner configuration and flow rate, the presence, strength, and frequency of the flow structures are dependent on the level of swirl imparted on the flow, agreeing with very early work on the subject of swirling flows (Syred and Beér, 1974).

5.3.2 The Effect of Flow Rate on Structures

Syred (2006) stated that frequency of a PVC would increase quasi-linearly with flow rate, and this is true of all structures in the flame, or flow region. This is demonstrated in Figure 58 (a), where the measured dominant frequency is plotted against a range of swirl chamber exit nozzle Reynolds numbers for the four geometric swirl numbers, with burner unconfined. Observed was a very strong linear relationship, with coefficients of determination ranging from 0.9986 to 0.9996. Dominant frequency is also plotted against the tangential inlet Reynolds number. Tangential inlet velocity is calculated by dividing the total volumetric flow rate by the total area of the tangential inlets to the swirl chamber. These inlets are restricted to varying amounts in order to alter the swirl number, as such for a given flow rate each swirl number will have a different inlet velocity. In Figure 58 (b) it can be seen that for a given turbulence level, the variance in dominant frequency is less for tangential inlet Re compared to exit nozzle Re. For a given tangential inlet Re the range of dominant frequencies recorded is 20% less than for a given nozzle velocity. Recent work has shown, when combustion is introduced, a high level of correlation exist between the flashback and blowoff limits of swirling flows and tangential inlet velocity (Syred et al., 2013b, Syred et al., 2013a, Syred et al., 2014).

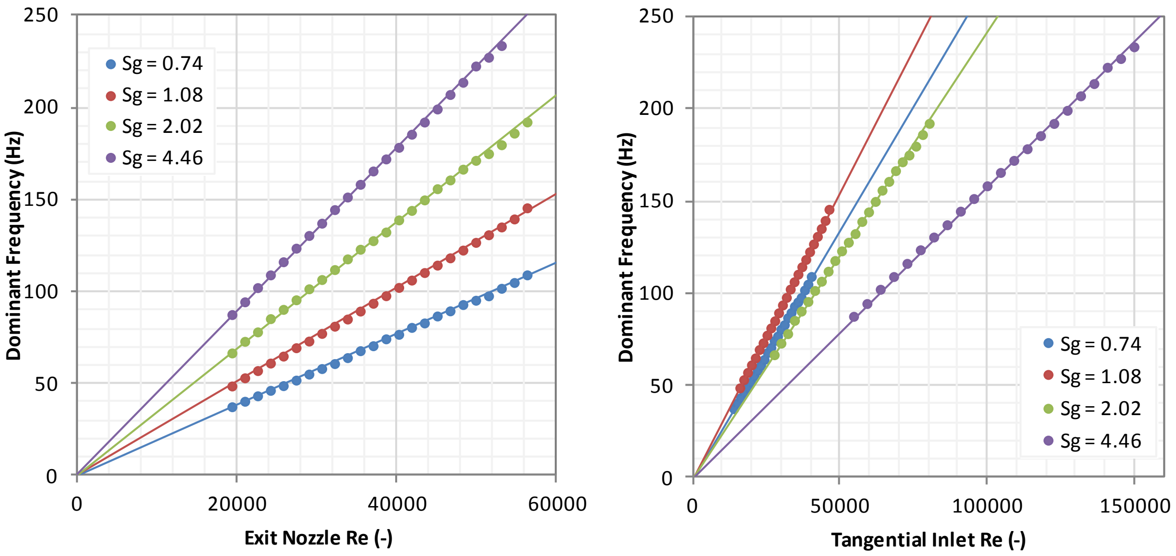

(a) *(b)*

Figure 58: Dominant frequency against (a) combustor chamber exit nozzle Re and (b) tangential inlet Re for unconfined burner

For the unconfined case, a relationship between Re and dominant frequency extended over the full range of flow rates. This was not the case when the combustion chamber was used, fitted with either confinement A or B, which are detailed in section 3.3.2. Figure 59 and Figure 60 show the results for confinements A and B respectively.

In both cases, when the flow has a geometric swirl number of 0.74, a proportional relationship between flow rate and dominant frequency does not exist. Instead, frequencies around 160 Hz were recorded across the entire range, corresponding to the natural resonance of the swirl chamber. Additional, far weaker, responses visible in the power spectrums around 208 Hz for confinement A and 115 Hz for confinement B. Rather than being caused by structures in the flow; these responses correspond to the natural frequencies of the fitted confinements. When confinement B was fitted an acoustic response was also recorded at around 208-210 Hz, although it is significantly weaker than when confinement A was fitted. This suggests that a permanent feature in the rig is also causing a response at this frequency.

For either confinement, and with all four swirl levels, no structures were detected at the lowest recorded flow rate of 1000 L/min (exit nozzle Re = 16070). As flow rate increased a transition point between coherent structures and a resonant frequency being the source of the dominant frequency was reached, the flow rate of this transition depended on the level of swirl and type of confinement. Based on the exit nozzle Re results in Figure 59 (a) and Figure 60 (a) there is no obvious relationship between swirl number and transition point, other than the higher the swirl number the lower the flow rate required for the structures to become apparent.

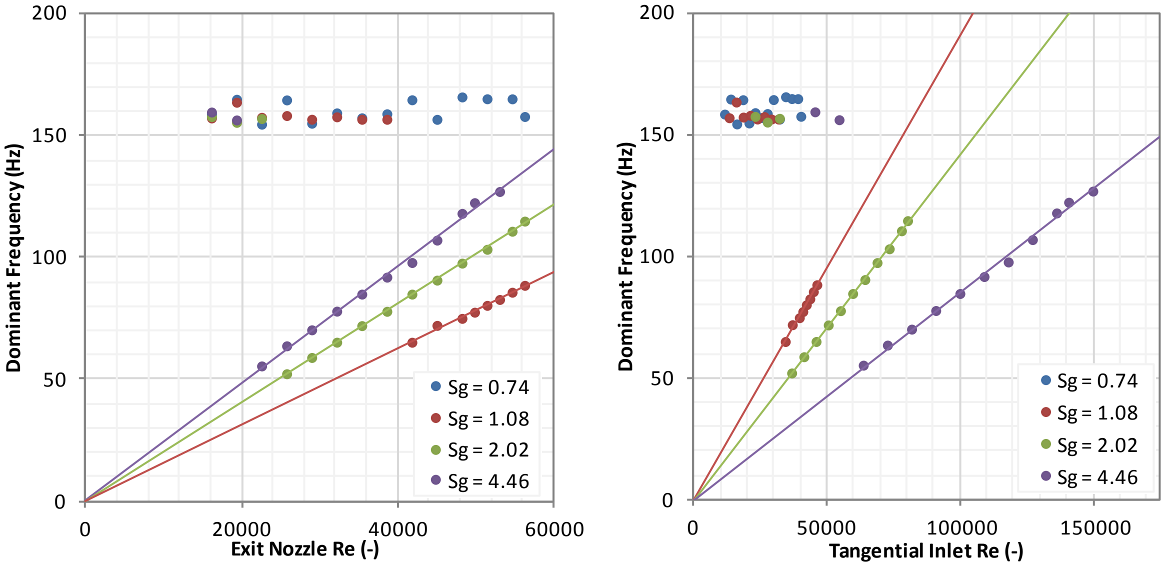

(a) *(b)*

Figure 59: Dominant frequency against (a) combustor chamber exit nozzle Re and (b) tangential inlet Re for the burner with confinement A

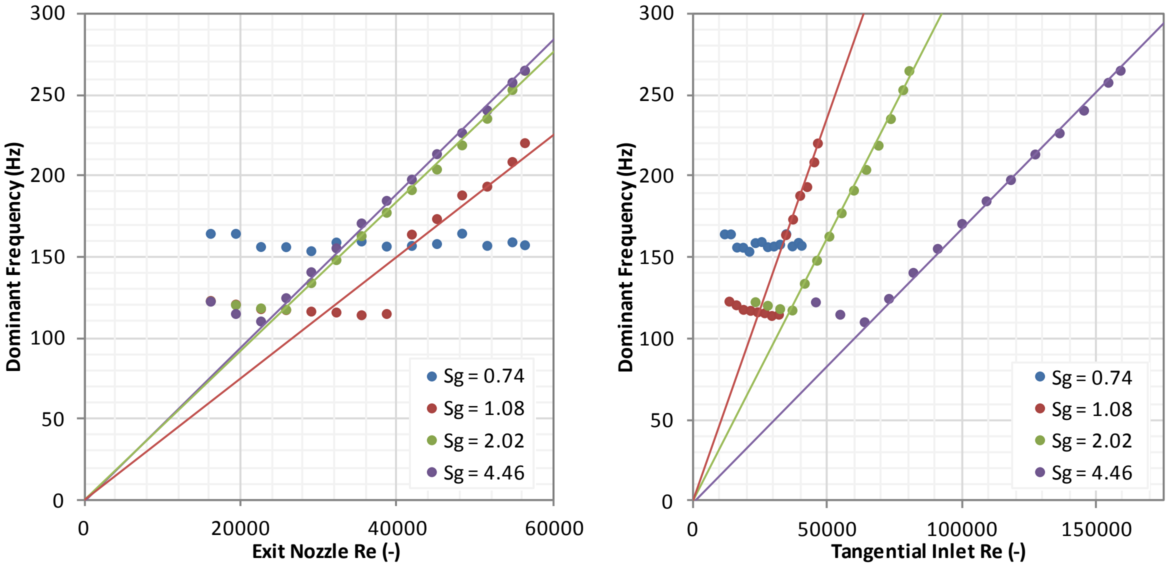

(a) *(b)*

Figure 60: Dominant frequency against (a) combustor chamber exit nozzle Re and (b) tangential inlet Re for the burner with confinement B

However, when the tangential inlet velocity is taken into consideration, the position of the transition points seem more structured and suggest that the transition point for S_g = 0.74 would be reached if the Re could be further increased. In Figure 59, the dominant frequencies observed before the transition point are all defined by the geometry of the swirl chamber, although the power spectrums show a smaller response at the estimated natural frequency of the fitted confinement. The same was true for S_g = 0.74 when the narrow confinement B was fitted, conversely, when geometric swirl number was 1.08, 2.02 or 4.46 the dominant frequency prior to the transition point was dictated by the geometry of the combustion chamber and confinement, with a weaker response present at around 160 Hz, the natural frequency of the swirl chamber.

Re was plotted against dominant frequency in Figure 61, this time the swirl number was fixed, with each data series corresponded to a different confinement. The transition point of the dominant frequency is very obvious for the confined cases.

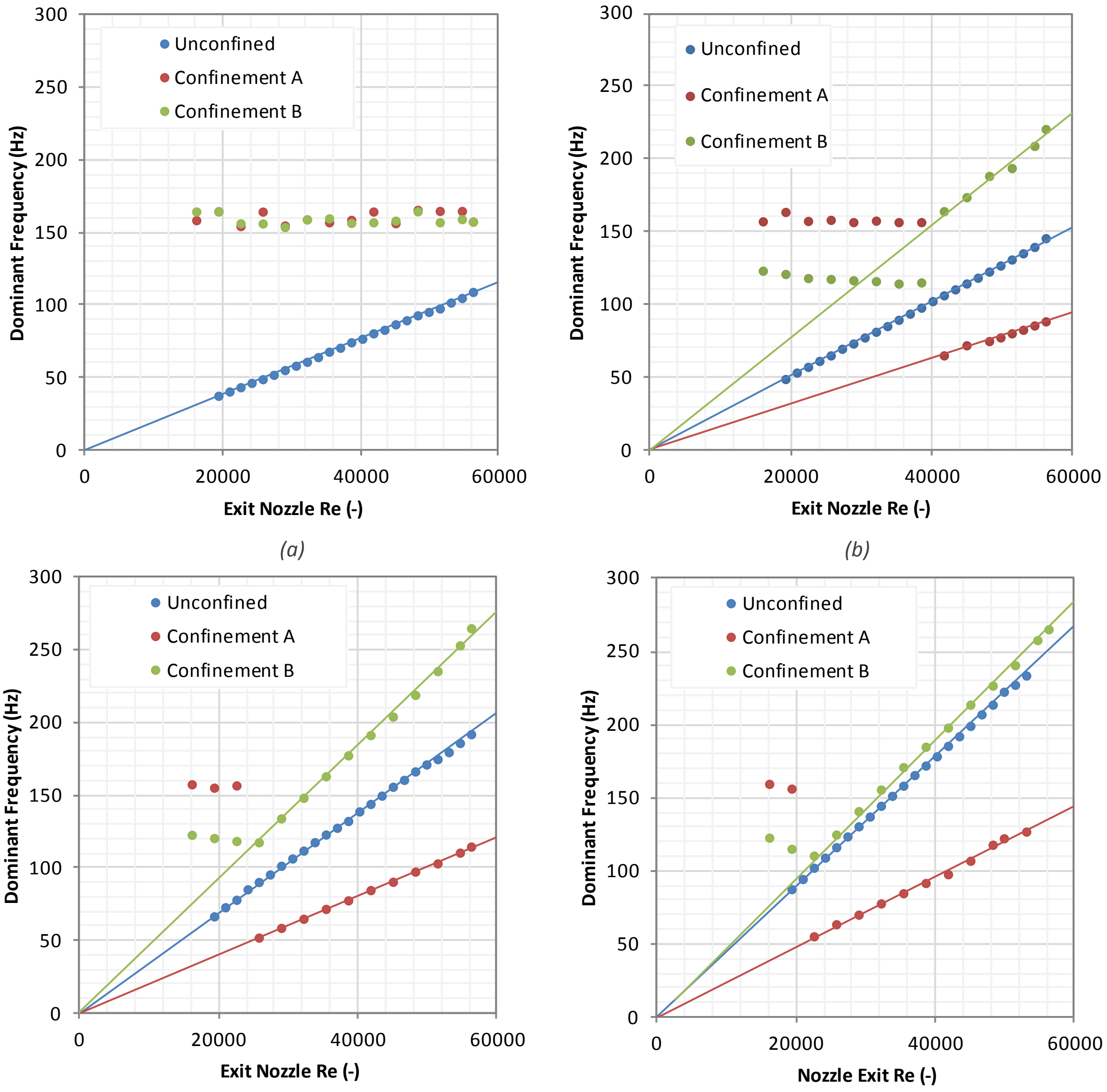

(a) *(b)*

(c) *(d)*

Figure 61: Dominant frequency against exit nozzle Re for (a) S_g = 0.74 (b) S_g = 1.08 (c) S_g = 2.02 (d) S_g = 4.46

Although there are not sufficient scenarios to confirm it, the data suggests that regardless of the confinement, a given swirl number has a critical nozzle exit Re for coherent structures to dominate the acoustic response. Figure 61 also shows clearly that the dominant frequencies recorded prior to the transition point decrease as flow rate increases, as suggested when Eq. (5.3) is substituted into Eq (5.1), further suggesting that they are caused by a resonance in a cavity.

5.3.3 Dimensionless Interpretation

It is preferable to interpret results in a dimensionless format, this allows better comparison between different burners, flow rate and level of swirl imparted on the flow are already been interpretted in terms of the dimensionless Reynolds and geometric swirl numbers. The frequency of oscillating flows can be expressed using the Strouhal and Roshko numbers.

The Strouhal Number (St) characterises the shedding of vortices, representing a measure of the ratio of inertial forces due to the unsteadiness of the flow or acceleration, to the inertial forces due to changes in velocity from one point to another in the flow field. However, the Strouhal number can be used to characterise the frequency of oscillations in swirling flows (Syred, 2006), in which case it is calculated as in Eq. (5.4):

$$St = \frac{f \cdot L}{U} \qquad \text{Eq (5.4)}$$

Where: f = Frequency of oscillations (Hz)

L = Characteristic length of exit (m)

U = Fluid velocity (m/s)

The results from Figure 58 (a), Figure 59 (a) and Figure 60 (a) have been reinterpretted, in Figure 62 (a-c) respectively, to display how the relationship between Strouhal number and Reynolds number is effected by confinement. The unconfined case, where dominant frequency is always defined by the oscillation of flow structures, shows that a constant geometric swirl number produces a constant St across the complete range of Re. As swirl number increases, and the frequency of oscillations increase, so does the Strouhal number.

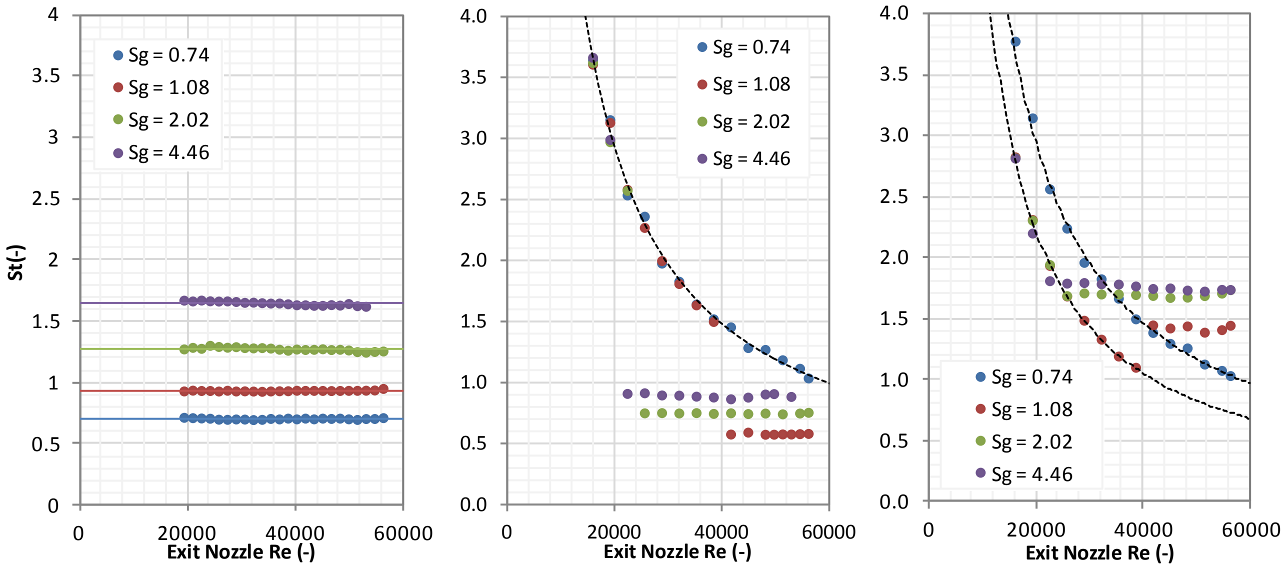

(a) (b) (c)

Figure 62: Strouhal number against Reynolds number for burner (a) unconfined and fitted with (b) confinement A and (c) confinement B

When confinement is added to the burner, and natural resonance dominates acoustic response, St no longer has a linear response with regard to Reynolds number. Refering back to Figure 59 (a), until a sufficient flow rate is reached, natural frequency of the swirl chamber dominates the burners response. Figure 62 (b) shows the response of the burner with confinement A fitted in terms of St. When flow structures dominate the response, again a constant St occurs, increasing as S_g increases. However, the value of the Strouhal number is reduced with regard to a specific geometric swirl number, and the variance is also reduced. All instances of dominant resonance fall on on one line, where St can be expressed as an inverse power of Re.

A similar pattern is observed for confinement B in Figure 62 (c). The values of constant St are increased on the unconfined case, with a small variance similar to when confinement A. The instances where resonance in the swirl chamber dominates the acoustic response fall on the same line as Figure 62 (b), the instances where the resonance in the confinement dominate the spectrum fall on another line where St can be expressed as an inverse power of Re.

In the same way that a Strouhal number can be used to non-dimensionally characterise oscillations resulting on flow structures, the Roshko number, which represents the product of the Strouhal and Reynolds numbers, can be used to characterise oscillations resulting from resonance within the burner. It is calculated below:

$$Ro = \frac{f \cdot L^2}{\nu} = St \cdot Re \qquad \text{Eq (5.5)}$$

Where: f = Frequency of oscillations (Hz)

L = Characteristic length of exit (m)

v = Fluid kinematic viscosity (m^2/s)

The results from Figure 58 (a), Figure 59 (a) and Figure 60 (a) have been reinterpretted, in Figure 63 (a), (b) and (c) respectively, with Roshko number plotted against Reynolds number.

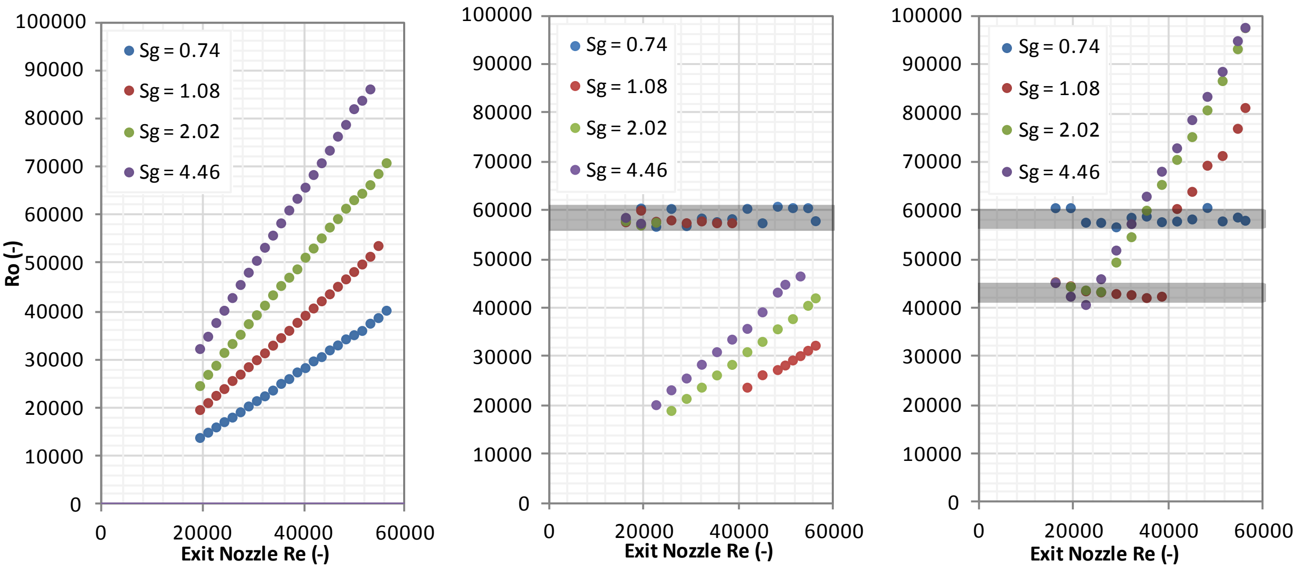

(a) (b) (c)

Figure 63: Roshko number against Reynolds number for burner (a) unconfined and fitted with (b) confinement A and (c) confinement B

Strouhal number effectively neutralises the effect of flow rate on the frequency of oscillations, multiplication with Reynolds numbers reintroduces the effect of flow, so the profile of the plots in Figure 63 are the same as in Figure 58 (a), Figure 59 (a) and Figure 60 (a). However, when interpretted in terms of Roshko number, there is a constant, non-dimensional range of values in which resonance can be characterised, demonstrated by the semi-tranparent bands in Figure 63 (b) and Figure 63 (c).

5.3.4 The Transition Points

It is concluded that there are two transition points in the dominant source of the acoustic response. The primary transition point is the result of Vortex Breakdown, and the second a result of flow structures becoming more prominent than Helmholtz resonance. The acoustic response over the full range of Reynolds numbers, when S_g = 1.08 and confinement B is fitted is analysed, with power spectrums recorded at intervals over the range shown in Figure 64.

Vortex breakdown manifests itself as an abrupt change in flow structure; it is one of the most important phenomena involved in swirl combustion and results in the formation of a CRZ. Its occurrence is a primarily a function of swirl and Reynolds numbers (Luca-Negro and O'Doherty, 2001). However, there is further reliance on other factors, including burner configuration, degree of confinement and flow rate (Valera-Medina et al., 2011b).

For the swirl number and confinement used to obtain the results detailed in Figure 64 the frequency of structures were represented by a Strouhal number of 1.426, the point at which the dotted line crosses each axis denotes the frequency that equates to the fixed St. The first response observed at St = 1.426 is when Re = 28942, although it is incredibly subtle and difficult to distinguish in Figure 64, it is concluded that vortex breakdown occurs when Re at the exit nozzle is between 25710 and 28942. Post breakdown, as Re increases, so does the amplitude of the response at St = 1.426. The secondary transition point defines where the amplitude of acoustic emissions caused by the structures within the flow exceeds those caused by resonance within the burner system. For the confinement used to obtain the results detailed in Figure 64 the primary natural resonance is defined by the combustion chamber, predicted to be 117 Hz. The range of Roshko numbers at which this resonance is detected is highlighted in Figure 64 by the semi-transparent band. Initially, as Re increases so does the amplitude of the resonance, with the highest amplitude observed when Re = 25710.

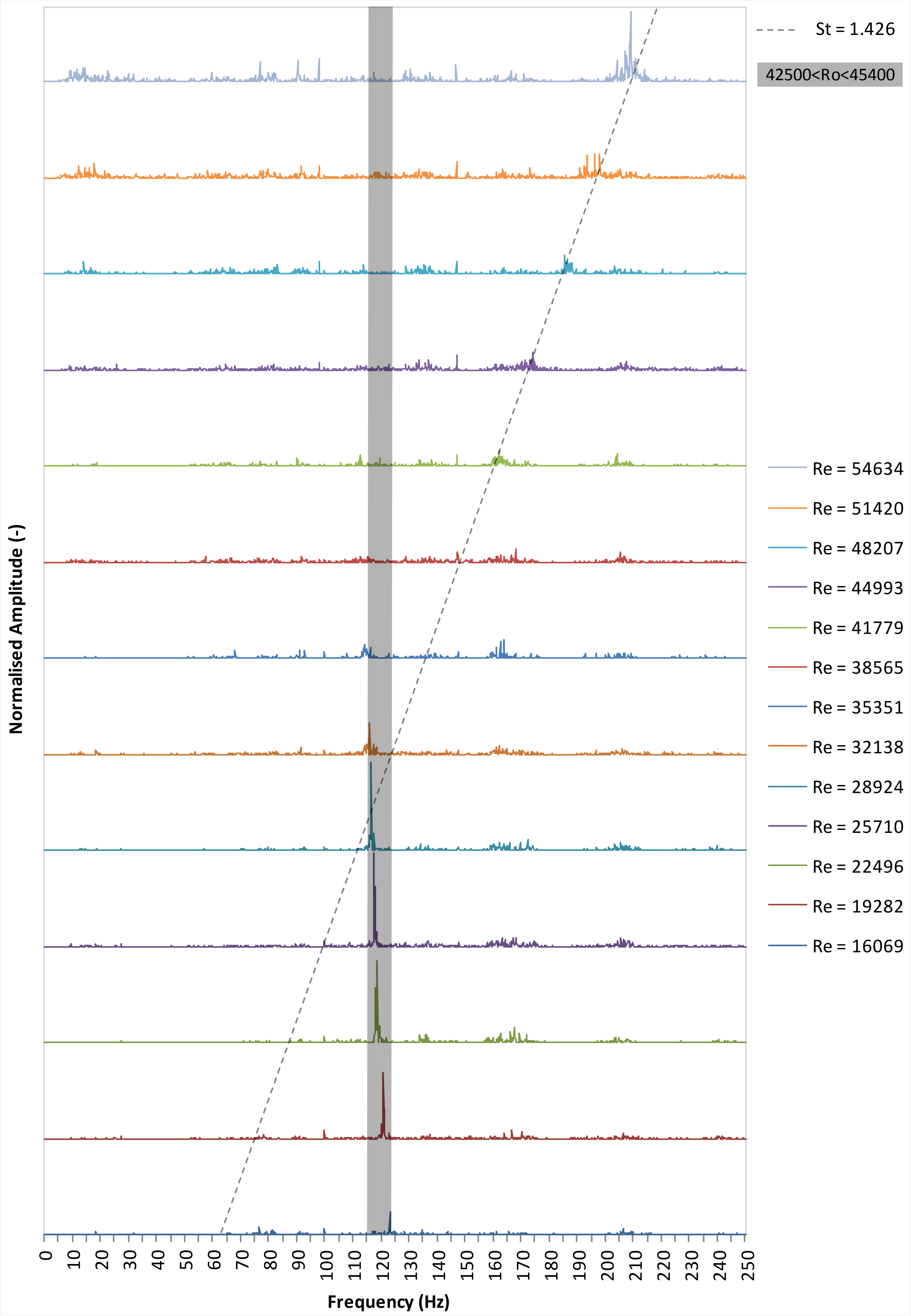

Figure 64: Power spectrums across the full range of exit nozzle Reynolds numbers for Sg = 1.08, with confinement B fitted

When Re equals 28924 the amplitude has decreased, a trend which continues when Re = 32138 until stabilising for higher values of Re, where resonance ceases but fluctuations continue to occur at a similar level to elsewhere in the spectrum. Figure 65 (a) shows an interpretation of how the two transition points affect the acoustic response of the burner under isothermal conditions. The primary transition point does not directly affect the dominant frequency recorded as it occurs when the Helmholtz resonance dominates the acoustic response of the burner, however the process of vortex breakdown interferes with resonance within the rig, which causes the amplitude of the resonance to decrease post breakdown, as observed in Figure 64.

The secondary transition point occurs when the amplitude of the flow structures exceed those caused by resonance, as such the cause dominant frequency in the acoustic response changes.

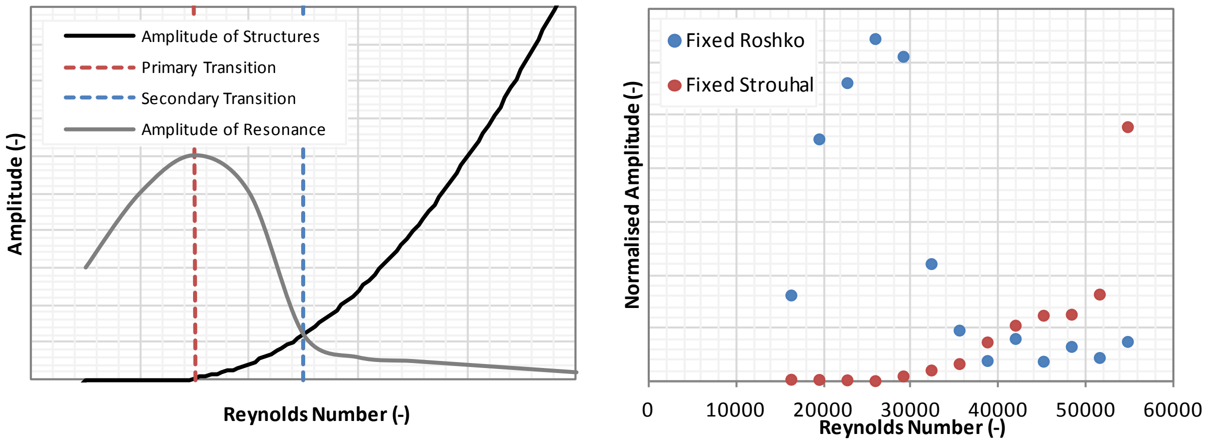

(a) *(b)*

Figure 65: (a) Interpretation of the transition point between the causes of dominant frequency in the spectrum analysis and (b) results taken from S_g = 1.08 with confinement B fitted

Figure 65 (b) shows the effect of the transition points on the results from Figure 64, where the peak amplitudes for constant Ro and St are plotted. The primary transition point occurs when Re at the exit nozzle is between 25710 and 28942. From this point the amplitude at the fixed Ro begins to decrease as the amplitude at the fixed St begins to increase. There is a slight disagreement with dominant frequency results in Figure 60 as to the position of the second transition. The transition between the sources of the peak amplitude occurs between Re equalling 35351 and 38565 Figure 65 (b), however the transition occurs between Re = 38565 and Re = 41779 in Figure 60. This is due to dominant frequency being calculated from the frequency spectrum as opposed to the power spectrums shown in Figure 64, from which the results in Figure 65 are calculated.

5.4 Chapter Summary

This chapter presents the results of isothermal experimentation on a radial swirl burner. The effects of flow rate, the level of swirl imparted on the flow and confinement are analysed.

Two mechanisms were found to define acoustic response under isothermal conditions, Helmholtz resonance and the precession of structures. The frequency and amplitude of oscillations caused by structure precession increased with geometric swirl number and air flow rate, whereas Helmholtz resonance demonstrated a tendency to reduce with flow rate. The frequency of structure rotation and Helmholtz resonance for a particular burner configuration can be characterised via the use of the dimensionless Strouhal and Roshko numbers respectively. With regard to the precession of structures, two transition points occur as Reynolds number increases. Firstly when vortex breakdown occurs, and secondly when the amplitude of oscillations caused by precessing structures exceeds those caused by resonance.

The characterisation of frequency and structure rotation and resonance will aid in the identification of mechanisms of acoustic response with reacting flows in the proceeding chapter.

Chapter 6: Thermo-Acoustic Response as a Performance Indicator

6.1 Introduction

The aim of this chapter is to assess the potential to utilise thermo-acoustic oscillations to infer flame conditions. The ultimate aim is to integrate this knowledge of flame condition into a control system, capable of making alterations to fuel and/or air flow rates. This would potentially prevent the thermo-acoustic oscillations developing into instabilities, and maintain circumstances of optimum flame stability. This could be used to counteract the effects of variable fuel composition observed in chapter 4. The isothermal characterisation performed in the previous chapter will aid in identifying mechanisms of acoustic response as flame conditions alter.

Putnam (1971) theorised that it would be almost impossible that combustion systems could exist without oscillations. A theory supported by the isothermal work in the previous chapter, which showed that pressure oscillations inside combustion chambers occur when a fluid passes through, regardless of combustion.

Several mechanisms may contribute to the manifestation of combustion driven oscillations. These thermo-acoustic oscillations are fundamentally caused by oscillations in pressure, varying rates of flow and heat release, as well being strongly influenced by the geometry of the combustor. There is a basic feedback mechanism which sees flow and mixture perturbations induce heat release oscillations, causing acoustic oscillations which in turn affect flow and mixture perturbations, closing the loop and creating a potentially self-excited maintainable mechanism (Lieuwen, 1999). However, there are many other factors that influence oscillations in the combustion system, including combustor pressure drop, variations in fuel composition and the formation of structures within the flame.

There is potential to control these instabilities in both a passive and active manner. To do so passively requires system design modification, but inherently, this cannot respond to changes in the acoustics in a dynamic way (Farhat and Mohamed, 2010). A common method of passive control involves making modifications to combustor's geometry, i.e. the fuel injector, which can eliminate variations in heat transfer or increase a systems acoustic damping (Lefebvre and Ballal, 2010). There is now, however, more focus being directed toward active techniques (Stone and Menon, 2002) from the point of view of adaptive flexibility (Tachibana et al., 2007), where incipient instability is dynamically detected and corrected. The general approach to active control is to minimise the difference between the instantaneous actual and desired behaviour of a system. A sensor is used to detect instabilities, a closed loop control system then modifies one of the burners input parameters in order to interrupt the coupling of acoustic pressure waves and unsteady heat release (Huang and Yang, 2009). Consideration of acoustics perturbations is important where the working life of gas turbine components are concerned (Lieuwen, 2012a). To extend the life of these components a control system can be employed to reduce the amplitude of pressure fluctuations, and thus the stresses experienced by their components.

6.2 Mechanisms of Acoustic Response

Just as isothermal resonance within the rig and the precession of structures were attributed to causing oscillations over a range of frequencies, thermo-acoustic oscillations may occur over a range of frequencies as a result of multiple mechanisms. Combustion was introduced to the cyclone burner described in section 3.2.2, and monitored with a condenser microphone as described in section 3.2.2.1.

Figure 66 shows how the power spectra change over the stability range of flames with differing powers, the lowest Reynolds numbers corresponding to flames on the verge of flashback. As the flow rate of air, and consequentially the exit nozzle Re increase, equivalence ratio decreases, this results in the flame speed of the mixture decreasing as the flame tends towards blowoff.

Three mechanisms of acoustic response are present over the stability range of the flame. With regards to the flame in Figure 66 (a), it is at its most stable at an equivalence ratio of 0.65. The flame is burning at the end of the swirl chamber exit nozzle and in the combustion chamber, as depicted in Figure 67 (d). With the flame positioned in the swirl chamber exit nozzle the Helmholtz frequency of the swirl chamber is excited, and is dominant in the power spectrum, with some sub 100 Hz frequencies caused by heat release fluctuations in the combustion chamber. As the flame becomes leaner, it lifts from the exit nozzle and moves slightly deeper into the combustion chamber, depicted in Figure 67 (e); the Helmholtz frequency of the swirl chamber becomes less apparent. Figure 67 (f) shows how, as the flame becomes leaner still, it continues to lift, with main reaction zone deep into the combustion chamber. As the flame approaches its lean blowoff limit its stability decreases, heat is released in an increasingly unsteady fashion as a process of local extinction and re-ignition is initiated, resulting in low frequency pressure fluctuations. As equivalence ratio reduces the effect of the Helmholtz, resonance diminishes significantly whilst amplitude and frequency of the pressure fluctuations caused by heat release in the furnace increase and decrease respectively.

As the flame becomes richer, the process of combustion induced vortex breakdown is initiated, resulting in an increase in amplitude of the pressure fluctuations at the frequency of the flame structures. The isothermal results for this swirl number and inlet geometry produce a Strouhal number of 0.578. Using this number, and by rearranging Equation 5.4, the frequency of any structures occurring in the range of exit nozzle Reynolds numbers from 26000 to 27600 can be predicted to occur between 41.6 and 44.2 Hz. Figure 66 (a) shows a significant increase in the amplitude of oscillations in this range as CIVB has been initiated and flashback approaches.

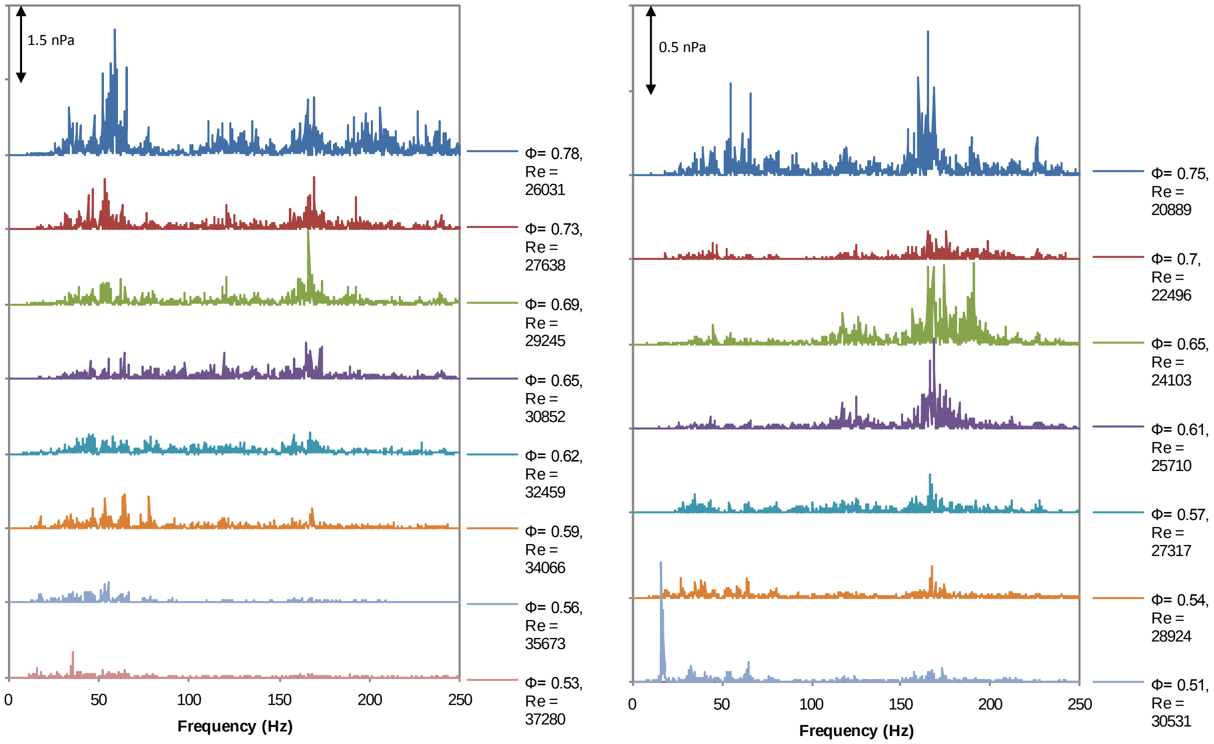

(a) *(b)*

Figure 66: Power spectra of acoustic response from flashback to blowoff for (a) 75.4 kW flame with Sg= 1.08 fitted with confinement A (b) 62.6 kW flame with Sg= 2.02 fitted with confinement B, in terms of mixture equivalence ratio and corresponding tangential inlet speed

After the initiation of CIVB the flame will propagate upstream through the swirl chamber exit nozzle, as shown in Figure 67 (c). Eventually it will reach the boundary between the exit nozzle and the swirl chamber itself, as depicted in Figure 67 (b). Inside the swirl chamber the global fluid velocity is significantly lower than in its exhaust nozzle, allowing the flame to propagate rapidly to the premix fuel injector in the air inlet pipe. This evolution of the flame means that a response at the Helmholtz frequency of the combustion chamber remains in the power spectrum up until the point of flashback. An additional response at around 215 Hz, first observed in Figure 57 (a) and attributed to resonance in an unconfirmed location within the rig, is also seen in the results in Figure 66.

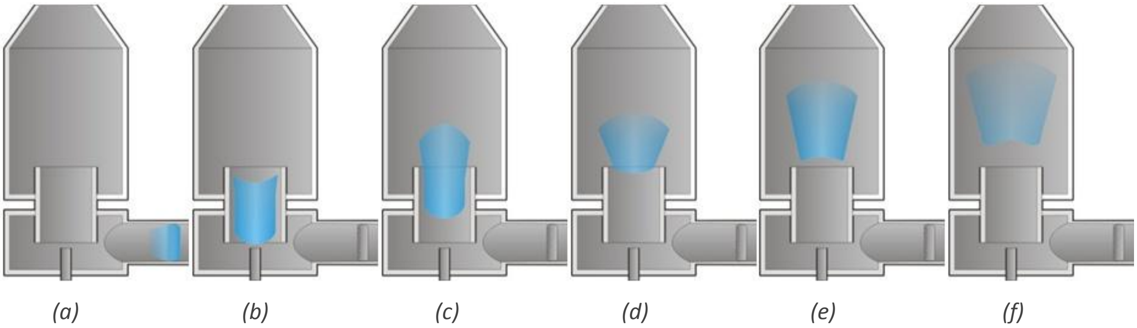

Figure 67: Flame position within the burner: (a) flashed back, (b) on the verge of flashback, (c) approaching rich limit, (d) optimum position, (e) approaching lean limit (f) on the verge of blowoff

Figure 66 demonstrates how the acoustic response of the burner changes with its configuration at a variety of equivalence ratios. The position of the flame as it makes the transition from rich to lean blowoff limits follows the same pattern; therefore, the FFT analysis of its acoustic response follows the same pattern. The amplitude of the different modes does however change, as do the transition points. Figure 66 (b) shows power spectra from flashback to blowoff for a 62.6 kW flame with a geometric swirl number of 2.02 and confinement B fitted; it should be noted that the y-axis is on a different scale to Figure 66 (a).

When the flame has an equivalence ratio of 0.75 and is on the verge of flashback, the amplitude of the oscillations around the Helmholtz frequency of the combustion chamber are very similar to those at the same point in Figure 66 (a). Yet the amplitude of the oscillations caused by the structures is noticeably less. When on the verge of blowoff, the amplitude of the oscillations caused by heat release in Figure 66 (b) are significantly greater than those in Figure 66 (a) when compared to other peak amplitudes over the stability range of the flame. The driving factor behind this was the reduced exit diameter of the constriction, this increased pressure drop across the burner and inside the combustion chamber, which caused the flame to sit further upstream.

Although it is possible to infer the condition of the flame based on the appearance of the FFT analysis, in the form shown in Figure 66, visual interpretation is required. In order to integrate knowledge of the flame condition into either a control, or warning system, a quantifiable method of interpreting the flame is preferred. As such, the mean amplitude ($\bar{a}$) and correlation coefficient (c_c) of the acoustics signal were calculated, as described in the Equations 6.1 and 6.2. Mean amplitude represents the acoustic power of the signal and correlation coefficient its uniformity.

$$\bar{a} = \frac{\left|\sum_{k=0}^{n-1} x_k \cdot x_{j+k}\right|}{n} \qquad \text{Eq (6.1)}$$

$$c_c = \frac{\sum(x-\bar{x})(y-\bar{y})}{\sqrt{\sum(x-\bar{x})^2(y-\bar{y})^2}} \qquad \text{Eq (6.2)}$$

For: $j = 0, 1, \ldots, (n-2), (n-1)$

Where: n = number of samples

$y_j = x_{j-10}$

6.2.1 Changes in Amplitude

Figure 68 (a) shows a schematic of how the mean amplitude of the acoustic response alters with relation to the flame positions defined in Figure 67. The x-axis represents tangential inlet velocity, which, for a given inlet geometry configuration, is related linearly to exit nozzle Reynolds number. An increase in amplitude is observed when a particular mode, or multiple modes, of excitation dominate the acoustic response. Namely flame structures and Helmholtz resonance near flashback, Helmholtz resonance when the flame is in optimal condition, and unsteady heat release near blowoff, represented by Figure 67 (b), (d) and (f) respectively. Mean amplitude and tangential velocity were plotted for flames of three power levels under the same conditions in Figure 68 (b), with the burner configured to provide a geometric swirl number of 2.02 and with confinement B fitted. The trend lines fitted to the results are fourth order polynomial, to account for the three turning points shown in Figure 68 (a), and accurately represent the data points, with coefficients of determination between 0.87 and 0.95. The behaviour is the same over all power levels; however, amplitude is shown to increase with power.

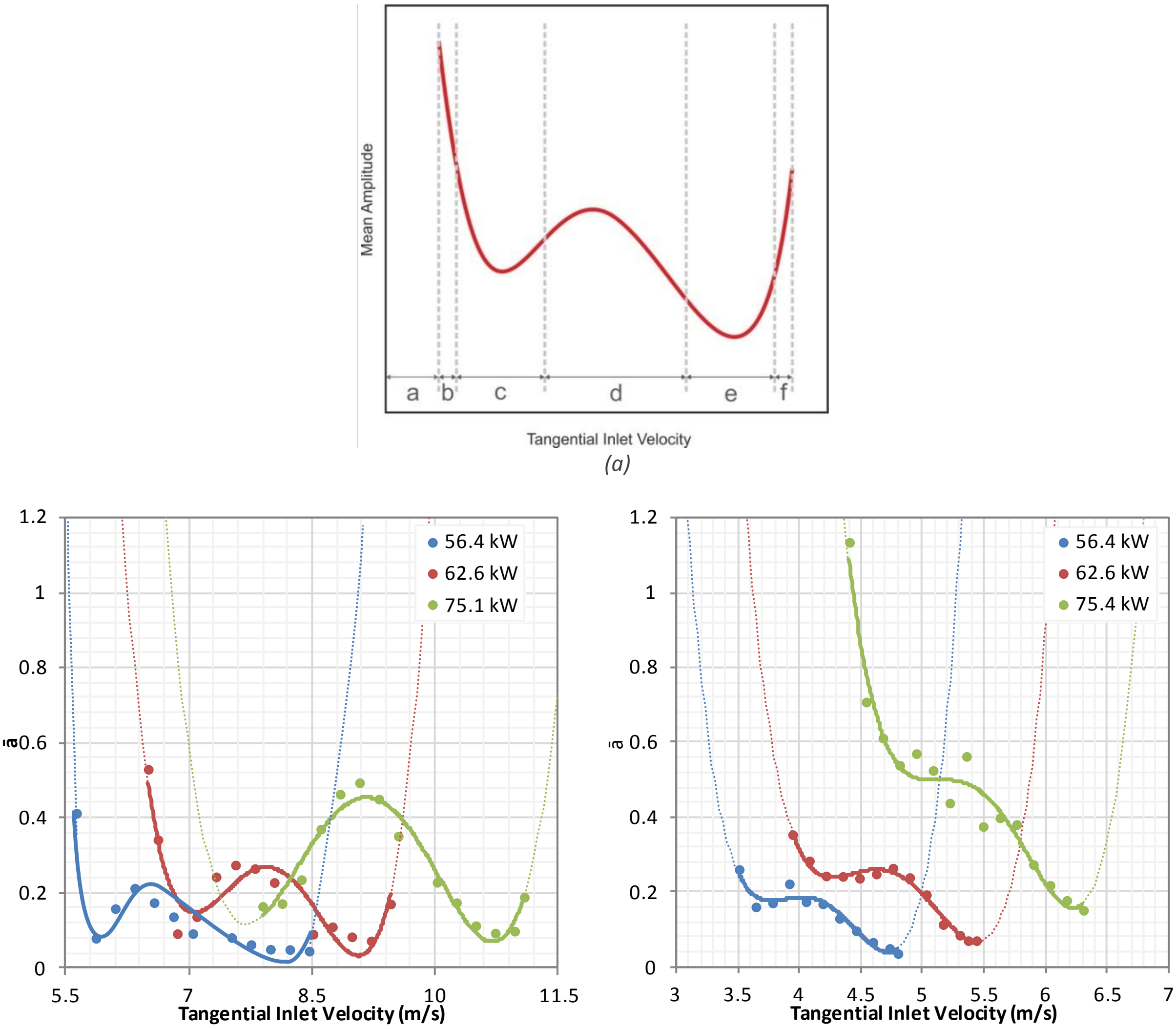

(a)

(b) *(c)*

Figure 68: Mean amplitude against tangential inlet velocity for three power levels (a) comparison with Figure 67 (b) Sg = 2.02 with confinement B fitted (c) Sg = 1.08 with confinement A fitted

Extinction events, both blowoff and flashback, happen very abruptly in this configuration, with significant changes in flame condition caused by relatively minor alterations in airflow. The large increment between readings on the air rotameters, 3%

of total flow with ±5% accuracy, meant that these significant changes often occurred between test points; as such they are not fully represented in the results in Figure 66, Figure 68 and Figure 69.

The same behavioural trend is observed regardless of burner configuration and power level, as seen in Figure 68 (b), when the inlet geometry provided a geometric swirl number of 1.08 and confinement A was fitted. The fourth order polynomial trend lines represent the data with coefficients of determination between 0.94 and 0.99. The results for the 75.4 kW flame capture the high amplitude of the oscillations that occur immediately prior to flashback. However, the larger confinement exit means that the burner is more susceptible to blowoff, with the extinction event happening rapidly in relation to changes in air flow. Combined with the reduced pressure drop across the burner with confinement A fitted, this results in a reduction in the amplitude of unsteady heat release oscillations immediately prior to blowoff. Further investigation with a greater level of accuracy in the air flow meters would give results with greater definition around extinction events.

6.2.2 Changes in Coherence

The coherence in the acoustic response also follow the same pattern for flames of different powers and different burner configurations, with a schematic relating the behaviour to the flame positions detailed in Figure 67 shown in Figure 69 (a). Figure 69 (b) shows how coherence changes for the flames shown in Figure 68 (b). The trend lines fitted to the results are third order polynomial, to account for the two turning points shown in Figure 69 (a). The coefficient of determination is poor for the 56.4 kW case, however, the shape of the curve is given credibility due to the similarity between it, and those of higher powered flames, which have high coefficients of determination. The trend observed is for the increased coherence when a single mechanism of oscillation, namely resonances in the combustion chamber or unsteady heat release, dominates the acoustic response. The greatest level of coherence is when the flame is in its optimum condition, the position detailed in Figure 67 (d), with the Helmholtz frequency of the combustion chamber entirely dominant. Coherence drops as the flame makes the transition towards either of its stability limits, when approaching flashback it continues to decrease as neither the effect of the flame structures or the

Helmholtz frequency are able to dominate the acoustic response. Conversely, when approaching its blowoff limit, when the unsteady heat release dominates the acoustic response, coherence rises again.

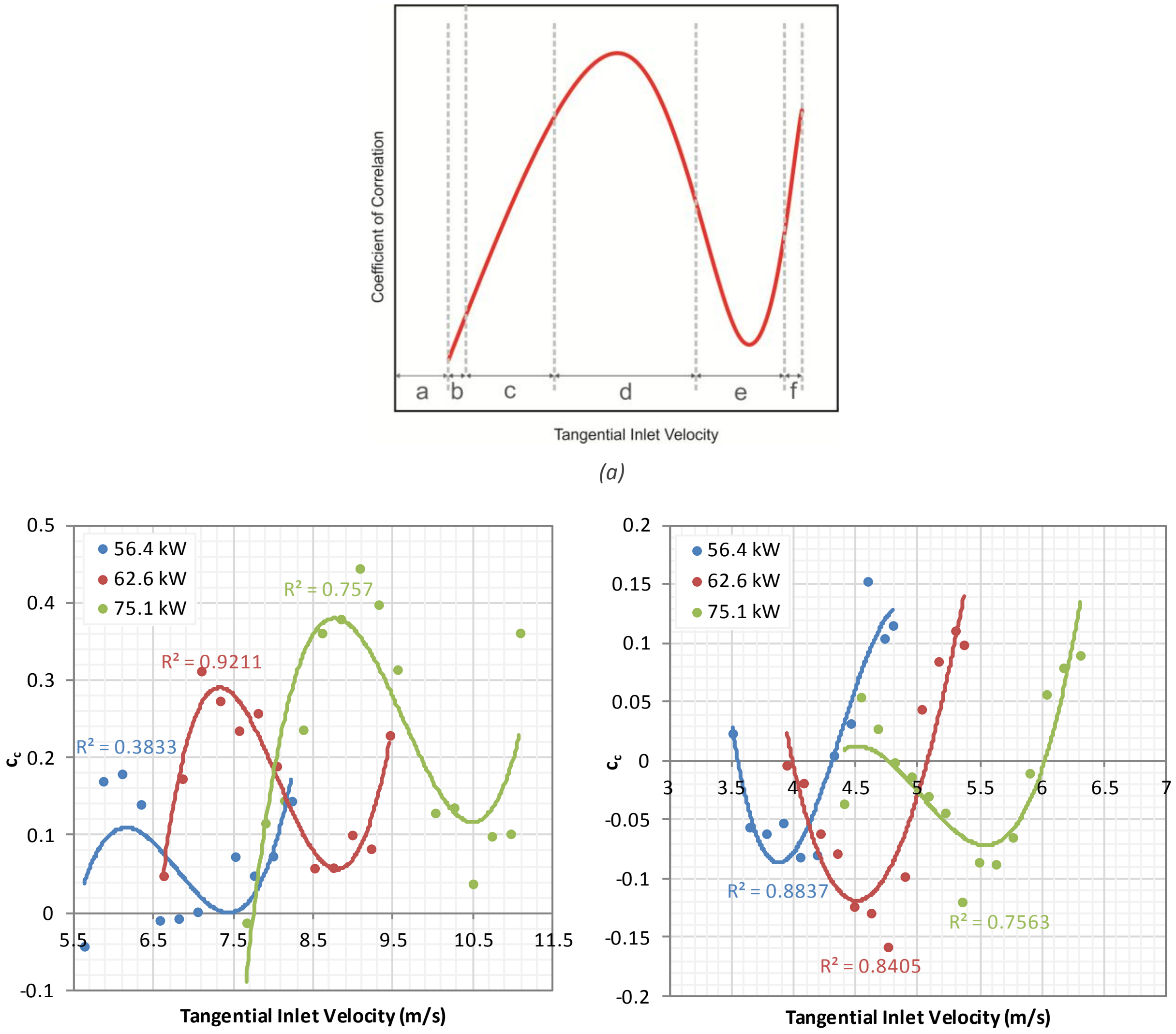

(a)

(b) *(c)*

Figure 69: Coefficient of correlation against tangential inlet velocity for three power levels (a) comparison with Figure 67 (b) Sg = 2.02 with confinement B fitted (c) Sg = 1.08 with confinement A fitted

The same trend is observed in Figure 69 (b), although the profiles of the curves are altered due to the intersection of the y-axis, with the coefficients of determination high for all three flame powers.

6.2.3 Isolation of Heat Release

It was observed that significant unsteady heat release occurs as the equivalence ratio decreases and the flame nears blowoff. Results in Figure 66 show that as the frequency of these oscillations becomes lower, their amplitudes increase as they cause more pronounced changes of pressure inside the combustion chamber. These low frequencies dominate power spectra when blowoff approaches.

To investigate the low frequency, high amplitude oscillations that precede blowoff and their relationship with unsteady heat release, high speed photography was used. The unsteady heat release will also result in an unsteady release of light energy, making light intensity a viable measure of change in the heat release (Hardalupas and Orain, 2004). Other works have also considered high fidelity imaging of unstable flames to be a good method of assessment (Balachandran et al., 2005, Durox et al., 1997, Durox et al., 2002, Santhanam et al., 2002). The development gas turbine combustor installed in the HPCR, as detailed in section 3.2.4, was used to investigate the release of light energy. The high pressure optical casing permits a radial view of the flame, without exposing the high speed camera to the high temperature exhaust gases.

Figure 70 provides an example of the images taken of the ignition of a diffusively injected methane pilot flame from the radial position, at 500 Hz; the flame is swirling clockwise, relative to the downstream position of the camera.

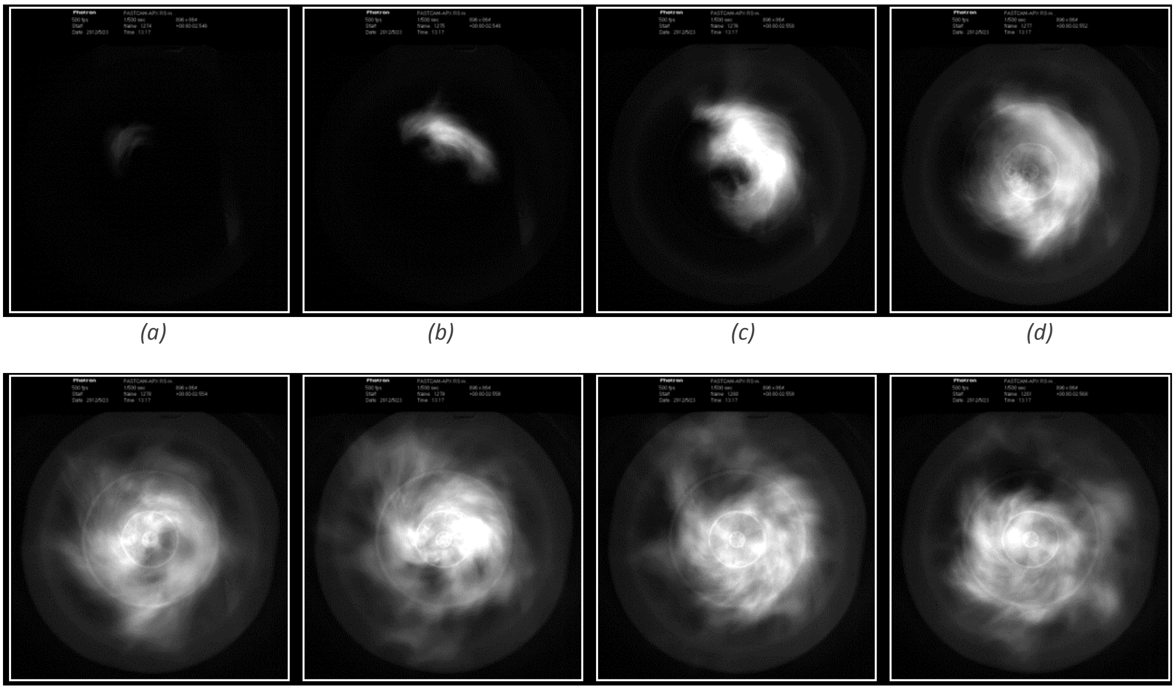

Figure 70: High speed imagery of light up of the gas turbine combustor at (a) ignition and (b) 2 ms, (c) 4 ms, (d) 6 ms, (e) 8 ms, (f) 10 ms, (g) 12 ms and (h) 14 ms post ignition

Figure 70 (a), (b), (c), (d) and (e) demonstrate how the intensity of the image changes as the flame propagates and increases in size post ignition. The images (e), (f), (g) and (h) represent a stable flame, in a fully ignited flow; as such the intensity of the images is very similar. To confirm that these low frequency oscillations are indeed caused by heat release, a lifted methane flame, very near its lean blowoff limit, with an equivalence ratio of 0.418 was recorded with a high-speed camera. Images were captured, at 1000 frames per second (2048 frames total). Figure 71 shows images captured 750 and 1500 ms after filming was initiated. They images are incredibly similar, with no obvious differences discernible from visual interpretation. In contrast to the flame in Figure 70, the lean premixed flame has a very even distribution, with no prominent reaction zones or flame fronts.

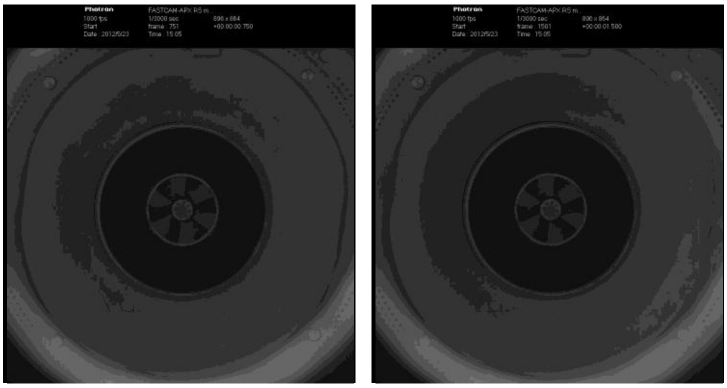

(a) *(b)*

Figure 71: Images of the relatively lean premixed flame captured (a) 750 ms and (b) 1500 ms after filming initiated

Using Maple mathematical software, each pixel in the gray scale images captured using the high speed camera was assigned a number between 0 (black) and 1 (white), the mean was then calculated to give the average intensity of each frame. A Fast Fourier Transform analysis, detailed in Equation 6.3, was applied to the image series in order to produce a power spectrum representing the frequency of intensity changes. In Figure 72 this spectrum is compared to the power spectrum recorded by the pressure transducer located in the exhaust section of the rig. The transducer data was also taken over two seconds, at a rate of 2 kHz, and the subject of a Fast Fourier Transform analysis.

$$X(f) = \boldsymbol{F}\{x(t)\} = \int_{-\infty}^{\infty} x(t)e^{-j\cdot 2\pi\cdot ft}dt \qquad \text{Eq (6.3)}$$

Where: x(t) = the time domain signal
X(f) = the FFT
ft = the frequency to analyse

The spectra have very similar profiles, although the acoustic spectrum has a higher resolution due the increased frequency of data capture, and more noise is discernible in the intensity spectrum. Both spectrums show a peak in amplitude at 19Hz; relating to the low frequency oscillations that occur before blowoff on the HPOC rig.

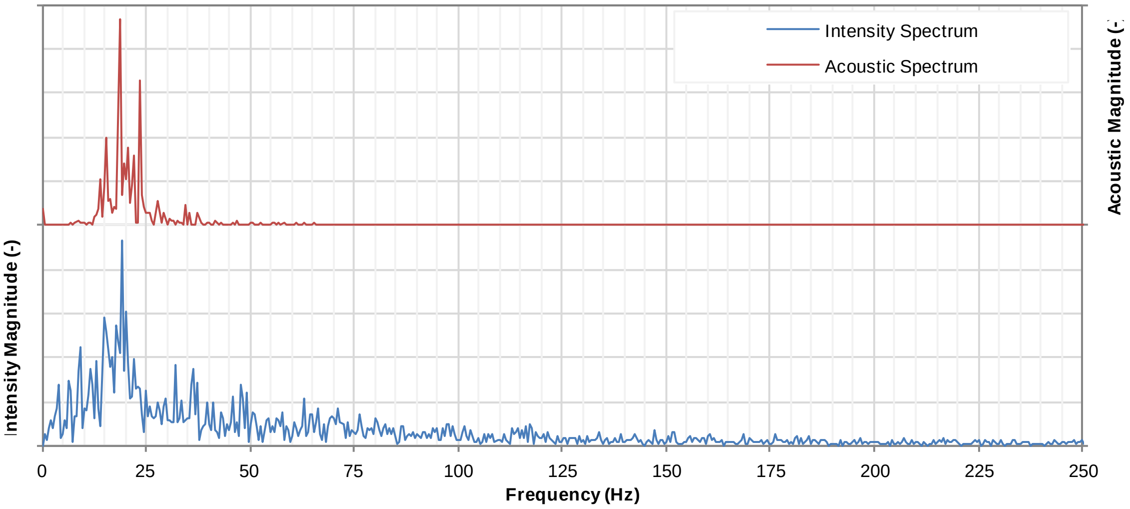

Figure 72: Power spectra of an oscillating methane flame

As a source of comparison the same analysis was performed for a relatively rich partially premixed flame. 1400 hundred frames were recorded, again at a rate of 1000 frames per second. Images of the flame taken 500 and 1000 ms after filming was initiated, shown in Figure 73, offer little means for visual differentiation. However, there is a clear increase in intensity compared to the images of the leaner flame in Figure 71.

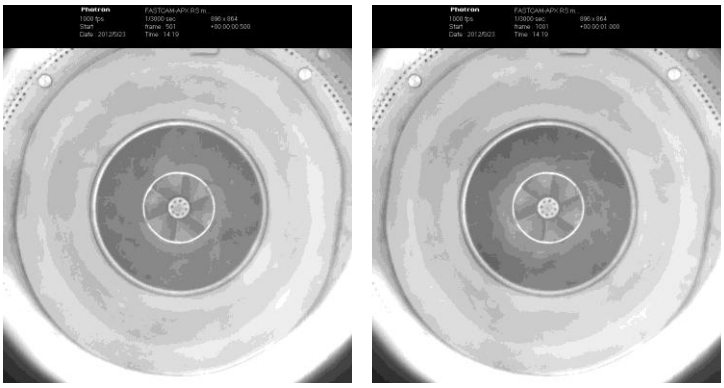

(a) *(b)*

Figure 73: Images of the partially premixed flame captured (a) 500 ms and (b) 1000 ms after filming initiated

This flame was stable, sitting comfortably within the stability limits for a flame of this power. As previously observed stable flames have a tendency to excite the natural resonance of the combustion chamber, in the HPCR the resonant frequency of the combustion chamber is defined by the quartz tube which is in place to protect the steel in the HPOC from the high combustion temperatures, whilst permitting visual access to the flame. The frequency in the acoustic spectra in Figure 74, where a large, distinctive peak is observed at 214 Hz, does not correspond to the natural frequency of the quartz tube. It is an additional resonance, attributed to another section of the combustor, upstream of the nozzle exit; a similar effect was observed with the cyclone burner under both combustion and isothermal conditions.

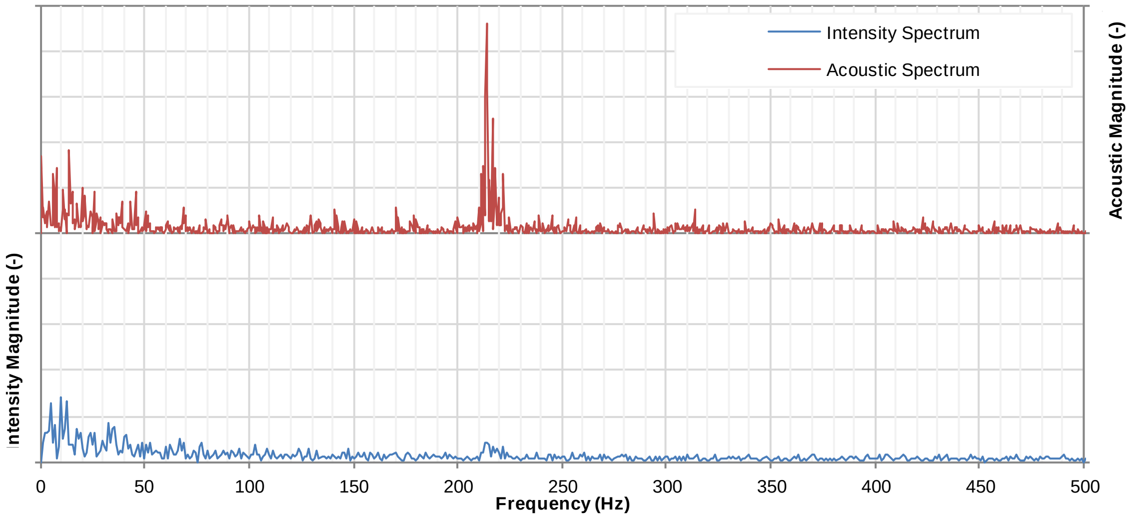

Figure 74: Power spectra of an oscillating methane flame

Between the frequency range of 0 and 500 Hz the acoustic and intensity spectra recorded have a similar profile, aside from the range of frequencies relating to resonance. As the oscillations are not a direct result of heat release, the size of the peak, relative to the rest of the spectrum is considerably smaller relative to the rest of the spectrum. However, there is a small, but noticeable increase in the amplitude of fluctuations around these frequencies in the intensity spectrum, indicating that the oscillations are causing secondary fluctuations in heat release, as described by Lieuwen (1999).

6.3 Resonance as a Flashback Indicator

A series of stability tests were performed using the development gas turbine combustor and a simulated syngas, containing 50 percent hydrogen and 50 percent carbon monoxide by volume.

With regard to the cyclone burner, prior to flashback occurring strong pressure fluctuations occur at the frequency that the structures rotate within, and at the natural frequency of, the combustion chamber section, as shown in Figure 66. As the flame approached flashback, the lesser the frequency of its oscillatory response to structures became, and the greater its amplitude. The fundamental reason behind this was the induction of flashback via the reduction of airflow, which decreases the velocity of mixture and increases its burning velocity. As such, frequency reduces linearly with flow rate (Syred, 2006). Pressure effects of the structures inside the cyclone combustor were not easily analysed as internal combustion chamber pressure was not directly monitored, the effect that flow rate has on the frequency and amplitude of the structures is more apparent in the results that were taken using the development gas turbine combustor.

The results in Figure 75 demonstrate how augmentation of structures within the HPOC rig affects the frequency of the pressure fluctuations for a partially premixed methane flame. The dominant frequency of each of the three transducers and the flow of premixed fuel are plotted against time. The Helmholtz frequency of the quartz tube, calculated as described in section 5.2.2, is also plotted. The other flows into the system are the premix air and pilot fuel; these are kept constant (within 0.5%) throughout the period shown, so the change in premix fuel flow rate is almost equal to the change in total flow rate.

From zero to thirteen minutes, as power and equivalence ratio is increased in steps, there is no coherence between the pressure transducers. The dominant frequencies registered by the combustor and inlet transducers are caused by broadband combustion noise, whilst the exhaust transducer is reacting to low heat release that is indicative of a very lean flame. It is sporadically the cause of the dominant pressure fluctuations in the inlet plenum via the previously discussed feedback mechanism (Lieuwen, 1999, Lieuwen, 2012a).

Whilst diffusive fuel injection dampens the pressure fluctuations caused by the precessing vortex core compared to isothermal conditions, premixed fuel injection actually increases said fluctuations (Claypole, 1980b, Claypole, 1980a, Claypole and Syred, 1980). The premix fuel flow rate was increased from 15.5 to 18.1 g/s, and at this point the amplitude of fluctuations at 510 Hz increased to the point that they dominate the response of the combustor face transducer.

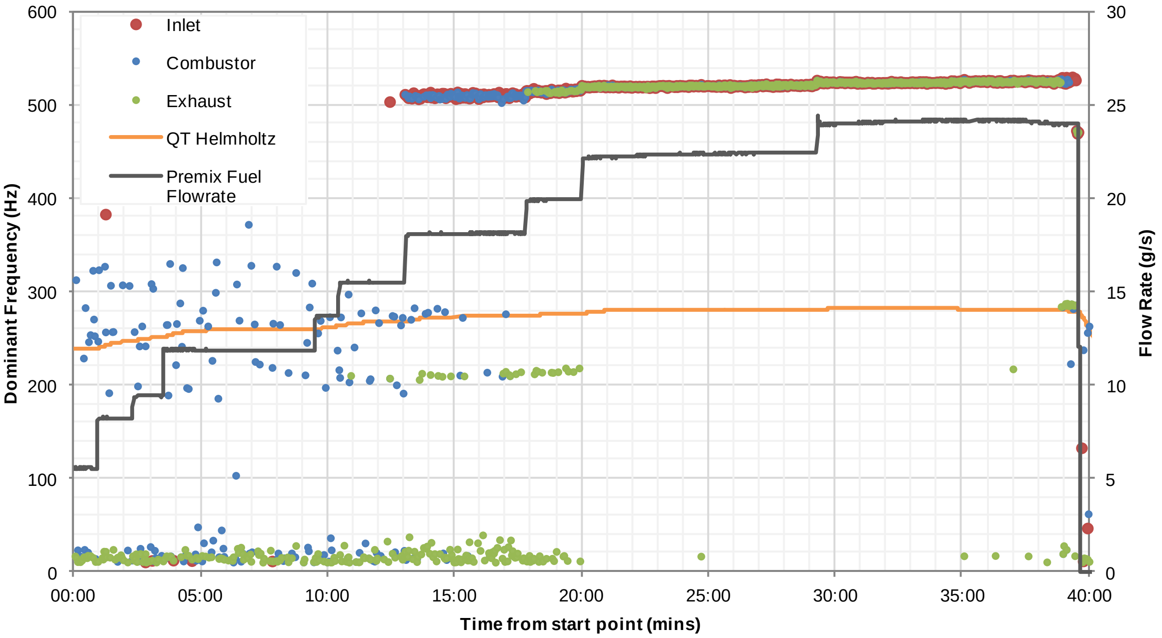

Figure 75: Structure formation dominating frequency of pressure oscillations in the HPOC rig

These fluctuations were significant enough that they were registered in the air inlet plenum, but not strong enough that they entirely dominated response across all transducers. The dominant frequency in the exhaust fluctuates between frequency ranges 10-20 Hz and 210-220 Hz, relating to the previously mentioned heat release fluctuations and the source of resonance observed in Figure 74.

The destruction of the CRZ via Combustion Induced Vortex Breakdown has been identified as the prevailing flashback mechanism in swirl burners (Choudhuri, 2012) as the shape and strength of the CRZ is influential on the stability of the system. The CRZ facilitates the formation of structures downstream, this actually increases propensity for flashback as the other structures effectively push the flame upstream (Valera-Medina, 2009). The upstream propagation causes the vortex breakdown region to progress into the burner nozzle.

Work by De and Acharya (2012) into flame propagation, related pressure fluctuations of a flame experiencing vortex breakdown to the unsteady motion of the recirculation bubble, which disappear as the flame front propagates sufficiently upstream.

When the flame has retreated into the nozzle, the augmented recirculation zone that is the consequence of vortex breakdown gives rise to a component of azimuthal vorticity. Following the Biot-Savart law, this produces a positive or negative induced velocity (Kiesewtter et al., 2007, Knole et al., 2008) causing pressure fluctuations in the air and fuel mixing zone, and providing a mechanism to produce further fluctuations both up and down stream (Lieuwen, 2012a). Consequentially, when the premixed fuel flow rate was increased to 19.9 g/s, causing sufficient flame propagation, complete syncopation is seen between all pressure transducers, as pressure fluctuations at the structure frequency dominated their responses.

Acoustic oscillations exist under stable conditions; therefore, their presence is not necessarily an indicator of an instability. In order for instabilities to develop a feedback mechanism must exist, the established feedback mechanism is for fluctuations in flow or thermodynamic variables to trigger unsteady heat release, the unsteady heat release cause acoustic oscillations that propagate away from the combustion zone, which in turn result in flow and thermodynamic disturbances (Lieuwen, 1999, Lieuwen, 2012a). In this case the feedback mechanism caused an increase in the amplitude of oscillations, resulting in flashback as the acoustic oscillations couple with those of the structures at the natural frequency of the quartz tube. The effect of this coupling is amplified by the Rayleigh criterion (Syred, 2006, Lefebvre and Ballal, 2010), and the phase relationship between the unsteady heat release and the acoustic pressure oscillations, which is fundamental to the feedback process (Fritsche, 2005), allows the instability to develop to the point of flashback occurring.

The development burner is an axial type swirler, and in this instance was operated with part, rather than complete, premixing, resulting in a particular response prior to flashback. However, the formation of structures and the way the position of the flame changes prior to flashback occurs in the same fashion. As previously stated, the frequency of any structures will increase linearly with flow rate (Syred, 2006), and in Figure 66 it was observed that the amplitude of the oscillations at the frequency of the flame structures increased with equivalence ratio.

However, due to the effects of combustion on swirl number, as described in section 2.2.1, a deviation from a linear relationship is expected in the results shown in Figure 75. Isothermal experimentation demonstrated how increasing swirl number, or at least geometric swirl number, increased the frequency of response. The increased heat of combustion that results from the fuel addition reduces the swirl number of the flow, which will affect the frequency of the response in the results in Figure 75.

Over the range of premix fuel flow rates, where the effects of flame structures were observed, mean dominant frequency and the mean, peak amplitude in the inlet chamber were calculated and plotted against total flow rate in Figure 76. The peak amplitudes are taken from the FFT analysis of the transducers response. The relationship between flow rate and frequency occurs in the same way as observed in chapter 5; with the expected deviation. The relationship can be represented by the Strouhal number, in the case of this configuration of the development burner is approximately 2.67.

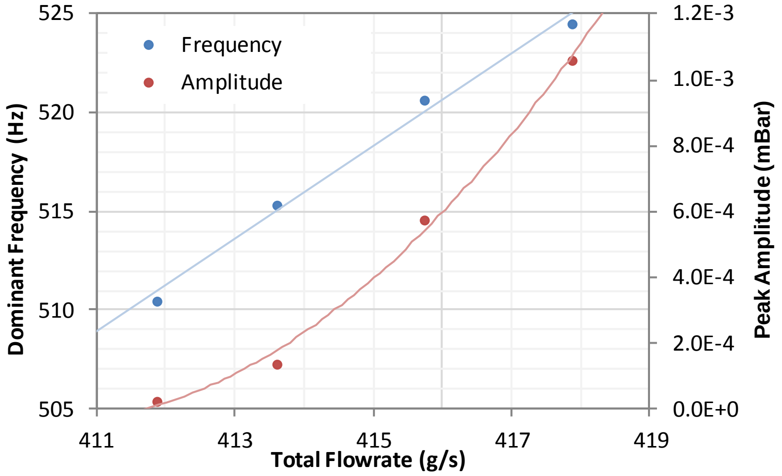

Figure 76: Relationships between flow rate, frequency, and amplitude of pressure fluctuations

The change in amplitude across the three transducers prior to flashback gives a good indication of flame position. Figure 77 shows how the dominant frequencies, (a), and amplitudes, (b), change as a fully premixed simulated Syngas flame, this time 85% hydrogen and 15% nitrogen by volume, approaches its rich flashback limit. In this case, the amplitude is calculated from the Power Spectral Density (PSD) of the transducers response.

At its 500kW design condition, which corresponded to a fuel flow rate of 12.2 g/s, the flame is very stable, with no frequency syncopation between the three transducers and low oscillations in pressure. An increase in fuel instantly results in partial coherence between the three transducers with a prominent frequency becoming apparent at 287 Hz, an increase in amplitude was also observed in the inlet and exhaust transducers.

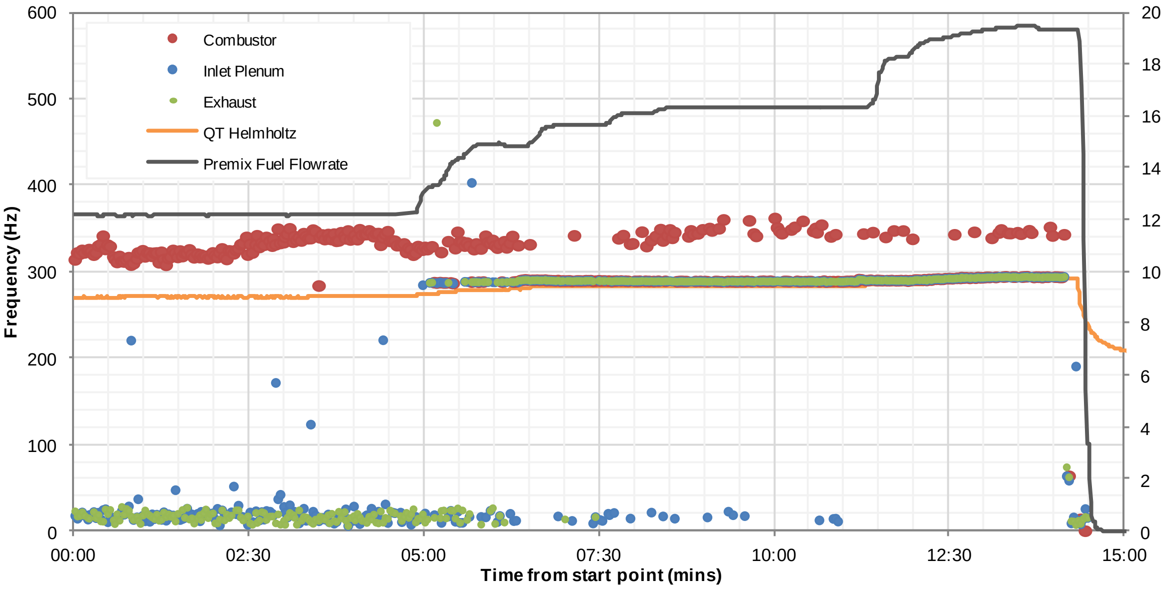

(a)

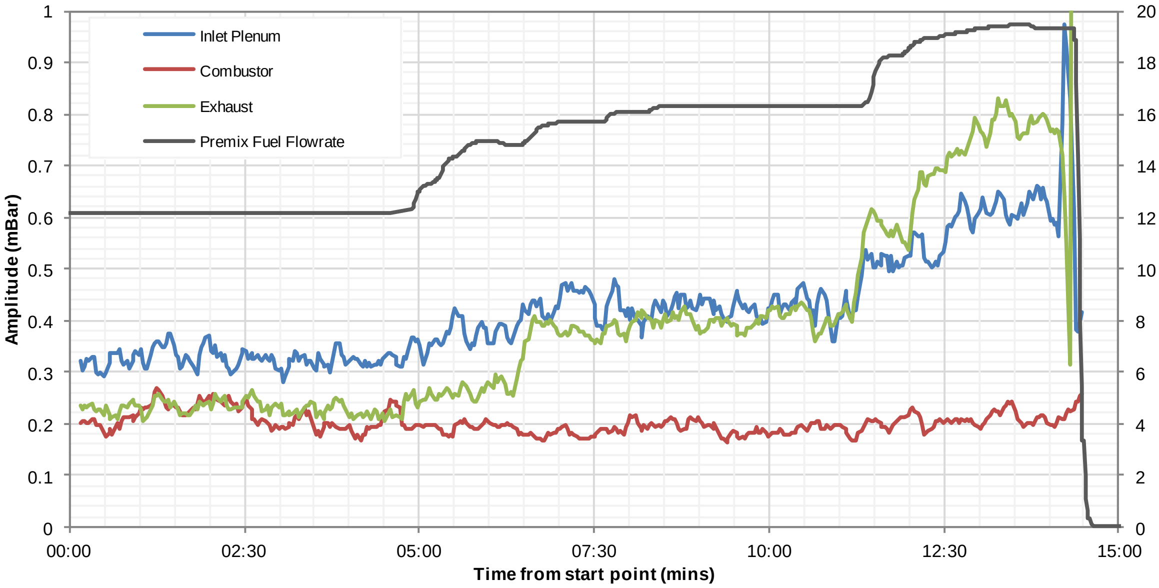

(b)

Figure 77: Alterations in frequency and amplitude prior to flashback (a) dominant frequency (b) amplitude of dominant frequency

The increased temperature of the flame compared to the previous Syngas blend results in a higher axial velocity at the nozzle exit, as such axial momentum is increased, and despite consistent burner geometry, swirl number is reduced, this results in a lower frequency of oscillations (De and Acharya, 2012). The reduction in the frequency of oscillations attributed to the unsteady motion the structures assisted feedback with resonance of the quartz tube, and unlike the coherence observed in Figure 75, the syncopation at 287 Hz corresponded with the calculated Helmholtz frequency.

The feedback mechanism discussed previously between the heat release fluctuations acoustics oscillations already exists. Subsequently, a sharp increase in the flow rate of premixed fuel at 11:30 minutes results in a significant amplification in the inlet plenum and exhaust, they appear to become saturated, as detailed by Fritsche (2005), before flashback occurs.

6.4 Chapter Summary

Using techniques that have also been reported by other researchers, microphones (Farhat and Mohamed, 2010) and dynamic pressure transducers in semi-infinite line assemblies (Iberall, 1950, Rohrssen, 2007, Straub and Ferguson, 2007) were used to monitor the acoustic response of swirl combustors under isothermal and combustion conditions.

In the cyclone burner, under isothermal conditions two mechanisms of acoustic response are present, those of cold flow structures, previously identified acoustically by Claypole (1980a) and Helmholtz resonance which has been identified by Allison (2013). It was confirmed that the frequency of structures have a linear relationship with flow rate, as described by Syred (2006), and increase with the level of swirl. A minimum flow rate, depending on the level swirl imparted upon it, is required for the structures to appear in, and dominate the acoustic response. This is in agreement with the previous research which indicates that vortex breakdown, which precludes structure formation (Gupta et al., 1984, Syred and Beér, 1974, Syred et al., 1971), is dependant on level of swirl and Reynolds number (Faler and Leibovich, 1978, Luca-Negro and O'Doherty, 2001, Sarpkaya, 1971a, Sarpkaya, 1971b).

Dominant frequencies and flow rates were interpreted in terms of the Reynolds, Strouhal and Roshko numbers, providing a dimensionless method of characterising the frequency of flow structures and Helmholtz resonance.

With combustion, a third mechanism of response is added, unsteady heat release, which develops into thermo-acoustic instabilities when a feedback mechanism between heat release and natural acoustics is excited (Lieuwen, 2012b, Mohammad et al., 2012). In both rigs unsteady heat release is indicative of a flame approaching its lean blowoff limit, and is caused by local extinction and re-ignition of the flame. This is a result of change in flame speed, one of the many factors that has the potential to induce thermo-acoustic instabilities identified by Lieuwen (2008). The presence of unsteady heat release of a methane flame near blowoff in the DIGCC was confirmed by the comparison with the frequency of light release, similar to techniques reported by Balachandran (2005), Durox (1998,2002), Hardalupas and Orain (2004) and Santhanam et al. (2002). Matching frequencies in acoustic and light fluctuations were observed for an oscillating flame near blowoff. When natural resonance was excited light fluctuations of significantly smaller amplitude occurred at the frequency of the resonance. These are secondary fluctuations as a result of the previously mention feedback mechanism (Lieuwen, 2012b, Mohammad et al., 2012).

The central recirculation zone is highly influential on flame stability, and its destruction during the process of combustion induced vortex breakdown is the prevailing mechanism for flashback in swirl combustors (Choudhuri, 2012). De and Acharya (2012) related pressure fluctuations of a flame experiencing CIVB to the unsteady precession of structures. These fluctuations are exacerbated by the Biot-Savart Law (Kiesewtter et al., 2007, Knole et al., 2008) providing a mechanism for further fluctuations (Lieuwen, 2012a). In both the CB and DIGCCC heat release at the frequency of flame structures was indicative of this process occurring and the flame approaching its rich flashback limit.

The presence of resonance at Helmholtz frequency in the acoustic response provided different indications in the CB and DIGCCC. In the cyclone burner, Helmholtz resonance, without the presence of structure defined heat release, indicated a stable flame. In the DIGCCC, when feedback with structure defined heat release caused resonance to dominate the pressure fluctuations it was an indication of approaching the rich flashback limit. Resonance prior to flashback occurring has been reported in other gas turbine combustors (Allison et al., 2013).

In the atmospheric rig, amplitude and correlation of the acoustic response were investigated as a method of inferring flame condition. The flame displayed high amplitude pressure fluctuations when the mechanisms of heat release were particularly prevalent. Low frequency heat release indicated an approaching blowoff, and heat release relating to the precession of structures indicated an approaching flashback limit. A high level of correlation indicated either a stable flame, with Helmholtz resonance the dominant mechanism, or a flame on the verge of flashback, when high amplitude heat release with a defined frequency occurred. Calculation of the Helmholtz frequency can be used to differentiate these instances of high correlation.

One the objective of this work was to determine whether a control system that ‘listens’ to the burner could be developed. This would require the combustion systems performance to be defined in terms of its acoustic response. Several different configurations of the cyclone burner were investigated, with the results suggesting that, for a given burner configuration, a relationship exists between acoustic response and flame stability that is consistent across differing power levels. Different configurations of the burner however only behave similarly. This suggests that acoustic feedback could successfully be integrated into active burner control system, but said control system would be applicable to a single burner design.

Chapter 7: Flow Structure Augmentation of Swirling Flames

7.1 Introduction

The previous chapters investigated the how the acoustic responses of flames alter depending on their stability; the theory that the monitoring of acoustic response could be integrated into a control system capable of compensating for variations in fuel composition. This approach is practical in static systems, such as boilers, and with fuels with low flame speeds, where blowoff is more likely to occur than flashback. In dynamic systems such as gas turbines, and with fuels with a propensity to flashback, this could be very difficult to implement. The aim of this chapter is to identify the mechanisms of flashback under lean conditions, a phenomena observed in the development gas turbine combustor, and establish the effect of the diffusive injection of different gases on the flow structure. The combined aim is to identify a method of extending flashback limits via diffusive injection, particularly for fuels with high hydrogen content in gas turbine combustors.

The design of a new piece of equipment is highly linked to its stability and thermo-acoustic patterns. These are issues that will directly impact upon the propagation of phenomena that can be highly detrimental to the performance and integrity of the system (Lieuwen, 2012b). Enhanced understanding of the phenomena that appear due to fuel changes in the system is needed to control combustion dynamics. The most important instabilities that can appear are produced by flashback, blowoff and thermo-acoustic oscillations.

A crucial feature of new burner technologies using alternative fuels is the formation of the central recirculation zone, a provider of heat to fresh reactants, anchoring the flame. However, unless its size and shape are properly controlled, problems can arise. The CRZ can, for instance, readily extend back into the burner and surround the fuel injector, facilitating early flashback (Subramanya and Choudhuri, 2007, Lieuwen et al., 2008, Thornton et al., 2007). Flashback can be caused by (i) boundary layer flame propagation, (ii) turbulent flame propagation in the core flow, (iii) thermo-acoustic oscillations/instabilities and (iv) upstream flame propagation of coherent vortical structures, known as Combustion Induced Vortex Breakdown (CIVB) (Lieuwen et al., 2008, Fritz et al., 2004, Kroner, 2002, Kroner et al., 2003). Two of these mechanisms, i.e. boundary layer flame propagation and upstream propagation of coherent structures, have been studied by several groups using natural gas, a conventional power derivative gas turbine fuel. However, the use of unconventional fuels, such as those derived from the gasification or digestion of carbonaceous material, can be extremely detrimental to the control of this phenomenon, and very little literature is available on this subject. High turbulence levels, one of the very useful features of swirling flow because of mixing potential, affects flashback limits detrimentally due to effects on turbulent flame speed (S_t). It has been reported that the current theoretical approximations of S_t do not agree with experimental values (Dam et al., 2011a, Dam et al., 2011b). Literature on this topic becomes more complex in terms of numerical modelling, but experiments tend to be different from numerical findings especially when complex flows are added to the field (Dam et al., 2011b). For instance, very little has been documented in terms of boundary layer propagation using atmospheric conditions (Eichler et al., 2012, Eichler and Sattelmayer, 2011, Eichler and Sattelmayer, 2012), and what documentation there is only shows the evolution of 2D structures without swirl and under atmospheric conditions. Thus, the current knowledge on these mechanisms cannot adequately describe the flashback propensity of most practical combustor designs. Therefore, the recognition of the real pattern of this phenomenon is crucial in order to have systems and models capable of utilising new alternative fuels.

Similarly, relatively little literature exists on blow-off when swirling flows and unconventional fuels are used. The studies that have been conducted consist of a large database on how to improve operability with natural gas, but there is little investigation on the fundamental behaviour underlying combustion stability (Tuttle et al., 2012). Shanbhogue et al. (2009) explained the different theories regarding blowoff, with most of the current theories being derived from a flamelet based description upon local extinction via excessive flame stretch (Driscoll, 2008). This theory has demonstrated that flame stretching starts blow-off with the initiation of holes in the flame, that are healed by the same flame creating stretching in areas that otherwise would have been unaffected. However, it is also recognised that this mechanism is not the one causing the final blow-off, as it is clear from data that the flame can withstand some extinction. Therefore, it is considered that the “critical extinction level” must be strongly influenced by the entrainment of reactants into the recirculation zone, the cooling of regions of the recirculation zone and the shrinking in size of the CRZ, thus confirming some relation between the phenomenon of blowoff and the existence of the CRZ (Tuttle et al., 2012). This is a theory that has not been corroborated.

Indeed, some authors (Valera-Medina, 2009, Valera-Medina et al., 2009, Valera-Medina et al., 2011a, Valera-Medina et al., 2011b, Valera-Medina et al., 2012, Stöhr et al., 2012) have observed that the CRZ has a close connection to the stability of the system, with its shape, strength and curvature being of high importance to its resistance to flashback and blow-off (Valera-Medina et al., 2012, Kedia and Ghoniem, 2012). Regular precession occurs in the CRZ, with the appearance of the CRZ dependent on the heat transfer regime. The mode of injection is also important, with an increase in the interaction of the hot products and fresh reactants when confinement is imposed. The recirculation zone behaves as an intermittent structure that will propagate downstream in order to release some internal pressure. The product of the confinement and intense recirculation at moderate to high swirl numbers (Valera-Medina et al., 2012). This, on the other hand, can also be detrimental to the phenomenon of flashback as the CRZ will evolve into combustion induced vortex breakdown (Kroner et al., 2007), Boundary Layer Propagation (Eichler and Sattelmayer, 2012) or the production of turbulent burning along the vortical axis (Blesinger et al., 2010), all damaging to the system. Its interaction with the Precessing Vortex Core (PVC) under combustion and isothermal conditions is also recognised in some works (Valera-Medina, 2009, Valera-Medina et al., 2009), and its influence in the thermo-acoustics of the system is of high impact especially to the wrinkling and stability of the flame (Yang and Lieuwen, 2005, Bellows et al., 2007). Hence, the understanding of the stability limits and thermo-acoustics represents an important topic of discussion with the use of new fuels.

7.2 Lean Flashback

It has been established that flashback is caused by either one, or a combination, of four factors (Fritz et al., 2004, Kroner, 2002, Kroner et al., 2003, Subramanya and Choudhuri, 2007); flame propagation in either the boundary layer or core flow, CIVB or via combustion instabilities.

Typically flashback occurs when local flame speed exceeds local flow velocity, allowing upstream flame propagation occur. Peak flame speeds for the majority of fuel-air mixtures occur when equivalence ratio is slightly greater than 1, and since the majority of combustion systems operate with a lean mixture; increasing flame speed relative to mixture velocity requires an increase in fuel relative to air. As such, the occurrence of lean flashback is highly unusual; nevertheless, it was observed when the development burner was operated within the HPCR using the two simulated syngas blends detailed in chapter 6, one being 50 percent hydrogen, 50 percent carbon monoxide (S50/50), and the other 85% hydrogen, 15% nitrogen (S85/15).

7.2.1 Observation of Lean Flashback

Two different final flame positions were observed as the result of these flashback events. The first position observed was upstream flame propagation in the main fuel and air mixture, one instance of its occurrence was during a test using S50/50 as the main fuel with a methane pilot. Axial and radial images taken of the flame in a state of flashback are shown in Figure 78. In the radial image the pilot swirler is clearly visible, indicating that the flame has propagated further upstream than the pilot swirler. A blue section of the flame is visible on the central axis of the burner, downstream of the pilot swirler, where the hot products ignite the pilot methane. Due to the tangential momentum of the flow, it is at its lowest velocity where its surrounds the pilot swirler. Prior to boundary layer effects of the burner exit nozzle causing a deceleration of the flow, velocity will increase as distance from the central axis of the burner increases. This means that the flame surrounds the pilot swirler, which would be damaged by prolonged exposure to a flame of this nature. Further indication of the final appearance of the flashbacked flame, with a sectioned axial view, is shown in Figure 79.

Prior to flashback, the combustor was operating at its desired power level with a near stoichiometric pilot mixture, with an Equivalence Ratio (Φ) of 0.970, and a lean main mixture, $\Phi = 0.329$. A reduction in the pilot flow saw the flame begin to propagate back to the combustor exit nozzle via the shear boundary layer, as is demonstrated in Figure 80 (a). This propagation in the shear layer has been seen in previous work with methane (Syred et al., 2012, Abdulsada et al., 2011) immediately prior to complete flashback, as seen in Figure 80 (b). In the previous case, the flashback was caused by increasing the equivalence ratio of a fully premixed flame.

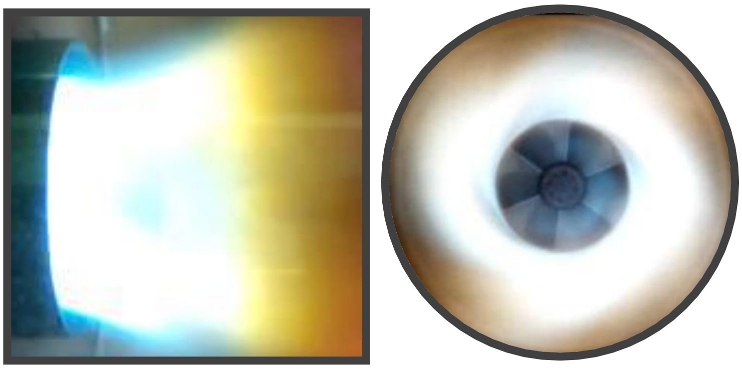

(a) *(b)*

Figure 78: Images of the first instance of lean flashback from (a) axial and (b) radial positions (Morris, 2012)

Strong shear layers develop where the high velocity swirling flow meets the relatively stagnant fluid in the combustion chamber. This shear layer produces regions of low velocity flow, and can allow the flame to propagate back to the combustor nozzle. The further downstream, the greater the fluid velocity is reduced, increasing the thickness of the shear layer; evidence of this is shown in both Figure 80 (a) and Figure 80 (b).

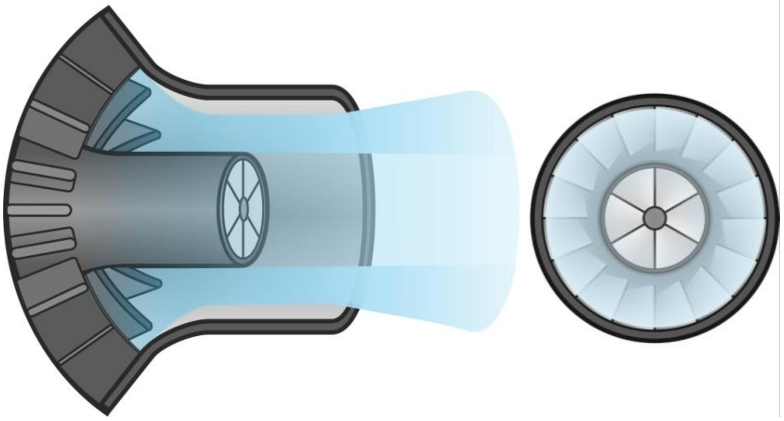

(a) *(b)*

Figure 79: Indication of the appearance of the ultimate position of the first instance of lean flashback from (a) axial and (b) radial perspectives

The diameter of the low velocity region in the centre of the flow also increases as the distance from the combustor nozzle increases, this can been seen in PIV data, from the combustor under isothermal flow conditions at the desired bulk exit velocity, in Figure 81. The result being that the annular area where overall flow velocity is too great for flame propagation reduces in as downstream distance increases. When flashback occurs in this way the conditions are such that the low velocity flammable regions of the flames main body and shear layer meet up allowing the flame to propagate into the shear layer.

(a) (b)

Figure 80: Still images of flames taken prior to boundary layer flashback (a) demonstration of flame seen during these trials (with S85/15 in the case shown) and (b) as seen by from Syred et.al. (2012) using methane

Once propagation through the shear layer has been established, it is possible for flashback to occur via the further propagation through the outer wall boundary layer of the combustor nozzle. This is controlled by critical velocity gradient (Bagdananvicius et al., 2010) as defined by Lewis and von Elbe (Lewis and Elbe, 1987).

The mixing layer that exists between the pilot flame and the main fuel mixture (Dhanuka et al., 2009) ensures that equivalence ratio in the shear layers is not affected by that of the pilot, this suggests that propagation of the flame is initiated by CIVB rather than changes in the mixtures burning velocity.

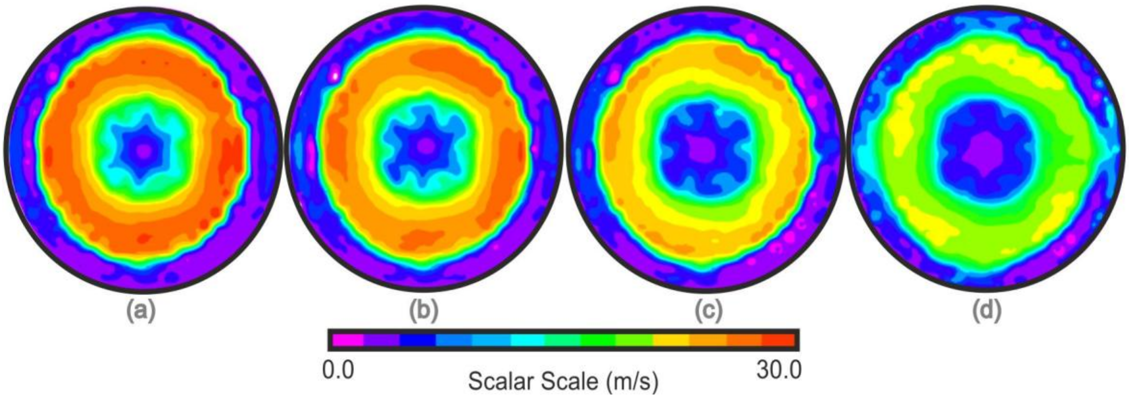

Figure 81: Plots of velocity on radial planes at (a) 0.05 x/D (b) 0.10 x/D (c) 0.25 x/D (d) 0.5 x/D from nozzle exit under desired power conditions for the gas turbine combustor (500 image pairs each with approximately 2000 vectors)

The shape of the CRZ strongly influences the stability of the combustion system, its presence causes the formation of other proceeding structures capable of pushing the flame upstream and increasing propensity for flashback (Valera-Medina et al., 2009). Previous work by Dam et. al. (2011a) shows when CIVB occurs the High Momentum Flow Region (HMFR) of the flame contracts and squeezes the CRZ, resulting in upstream flame propagation. The work also demonstrates how the mixing layer approaches combustor's exit nozzle. Valera-Medina (2009) identified a type of flashback that occurred when CIVB, identified as the primary cause of flashback in swirl burners (Kroner et al., 2007), caused the CRZ to propagate upstream, resulting in the flame attaching to an axial fuel injector that protruded into the combustor nozzle, resembling the flashback seen with S85/15 main fuel and methane pilot. Axial and radial images taken of the flame in a state of flashback are shown in Figure 82.

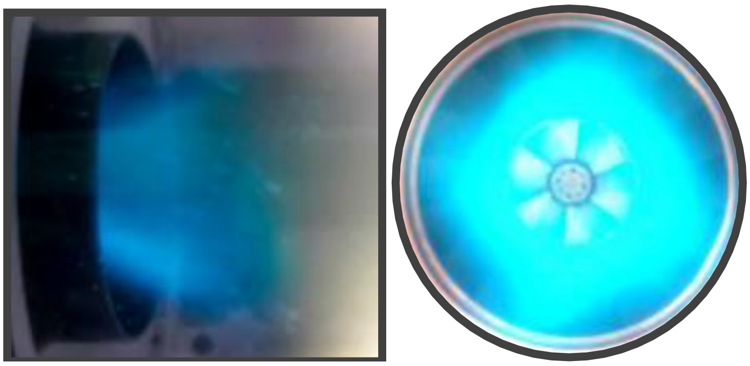

(a) *(b)*

Figure 82: Images of the second instance of lean flashback from (a) axial and (b) radial positions (Morris, 2012)

In the radial image the pilot swirler is barely visible, which indicates that the flame has attached to the pilot swirler, and that combustion is occurring downstream of the pilot swirler exit. The colour of the flame indicates that the pilot methane is well mixed in the combustion zone. Further indication of the final appearance of the flashbacked flame, with a sectioned axial view, is shown in Figure 83.

Due to the significantly higher hydrogen content in S85/15, its burning velocity is greater than S50/50; this results in the flame shape being significantly shorter and narrower. The narrow shape of the flame prevents propagation into the shear and boundary layers, as observed previously, allowing vortex breakdown to continue. Eventually the CRZ contracts upon the body of the pilot injector in the centre of the flow, a process that was demonstrated clearly by Dam et. al. (2011a). From standard operating conditions two alterations in flow conditions resulted in flashback of this type occurring. The first was a reduction in pilot fuel, the result of which was a flame fluctuating between a seemingly stable and flashbacked state before permanently attaching on the pilot injector. The second was to increase airflow steadily, global equivalence ratio decreased from 0.221 to 0.157 before axial flashback occurred.

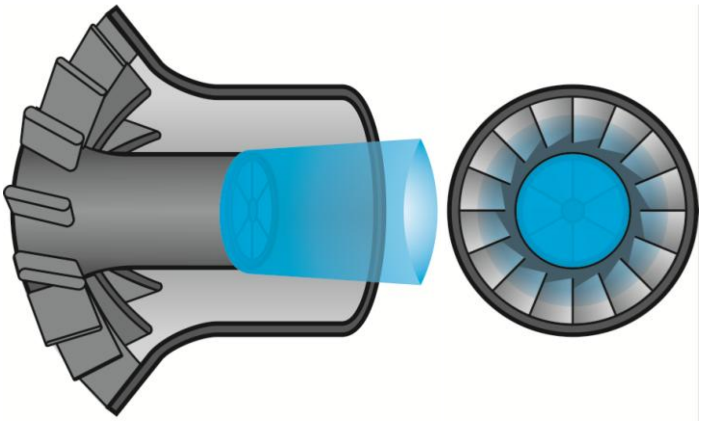
(a) (b)

Figure 83: Indication of the appearance of the ultimate position of the second instance of lean flashback from (a) axial and (b) radial perspectives

7.2.2 Initiation of CIVB

Work on combustors with co-swirlers provides examples of cases where, under isothermal conditions, the flow patterns resemble those of a single swirler (Hadef and Lenze, 2007), and where flow patterns differ (Dhanuka et al., 2009). However the burner used by Dhanuka et. al. (2009) which resulted in a different pattern had a significant area between the outlet of the swirlers which acted as bluff body, creating additional recirculation zones. Isothermal PIV of the development IGCC combustor, shown in Figure 84, confirmed a CRZ structure resembling that created by a single swirler.

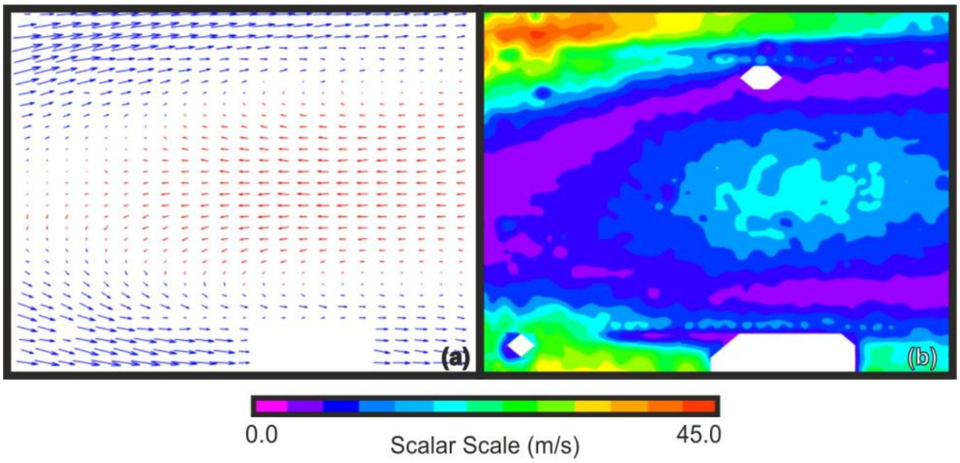

Figure 84: (a) Vector and (b) magnitude plots of combustor under typical gas turbine operating conditions (500 image pairs with approximately 3500 vectors)

This structure is largely due to its co-swirl configuration and the dissimilarity between flow rates through the pilot and main annular swirlers. The result is a pilot swirler that acts in a similar fashion to a bluff body, as seen in the atmospheric generic burner, and commonly used to stabilise flames in fast flowing fluids (Gerrard, 1966).

It is believed that the lean flashback observed is the result of CIVB; and after the initiation of CIVB both types of flashback encountered have been adequately explained by previous studies (Valera-Medina, 2009, Dam et al., 2011a, Syred et al., 2012). These studies, however, relate to burners that use a single device to impart swirl on the flow, with both axial and radial flashback being caused by an increase in equivalence ratio.

In the previously referenced work of Dam et. al. equivalence ratio was increased by increasing the flow of fuel whilst keeping air constant. As such, adiabatic flame temperature, the expansion and, as a result, volume of hot gas also increased and the intensity in high velocity zones increased.

It is believed that it is the subsequent increase in the volume of gases, and not directly the change in equivalence ratio, that is linked to the change velocity of the HMFR, or high velocity zones, that initiates CIVB. This theory is investigated using flow field analysis of the atmospheric generic burner and the methodology described in section 3.3.4.

7.2.2.1 Flow Field Analysis of Flames with Varying AFR

Experimentation into the onset of the lean flashback observed involved performing stereo PIV analysis of 12.5 kW methane flames with varying equivalence ratio. The aim being to assess how flow structures were altered as air to fuel ratio increased. During these tests the methane-air mixture was fully premixed, details of flow rates are in Table 14, where Test Points (TP) I to VI are of current interest.

The scalar plots in Figure 85 represent tangential velocity of TP I to TP VI, on an axial-radial plane that intersected the central burner axis. Vectors are overlaid to give an indication of flow direction, for further reference the individual vector plots are shown in Figure A. 1 which can be found with all additional images in Appendix A. The scalar plots, which are all displayed on the same scale, demonstrate that the velocity of fluid increases as the air flow is increased and the flame becomes leaner. In the results for

TP I the highest tangential velocity occurs at x/D = ±0.5 and y/D = 0, when the swirling flow, escapes the confinement of the exit nozzle. Tangential velocity is then reduced due to two reasons.

Table 14: Details of AGSB test points I-X

Test Point	Mass Flow Rate (g/s)				Φ	AFT (K)
	CH_4	Air	CO_2	Total		
I	0.25	5.00	0.000	5.25	0.86	2083
II	0.25	4.78	0.000	5.03	0.90	2134
III	0.25	4.30	0.000	4.55	1.00	2226
IV	0.25	3.91	0.000	4.16	1.10	2211
V	0.25	3.58	0.000	3.83	1.20	2137
VI	0.25	3.31	0.000	3.56	1.30	2057
VII	0.25	3.31	0.049	3.61	1.30	2038
VIII	0.25	3.31	0.103	3.66	1.30	2017
IX	0.25	3.31	0.116	3.68	1.30	2012
X	0.25	3.31	0.130	3.69	1.30	2007

As the flow is now able to expand, some of the tangential momentum is transferred into radial momentum. And combustion in the main reaction zone of the flame causes axial momentum to increase relative to tangential momentum (Syred and Beér, 1974). As velocity in the axial-radial plane reduces, due to radial expansion of the flow and the completion of hot gas expansion due to combustion, the tangential velocity increases again.

This process of tangential velocity acceleration and deceleration is particularly clear in the results of TP III, in the region of positive tangential velocity. The region of highest velocity in the axial-radial plane, indicated by the grouping of long, red vectors, is sandwiched between the regions of highest tangential velocity, indicated by the darkest orange regions of the scalar plot.

Visual interpretation of the stereo and single camera PIV images, in Figure 85 and Figure A. 1 respectively, shows that the size of the central recirculation zone changes, as does the size and velocity of the high velocity zones, or High Momentum Flow Region (HMFR). In order to provide quantitative results, the size and velocity of structures within the flow fields were assessed using the exported numeric data from the PIV results. Methods for defining structures and their properties are detailed in Appendix B.

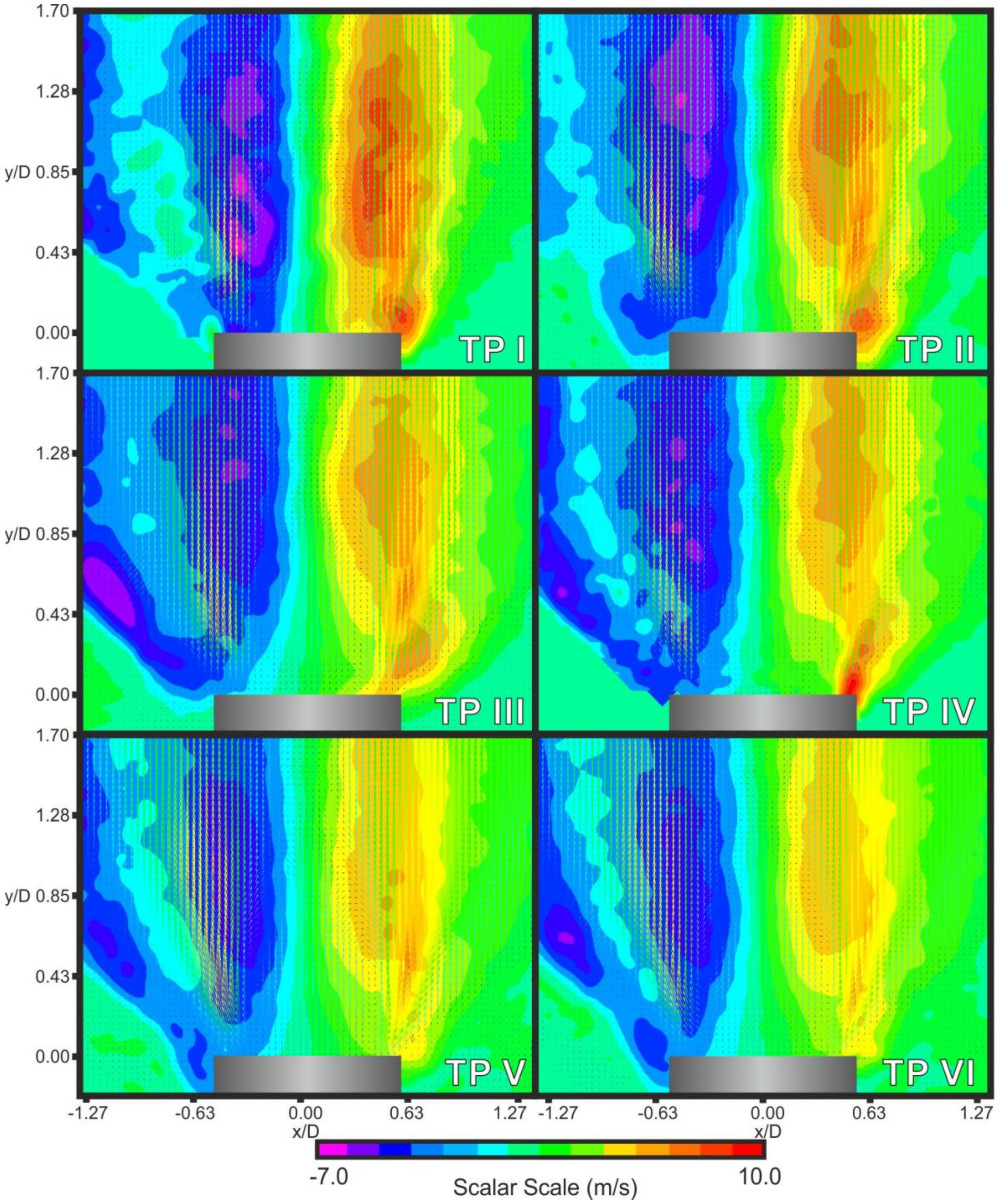

Figure 85: Stereo PIV of TP I to TP VI in the AGSB with altered premix air flow rate as detailed in Table 14, Scalar plots show tangential velocity (U_t)

The minutiae of the HMFR are taken from the numerical PIV data, with areas where total velocity exceeds 3 m/s considered to be of a high momentum, as described in Appendix B. The change in the volume of these regions, and the mean velocity of the flow within them, are demonstrated in Figure 86 (a) and (b) respectively, with all values having been normalised against those of TP VI.

Between TP I and TP VI it can be seen that increasing the air flow rate increases the HMFR velocity; however, the size of the HMFR is reduced. The result being, that as equivalence ratio reduces, the HMFR reduces in size but increases in intensity. Figure 86 (a) and (b) also show the mean velocity and volume of the CRZ for the same conditions, as calculated from the same numerical PIV data. The results show that rather than an increasing HMFR volume coinciding with a reduction in CRZ volume, they rise together, indicating an increase in the total size of the structures. Increasing flow rate through the exit nozzle increased the axial momentum of the flow, which in turn elongated the flame structure, and resulted in higher velocities. This indicates that an increase in HMFR velocity, rather than size, is linked to the contraction of CRZ.

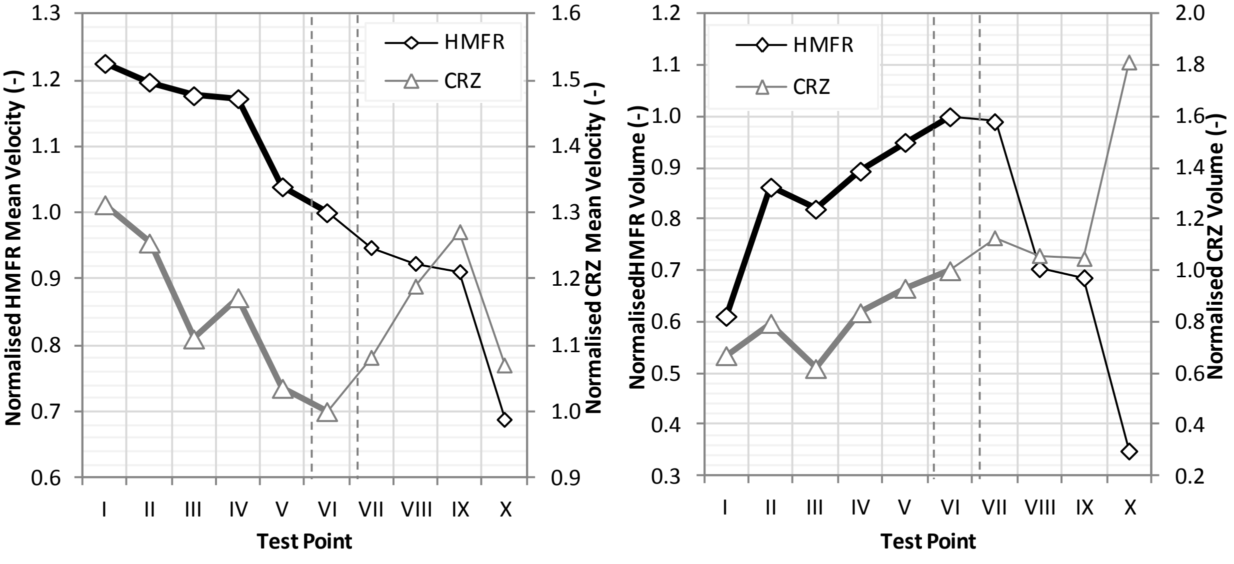

(a) *(b)*

Figure 86: The effect of air and carbon dioxide flow rates on the (a) velocities and (b) volumes of the HMFR and CRZ

7.2.3 Initial CO_2 Injection

In terms of unconventional fuels, the primary goal of introducing CO_2 into the gas turbine combustor is to reduce the emissions of NO_x. This is achieved by cooling the flame, thus the Zeldovich mechanism can be reduced (Warnatz et al., 1999). Previous experimental and numerical studies have investigated the effect of dilution of Syngas fuels with various additives, including carbon dioxide, nitrogen and steam (Lee et al., 2012, Pack et al., 2008, Konnov et al., 2002, Natarajan et al., 2007, Burbano et al., 2011, Giles et al., 2006). In the main, these studies focus on fundamental characteristics of the combustion process. However, the work by Lee et. al. (2012) and

Khalil et al (2012) actually investigated the effect of diluting the premix fuel had on the emission of NO_x and CO from a model gas turbine.

Lee et al (2012) showed that reduction in ppmv NO_x per unit power is logarithmically related to the heat capacity of the total diluent added. Since carbon dioxide has a higher heat capacity than steam or nitrogen, a smaller mass flow rate is required for a comparable reduction in NO_x. Moreover, the use of CO_2 from carbon capture and storage facilities could reduce costs as well as capture equipment further downstream the combustion zone.

The effect of diffusive carbon dioxide injection on flame structure was initially investigated using the AGSB, with the flow rates of TP VII through X detailed in Table 14. Stereo PIV images in Figure 87 show how the injection of differing amounts of carbon dioxide through the pilot of the generic burner affected the velocity of the flame. In each instance the same pattern of velocity change with increasing y/D seen in Figure 85 is observed.

The scalar, tangential velocity plots in Figure 87 are on the same scale as those in Figure 85. Between TP VI and TP X a general reduction in tangential velocity is evident. Changes in structure and velocity from TP I to TP VI were largely attributed to changes in flow rates, with a 47.5% decrease from TP I to TP VI. However, between TP VI and TP X premix flow is constant, with change in total mass flow equal to 3.7%; despite this relatively small effect on mass flow rate through the burner exit, the changes in structure and velocity are significant, as detailed in Figure 86. Through TP VI to IX the introduction of CO_2 results in a decrease in HMFR velocity, however the velocity in the CRZ increases sharply, most likely due to the entrainment of the diffusive carbon dioxide into the recirculation zone.

The CRZ stabilises the flame by recirculating thermal energy and active chemicals whilst allowing turbulent flame speed to match flow velocities (Syred and Beér, 1974, Gupta et al., 1984), all are inhibited by the injection of CO_2, as such, as its flow rate is increased the flame tends towards blowoff. The vector plot of TP X in Figure 88 represents the flow field of a flame in a quasi-stable state, on the verge of blowoff.

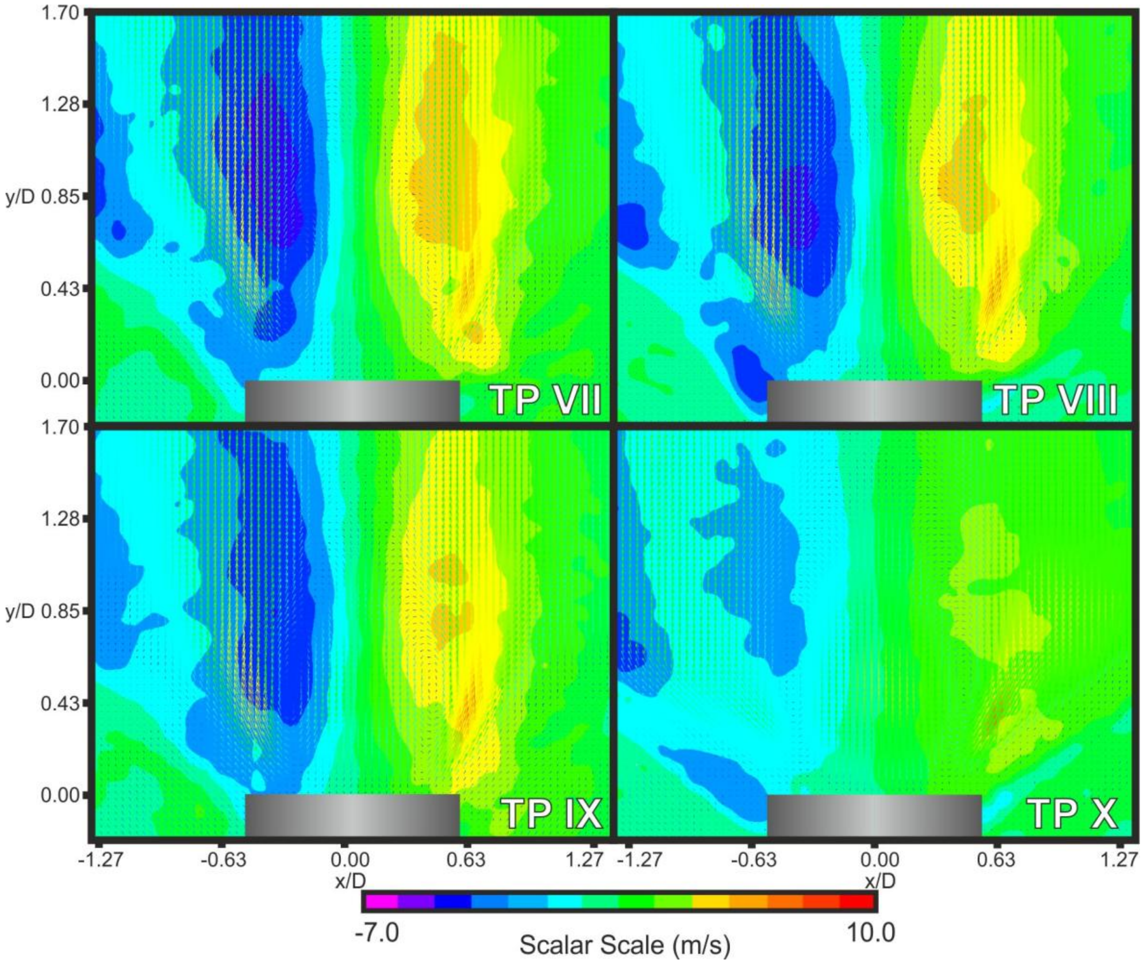

Figure 87: Stereo PIV of TP VII to TP X in the AGSB with altered premix air flow rate and pilot CO2 flow rate as detailed in Table 14, Scalar plots show tangential velocity (U_t)

The flame was visibly and audibly unstable, with extinction and re-ignition events occurring. At this point the flame shape has changed significantly, as demonstrated by the difference between the vector plots of TP X and TP VII to TP XI. There is no major difference in the size of the recirculation zone between TP VI and TP. The velocity of the gases within the CRZ increases relative to the peak velocity in the HMFR, indicated by the colour of the vectors inside becoming greener. Between TP IX and TP X there is significant increase in the size of the CRZ. Despite the colour of the vectors, a significant deceleration of the gases within it occurs, as detailed in Figure 86, which also shows how the injection of carbon dioxide reduces the size and velocity within the HMFR

The results show how the injection of a small flow rate of CO_2 can have significant effects on flame structure. When premixed conditions are kept constant the injection of CO_2 causes the size and the velocity of the CRZ to increase, relative to the HMFR. As this action opposes those reported to occur during the onset of CIVB, they can be utilised to increase the stability range of a combustor.

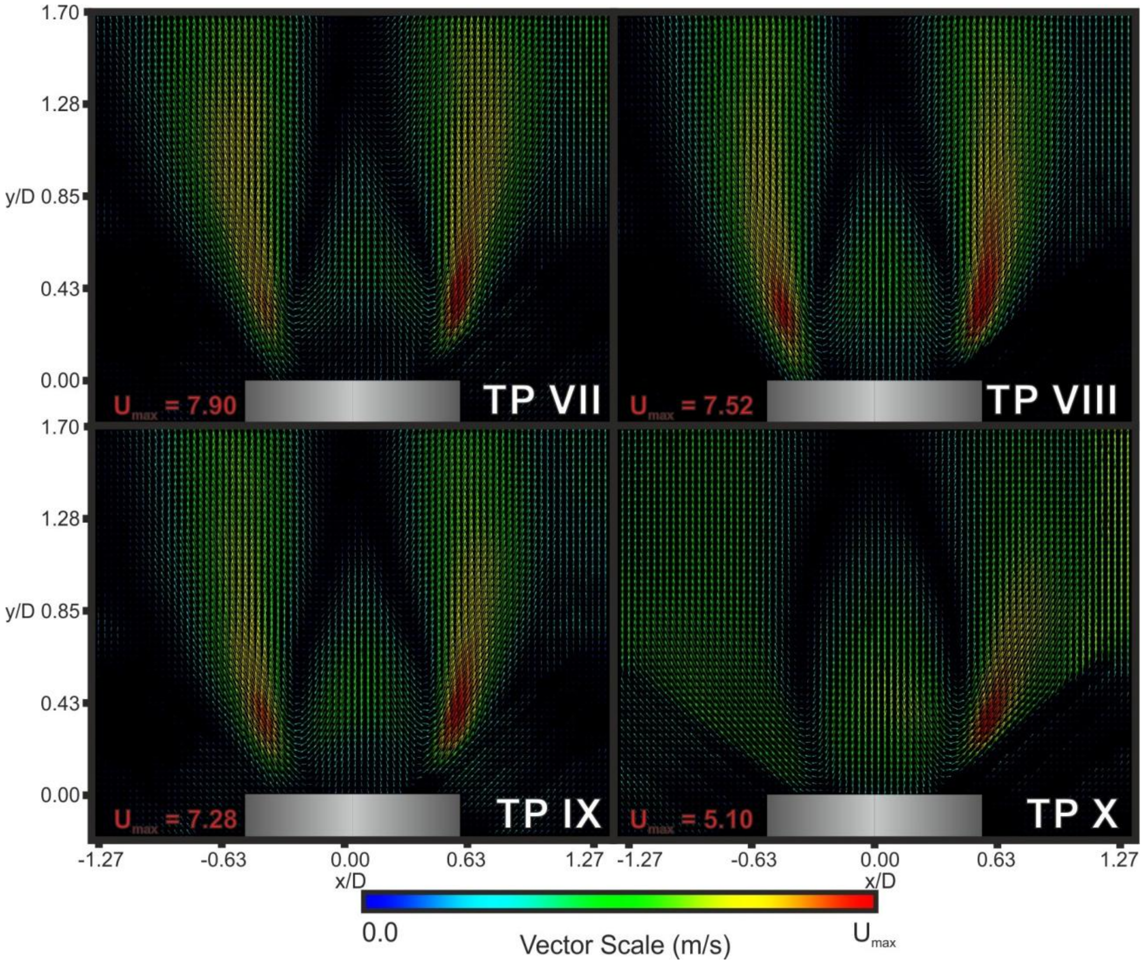

Figure 88: Single camera vector plots of TP I to TP IV in the AGSB with altered premix air flow rate and pilot CO_2 flow rate as detailed in Table 14, vectors indicate velocity and direction.

7.3 Diffusive Injection of Different Gases

Following on from the initial experimentation of diffusive carbon dioxide injection altering the flame structures (Lewis et al., 2014), varying amounts of carbon dioxide, air and methane were injected through the diffusive pilot of the AGSB to assess the effect on flame structure. The three gases were selected for their differing combustion properties:

- Methane, which is often used as a pilot fuel in gas turbines and will increase the global equivalence ratio of the flame.

- Carbon dioxide, which does not affect oxidant-to-fuel ratio, but which has been shown in previous studies to alter flame conditions (Lee et al., 2012, Pack et al., 2008, Konnov et al., 2002, Natarajan et al., 2007, Burbano et al., 2011).
- Air, which will reduce the flames global equivalence ratio.

In order to allow comparison between results, premix flow rates of 0.2 g/s methane and 3.44 g/s air were kept constant; these equate to a 10kW, stoichiometric mixture. Details of the test points are displayed in Table 15. The flames are un-confined, as such ambient air will be entrained, and they will actually be leaner than the defined equivalence ratio.

The experimental method was the same for all three gases: the flame was lit and 150 images were recorded with the PIV system, the flow rate of diffusion gases was then increased in regular intervals, with a further 150 images recorded at each interval, until the flame reached a point of quasi-stability. Between results taken using with the same diffusive gas the flame was not extinguished; in order accurately maintain conditions between test points.

The PIV results in Figure 89 demonstrate the effect of introducing methane through the pilot on the flame structure. The left hand side of the PIV images show the axial velocity (U_a) of the flows on scale of -5 to 8 meters per second. Negative velocities indicate that the flow downstream, towards the burner exit. On the right hand side of images total velocity (U_t) is shown, on a scale of 0 to 8 metres per second. The total velocity is a measure of magnitude, regardless of direction, so no negative velocities are possible. The vector maps of test points 1 to 8 are shown in Figure A. 2.

The combination of image masking and the neighbourhood validation causes the data shown to underestimate the velocity of the fluid as it leaves the exit nozzle, as discussed in section 3.3.4.3. This is why the fluid appears to have exceptionally low velocities in the region where $0 < y/D < 0.1$.

The flow in TP 1 has highest velocities at 0.25 y/D and ±0.55 x/D, indicated by the red regions in both scalar plots, there is also a sub-region where axial velocity exceeds the 8 m/s on the scale shown. The unburned, premixed reactants are at their greatest velocity near the outside of the exit nozzle, where the tangential-radial momentum imparted by the radial swirl passages has forced the flow away from the burner axis but boundary effects are negligible. The centrifugal force on the fluid also means that the reactants are densest at the inner wall of the exit nozzle. Combustion occurs when the reactants leave the exit nozzle, a significant increase in axial velocity results from hot gas expansion. An increase in radial velocity also occurs. The combined tangential-radial and axial momentum of the products results in flow spreading in the x and y directions on the plane shown. As spreading occurs and the combustion process is complete, velocities decrease. Tangential-radial momentum results in predominant expansion in the x direction being away from the burner axis. This creates a low pressure zone along the vertical burner axis, with a pressure differential that causes combustion products to flow towards the central axis and burner exit. The stagnation of the flow prior to being recirculated is indicated by the turquoise region in the axial velocity profile.

Table 15: Details of AGSB test points 1-26

		Flow Rates (g/s)							
	Test Point	Pilot	Total	Φ	Total Power (kW)	Isothermal S_g	Bulk Exit Velocity (m/s)	Re	AFT (C)
Methane	1	0.000	3.640	1.00	10.0	1.05	4.88	4361	1953
	2	0.015	3.655	1.07	10.7	1.04	4.90	4379	1928
	3	0.030	3.670	1.15	11.5	1.02	4.92	4397	1875
	4	0.045	3.685	1.22	12.2	1.01	4.94	4415	1816
	5	0.059	3.699	1.30	13.0	0.99	4.96	4433	1760
	6	0.074	3.714	1.37	13.7	0.98	4.98	4451	1702
	7	0.089	3.729	1.45	14.5	0.97	5.00	4468	1645
	8	0.104	3.744	1.52	15.2	0.95	5.02	4486	1589
Air	9	0.000	3.640	1.00	10.0	1.05	4.88	4361	1953
	10	0.100	3.740	0.97	10.0	1.00	5.02	4482	1924
	11	0.201	3.841	0.94	10.0	0.95	5.15	4602	1902
	12	0.301	3.941	0.92	10.0	0.90	5.29	4722	1875
	13	0.402	4.042	0.90	10.0	0.86	5.42	4843	1846
	14	0.502	4.142	0.87	10.0	0.82	5.56	4963	1817
Carbon Dioxide	15	0.000	3.640	1.00	10.0	1.05	4.88	4361	1953
	16	0.025	3.665	1.00	10.0	1.04	4.92	4391	1931
	17	0.050	3.690	1.00	10.0	1.03	4.95	4421	1923
	18	0.074	3.714	1.00	10.0	1.03	4.98	4451	1914
	19	0.099	3.739	1.00	10.0	1.02	5.02	4481	1906
	20	0.124	3.764	1.00	10.0	1.01	5.05	4510	1897
	21	0.149	3.789	1.00	10.0	1.00	5.08	4540	1889
	22	0.174	3.814	1.00	10.0	0.99	5.12	4570	1881

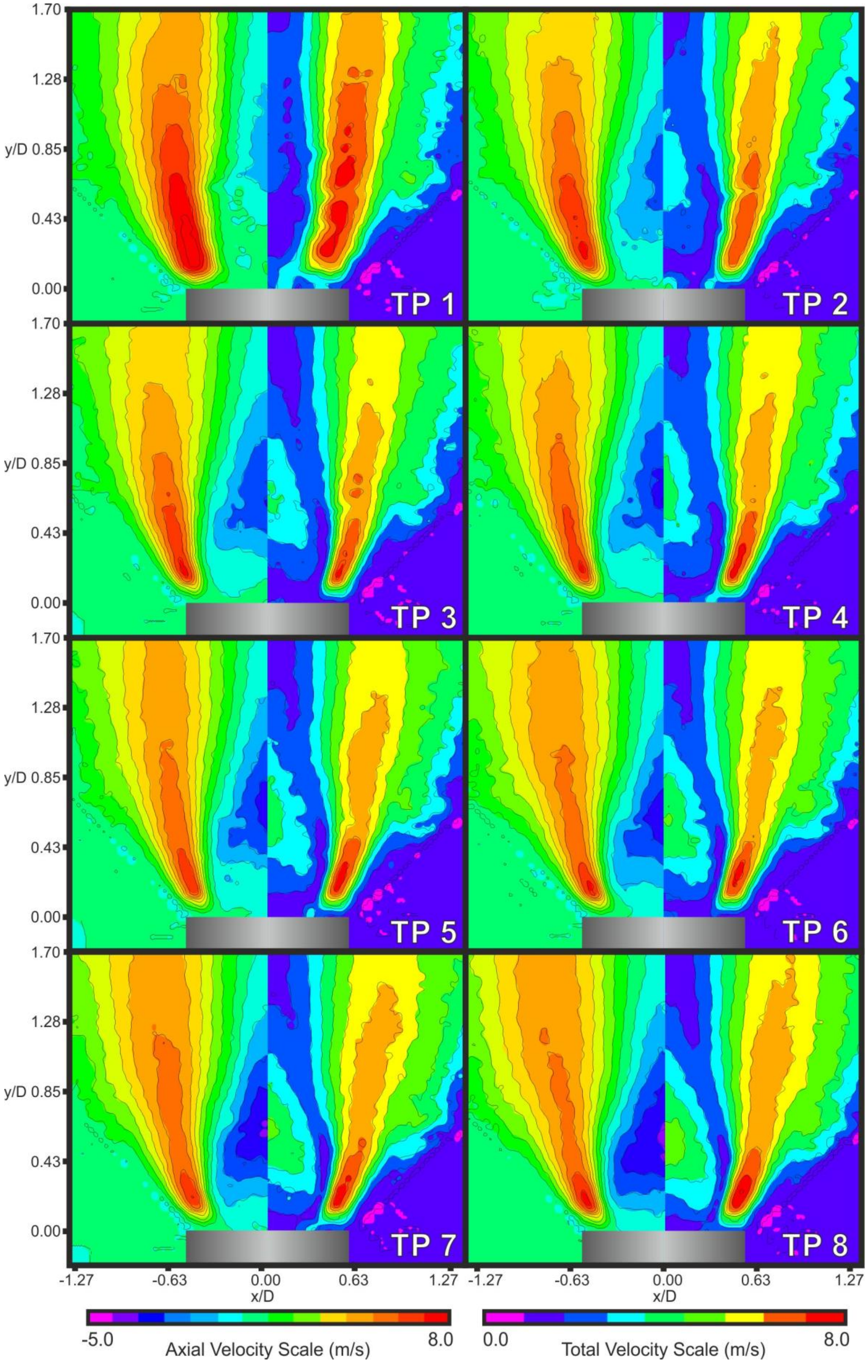

Figure 89: Scalar plots of TP 1 to TP 8 in the AGSB as detailed in Table 15, the left half of each image indicates axial velocity, and the right half total velocity.

TP 1 and has a very narrow, low velocity, CRZ. Within the recirculation zone the maximum value of U_t is 2 m/s and the minimum value of U_a is -1 m/s. The axial velocity of the recirculated gases become positive at $y/D = 0.4$. The introduction of methane through the pilot results in an increase in size and velocity of the CRZ, which can be seen in TP 2. The shape of recirculation zone also changes; with the width increasing disproportionally at its base. The negative axial velocity of the recirculated gases at the centre of the CRZ increases significantly, exceeding 2 m/s. Due to the increase in velocity of the recirculated gases, the region of negative axial velocity extends toward the burner exit, as a result the CRZ becomes elongated. The velocity in the HMFR in TP 2 is significantly lower than that in TP 1, in terms of both axial and total velocity; it appears to have become narrower as a result of the CRZ expanding.

The alteration in shape becomes further exaggerated as the flow rate of pilot methane increases through test points 3 to 8. With each increase in the flow rate of diffusive methane the width of the reverse flow region increases, as do the negative axial and total velocities of the gases within them. The injection of methane reduces the peak velocity of the reacting flows in the HMFR, however, the shape and overall velocity profiles in these regions remain largely unaffected.

The diffusive injection of air has a markedly different effect on the flow structure than was observed with methane. PIV images in Figure 90 effectively demonstrate how the air causes the size and mean velocity of the CRZ to reduce, eventually leading to its complete destruction. Test points 9 through 12 are displayed as in Figure 89, the left hand side of the images showing axial velocity (U_a), and the right hand side of images total velocity (U_t). The full, axial and total velocity profiles of test points 13 and 14 are shown due to the high level of asymmetry in the flow structure. For further reference, the vector maps of test points 9 to 14 are shown in Figure A. 3.

The flow structure and velocities of TP 9 are very similar to those observed in TP 1, this is to be expected as the premixed flow rates are the same. The structure of TP 10 however is very different to that of TP 2. Rather than increasing with diffusive flow rate, the width of the recirculation zone is unaltered from TP 9. Although total velocity is also unaltered, negative axial velocity is actually reduced.

The total and axial velocities in the HMFR of TP 11 are considerably lower than in TP’s 9 and 10. The flame is also displaying significant asymmetry, with the low velocity recirculation zone positioned left of the central axis of the burner. The increased addition of air continues to reduce the the velocity of the flow within the CRZ and the HMFR in TP 12, whilst the asymmetry becomes more exagerated. The diffusive flow rate in TP 13 has caused an almost complete reduction of the CRZ, although a region exists where axial velocities are just below 0. In TP 14 the CRZ no longer exists, with no flow in the negative axial direction. Instead the CRZ is replaced by a central region of high positive axial velocity, on the right of the central burner axis as shown. The likely cause of the CRZ destruction is combustion inside of the CRZ, causing an expansion of gases along the central axis of the burner. This gradually reduces the pressure differential that is required in order to induce recirculation.

Carbon dioxide has a very similar effect of flow structure to methane; as a result the progression caused by its diffusive injection between TP 15 to TP 22, which is shown in Figure 91, resembles the progression in Figure 89.

Test points 15 through 22 are displayed as in Figure 89, the left hand side of the images showing axial velocity (U_a), and the right hand side of images total velocity (U_t). For further reference, the vector maps of test points 15 to 22 are shown in Figure A. 4.

The flow structure of TP 15 resembles those of TP 1 and TP 9 where a narrow and low velocity recirculation zone exists. However, over the measured plane, the velocities of the flows in TP 15 are lower than those observed in TP’s 1 and 9. This is likely the result of slightly different initial flow rates, which can be caused by changes in ambient conditions or compressor pressure. As the proceeding alterations in flow structure are of interest, this inconsistency in initial condition is acceptable.

In TP 16 it can be seen that the CRZ increases in width as carbon dioxide is diffusively injected, the total and axial velocities within the CRZ are also increased. With methane this increase in velocity coincided with an elongation of the recirculation, with the region of reverse flow approaching the burner exit, with carbon dioxide this was not observed. A reduction in velocity in the HMFR is evident between TP 15 and TP 16.

Between TP 16 and TP 22, the increase in diffusive CO_2 flow rate results in an increase in the size of the CRZ, and axial and total velocities within it also increase, with the reverse flow region propagating slightly upstream. A reduction in total velocity is seen in the high momentum flow region; this is more evident in the vector plots in Figure A. 4 than Figure 91.

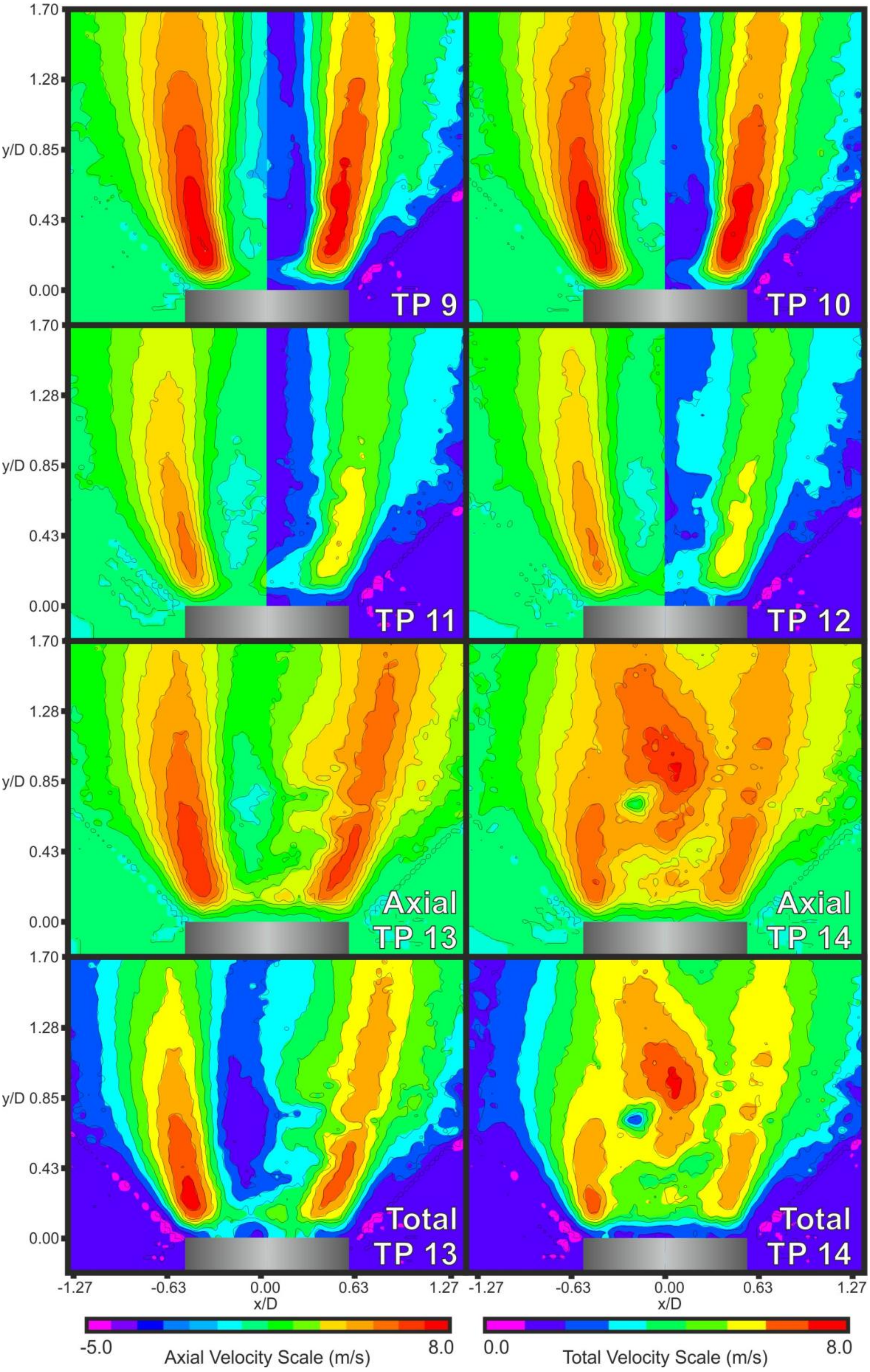

Figure 90: Scalar plots of TP 9 to TP 14 in the AGSB as detailed in Table 15, TP 9 to TP 12 the left half of each image indicates axial velocity, and the right half total velocity. TP 13 and TP 14 show full frames of axial and total velocity.

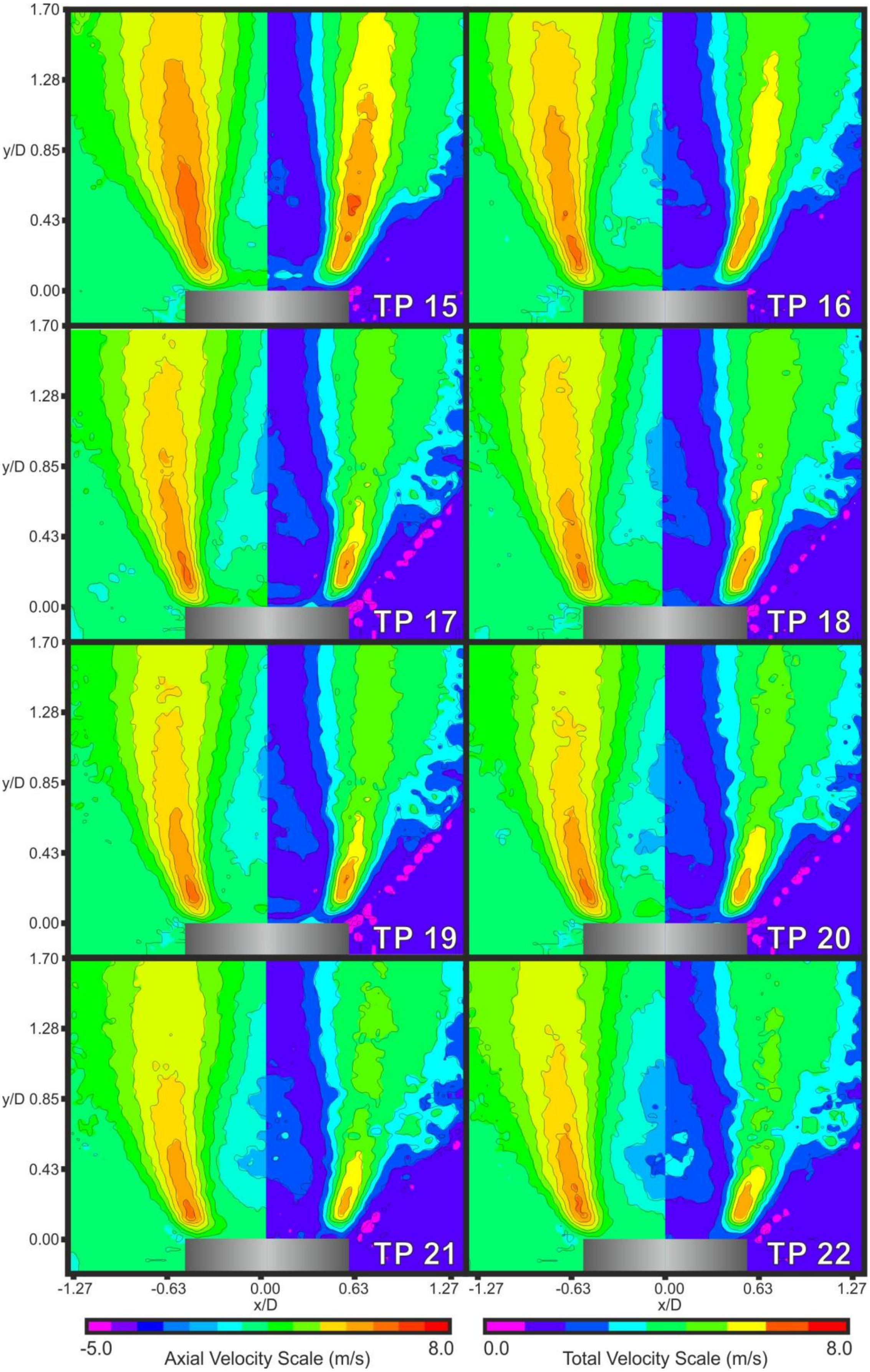

Figure 91: Scalar plots of TP 15 to TP 22 in the AGSB as detailed in Table 15, the left half of each image indicates axial velocity, and the right half total velocity.

This reduction is expected as the dilution effect of the CO_2 will reduce flame temperatures and the expansion of the gas. The observed reduction in axial velocity is less pronounced than the reduction in total velocity, which suggests that tangential-radial velocity is reduced significantly.

7.3.1 Effect on Turbulence

When CO_2 is diffusively injected, the low velocity boundary that exists between the CRZ and the HMFR appears to be wider than when CH_4 is injected. This is particularly evident when comparing vector plots of TP 5, with methane injection and TP 19, with carbon dioxide injection, which are shown in Figure 92. The CRZ is also visibly less defined in TP 19 than in TP 5, this is the result of higher levels of turbulence within the recirculation zone.

When all gases entering the burner are introduced tangentially, they are considered to be fully mixed prior to entering the combustion zone. With diffusive injection mixing is forced to occur in the region of the burner exit, resulting in unequal mixtures within the combustion zone.

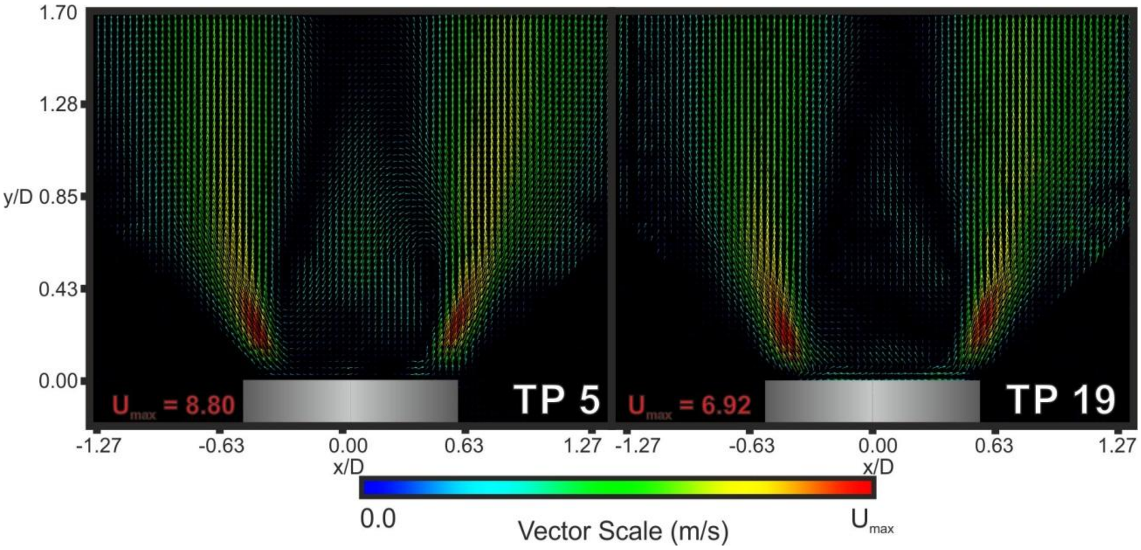

Figure 92: Vector plots of TP 5 and TP 19 in the AGSB with altered premix air flow rate and pilot CO_2 flow rate as detailed in Table 15, vectors indicate velocity and direction.

Simulation with CHEMKIN using the GRIMech 3.0 mechanism (Bowman et al., 1999) predicts that under laminar conditions the peak methane burning rate occurs at a rich equivalence ratio of approximately 1.1. Previous work has also utilised the combination of CHEMKIN and GRIMech 3.0 to show how CO_2 dilution reduces laminar burning rates (de Persis et al., 2013). With premixed gaseous fuel, combustion normally occurs at the boundary between the CRZ and the HMFR, where fresh reactants and hot products combine. The amalgamation of delayed mixing and unequal alterations in burning rates affect the ability of the flame to propagate toward the CRZ when CO_2 and CH_4 are injected.

The increase is in both size and mean velocity caused by CO_2 injection are not as prominent as with methane, and the CRZ has a less well defined shape as an irregular flame front develops at the boundary between it and the HMFR, as is reflected in the level of the turbulent intensity. Figure 93 represents the turbulent intensity of the flames in Figure 89 (b) and Figure 91 (b) in the axial-radial plane. The method for calculating turbulent intensity in the measured plane (I), at each measurement point in the PIV frame, is shown in Equation 7.1:

$$I = \frac{\sqrt{k}\mathrm{e}}{\sqrt{U_a^2+U_r^2}} \qquad \text{Eq (7.1)}$$

Where: *ke* = Turbulent Kinetic Energy (m^2/s^2)

$$ke = \frac{1}{2} \cdot \left({u'}_a^2 + {u'}_r^2\right) \qquad \text{Eq (7.2)}$$

And: u_a' = root-mean-square of turbulent velocity fluctuations in the axial direction (m/s)
u_r' = root-mean-square of turbulent velocity fluctuations in the radial direction (m/s)
U_a = axial velocity (m/s)
U_r = radial velocity (m/s)

The flame with diffusive methane injection has a very low turbulent intensity CRZ ($\bar{I}$ = 1.12 %) and HMFR ($\bar{I}$ = 0.32 %), with the intermediary boundary layer standing out due to the increased turbulent intensity ($\bar{I}$ = 3.07 %). The HMFR of the flame with diffusive carbon dioxide injection also has a very low turbulence level ($\bar{I}$ = 0.44 %). However the turbulent intensity of the CRZ (Ī = 2.93 %) and the intermediate boundary layer (Ī = 4.73 %) are significantly higher.

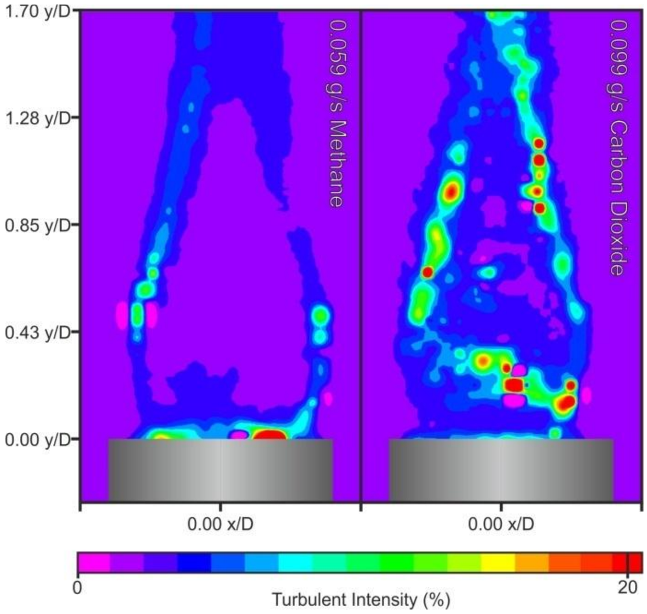

Figure 93: Comparison of turbulent intensity between flames in Figure 89 (b) and Figure 91 (b)

The velocities in the methane injected flame are greater than those of the carbon dioxide injected flame, which has to be considered when comparing turbulent intensity, which is dependent on local velocity. When comparing the root-mean-square of the turbulent velocity fluctuations in the axial-radial plane, the mean turbulent kinetic energy levels in the CRZ boundaries of the methane and carbon dioxide flames are actually very similar, $\bar{k}$ = 48.32 m^2/s^2 and $\bar{k}$ = 44.70 m^2/s^2 respectively, whereas the CRZ of the carbon dioxide injected flame displays significantly more turbulence ($\bar{k}$ = 15.22 m^2/s^2) than that of the methane flame ($\bar{k}$ = 0.93 m^2/s^2).

7.3.2 Effect on Momentum

The axial velocity profiles at y/D = 0.5 for all test points are plotted in Figure 94, a moving average of 5 data points is applied to smooth out local fluctuations from the global trend, for easier visual interpretation. In Figure 94 (a), the profile of test point 1 demonstrates the negative axial velocities of the CRZ on the central axis of the burner, at x/D = 0. The velocities increase either side of the burner axis, peaking at the centre of the HMFR before reducing again as the unconfined flow dissipates. The progressive introduction of methane produces incremental increases in the negative velocities in recirculation zone, whilst incrementally reducing the velocity within the high momentum flow region. The point at which the lines cross the axis also diverge from x/D = 0, indicating that the CRZ is increasing in width whilst the HMFR is getting narrower. The profiles in Figure 94 (b) demonstrate how the introduction of air causes an asymmetrical distortion, and ultimate destruction of the CRZ. Between test point 9 and TP 10 the changes in velocity resemble those seen due to the injection of methane. Between TP 10 and TP 13 there is a significant reduction in the peak velocity in the right hand side of the HMFR. The CRZ in the positive radial direction of the burner is also subject to a greater change than in the negative radial direction, with a large incremental increase in the axial velocity seen. Between test points 13 and 14 a dramatic change occurs, with the entire range of axial velocities becoming positive, and the peak velocity occurring at x/D = 0.

However, the axial velocity profiles of the flames with CO_2 injection, test points 15 to 22 shown in Figure 94 (c), display the same behaviour as observed with the injection of CH_4. The diffusive injection causes the positive axial velocities in the HMFR to decrease, whilst the negative axial velocities in the CRZ increase. There is also evidence of the CRZ becoming wider as the value of x/D when axial velocity equals 0 increases with diffusive flow rate, although the expansion is not as prominent as observed with methane injection.

The amount of stabilisation provided by the CRZ can be assessed by the Reverse Flow Momentum of the gases within it. Momentum is a product of velocity and mass, as the temperature, and as a result density of the gases within the CRZ and the reverse flow momentum are unknown. The volume of a particular measurement point is fixed, therefore, if variations in density are ignored, it is possible to compare the flow momentum by comparing velocity. As such, changes in Reverse Flow Momentum (RFM) at y/D = 0.5 are assessed by determining the areas below the x-axis; which are bound by the curves plotted in Figure 94.

The RFM of each test point is plotted against the isothermal geometric swirl number in Figure 95 (a), with the results of TPs 1 to 8 normalised against the fully premixed flame of TP 1. Similarly, TPs 9 to 14 are normalised against TP 9, and TPs 15 to 22 are normalised against TP 15.

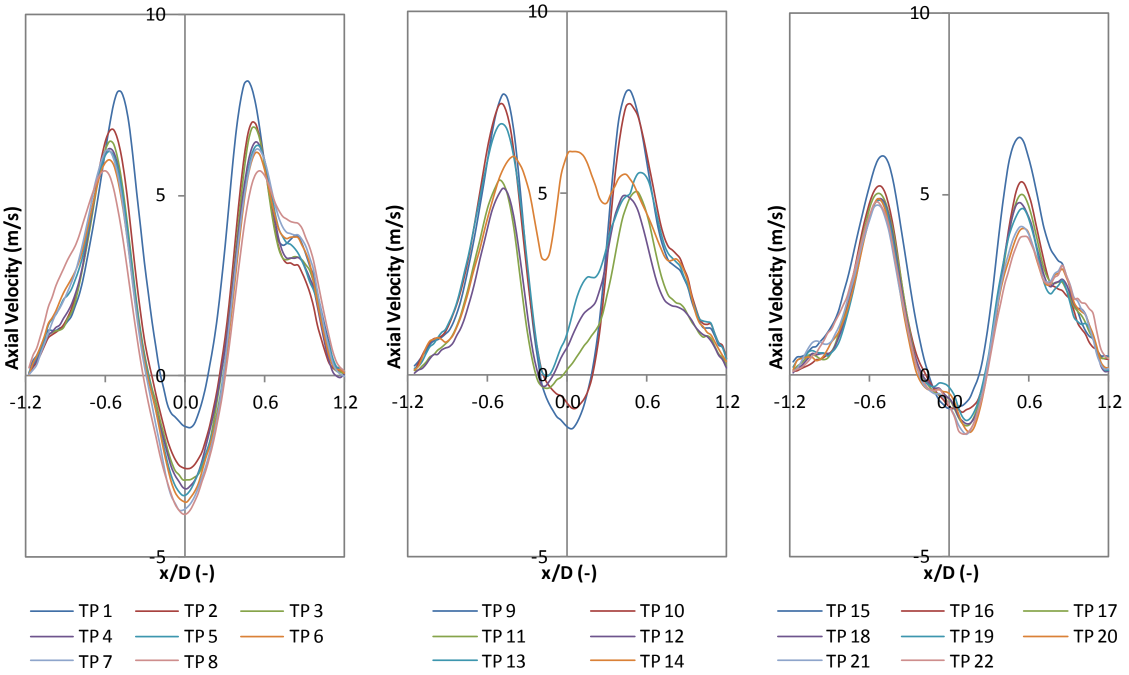

(a) *(b)* *(c)*

Figure 94: Axial velocities at y/D = 0.5 for test points detailed in Table 15 with the diffusive injection of (a) methane (b) air and (c) carbon dioxide.

The increased diffusive injection of methane, which reduces S_g in accordance with Equation 1, results in an increase in the RFM of the CRZ. Initially there is a very large increase, with the RFM of TP 2 2.3 times greater than TP 1, RFM then increases linearly with diffusive flow rate. The injection of diffusive CO_2 also increases the RFM of the CRZ; however the rate of increase is significantly less than observed with CH_4. Injection of air has an opposing effect, with RFM reducing as the amount of air injected increases. The effects on Positive Flow Momentum (PFM), which are calculated in a similar fashion to RFM at y/D = 0.5, with the area bound by the curve being positive of the x-axis, are shown in Figure 95 (b). The initial injection of both CO_2 and CH_4 both result in significant reductions in PFM, 21% and 26% respectively. The increase in diffusive flow rate then has very little effect on the PFM, with the range of reduction of CH_4 being 21-25% and the range of reduction of CO_2 being 26-32%.

The complete alteration in structures caused by the introduction of air means that there are two effects on the PFM. The gradual destruction of the CRZ means that the main reaction zone expands, and the velocity in the HMFR reduces. Conversely, the destruction of the CRZ means that the regions of positive flow increases, the velocity in these regions will also increase due to the axial momentum of the injected air.

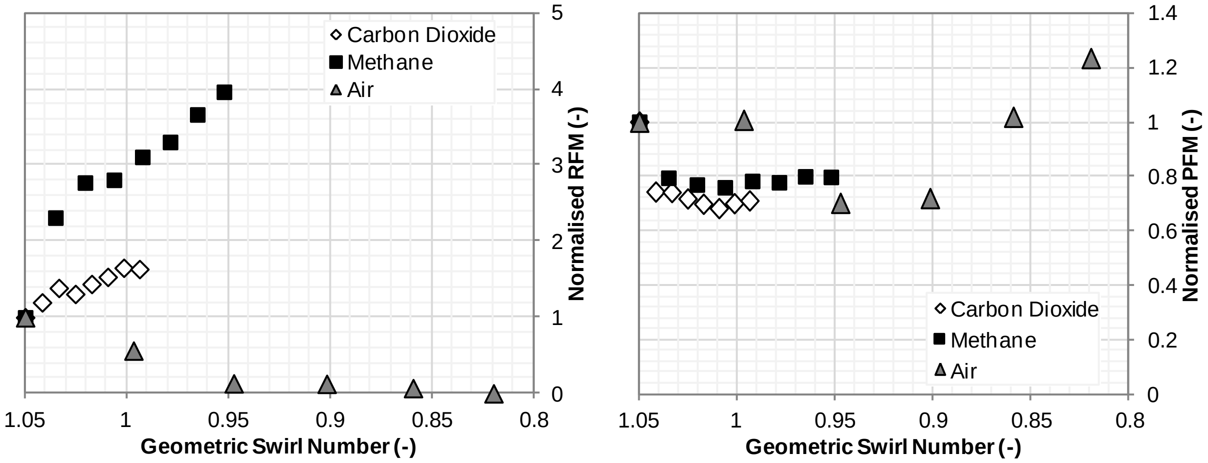

(a) (b)

Figure 95: The (a) reverse and (b) positive flow momentum for all test points at y/D = 0.5

The radial velocity profiles at y/D = 0.5 for all test points are plotted in Figure 96, again a moving average of 5 data points is applied. In Figure 96 (a) the radial velocities of TPs 1 to 8 are shown. Rotational symmetry about the origin is expected with regard to radial velocity, however, due to the slight asymmetry in the burner this is not seen, with TP 1 displaying entirely negative radial velocities within the CRZ. The increased injection of CH_4 causes, in a general, an incremental increase in radial velocity. TP 8 displays peak positive and negative values that are approximately twice those seen in TP 1.

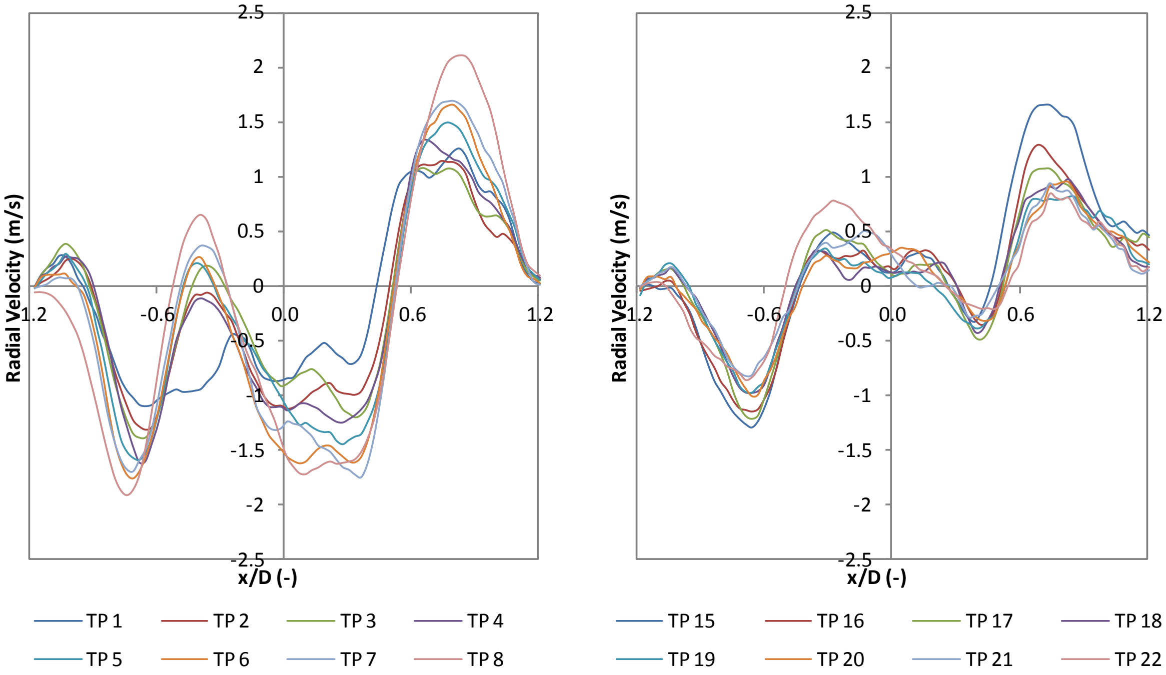

(a) (b)

Figure 96: Radial velocities at y/D = 0.5 for test points detailed in Table 15 with the diffusive injection of (a) methane (b) carbon dioxide

Coupled with the decrease in axial velocities these results suggest that the level of swirl has increased, which is why the RFM has increased relative to the PFM. The different effect is observed with the diffusive injection of CO_2; the radial plots for test points 15 to 22 are shown in Figure 96 (b). A slight change in flame structure means that velocities within the CRZ are all positive. The injection of CO_2 has very little effect on the radial velocity inside the recirculation zone, however, the radial velocity in the HMFR decreases.

7.3.3 Effect on the CRZ

Figure 97 shows the effect on the size and velocity of the central recirculation zone, based on the corresponding geometric swirl number. As in Figure 94, the results are normalised against the fully premixed case to allow easier comparison. Figure 97 (a) shows how both CO_2 and CH_4 injection cause the size of the CRZ to increase dramatically until reaching Sg = 1.03 for CO_2, 1.02 for CH_4, the size then increases at a steady linear rate. The injection of CH_4 has a greater effect on the size of the CRZ than CO_2 does, with the increased velocity of the recirculated flow resulting in the wider CRZ base seen in Figure 89 (b) and (c).

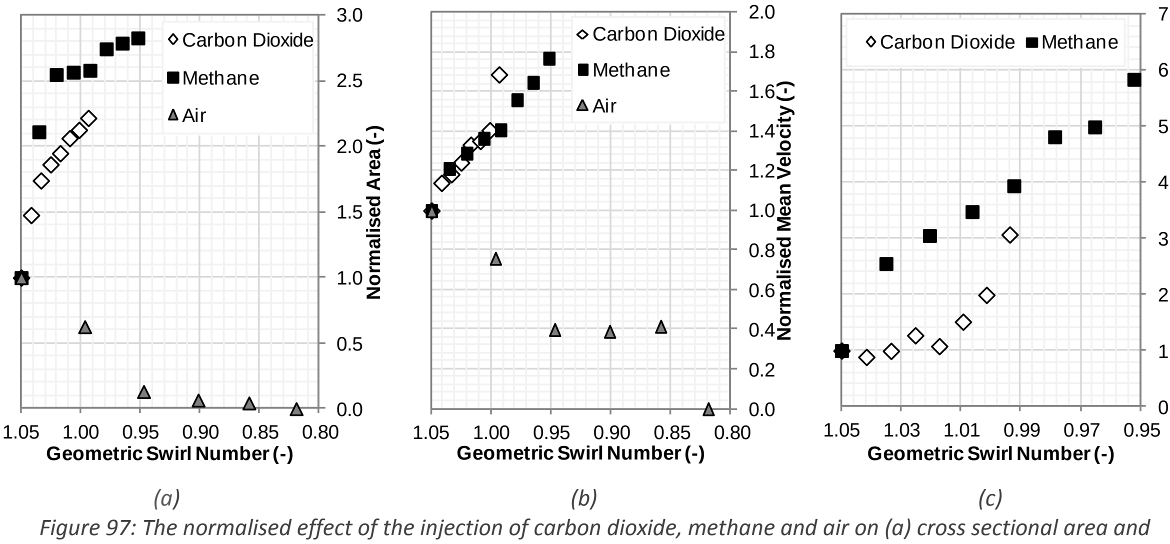

(a) (b) (c)

Figure 97: The normalised effect of the injection of carbon dioxide, methane and air on (a) cross sectional area and (b) mean velocity of the entire CRZ and (c) mean velocity of the CRZ centre

This increased velocity is demonstrated in Figure 97 (b) and (c), where the mean velocity in the CRZ in its entirety, and its central region are calculated. Over the region as a whole a steady linear increase, of a similar order, is observed with both CO_2 and CH_4, with all but one point falling on the same line. However, as the position and size of CRZ is calculated based on a component of the velocity, the mean velocity over the entire CRZ is influenced by the constraints applied. The central region, which is determined geometrically, is a better reflection on changes in velocity; a linear, six fold increase is observed with methane, whereas CO_2 only causes a threefold, non-linear, increase.

7.3.4 Effect on the HMFR

Another structure in a swirling flame is the high momentum flow region; this is high velocity region which contains the main reaction zone of the flame. In this study it is defined as being the region where axial velocity exceeds 3 m/s, as described in Appendix B.

The effect of pilot injection on the size and mean velocity in this region are shown in Figure 98, it is observed that the effects of CO_2 and CH_4 injection differ. As increasing diffusive flow rates of both CO_2 and CH_4 cause S_g to approach 1.02, a reduction in cross sectional area of the HMFR is observed, below values of S_g = 1.02, CO_2 continues to cause a reduction in HMFR area, whilst CH_4 results in a linear increase. A similar pattern is observed with regard to mean velocity, with both gases causing a reduction as S_g approaches 1.02, after which CO_2 continues to cause a reduction whilst CH_4 displays a trend of increasing velocity.

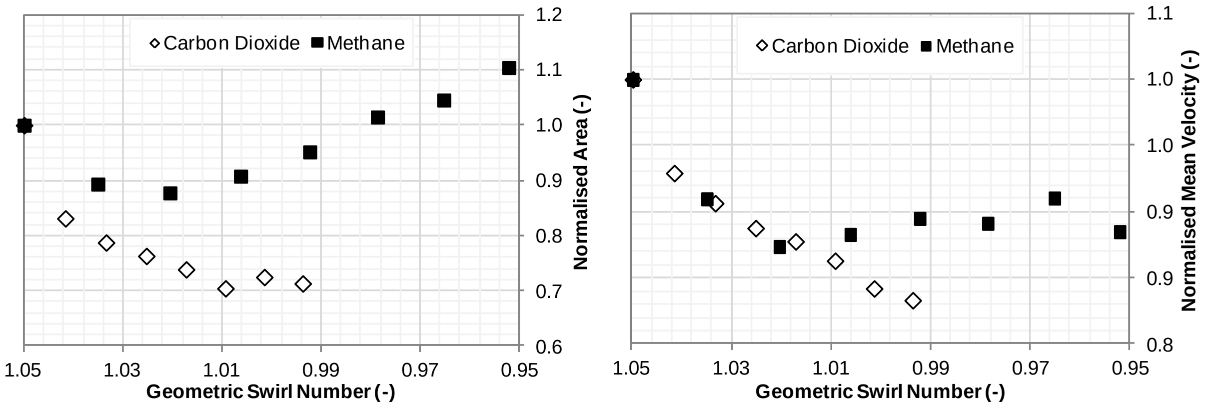

(a) *(b)*

Figure 98: The normalised effect of the injection of carbon dioxide and methane on (a) the cross sectional area and (b) mean velocity of the HMFR

Between S_g = 1.05 and 1.02, methane and carbon dioxide both cause a reduction in size and velocity of HMFR as the CRZ is increasing in size. Although the premixed air and fuel mixture was stoichiometric, the flame was unconfined, and in an environment with a large excess of oxidant. This facilitated a large increase in the volume of the structures when methane was injected, whereas the cooling effect of the carbon dioxide actually reduced structure volume.

There are four mechanisms that may result in flame flashback (Lieuwen et al., 2008, Fritz et al., 2004, Kroner, 2002, Kroner et al., 2003); upstream flame propagation of coherent structures and boundary layer flame propagation in particular are symptomatic of combustion induced vortex breakdown.

Previous studies have demonstrated that CIVB can be the result of the CRZ being 'squeezed' by the HMFR, which causes the CRZ to be displaced, upstream, ultimately surrounding a central body in the combustor (Dam et al., 2011a). An increase in equivalence ratio caused this process to occur. However, depending on burner design, and critically the level of turbulence of the flow, it may also be caused by a reduction in equivalence ratio (Lewis et al., 2014).

Regardless of equivalence ratio changes, the interaction between the CRZ and HMFR flow structures are important factors relating to the initiation of CIVB; and this interaction may be altered by the diffusive injection of gases.

For the results taken in these trials the interaction between the CRZ and HMFR is assessed as described in Equation 7.3, where R_M refers to the ratio of total RFM in the CRZ and total PFM in the HMFR; A_{CRZ}, A_{HMFR}, $\bar{U}_{CRZ}$, and $\bar{U}_{HMFR}$ refer to the cross sectional area and mean axial velocities of the CRZ and HMFR respectively:

$$R_M = \frac{A_{CRZ} \cdot \bar{U}_{CRZ}}{A_{HMFR} \cdot \bar{U}_{HMFR}} \qquad \text{Eq (7.3)}$$

The full size of the HMFR is cropped by the measurement area. However, local changes in the measured area are indicative of global changes. The increasing value of R_M as more diffusive fuel is added indicates that the RFM of the CRZ is increasing compared to the PFM of the HMFR, and as a result reducing the propensity of the flame to flashback due to combustion induced vortex breakdown. The normalised effects of carbon dioxide and methane on R_M are displayed in Figure 99.

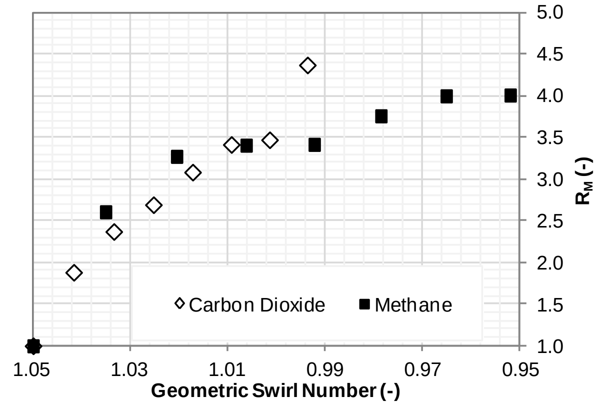

Figure 99: Normalised effect of the injection of carbon dioxide and methane on the ratio between RFM and PFM

The differing effects of CO_2 and CH_4 on the CRZ, and in particular the HMFR, compensate for each other to produce a very similar response on the flame structure as a whole. The introduction of methane causes a large initial rise in R_M as S_g approaches 1.02, at which point the rate of change reduces dramatically. When $1.05 < S_g < 1.02$ there is a strong change in R_M as the interaction between the CRZ and HMFR is altered, $S_g < 1.02$ the change in R_M becomes less significant as the increased flow rate of methane, causes an increase in global flame structure size and velocity.

Carbon dioxide produces a near linear response over the range of results, with highest value of R_M being greater than that of methane.

7.4 NO_x Reduction

The diffusive injection of methane and carbon dioxide augment flow structures in way that opposes the changes that are reported to occur during the process of combustion induced breakdown (Dam et al., 2011a). The process of CIVB was observed in the DIGCCC, and was reported in section 7.2.1.1. To prevent CIVB, the diffusive injection of carbon dioxide, as an alternative to methane, was investigated.

Running gas turbine combustors without the injection of a combustible pilot fuel is very beneficial with regard to the reduction of NO_x produced during the combustion process. It has been established that when operating the DIGCCC with both S50/50 and S85/15, steadily reducing pilot fuel induces combustion induced vortex breakdown, and as a result flashback. Suddenly turning off pilot fuel did not instantly cause flashback, however, the process of CIVB and propagation of the CRZ will eventually result in flame attachment. The introduction of CO_2 through the pilot injector as a method of flame stabilisation was investigated using the gas turbine combustor operating using S85/15. The flow rate of pilot methane used to stabilise the flame was 2.2 g/s. When volumetric flow rates of CO_2 equalling or exceeding that of the initial pilot methane were introduced, lean flashback was prevented from occurring. This was true whether the methane pilot fuel was turned off instantly or phased out, essentially stabilising the flame without the need to use methane. Details of the gas turbine combustor test points are listed in Table 16.

After it had been established that the flame was stable, the flow rate of CO_2 was steadily increased to 15.3 g/s, not only did the flame remain stable, but the injection of CO_2 actually reduced the tip temperature of the combustor, as shown in Figure 100 (a), which was measured at the extreme downstream location of the pilot swirler. This reduction further reduces the likelihood of flashback as the initial temperature and volume of gas leaving the pilot injector is reduced. As a consequence, the localised level of turbulence and burning rate of the mixture are also reduced. It is also potentially beneficial for the longevity of the combustor as damage that may result from exposure to high temperatures is less likely.

Despite the significant drop in burner tip temperature, from 399°C to 319°C, the temperature of the exhaust was not greatly affected, dropping from 1003°C to 980°C. This is important as exhaust temperature equates to the turbine inlet temperature, which is a determining factor in the efficiency of a gas turbine (Boyce, 2006). As the mass flow rate of carbon dioxide injected increased from 0 to 15.3 g/s, the burner tip temperature dropped 20.8 %, however the exhaust temperature, effectively the turbine inlet temperature, only dropped by 2.3 %.

Over this range of CO_2 flow rates, as the specific heat capacity of the CO_2 increases linearly with its mass flow rate, the temperatures are reduced linearly. The coefficients of determination for a linear relationship are 0.9654 and 0.9665 for exhaust and tip temperatures respectively. A drop in temperature is expected due to the addition of the carbon dioxide’s specific heat, which reduces the flame temperature as per Equation 4.4. The exhaust and burner tip temperatures are compared to the calculated adiabatic flame temperatures in Figure 100 (b). The burner tip temperature drops at a rate of 1.67 degrees per degree adiabatic flame temperature, whilst the exhaust drops at a rate of 0.49 degrees per degree adiabatic flame temperature. This shows that an effect greater than dilution is reducing the burner tip temperature.

Table 16: Details of DIGCCC test points

Mass Flow Rate (g/s)						
Premixed		Pilot		Ø	AFT (°C)	Re
S85/15	Air	CH_4	CO_2			
12.2	359.7	2.2	0.0	0.443	1490	62023
12.3	363.8	0.0	0.0	0.337	1300	62357
12.2	360.3	0.0	3.0	0.338	1296	62268
12.1	359.4	0.0	5.2	0.338	1291	62477
12.1	362.3	0.0	7.2	0.333	1277	63277
12.1	361.0	0.0	10.5	0.335	1274	63613
12.0	362.6	0.0	15.3	0.332	1258	64660

According to the extended Zeldovich mechanism (Warnatz et al., 1999), as flame temperatures increases so do emissions of NO_x, with reaction rates determined experimentally with reasonable accuracy (Owen et al., 1977). Introducing CO_2 into the gas turbine combustor reduces the emissions of NO_x by cooling the flame in two ways. Firstly, stabilising the flame when no pilot fuel is injected, this has a significant effect on the heat of the flame at the pilot injection point, and secondly by absorbing heat from the combustion process.

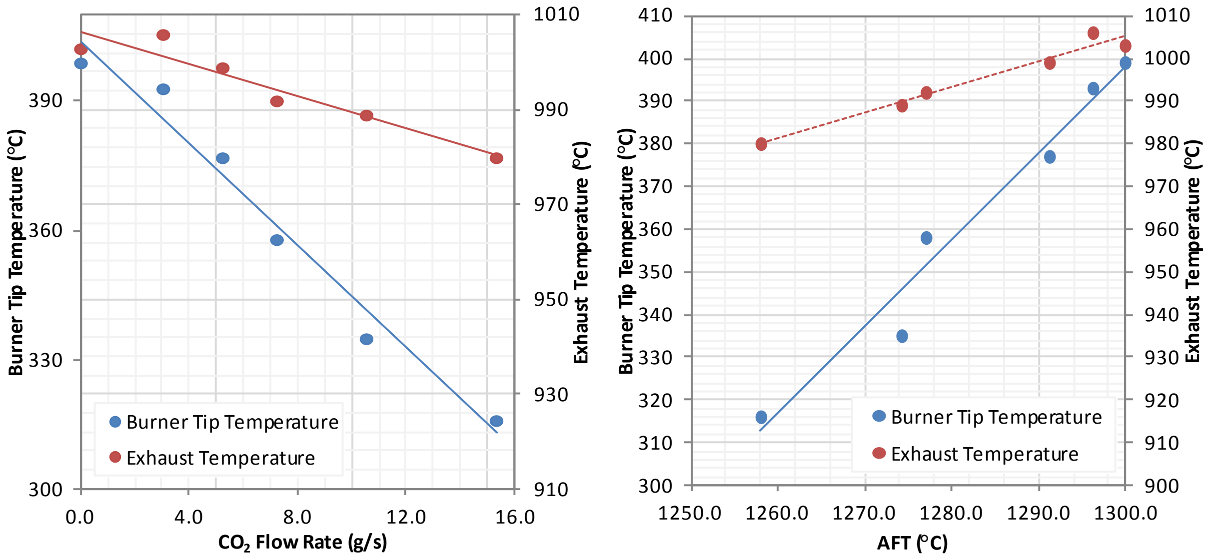

(a) (b)

Figure 100: Effect of CO_2 injection on combustor temperatures with regard to (a) CO_2 flow rate and (b) adiabatic flame temperature

When methane pilot fuel was used, the combustion process produced 17.29 ppmv of NO_X. When the pilot fuel was switched off and not replaced by a similar amount of CO_2 the NO_X produced dropped to 10.26 ppmv, a 40.6% decrease. The injection of CO_2 saw the NO_X levels drop further, with 8.12 ppmv recorded when the amount of CO_2 equalled 15.3 g/s, as the results in Figure 101 demonstrate.

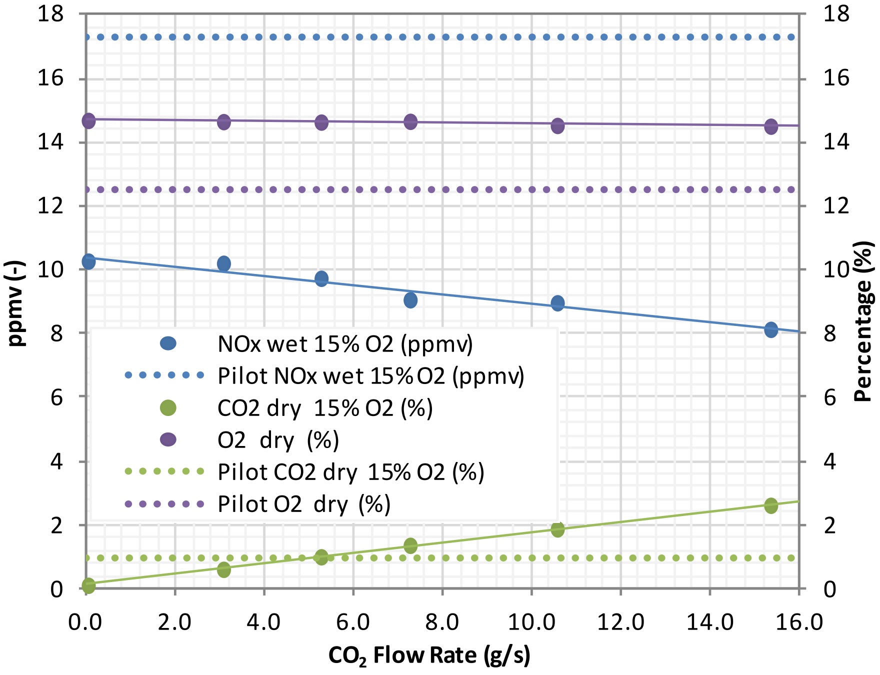

Figure 101: Effect of CO_2 injection on exhaust gases

Disregarding the decrease in NO_X that resulted from turning off the pilot fuel, the drop in NO_X caused by CO_2 addition was 20.9%. The addition of the CO_2 will increase the mass of the exhaust gases, so this drop is due partly to the dilution effect. However, when compensating for dilution, the reduction of NO_X caused by CO_2 addition is still 17.9%. When the effects of replacing the methane pilot with 15.3 g/s of CO_2 are considered, the total reduction in NO_X observed was 51.0%.

During these trials the mass flow rate of both Syngas and air was kept constant (within 1.1%), as it would be in a gas turbine, therefore the injection of carbon dioxide does not alter the oxidant to fuel ratio of the reactant mixture. As such, the percentage of oxygen in the exhaust increases from 12.5% to 14.5% when the pilot fuel is switched off, after that it also remains constant within ±1%. The amount of unburned hydrocarbons in the exhaust showed a reduction with CO_2 injection, but the results do not produce a trend strong enough to draw any firm conclusions.

7.5 Discussion of Burner Dissimilarity

It is important to note the differences between the two burners used for this section of experimentation, the DIGCCC and the AGSB. Whilst both are swirl combustors with similar exit configurations, the generic burner is of a radial type and the gas turbine burner is of an axial type, they are also using different fuels.

The high turbulence generated, along with the large pilot injector in the gas turbine burner results in high resistance to blowoff, whereas the low turbulence and exit geometry of the generic burner makes it very resistant to flashback. This difference is exacerbated by the different fuels, with the Syngas used in the gas turbine combustor having a significantly higher burning rate than that of methane, which was used in the generic burner. One of the results of these differences is that in terms of equivalence ratio, the operating ranges are very different, and the natures of extinction events are also very different. Due to the similarity between the flow structures produced by the generic burner and the gas turbine combustor, both of which are typical of those seen by swirl combustors, it is assumed that the structure augmentation that occurred in the generic burner due to the injection of CO_2, and was confirmed with PIV analysis, is representative of the effect of CO_2 injection in the gas turbine. Without performing an analysis of the gas turbine flow patterns under combustion conditions this assumption cannot be confirmed.

7.6 Chapter Summary

This chapter details experimentation into flame structure augmentation using two burners. The burners are of different type, one axial one radial, and operate under very different turbulent levels. Despite this, two types of flashback have been identified with both burners, and the ability to augment flame structure and stability with the diffusive injection of carbon dioxide and methane was observed with both burners.

7.6.1 Combustion Induced Vortex Breakdown

The DIGCCC, with two different compositions of Syngas, showed a propensity for lean flashback. This is unexpected, as flashback normally occurs when increasing equivalence ratio causes local flame speed to exceed local flow velocity. However, the central recirculation zone can extend upstream and cause early onset flashback (Lieuwen et al., 2008, Subramanya and Choudhuri, 2007, Thornton et al., 2007). The high turbulence nature of the DIGCCC, combined with the bluff body like pilot swirler (Gerrard, 1966) and the high burning velocity of the air-fuel mixtures inhibited blowoff. Despite the presence of the injector, the length of the exit nozzle means that the primary flow stabilisation is aerodynamic, which is preferable for CIVB initiation (Noble et al., 2006).

Two final flame positions were seen after flashback; where the flame propagated in the main fuel mixture via boundary layer propagation, as previously observed by Syred et al. (2012) and Abdulsada et al. (2011), and when the CRZ attached to the central injector, as previously observed by Valera-Medina (2009) and Dam et al. (2011a). Both were preceded by combustion induced vortex breakdown, images taken by Konle and Sattelmayer (2008) showed how CIVB caused the CRZ to extend upstream, toward where the central injector would be located, facilitating the flame attachment that was observed. The work by Fritz et al. (2001) showed how this propagation resulted in the width of the flame increasing at the nozzle exit, which allowed the observed propagation through the shear and boundary layers.

Augmentation of the CRZ and HMFR pairing, caused by changes in premix air flow, was demonstrated by performing PIV analysis on the AGSB. It has been reported that HMFR intensity is critical to the process of CIVB (Dam et al., 2011a), and in this work it was shown to increase relative to the intensity of the CRZ as air flow reduced the equivalence ratio of the flame. Initial tests involving the diffusive injection of CO_2 showed an increase in intensity and size of the CRZ relative to the HMFR (Lewis et al., 2014), opposing the effects seen previously.

7.6.2 Structure Augmentation

Experimentation using the AGSB, and a PIV system effectively used to identify flow structures in previous research (Abdulsada, 2012, Valera-Medina et al., 2009, Valera-Medina et al., 2011b), demonstrated how the diffusive injection of different gases into a premixed methane flame altered the coherent structures in its flow field.

The injection of both methane and carbon dioxide resulted in an increase in cross sectional area and velocity of gases within the central recirculation zone. As the flame is unconfined it will entrain air and become fuel lean (Delichatsios, 1987), as such the diffusive injection of methane will increased the flame speeds (Egolfopoulos et al., 1989) and temperatures (Van Maaren et al., 1994) within the swirling flows, effecting flame propagation and hot gas expansion. Radial momentum increased whilst axial momentum decreased, increasing the volume of the recirculated gases when methane was injected. This leads to an expansion of the recirculation zone near the burner exit and a stable, well defined boundary between the CRZ and high momentum flow region. The injection of carbon dioxide reduced the flame speed (Natarajan et al., 2007) and temperature (Zheng, 2011) of gases within the flame, inhibiting flame propagation and reducing the hot gas expansion. Both axial and radial momentums were proportionally reduced, resulting in the increased mass flow rate increasing the size and velocity of the recirculation zone.

Methane and carbon dioxide had differing effects on the high momentum flow region of the flame. When flow rates of the diffusively injected gases produced isothermal geometric swirl numbers above 1.02, the size and velocity of the HMFR decreased, due to CH_4 increasing the radial momentum relative to the axial momentum, and CO_2 decreasing flame temperatures. When methane flow rates resulted in $S_g < 1.02$, thus the cumulative effect of increasing swirl and flame temperature resulted in an increase in HMFR size and velocity.

Despite differing effects on the level of swirl and flame temperature, the actual effect on the reverse flow momentum of the CRZ compared to the positive flow momentum of the HMFR was the same. The expansion of the CRZ compared to the HMFR opposes the changes in flame structure that result in combustion induced vortex breakdown (Dam et al., 2011a), therefore the diffusive injection of either CH_4 or CO_2 could be used to as a measure to mitigate CIVB.

The diffusive injection of air was also investigated. Its effect on the flow structures heavily contrasted those of CO_2 and CH_4, reducing the size and velocity of the CRZ before completely preventing recirculation occurring. Although the overall result would almost certainly reduce the likelihood of CIVB occurring, the destruction of the

CRZ would result in an inherently unstable flame that would be highly susceptible to blowoff.

7.6.3 Reducing Temperature and Emissions

As well as displaying a propensity for lean flashback, the gas turbine combustor proved to be consistently unstable without a methane pilot, a problem which has been observed by others (Dhanuka, 2008). This is undesirable due to a reliance on methane or natural gas, and the increased emission of nitrous oxides caused by the increased flame temperature via the Zeldovich mechanism (Warnatz et al., 1999). Lack of methane pilot resulted in a temporarily quasi-stable flame; however NO_x emissions were reduced by 40.6%. The injection of CO_2 through the pilot of the gas turbine combustor continued to reduce the levels of NO_x emitted, as has been reported by others, including Lee et al. (2012) and Khalil et al. (2012).

The maximum amount of CO_2 injected, which was dictated to by the choke point in the rig delivery line rather than flame stability, equated to 126% the mass flow rate of the fuel. With maximum CO_2 injection the reduction of NO_x was 50.8%. Modifications to the CO_2 delivery line would allow further reductions.

The temperature of the burner tip was also reduced significantly, by 20.8%, which is beneficial for burner longevity. The exhaust temperature only dropped by 2.3%, as this equates to turbine inlet temperature, which defines efficiency (Boyce, 2006), this is also advantageous. The CO_2 reduces the adiabatic flame temperature, the burner tip temperature reduces at a rate 1.67 times greater than adiabatic flame temperature whilst exhaust temperature reduced at rate 2.04 times smaller than AFT.

Chapter 8: Conclusions and Further Work

8.1 Conclusions

The effect of variations in fuel composition were assessed, and methods of stabilisation were investigated to compensate for the changes in fuel property that result. The following conclusions are drawn:

- A close relationship exists between producer gas composition and gasifier throat temperature. As a consequence a relationship exists between gasifier throat temperature and certain combustion properties of the producer gas.
- Although noteworthy variations in composition occurred in modelled results, up to 50.1% in hydrogen content for example, the lower heating value and stoichiometric air-to-fuel ratio of the fuel remain steady, within 7.7% and 6.7% respectively.
- Due to fluctuations in hydrogen content, the laminar flame speed varies considerably, by up to 52.2%, which can have a striking effect on stability limits.
- Large fluctuations in hydrogen content also cause changes in Wobbe index, although proportionally they are far smaller than flame speed, only up to 14.0%.
- At atmospheric pressure and ambient temperature, only when the equivalence ratio of the producer gas in question equals 1.16 can both S_L and WI be simultaneously replicated. Similarly, a singular equivalence ratio will exist under different conditions or for other producer gases.
- For variations in fuels where the main changes in constituents are hydrocarbons, and inerts are not present, a near linear relationship exists between WI and S_L, even when alterations in AFR are considered. This supports WI being a good way to specify acceptable fuels.
- For variations in syngas or natural gas composition, where there are percentages of inerts in the fuel, the relationship between WI and S_L displays less linearity. This is particularly true when alterations in AFR are considered. Therefore WI is not be a suitable method of specifying fuel acceptability with regard to stability.

- For different fuels, equitable WI can have incredibly large variations in S_L. When WI was equal to 46 MJ/m^3 and equivalence ratio was 1, laminar flame speeds of the methane/propane and hydrogen/nitrogen blends simulated were 94.8 cm/s and 837.6 cm/s respectively, a discrepancy of 883.5%.
- Under isothermal conditions two mechanisms were found to define the acoustic response, Helmholtz resonance, and the precession of structures.
- The frequency and amplitude at which the structures rotated were shown to increase as the level of swirl imparted on the flow, (characterised by geometric swirl number), increased.
- The frequency and amplitude at which the structures rotated were shown to increase as the flow rate of air and exit nozzle Reynolds number increased.
- The frequency of Helmholtz resonance demonstrated a tendency to reduce as flow rate increased.
- The frequency of structure rotation and Helmholtz resonance for a particular burner configuration can be characterised via the use of the dimensionless Strouhal and Roshko numbers respectively.
- For a confined burner, the dominant mechanism of acoustic response is dependent on flow rate, with two transition points occurring as exit nozzle Re increases:
    - The first transition point occurs when vortex breakdown, which is a function of S_g and Re occurs, causing oscillations at the frequency of the resulting structures.
    - The second transition point occurs when the amplitude of oscillations caused by precessing structures exceeds the amplitude of oscillations caused by resonance.
- Under combustion conditions three mechanisms are found to define the acoustic response, Helmholtz resonance, the precession of structures and unsteady heat release.
- High amplitude, low frequency oscillations near the lean stability limit were found to be the result from repeated extinction/ignition events. As such these indicate impending blowoff.

- The amplitude of oscillations at the frequency of the precessing structures increased when approaching the rich stability limit. As such these indicate impending flashback.
- The amplitude of oscillations due to resonance are strong during both stable operation, and approaching the rich stability limit. Oscillations dominated acoustic response prior to flashback occurring in the gas turbine combustor.
- The amplitude and coherence of the acoustic response is greatest when a single mechanism is dominant.
- Flashback of two syngas fuels was observed when a leaning of the combustible air and fuel mixture occurred in the development gas turbine combustor.
- The types of flashback have been indentified in two burners with differing swirl type, flow regime and fuel.
- The flashback was the result of CIVB.
- After the initiation of the CIVB process, flashback continued in one of two ways, via boundary layer propagation, and via the CRZ attaching to the central pilot swirler.
- An increase in HMFR velocity is linked to the contraction of the CRZ, and the initiation of CIVB.
- The diffusive injection of carbon dioxide effects flow structures in a way that inhibits CIVB initiation.
- The diffusive injection of both methane and carbon dioxide causes the reverse flow momentum of the CRZ to increase relative to the positive flow momentum of the HMFR.
- The diffusive injection of carbon dioxide has the potential to increase the stability limits of flames with high hydrogen content by inhibiting flashback.
- The diffusive injection of air results in flame propagation along the central axis of the burner, preventing the recirculation of product gases.
- Diffusive carbon dioxide injection reduces burner tip temperature and NO_X emissions.

8.2 Recommendations for Further Work

This work was performed on a variety of burners at the Gas Turbine Research Centre. Performing all the work on a single burner with all diagnostic techniques available at all times would have been preferable, but was not possible. With the commission of a new Pressurised Generic Swirl Burner (PGSB), which is detailed in Appendix C, it now is. Additional diagnostics equipment is also now available. As an extension of this work, the following research is recommended:

- The acoustic monitoring of flames in order to infer flame condition is a novel application of thermo acoustic analysis. A control system can be deployed as part of the HPCR, based on the coherence and amplitude of the thermo-acoustic signal. The aim being that it would respond to alterations in fuel composition to prevent flame extinction, and optimise combustion. Changes in fuel composition could be achieved using the diluting of methane, as discussed in chapter 4, using a gas mixing facility.
- The use of different diluents diffusively injected has been shown to improve flame stability. With the PGSB it is possible to investigate the effect of further diluents on flame stabilisation and emission reduction, such as nitrogen or steam, as well as different modes of injection, i.e. diffusive or premixed could be investigated. Using the HPCR and newly commissioned PGSB dilution can be investigated under pressurised conditions, where there this is a lack of literature. The simultaneous use of Particle Laser Velocimetry (PIV) and Planar Laser-Induced Fluorescence (PLIF) can be used to ascertain effects on flow patterns and flame fronts respectively, radial PIV can be used to determine the effect on swirl number (S). Gas analysis to establish the potential environmental benefits achieved through reduced emissions would also of great benefit. Flame temperature measurements would also be useful in order to more accurately determine changes in positive and reverse flow momentum. Thermo-acoustic pressure fluctuations under varying conditions can also offer an insight into what effect is had on the stability of the flame.

References

ABBOTT, D., BOWERS, J. & JAMES, S. 2012. The Impact of Natural Gas Composition Variations on the Operation of Gas Turbines for Power Generation. *The Future of Gas Turbine Technology 6th International Conference.* Brussels.

ABDULSADA, M. 2012. *Flashback and Blowoff Characteristics of Gas Turbine Swirl Combustor.* PhD, Cardiff University.

ABDULSADA, M., SYRED, N., BOWEN, P., O'DOHERTY, T., GRIFFITHS, A., J. & MARSH, R. 2011. Effect of Swirl Number and Fuel Type upon the Blowoff Limits in Unconfined and Confined Swirl Combustors. Newcastle.

ABDULSADA, M., SYRED, N., BOWEN, P., O'DOHERTY, T., GRIFFITHS, A., J., MARSH, R. & CRAYFORD, A. 2013. Effect of exhaust confinement and fuel type upon the blowoff limits and fuel switching ability of swirl combustors". *Applied Thermal Engineering,* 53**,** 348-357.

AEROSPACE RECOMMENDED PRACTICE 1996. Procedure for the calculation of basic emissions parameters for aircraft turbine engines. *Aerospace Recommended Practice ARP 1533*.

AL-ABDELI YM, M. A. 2003. Stability characteristics and flowfields of turbulent non-premixeed swirling flames. *Combustion Theory and Modelling,* 7**,** 731-766.

AL-ABEDI YM, M. A. 2003. Recirculation and flowfield regimes of unconfined non-reacting swirling flows. *Exp Therm Fluid Sci,* 27.

ALESEENKO, S., KUIBIN, P., OKULOV, V. & SHTORK, S. 1999. Helical Vortex in Swirl Flow. *Journal of Fluid Mechanics,* 382**,** 195-243.

ALLISON, P., DRISCOLL, J. & IHME, M. 2013. Acoustic characterization of a partially-premixed gas turbine model combustor: Syngas and hydrocarbon fuel comparisons. *Proceedings of the Combustion Institute,* 34**,** 3145-3153.

AMERICAN GAS ASSOCIATION 1946. Bulletin No. 36.

ANIS, S. & ZAINAL, Z. A. 2011. Tar reduction in biomass producer gas via mechanical, catalytic and thermal methods: A review. *Renewable and Sustainable Energy Reviews,* 15**,** 2355-2377.

ANSALDO ENERGIA 2010. State of the art IGCC Power Stations. Document ISV/TMC/10.002.

ASSADI, M. & OHLSSON, F. 2008. Ny gasturbinteknik slutrapport Elforsk-projektet *Elforsk Report 08:16.*

ASTM Standard Specification for Diesel Fuel Oils. West Conshohocken, PA: ASTM International.

ASTM 1998. ASTM D388: Standard Classifcation of Coals by Rank.

BAGDANANVICIUS, A., SHELIL, N., SYRED, N., GRIFFITHS, A., J. & BOWEN, P. 2010. Premixed swirl combustion and flashback analysis with hydrogen/methane mixtures. *AIAA 47th Aerospace Sciences Meeting.* Florida.

BAKER, R. W. 2002. Future Directions of Membrane Gas Separation Technology. *Industrial & Engineering Chemistry Research,* 41**,** 1393-1411.

BAKEWELL, S. 2012. *U.K. Government Lifts Ban on Shale Gas Fracking* [Online]. Bloomberg News. Available: http://www.bloomberg.com/news/2012-12-13/u-k-government-lifts-ban-on-shale-gas-fracking.html [Accessed 13th February 2014].

BAL´AˇS, M., LIS´Y, M. & STELCL, O. 2012. The Effect of Temperature on the Gasification Process. *Acta Polytechnica,* 52**,** 7-11.

BALACHANDRAN, R., AYOOLA, B. O., KAMINSKI, C. F., DOWLING, A. P. & MASTORAKOS, E. 2005. Experimental investigation of the nonlinear response of turbulent premixed flames to imposed inlet velocity oscillations. *Combustion and Flame,* 143**,** 37-55.

BALLESTER, J. & GARCIA-ARMINGOL, T. 2010. Diagnostic Techniques for the Monitoring and Control of Practical Flames. *Progress in Energy and Combustion Science,* 36**,** 375-411.

BARATIERI, M., BAGGIO, P., BOSIO, B., GRIGIANTE, M. & LONGO, G. A. 2009. The use of biomass syngas in IC engines and CCGT plants: A comparative analysis. *Applied Thermal Engineering,* 29**,** 3309-3318.

BASS, M. 1995. *The Handbook of Optics. 2nd Edition*, McGraw Hill.

BASU, P. 2010. *Biomass Gasification and Pyrolosis: Practical Design*, Elsevier.

BEÉR, J. M. & CHIGIER, N. A. 1972. Combustion Aerodynamics. *Applied Science*.

BELLOWS, B. D., BOBBA, M. K., FORTE, A., SEITZMAN, J. M. & LIEUWEN, T. 2007. Flame transfer function saturation mechanisms in a swirl-stabilized combustor. *Proceedings of the Combustion Institute,* 31**,** 3181-3188.

BENDER, W. 2012. *Lean Premixed Combustion* [Online]. Available: http://www.netl.doe.gov/technologies/coalpower/turbines/refshelf/handbook/3.2.1.2.pdf [Accessed 20th February 2013.

BERGH, H. & TIJDEMAN, J. 1965. Theoretical and Experimental Results For The Dynamic Response of Pressure Measuring Systems, Report NLR-TRF.238. Amsterdam: National Aero- and Astronautical Research Institute.

BEYCHOK, M. Coal gasification and the Phenosolvan process. American Chemical Society 168th National Meeting, 1974 Atantic City.

BLESINGER, G., KOCH, R. & BAUER, H. J. 2010. Influence of flow field scaling on flashback of swirl flames. *Experimental Thermal and Fluid Science,* 34**,** 290-298.

BOWMAN, C. T., FRENKLACH, M., GARDINER, W. C. & SMITH, G. P. 1999. *The “GRIMech 3.0” chemical kinetic mechanism* [Online]. Available: www.me.berkeley.edu/grimech [Accessed 20th January 2012].

BOYCE, M. 2006. *Gas Turbine Engineering Handbook,* Houston, Texas, U.S.A., Gulf Proffesional Publishing.

BRAMMER, J. G. & BRIDGWATER, A. V. 2002. The influence of feedstock drying on the performance and economics of a biomass gasifier–engine CHP system. *Biomass and Bioenergy,* 22**,** 271-281.

BRENNAN, C. 2005. *Fundementals of Multiphase Flow,* Cambridge, Cambridge University Press.

BROWN, M. Changing the way the world makes electricity. Distributed Generation Conference, 2002 Sao Paolo.

BRUNDISH K. D, MILLER M. N, WILSON C. W, MACQUISTEN M & J., M. 2002. Internal traversing of combustion species inside a methane fuelled DLE combustor. *ASME Turbo Expo 2002: Power for Land, Sea, and Air.* Amsterdam, The Netherlands.

BURBANO, H. J., PAREJA, J. & AMELL, A. A. 2011. Laminar burning velocities and flame stability analysis of H2/CO/air mixtures with dilution of N2 and CO2. *International Journal of Hydrogen Energy,* 36**,** 3232-3242.

CANDEL, S. 1992. Combustion Instabilities Coupled by Pressure Waves and Their Active Control. *Proceedings of The Combustion Institute,* 24**,** 1227-1296.

CANDEL, S. 2002. Combustion Dynamics and Control: Progress and Challenges. *Proceedings of the Combustion Institute,* 29**,** 1-28.

CASTEN, T. 2003. Energy Policy, Income Growth and Ecocide. *Journal of Foreign Affairs*.

CENTRAL INTELLEGENCE AGENCY 2013. World Factbook.

CHANAUD, R. 1962. Observations of oscillatory motion in certain swirling flows. *Journal of Fluid Mechanics,* 21**,** 111.

CHENG, R. K., LITTLEJOHN, D., STRAKEY, P. A. & SIDWELL, T. 2009. Laboratory investigations of a low-swirl injector with H2 and CH4 at gas turbine conditions. *Proceedings of the Combustion Institute,* 32**,** 3001-3009.

CHOUDHURI, A. 2012. *Effects of Combustion-Induced Vortex Breakdown on Flashback Limits of a Syngas Fuelled Swirl Combustor* [Online]. Available: <http://www.netl.doe.gov/publications/proceedings/10/utsr/presentations/wednesday/Choudhuri.pdf> [Accessed 28th September 2012].

CHU, M., NOGAMI, H. & YAGI, I. 2004. Numerical analysis on blast furnace performance under operation with top gas recycling and carbon composite agglomerates charging. *ISIJ International,* 44**,** 2159-2167.

CLAYPOLE, T. C. 1980a. Coherent structures in swirl generators and combustors. *Proceedings of the ASME symposium vortex flows, winter annual meeting.* Chicago: Library of Congress catalogue card.

CLAYPOLE, T. C. 1980b. *PhD Thesis.*

CLAYPOLE, T. C. & SYRED, N. 1980. The precessing vortex core in swirl stabilised combustors. *La Rivista dei Combustili,* 34**,** 150-65.

CLAYPOLE, T. C. & SYRED, N. 1983. Construction, Operation and Optimisation of a Furnace for the Ecomomic Burning of Low Calorific Value Gases. *CEC Energy Conservation and Development Program.* Cardiff.

CLAYPOLE, T. C. & SYRED, N. 1985. Construction, Operation and Optimisation of a Furnace for the Ecomomic Burning of Low Calorific Value Gases. *CEC Energy Conservation and Development Program.* Cardiff.

COCKROFT, J. & KELLY, N. 2006. A comparative assessment of future heat and power sources for the UK domestic sector. *Energy Conversion and Management,* 47**,** 2349-2360.

COGHE, A., SOLERO, G. & SCRIBANO, G. 2004. Recirculation phenomena in a natural gas swirl combustor. *Experimental Thermal and Fluid Science,* 28**,** 709-714.

COLE-PARMER. 2006. *Variable Area Flowmeters Tech Info* [Online]. Available: http://www.coleparmer.co.uk/TechLibraryArticle/813 [Accessed 18th February 2014].

COLORADO STATE UNIVERSITY. 2007. *IC engine four-stroke cycle* [Online]. Available: http://www.engr.colostate.edu/~dga/mech324/handouts/cam_stuff/four_stroke_cycle.jpg.

COYLE, D., DE LA VEGA, F. & DURR, C. 2007. Natural gas Sepcification Challenges in the LNG Industry. *15th International Conference and Exhibition on Liquefied Natural Gas.* Barcelona, Spain.

CULICK , F. & YANG, V. 1995. Overview of Combustion Instabilities in Liquid-Propellant Rocket Engines'. *Progress in Astronautics and Aeronautics*.

CUSTOMHOUSE, T. 2012. *Kelvin-Helmholtz Instability* [Online]. WordPress. Available: http://thecustomhouse.wordpress.com/2012/01/20/kelvin-helmholtz-instability/ [Accessed 17th February 2014].

DAM, B., CORONA, G., HAYDER, M. & CHOUDHURI, A. 2011a. Effect of Syngas Composition on Combustion Induced Vortex Breakdown (CIVB) Flashback in a Swirl Stabilized Combustor. *Fuel,* 90**,** 3274-3284.

DAM, B., LOVE, N. & CHOUDHURI, A. 2011b. Flashback propensity of syngas fuels. *Fuel,* 90**,** 618-625.

DANISH ENERGY AGENCY. 2011. *Wind Power: Key Figures and Statistics* [Online]. Copenhagen: DEA. Available: http://www.ens.dk/en-US/supply/Renewable-energy/WindPower/Facts-about-Wind-Power/Key-figures-statistics/Sider/Forside.aspx [Accessed 25th May 2011].

DANTEC. 2006. *Measurement Principles of PIV* [Online]. Available: http://www.dantecdynamics.com/piv/princip/index.html.

DANTEC. 2013. *Measurement Principles of PIV* [Online]. Available: http://www.dantecdynamics.com/measurement-principles-of-piv [Accessed 11/26/2013.

DE, A. & ACHARYA, S. 2012. Dynamics of upstream flame propagation in a hydrogen-enriched premixed flame. *International Journal of Hydrogen Energy,* 37**,** 17294-17309.

DE PERSIS, S., FOUCHER, F., PILLIER, L., OSORIO, V. & GÖKALP, I. 2013. Effects of O2 enrichment and CO2 dilution on laminar methane flames. *Energy,* 55**,** 1055-1066.

DEC, J., KELLER, J. & VEDAT, A. 1990. Heat transfer enhancement in the oscillating turbulent flow of a pulse combustor tail pipe. *International Journal of Heat and Mass Transfer,* 35**,** 2311-2325.

DELAAT, J. & PAXSON, D. 2008. *Characterization and Simulation of Thermoacoustic Instability in a Low Emissions Combustor Prototype* [Online]. Available: http://ntrs.nasa.gov/archive/nasa/casi.ntrs.nasa.gov/20080047459_2008047198.pdf [Accessed 20th February 2013.

DELICHATSIOS, M. A. 1987. Air entrainment into buoyant jet flames and pool fires. *Combustion and Flame,* 70**,** 33-46.

DEMIRBAŞ, A. 1997. Calculation of higher heating values of biomass fuels. *Fuel,* 76**,** 431-434.

DEMIRBAŞ, A. 1998. Determination of combustion heat of fuels by using non-calorimetric experimental data. *Energy Edu Sci Technol,* 1**,** 7-12.

DHANUKA, S. 2008. *An Experimental Study of teh Stable and Unstable Operation of an LPP gas turbine combustor.* PhD, The University of Michigan.

DHANUKA, S., TEMME, E., DRISCOLL, J. & MONGIA, H. 2009. Vortex-shedding and mixing layer effects on periodic flashback in a lean premixed prevaporized gas turbine combustor. *Proceedings of the Combustion Institute,* 32**,** 2901-2908.

DRISCOLL, J. 2008. Turbulent premixed combustion: Flamelet structure and its effect on turbulent burning velocities. *Progress in Energy and Combust Science,* 34**,** 91-134.

DUROX, D., BAILLOT, F., SEARBY, G. & BOYER, L. 1997. On the shape of flames under string acoustic forcing: a mean flow controlled by an oscillating flow. *Journal of Fluid Mechanics,* 350**,** 295-310.

DUROX, D., SCHULLER, T. & CANDEL, S. 2002. Self-induced instability of a premixed jet flame impinging on a plate. *Proceedings of the Combustion Institute.*

EASEE-GAS 2005. Common Business Practice, Number 2005-001/0, Harmonistaion of Natural Gas Quality.

EGOLFOPOULOS, F. N., CHO, P. & LAW, C. K. 1989. Laminar flame speeds of methane-air mixtures under reduced and elevated pressures. *Combustion and Flame,* 76**,** 375-391.

EICHLER, C., BAUMGARTNER, G. & SATTELMAYER, T. 2012. Experimental Investigation of Turbulent Boundary Layer Flashback Limits for Premixed Hydrogen Air Flames Confined in Ducts. *J. Eng Gas Turbine Power,* 134**,** ref. 011502.

EICHLER, C. & SATTELMAYER, T. 2011. Experiments on Flame Flashback in a Quasi-2D Turbulent Wall Boundary Layer for Premixed Methane-Hydrogen-Air Mixtures. *Journal of Engineering for Gas Turbines and Power,* 133**,** 011503.

EICHLER, C. & SATTELMAYER, T. 2012. Premixed flame flashback in wall boundary layers studied by long-distance micro-PIV. *Experiments in Fluids,* 52**,** 347-360.

EMERSON PROCESS MANAGEMENT. 2014. *F-Series High Performance Compact Drainable Coriolis Flow and Density Meters* [Online]. Available: http://www2.emersonprocess.com/en-US/brands/micromotion/coriolis-flow-density-meters/F-Series-Meters/Pages/index.aspx
[Accessed 18th February 2014].

ENGLAND, D. R. & RICHARDS, W. B. The Infinite Line Pressure Probe. 30th International Instrumentation Symposium, 1984 Denver, CO. Instrument Society of America.

EROL, M., HAYKIRI-ACMA, H. & KÜÇÜKBAYRAK, S. 2010. Calorific value estimation of biomass from their proximate analyses data. *Renewable Energy,* 35**,** 170-173.

EUROPEAN COMMISION 2008. Denmark Renewable Energy Factsheet. Directorate-General for Energy and Transport.

FAAIJ, A., VAN DOORN, J., CURVERS, T., WALDHEIM, L., OLSSON, E., VAN WIJK, A. & DAEY-OUWENS, C. 1997. Characteristics and availability of biomass waste and residues in The Netherlands for gasification. *Biomass and Bioenergy,* 12**,** 225-240.

FALER, J. & LEIBOVICH, S. 1978. An experimental map of the internal structure of a vortex breakdown. *Journal of Fluid Mechanics,* 86**,** 313-335.

FARHAT, S. A. & MOHAMED, A. K. 2010. Combustion Oscillations Diagnostics in a Gas Turbine Using Acoustic Emissions. *Jordan Journal of Mechanical and Industrial Engineering,* 4**,** 352-357.

FERRARA, G., FERRARI, L. & SONNI, G. 2005. Experimental Characterization of a Remoting System for Dynamic Pressure Sensors, ASME Paper GT2005-68733.

FIASCHI, D. & CARTA, R. 2007. CO2 abatement by co-firing of natural gas and biomass-derived gas in a gas turbine. *Energy,* 32**,** 549-567.

FICHERA, A., LOSENNO, C. & PAGANO, A. 2001. Experimental Analysis of Thermo-Acoustic Combsution Instability. *Applied Energy,* 70**,** 179-191.

FICK, W. 1998. *Characterisation and Effects of The Precessing Vortex Core in Swirl Burners.* PhD, The University of Wales College Cardiff.

FICK, W., SYRED, N., KLINGE, T., GRIFFITHS, A., J. & O'DOHERTY, T. 1998. Clean and Efficient Combustion of Simulated low-calorific-value gases in Swirl burner/furnace systems. *Journal of the Institute of Energy,* 71**,** 9.

FRAGAKI, A. & ANDERSEN, A. N. 2011. Conditions for aggregation of CHP plants in the UK electricity market and exploration of plant size. *Applied Energy,* In Press, Corrected Proof.

FRITSCHE, D. 2005. *Origin and Control of Thermoacoustic Instabilities in Lean Premixed Gas Turbine Combustion.* D.Sc, Zurich University.

FRITSCHE, D., FÜRI, M. & BOULOUCHOS, K. 2007. An experimental investigation of thermoacoustic instabilities in a premixed swirl-stabilized flame. *Combustion and Flame,* 151**,** 29-36.

FRITZ, J., KRONER, M. & SATTELMAYER, T. Flashback in a Swirl Burner With Cylindrical Premixing Zone. Proceedings of the ASME Turbo Expo, 2001 Los Angeles, California.

FRITZ, J., KRONER, M. & SATTELMAYER, T. 2004. Flashback in a Swirl Burner With Cylindrical Premixing Zone. *Journal of Engineering for Gas Turbines and Power,* 126**,** 276-283.

FROUD, D. 1995. *A study of the precessing vortex core in a swirl burner* University of Wales College Cardiff.

FROUD, D., O'DOHERTY, T. & SYRED, N. 1995. Phase averaging of the precessing vortex core in a swirl burner under piloted and premixed combustion conditions. *Combustion and Flame,* 100**,** 407-412.

FROUD. D, B. A., O'DOHERTY, T. SYRED. N 1996. Studies of Helmholtz Resonance in a Swirl Burner/Furnace System. *Twenty-Sixth Symposium (International) on Combustion/The Combustion Institute,* 26**,** 3355-3362.

GARCÍA, R., PIZARRO, C., LAVÍN, A. G. & BUENO, J. L. 2013. Biomass proximate analysis using thermogravimetry. *Bioresource Technology,* 139**,** 1-4.

GARY, J. H. & HANDWERK, G. E. 1984. *Petroleum Refining Technology and Economics (2nd Edition)*, Marcel Dekker, Inc.

GE ENERGY. 2011. *How a Gas Turbine Works* [Online]. Available: http://www.ge-7fa.com/businesses/ge-7fa/en/basics-how-a-gas-turbine-works.html [Accessed 2nd March 2011].

GERRARD, J. 1966. The mechanics of the formation region of vortices behind bluff bodies. *J Fluid Mech,* 25**,** 401-413.

GILES, D., SOM, S. & AGGARWAL, K. 2006. A Numerical Investigation on the Structure and Emission Characteristics of Counterflow Syngas Diffusion Flames. *Fuel,* 85**,** 1729-1742.

GREENPEACE 2005. Decentralising Power: An Energy Revolution for the 21st Century.

GRIFFITHS, J. C. 2004. Murdock , William (1754–1839). *Oxford Dictionary of National Biography.* Oxford.

GROENENDIJK. W. The Global Gas Quality Perspective: The "European NGC" View Platts 2nd Annual Gas Quality/Interchangeability Forum, 13-14 November 2006 Houston.

GUO B, F. D., MARQUEZ G, AL-ABDELI YM, STARNER SH. RANS calculations and measurement of instabilities in swirl stabilised jets and flames. 2003 Australian symposium on combustion and eighth Australian flame day, 8–9th December, 2003 Australia: Monash University.

GUPTA, A. K., SYRED, N. & LILLEY, D. 1984. *Swirl flows*, Abacus Press.

GYSLING, D., COPELAND, G., MCCORMICK, D. & PROCIA, W. 2000. Combustion System Damping Augmentation with Helmholtz Resonators. *Journal of Engineering for Gas Turbines and Power,* 122**,** 269-274.

HADEF, R. & LENZE, B. 2007. Effects of co- and counter-swirl on the droplet characteristics in a spray flame. *Chemical Engineering and Processing,* 47**,** 2209-2217.

HAJI-SULAIMAN, Z., LIM, C. J. & WATKINSON, A. P. 1986. Gas composition and temperature profiles in a spouted bed coal gasifier. *The Canadian Journal of Chemical Engineering,* 64**,** 125-132.

HARDALUPAS, Y. & ORAIN, M. 2004. Local measurements of the time-dependent heat release rate and equivalence ratio using chemiluminescent emission from a flame. *Combustion and Flame,* 139**,** 188-207.

HATHOUT, P. 2012. *Thermoacoustic instability.* MIT.

HE, M., HU, Z., XIAO, B., LI, J., GUO, X., LUO, S., YANG, F., FENG, Y., YANG, G. & LIU, S. 2009. Hydrogen-rich gas from catalytic steam gasification of municipal solid waste (MSW): Influence of catalyst and temperature on yield and product composition. *International Journal of Hydrogen Energy,* 34**,** 195-203.

HOFFMANN, S., HABISREUTHER, P. & LENZE, B. 1994. Development and Assessment of Correlations for Predicting Stability Limits of Swirling Flames. *Chemical Engineering and Processing,* 33**,** 393-400.

HOINKINS, J. & LINDNER, E. *Chemie für Ingenieure*.

HUANG, Y. 2003. *Modelling and Simulation of Combustion Dynamics in Lean-Premixed Swirl-Stabilized Gas Turbine Engines.* PhD Thesis, The Pennsylvania State University.

HUANG, Y. & YANG, V. 2009. Dynamics and Stability of Lean-Premixed Swirl-Stabilized Combustion. *Progress in Energy and Combustion Science,* 35**,** 293-364.

IBERALL, S. 1950. Attenuation of Oscillatory Pressures in Instrument Lines. *NBS research Paper RP2115,* 45.

IEA. 2007. Improved Oxygen Production Technologies.

JACKSON, G. S., SAI, R., PLAIA, J. M., BOGGS, C. M. & KIGER, K. T. 2003. Influence of H2 on the response of lean premixed CH4 flames to high strained flows. *Combustion and Flame,* 132**,** 503-511.

JOHANSSON, L. S., TULLIN, C., LECKNER, B. & SJÖVALL, P. 2003. Particle emissions from biomass combustion in small combustors. *Biomass and Bioenergy,* 25**,** 435-446.

KALISZ, S., PRONOBIS, M. & BAXTER, D. 2008. Co-firing of biomass waste-derived syngas in coal power boiler. *Energy,* 33**,** 1770-1778.

KEDIA, K. S. & GHONIEM, A. F. 2012. Mechanisms of stabilization and blowoff of a premixed flame downstream of a heat-conducting perforated plate. *Combustion and Flame,* 159**,** 1055-1069.

KEHLHOFER, R. H., WARNER, J., NIELSEN, H. & BACHMAN, R. 1999. *Combined Cycle Gas & Steam Turbine Power Stations. 2nd Edition,* Tulsa, Oklahoma, Pennwell Publishing.

KELSALL, G. & TROGER, C. 2003. Prediction and Control of Combustion Instabilities in Industrial Gas Turbines. *Applied Thermal Engineering,* 24**,** 1371-1582.

KHALIL, A., VAIBHAV, A., GUPTA, A. K. & LEE, S. 2012. Low Calorific value fuelled distributed combustion with swirl for gas turbine applications. *J Applied Energy,* 98**,** 69-78.

KIESEWTTER, F., KNOLE, M. & SATTERLMAYER, T. 2007. Analysis of combustion induced vortex breakdown driven flame flashback in a premix burner with cylindrical mixing zone. *J Eng Gas Turbines Power,* 129**,** 929-936.

KING, G. 2012. Hydraulic Fracturing 101: What Every Representative, Environmentalist, Regulator, Reporter, Investor, University Researcher, Neighbor and Engineer Should Know About Estimating Frac Risk and Improving Frac Performance in Unconventional Gas and Oil Wells. . Society of Petroleum Engineers.

KNOLE, M., SATTERLMAYER, T. & FRITZ, M. 2008. Simultaneous high repetition rate PIV-LIF measurements of CIVB driven flashback. *Exp Fluids,* 44**,** 529-538.

KOHL, A. & NEILSON, R. 1997. Gas Purification. Gulf Professional Publishing.

KONLE, M. & SATTELMAYER, T. 2008. Interaction of Heat Release and Vortex Breakdown in Swirling Flames *14th Int Symp on Applications of Laser Techniques to Fluid Mechanics* Lisbon, Portugal.

KONNOV, A., DYAKOV, I. & RUYCK, J. 2002. Nitric oxide formation in premixed flames of H2 + CO+ CO2 and air. *Proceedings of the Combustion Institute.*

KRONER, M. 2002. Flashback Limits for Combustion Induced Vortex Breakdown in a Swirl Burner: ASME Paper GT-2002-30075. *ASME Turbo Expo.* Amsterdam.

KRONER, M., FRITZ, J. & SATTELMAYER, T. 2003. Flashback Limits for Combustion Induced Vortex Breakdown in a Swirl Burner. *Journal of Engineering for Gas Turbines and Power,* 125**,** 693-700.

KRONER, M., SATTELMAYER, T., FRITZ, J., KIESEWETTER, F. & HIRSCH, C. 2007. Flame Propagation in Swirling Flows - Effect of Local Extinction on Combustion Induced Vortex Breakdown. *Combustion Science and Technology,* 179**,** 1385-1416.

KUNZE, C., RIEDL, K. & SPLIETHOFF, H. 2011. Structured exergy analysis of an integrated gasification combined cycle (IGCC) plant with carbon capture. *Energy,* 36**,** 1480-1487.

LAMPERT, K., ZIEBIK, A. & STANEK, W. 2010. Thermoeconomical analysis of CO2 removal from the Corex export gas and its integration with the blast-furnace assembly and metallurgical combined heat and power (CHP) plant. *Energy,* 35**,** 1188-1195.

LEE, M., SEO, S., YOON, J., KIM, M. & YOON, Y. 2012. Experimental study on the effect of N2, CO2, and steam dilution on the combustion performance of H2 and CO synthetic gas in an industrial gas turbine. *Fuel,* 102**,** 431-438.

LEE, S.-Y., SEO, S., BRODA, J., PAL, S. & RJ., S. An experimental estimation of mean reaction rate and flame structure during combustion instability in lean premixed gas turbine combustor. Proceedings of the Combustion Institute, 2000.

LEFEBVRE, A. H. 1999. Gas Turbine Combustion. New York: Taylor & Francis Group.

LEFEBVRE, A. H. & BALLAL, D. R. 2010. *Gas Turbine Combustion: Alternative Fuels and Emissions, Third Edition,* Florida, CRC Press.

LEWIS, B. & ELBE, G. 1987. *Combustion, Flames and Explosions of Gases*, New York: Academic Press.

LEWIS, C. W. 1981. Biomass through the ages. *Biomass,* 1**,** 5-15.

LEWIS, J., MARSH, R., MORRIS, S., SEVCENCO, Y., GRIFFITHS, A. & BOWEN, P. 2012. The Effect of Variable Fuel Composition on a Swirl-Stabilised Producer Gas Combustor. *Energy Conversion and Management,* 64C**,** 52-61.

LEWIS, J., MARSH, R., VALERA-MEDINA, A., MORRIS, S. & BAEJ, H. The Use of CO2 to Improve Stability and Emissions of an IGCC Combustor. ASME Turbo Expo 2014: Turbine Technical Conference and Exposition, 6-10 June 2014 Dusseldorf, Germany.

LI, J., ZHAO, Z., KAZAKOV, A., CHAOS, M. & DRYER, F. L. 2007. A comprehensive kinetic mechanism for CO, CH2O, and CH3OH combustion. *Int. J. Chem. Kinet,* 39**,** 109-136.

LIAO, C.-H., OU, H.-H., LO, S.-L., CHIUEH, P.-T. & YU, Y.-H. 2011. A challenging approach for renewable energy market development. *Renewable and Sustainable Energy Reviews,* 15**,** 787-793.

LIEUWEN, T. 1999. *Investigation of Combustion Instability Mechanisms in Premixed Gas Turbines.* PhD, Georgia Institute of Technology.

LIEUWEN, T. 2005. Nonlinear kinematic response of premixed flames to harmonic velocity disturbances. *Proceedings of the Combustion Institute,* 30**,** 1725-1732.

LIEUWEN, T. 2012a. *Static and Dynamic Combustion Stability* [Online]. Available: <http://www.netl.doe.gov/technologies/coalpower/turbines/refshelf/handbook/3.1.1.pdf> [Accessed 24th September 2012.

LIEUWEN, T. 2012b. *Unsteady Combustor Physics,* U.S.A., Cambridge University Press.

LIEUWEN, T., MCDONELL, V., SANTAVICCA, D. & SATTELMAYER, T. 2008. Burner Development and Operability Issues Associated with Steady Flowing Syngas Fired Combustors. *Combustion Science and Technology,* 180**,** 1169-1192.

LIEUWEN, T. & MCMANUS, K. 2003. Combustion Dynamics in Lean-Premixed Prevaporized (LPP) Gas Turbines. *Journal of Propulsion and Power,* 19**,** 721-846.

LORD RAYLEIGH 1896. *The Theory of Sound: 2nd Edition,* London, Macmillan.

LOUBAR, K., RAHMOUNI, C., LE CORRE, O. & TAZEROUT, M. 2007. A combustionless determination method for combustion properties of natural gases. *Fuel,* 86**,** 2535-2544.

LUCA-NEGRO, O. & O'DOHERTY, T. 2001. Vortex Breakdown: A Review. *Progress in Energy and Combustion Science,* 27**,** 431-481.

LUI, Y., WANG, Y., WANG, H. & LI, P. 2009. Experimental investigations on combustion characteristics of the blast furnace gas. *3th International Conference on Bioinformatics and Biomedical Engineering.* Beijing.

MAKARTCHOUK, A. 2002. *Diesel Engine Engineering: Thermodynamics, Dynamics, Design, and Control,* Boca Raton, Florida, U.S.A., CRC Press.

MARSH, R., LEGONDA, I., GRIFFITHS, M. & STEER, J. 2010. *Refgas Syngas Composition*. Cardiff: Cardiff University.

MARTENS, A. 1998. The energetic feasibility of CHP compared to the separate production of heat and power. *Applied Thermal Engineering,* 18**,** 935-946.

MASRI AR, K. P., BARLOW RS 2004. The compositional structure of swirl-stabilised turbulent nonpremixed flames. *Combustion and Flame,* 137**,** 1-37.

MELVIN G.R, C. 2003. Carbon sequestration and biomass energy offset: theoretical, potential and achievable capacities globally, in Europe and the UK. *Biomass and Bioenergy,* 24**,** 97-116.

MHILU, C. F. 2012. Modeling Performance of High-Temperature Biomass Gasification Process. *ISRN Chemical Engineering,* 2012**,** 13.

MOECK, J. P., BOURGOIN, J.-F., DUROX, D., SCHULLER, T. & CANDEL, S. Precessing-Vortex-Core-Flame Interaction Based on Tomographic Reconstruction Techniques. Proceedings of ASME Turbo Expo 2012, 2012 Copenhagen.

MOHAMMAD, B., BALASUBRAMANYAM, P., MCMANUS, K., RUSZCZYK, J., ELKADY, A. & MUELLER, M. Combustion Dynamics Diagnostics and Mitigation on a Prototype Gas Turbine Combustor. ASME Turbo Expo 2012, 2012 Copenhagen.

MOHON ROY, M., TOMITA, E., KAWAHARA, N., HARADA, Y. & SAKANE, A. 2009. Performance and emission comparison of a supercharged dual-fuel engine fueled by producer gases with varying hydrogen content. *International Journal of Hydrogen Energy,* 34**,** 7811-7822.

MONTEIRO, E., BELLENOUE, M., SOTTON, J., MOREIRA, N. A. & MALHEIRO, S. 2010. Laminar burning velocities and Markstein numbers of syngas-air mixtures. *Fuel,* 89**,** 1985-1991.

MORRIS, S. 2012. ETN H2 - IGCC: SP1.3 "Combustion". Gas Turbine Research Centre, Margam, Port Talbot.

NAIR, S., THIRUCHENGODE, M., HUGHES, R., WU, L., SEITZMAN, J. & LIEUWEN, T. 2002. Acoustic Characterization of a Piloted Premixed Flame Under Near Blowout Conditions.

NARVAEZ, I., ORIO, A., AZNAR, M. P. & CORELLA, J. 1996. Biomass Gasification with Air in an Atmospheric Bubbling Fluidized Bed. Effect of Six Operational Variables on the Quality of the Produced Raw Gas. *Industrial & Engineering Chemistry Research,* 35**,** 2110-2120.

NATARAJAN, J., LIEUWEN, T. & SEITZMAN, J. 2007. Laminar flame speeds of H2/CO mixtures: effect of CO2 dilution, preheat temperature, and pressure. *Combustion and Flame,* 151**,** 104-119.

NATIONAL GRID 2011. Gas Ten Year Statement- UK Gas Transmission.

NATURALGAS.ORG. 2010. *Overview of Natural Gas* [Online]. [Accessed 17/07/2013 2013].

NOBLE, D. R., ZHANG, Q., SHAREEF, A., TOOTLE, J., MEYERS, A. & LIEUWEN, T. Syngas Mixture Composition Effects Upon Flashback and Blowout. Proceedings of the ASME Turbo Expo, 2006 Spain.

NOIRAY, N. & SCHUERMANS, B. 2012. Theoretical and Experimental Investigations on Damper Performance for Suppression of Thermoacoustic Oscillations. *Journal of Sound and Vibration,* 331**,** 2753-2763.

O'DOHERTY T, F. D., BATES CJ, SYRED N 1994. Characteristics of a power station boiler. *Proc Inst Mech Eng Part A J Power Energy,* 208**,** 36-89.

O'DOHERTY, T., GRIFFITHS, A., J., SYRED, N., BOWEN, P. & FICK, W. 1999. Experimental Analysis of Roatating Instabilities in Swirling and Cyclonic Flows. *Developments in Chemical Engineering and Mineral Processing,* 7**,** 245-267.

OFGEM 2001. Report to the DTI on the initial impact of NETA on smaller generators.

OFGEM 2003. Electricity Distribution Losses.

OWEN, F. K., SPADACCINI, L. J. & BOWMAN, C. T. 1977. Pollutant formation and energy release in confined turbulent diffusion flames. *Symposium (International) on Combustion,* 16**,** 105-117.

PACK, J., BAE, D., CHA, M., YUN, J., KEEL, S. & CHO, H. E. A. 2008. Flame characteristics in H2/CO synthetic gas diffusion flames diluted with CO2: effects of radiative heat loss and mixture composition. *Hydrogen Energy,* 33**,** 7256-64.

PAREJA, J., BURBANO, H. J., AMELL, A. & CARVAJAL, J. 2011. Laminar burning velocities and flame stability analysis of hydrogen/air premixed flames at low pressure. *International Journal of Hydrogen Energy,* 36**,** 6317-6324.

PASCHEREIT, C., GUTMARK, E. & WEISENSTEIN, W. 1998. Control of Thermoacoustic Instabilities and Emissions in an Industrial-Type-Gas Turbine. *Twenty-Seventh Symposium (International) on Combustion/ The Combustion Institute***,** 1817-1824.

PASCHEREIT, C. O. & GUTMARK, E. 2006. Control of High-Frequency Thermoacoustic Pulsations by Distributed Vortex Generators. *AIAA Journal,* 44**,** 550-557.

PCB PIEZOTRONICS 2003. Model 102M206 ATEX Approved Pressure Sensors Installation and Operating Manual.

PRASAD, B. V. V. S. U., SHARMA, C. S., ANAND, T. N. C. & RAVIKRISHNA, R. V. 2011. High swirl-inducing piston bowls in small diesel engines for emission reduction. *Applied Energy,* 88**,** 2355-2367.

PUGH, D., O'DOHERTY, T., GRIFFITHS, A., J., BOWEN, P., CRAYFORD, A., MARSH, R., GILES, A. & HOPKINS, A. 2012. Laminar Burning Velocity And Markenstein Length Characteristic Of Compositionally Dynamic Blast Furnace Gas. *Proceedings of ASME Turbo Expo 2012.* Copenhagen, Denmark.

PUTMAN, A. 1971. *Combustion Driven Oscillations in Industry,* New York, American Elsevier.

RANGA DINESH, K., JIANG, X. & VAN OIJEN, J. 2014. Hydrogen-enriched non-premixed jet flames: Analysis of the flame surface, flame normal, flame index and Wobbe index. *International Journal of Hydrogen Energy*.

REOTEMP INSTRUMENTS. 2011. *Type K Thermocouple* [Online]. Available: http://www.reotemp.com/thermocoupleinfo/type-k-thermocouple.htm [Accessed 18th February 2014].

RODRIGUES, M., WALTER, A. & FAAIJ, A. 2003. Co-firing of natural gas and Biomass gas in biomass integrated gasification/combined cycle systems. *Energy,* 28**,** 1115-1131.

ROHRSSEN, R. 2007. *Acoustic Characteristics of a Dynamic Pressure Sensing Apparatus with Applications to Gas Turbine Combustors.* BSc, West Virginia University.

SAHOO, B. B., SAHA, U. K. & SAHOO, N. 2011. Theoretical performance limits of a syngas-diesel fueled compression ignition engine from second law analysis. *Energy,* 36**,** 760-769.

SAMUELSON, R. D. 1967. Pneumatic Instrumentation Lines and Their Use in Measuring Rocket Nozzle Pressure. Nuclear Engine for Rocket Vehicle Applications (NERVA) Program, Report No. RN-DR-0124.

SAN MARTIN, J. I., ZAMORA, I., SAN MARTIN, J. J., APERRIBAY, V. & EGUIA, P. 2008. Tri-generation Systems with Fuel Cells. *ICREPQ '08.* Santander, Spain.

SANTHANAM, V., KNOPF, F., ACHARYA, S. & GUTMARK, E. 2002. Flourescence and Temperature Measurements in an Actively Forced Swirl-Stabilized Spray Combustor. *Journal of Propulsion and Power,* 18**,** 855-865.

SARPKAYA, T. 1971a. On stationary and travelling vortex breakdowns. *Journal of Fluid Mechanics,* 45**,** 545-559.

SARPKAYA, T. 1971b. Vortex breakdown in swirling conical flows. *Journal of the AIAA,* 9**,** 1792-1799.

SCHADOW, K. C. & GUTMARK, E. 1992. Combustion Instability Related to Vortex Shedding in Dump Combustors and Their Passive Control. *Progress in Energy and Combustion Science,* 18**,** 117-132.

SCHEFER, R. G., PJ 1998. Mechanism of Flame Stabilisation in Turbulent, Lifted-Jet Flames. *Combustion and Flame,* 112**,** 559-574.

SHANBHOGUE, S., HUSAIN, S. & LIEUWEN, T. 2009. Lean blowoff of bluff body stabilized flames: Scaling and dynamics. *Prog Energy Combust Sci,* 35**,** 98-120.

SIMBECK, D. 2007. Gasification opportunities in Alberta. *Paper presented at Seminar on Gasification Technologies sponsored by Alberta Government and GTC, Edmonton.*

SLIM, B. K., DARMEVEIL, H. D., GERSEN, S. & LEVINSKY, H. B. 2011. The combustion behaviour of forced-draught industrial burners when fired within the EASEE-gas range of Wobbe Index. *Journal of Natural Gas Science and Engineering,* 3**,** 642-645.

SLUDER. C, STOREY. J, LEWIS. W & R, W. 2004. A Thermal Conductivity Approach for Measuring Hydrogen in Engine Exhaust. *In:* 2004-01-2908 (ed.).

SNYDER, D. B., ADI, G. H., BUNCE, M. P., SATKOSKI, C. A. & SHAVER, G. M. 2010. Fuel blend fraction estimation for fuel-flexible combustion control: Uncertainty analysis. *Control Engineering Practice,* 18**,** 418-432.

SON, Y.-I., YOON, S. J., KIM, Y. K. & LEE, J.-G. 2011. Gasification and power generation characteristics of woody biomass utilizing a downdraft gasifier. *Biomass and Bioenergy,* 35**,** 4215-4220.

SPRRUYT, A. Akoestiche effecten door wervel-precessie in roterende stromingen. Nederlands akoestich genootschap, 1972 Utrecht. 9-20.

SRIDHAR, G., PAUL, P. J. & MUKUNDA, H. S. 2001. Biomass derived producer gas as a reciprocating engine fuel--an experimental analysis. *Biomass and Bioenergy,* 21**,** 61-72.

STASSEN, H. E. & KOELE, H. J. 1997. The use of LCV gas from biomass gasifiers in internal combustion engines. *In:* KALTSCHMITT, M. (ed.) *Biomass Gasification Pyrolysis Conference.* A.V. Bridgwater: CPL Press, Newbury, UK.

STÖHR, M., BOXX, I., CARTER, C. D. & MEIER, W. 2012. Experimental study of vortex-flame interaction in a gas turbine model combustor. *Combustion and Flame,* 159**,** 2636-2649.

STONE, C. & MENON, S. 2002. Swirl Control of Combustion Instabilities in a Gas Turbine Combustor. *Proceedings of the Combustion Institute,* 29**,** 155-160.

STRACHAN, N. & FARRELL, A. 2006. Emissions from distributed vs. centralized generation: The importance of system performance. *Energy Policy,* 34**,** 2677-2689.

STRAUB, D. & FERGUSON, D. 2007. Design Considerations For Remote High-Speed Pressure Measurements Of Dynamic Combustion Phenomena. *In:* U.S. DEPARTMENT OF ENERGY (ed.). National Energy Technology Laboratory, Morgantown, WV.

STUTTAFORD, P., MARTLING, V., GREEN, A. & LIEUWEN, T. 2003. Combustion Noise Measurement System for Low Emissions Combustor Performance Optimization and Health Monitoring, ASME Paper GT2003-38255.

SUBRAMANYA, M. & CHOUDHURI, A. 2007. Investigation of Combustion Instability Effects on the Flame Characteristics of Fuel Blends. *5th International Energy Conversion Engineering Conference and Exhibit (IECEC).* St. Louis, Missouri.

SYRED, C., GRIFFITHS, A. J., SYRED, N. & FICK, W. 2004. Cyclone gasifier and cyclone combustor for the use of biomass derived gas in the operation of a small gas turbine in cogeneration plants. *Fuel,* 83**,** 2381–2392.

SYRED, N. 2006. A review of oscillation mechanisms and the role of the precessing vortex core (PVC) in swirl combustion systems. *Progress in Energy and Combustion Science,* 32**,** 93-161.

SYRED, N., ABDULSADA, M., GRIFFITHS, A., O'DOHERTY, T. & BOWEN, P. 2011. The effect of hydrogen containing fuel blends upon flashback in swirl burners. *Applied Energy,* In Press, Corrected Proof.

SYRED, N., ABDULSADA, M., GRIFFITHS, A., O’DOHERTY, T. & BOWEN, P. 2012. The effect of hydrogen containing fuel blends upon flashback in swirl burners. *Applied Energy,* 89**,** 106-110.

SYRED, N. & BEÉR, J. M. 1974. Combustion in Swirling Flows: A Review. *Combustion and Flame,* 23**,** 143-201.

SYRED, N., CHIGIER, N. A. & BEÉR, J. M. 1971. Flame stabilization in recirculation zones of jets with swirl. *Symposium (International) on Combustion,* 13**,** 617-624.

SYRED, N., DAHMEN, K., STYLES, A. & NAJIM, S. 1997. A review of combustion problems associated with low calorific value gases. *J Institute Energy,* 50**,** 195-207.

SYRED, N., GILES, A., LEWIS, J., ABDULSADA, M., VALERA MEDINA, A., MARSH, R., BOWEN, P. & GRIFFITHS, A. 2013a. Effect of inlet and outlet configurations on blow-off and flashback with premixed combustion for methane and a high hydrogen content fuel in a generic swirl burner. *ICAE* Pretoria, South Africa.

SYRED, N., GILES, A., LEWIS, J., ABDULSADA, M., VALERA MEDINA, A., MARSH, R., BOWEN, P. J. & GRIFFITHS, A. J. 2014. Effect of inlet and outlet configurations on blow-off and flashback with premixed combustion for methane and a high hydrogen content fuel in a generic swirl burner. *Applied Energy,* 116**,** 288-296.

SYRED, N., GILES, A., LEWIS, J., VALERA-MEDINA, A., BOWEN, P. & GRIFFITHS, A., J. Tangential Velocity Effects and Correlations for Blow-Off and Flashback in a Generic Swirl Burner and the effect of a Hydrogen containing Fuel. 51st AIAA Aerospace Sciences Meeting, 2013b Grapevine, Texas.

SYRED N, O. D. T., FROUD D 1994. The interaction of the precessing vortex core and reverse flow zone in the exhaust of a swirl burner. *Proc Inst Mech Eng Part A J Power Energy,* 208**,** 27-36.

TACHIBANA, S., ZIMMER, L., KUROSAWA, Y. & SUZUKI, K. 2007. Active Control of Combustion Instabilities in a Lean Premixed Combustor by Secondary Fuel Injection Coupling with Chemiluminescence Imagine technique. *Proceedings of the Combustion Institute,* 31**,** 2917-2924.

THE EUROPEAN PARLIMENT 2000. DIRECTIVE 2000/76/EC OF THE EUROPEAN PARLIAMENT AND OF THE COUNCIL of 4 December 2000 on the incineration of waste. *Official Journal of the European Communities***,** 21.

THE WOOD RECYCLERS ASSOCIATION 2009. Grades of Recycled Wood. The Wood Recyclers Association.

THIESSEN, S., KHALIL, E. & KARIM, G. 2010. The autoignition in air of some binary fuel mixtures containing hydrogen. *International Journal of Hydrogen Energy,* 35**,** 10013-10017.

THORNTON, J. D., CHORPENING, B. T., SIDWELL, T. G., STRAKEY, P. A., HUCKABY, E. D. & BENSON, K. J. 2007. Flashback Detection Sensor for Hydrogen Augmented Natural Gas Combustion. *ASME Conference Proceedings,* 2007**,** 739-746.

TINAUT, F. V., MELGAR, A., HORRILLO, A. & DÍEZ DE LA ROSA, A. 2006. Method for predicting the performance of an internal combustion engine fuelled by producer gas and other low heating value gases. *Fuel Processing Technology,* 87**,** 135-142.

TRAN, N., DUCRUIX, S. & SCHULLER, T. 2008. Damping Combustion Instabilities with Perforates at the Premixer Inlet of a Swirled Burner. *Proceedings of the Combustion Institute,* 32**,** 2917-2924.

TROPEA, C. & YARIN, A. 2007. *Springer Handbook of Experimental Fluid Mechanics*.

TUSIANI, M. & SHEARER, G. 2007. *LNG: A Nontenchnical Guide,* Tulsa, PennWell Books.

TUTTLE, S. G., CHAUDHURI, S., KOSTKA JR, S., KOPP-VAUGHAN, K. M., JENSEN, T. R., CETEGEN, B. M. & RENFRO, M. W. 2012. Time-resolved blowoff transition measurements for two-dimensional bluff body-stabilized flames in vitiated flow. *Combustion and Flame,* 159**,** 291-305.

U.S. DEPARTMENT OF THE INTERIOR & SURVEY, U. S. G. 2013. *Diagram showing classification of coals by rank in the U.S* [Online]. Available: http://pubs.usgs.gov/circ/c1143/html/fig17.html [Accessed 17th February 2014].

U.S. ENERGY INFORMATION ADMINISTRATION. 2010. *Natural Gas* [Online]. Available: http://www.eia.gov/oil_gas/natural_gas/special/ngresources/ngresources.html [Accessed 18th July 2013].

VALERA-MEDINA, A. 2009. *Coherent structures and their effects on processes occurring in swirl combustors.* PhD, Cardiff University.

VALERA-MEDINA, A., SYRED, N. & BOWEN, P. 2012. Central Recirculation Zone Analysis using a Confined Swirl Burner for Terrestrial Energy. *J AIAA Propulsion Power.*

VALERA-MEDINA, A., SYRED, N., BOWEN, P. & CRAYFORD, A. 2011a. Studies of Swirl Burner Characteristics, Flame Lengths and Relative Pressure Amplitudes. *Journal of Fluids Engineering,* 133**,** 101302-11.

VALERA-MEDINA, A., SYRED, N. & GRIFFITHS, A. 2009. Visualisation of isothermal large coherent structures in a swirl burner. *Combustion and Flame,* 156**,** 1723-1734.

VALERA-MEDINA, A., SYRED, N., GRIFFITHS, A., J. & KAY, P. 2011b. Central Recirculation Zone Analysis in an Unconfined Tangential Swirl Burner with Varying Degrees of Premixing. *Experiments in Fluids,* 50**,** 1611-1623.

VAN MAAREN, A., THUNG, D. & DE GOEY, P. 1994. Measurement of Flame Temperature and Adiabatic Burning Velocity of Methane/Air Mixtures. *Combustion Science and Technology,* 96**,** 327-344.

VAN OMMEN, J. R., SCHOUTEN, J. C., VANDER STAPPEN, M. L. M. & VAN DEN BLEEK, C. M. 1999. Response Characteristics of Probe-Transducer Systems For Pressure Measurements in Gas-Solid Fluidized Beds: How to Prevent Pitfalls in Dynamic Pressure Measurements. *Powder Technology,* 106**,** 199-218.

VU, T. M., SONG, W. S., PARK, J., BAE, D. S. & YOU, H. S. 2011. Measurements of propagation speeds and flame instabilities in biomass derived gas–air premixed flames. *International Journal of Hydrogen Energy,* 36**,** 12058-12067.

WARNATZ, J., MAAS, U. & DIBBLE, R. 1999. *Combustion,* Germany, Springer.

WEDLOCK, M., WOOD, J., MILLER, N. S., J., K. LIU, K., SYED, K., BOWEN, P., CRAYFORD, A. & SEVCENCO, Y. 2008. Detailed Internal Measurements of a Siemens Combustor Operating at Gas Turbine Relevant Conditions. *Proceedings of ASME Turbo Expo 2008: Power for Land, Sea and Air.* Berlin, Germany.

WHALEY, S. 2007. Clean Energy Summit: Reid opposes coal-fired power plants. Las Vegas Review-Journal.

WILLIAMS, J. L. 2011. Oil Price History and Analysis. WRTG Economics.

WRIGHT, O., MCCARTHEY, M. & BAWDEN, T. 2012. David Cameron: 'Britain must be at the heart of shale gas revolution. *The Indepedent*.

WU, X., LI, T., CAI, J., PENG, Z. & YUAN, Z. 2009. Numerical prediction of particle number concentration distribution in scrubbing-cooling chamber of entrained-flow coal gasifier. *Chemical Engineering Journal,* 149**,** 325-333.

YAN, F., LUO, S.-Y., HU, Z.-Q., XIAO, B. & CHENG, G. 2010. Hydrogen-rich gas production by steam gasification of char from biomass fast pyrolysis in a fixed-bed reactor: Influence of temperature and steam on hydrogen yield and syngas composition. *Bioresource Technology,* 101**,** 5633-5637.

YANG, V. & LIEUWEN, T. 2005. Combustion Instabilities in Gas Turbine Engines. *AIAA, Prog Astronautics Aeronautics.* U.S.A.

YAZDABADI, Y. 1995. *A Study of the Precessing Vortex Core in Cyclone Dust Separators and a Method of Prevention.* PhD, The University of Wales College Cardiff.

YI, T. & GUTMARK, E. 2008. Online Prediction of the Onset of Combustion Instability Based on the Computation of Damping Ratios. *Journal of Sound and Vibration,* 310**,** 422-447.

ZACHARIAH-WOLFF, J., EGYEDI, T. & HEMMES, K. 2007. From natural gas to hydrogen via the Wobbe index: The role of standardized gateways in sustainable infrastructure transitions. *International Journal of Hydrogen Energy,* 32**,** 1235-1245.

ZHAO, Z., LI, J., KAZAKOV, A., DRYER, F. L. & ZEPPIERI, S. P. 2004. BURNING VELOCITIES AND A HIGH-TEMPERATURE SKELETAL KINETIC MODEL FOR n-DECANE. *Combustion Science and Technology,* 177**,** 89-106.

ZHENG, L. 2011. *Oxy-Fuel Combustion for Power Generation and Carbon Dioxide (CO2) Capture,* Cambridge, Woodhead Publishing.

ZIEBIK, A., LAMPERT, K. & SZEGA, M. 2008. Energy analysis of a blast-furnace system operating with the Corex process and CO2 removal. *Energy,* 33**,** 199-205.

Appendices

Appendix A - Additional Images

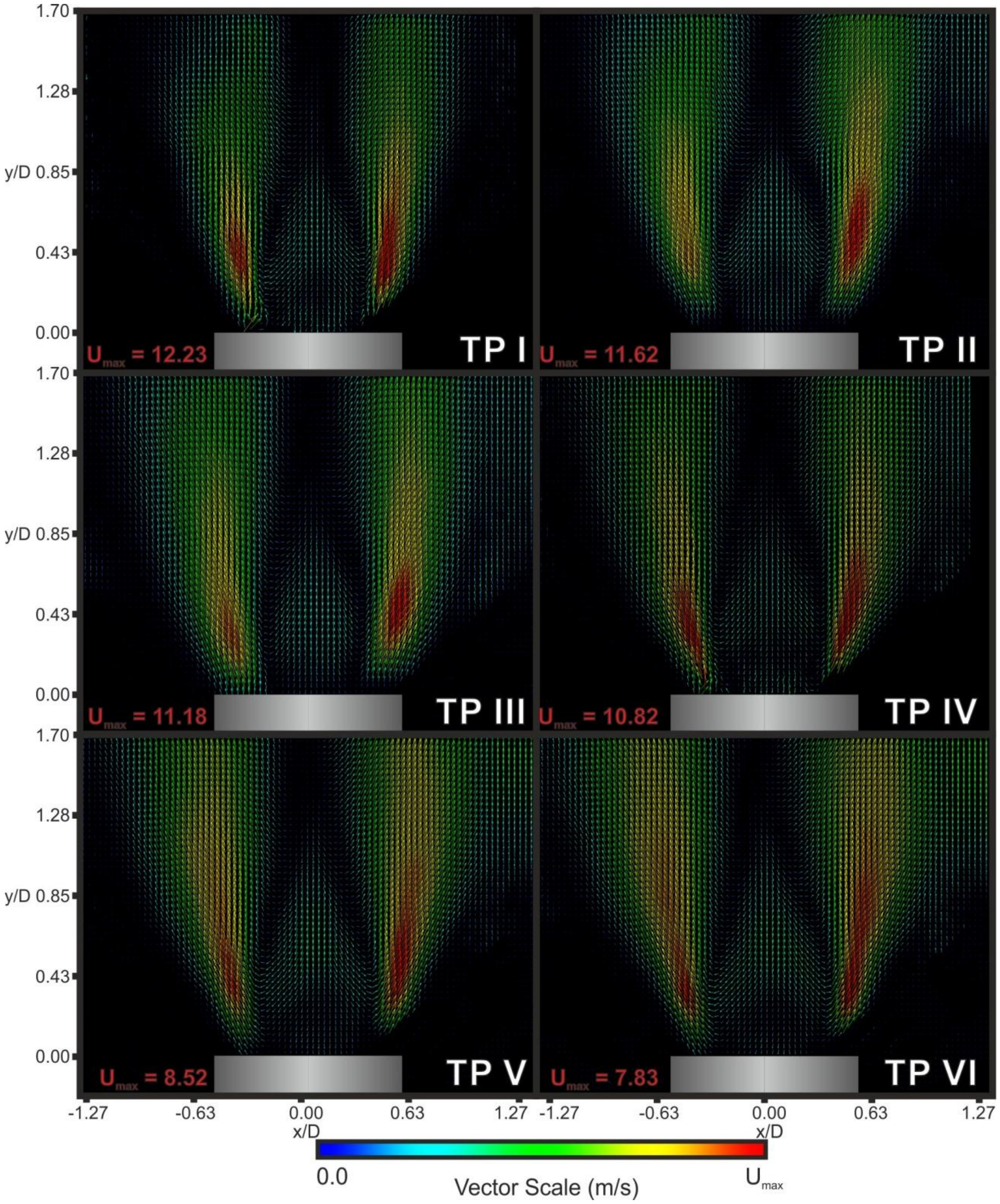

Figure A. 1: Single camera vector plots of TP I to TP IV in the ASBG as detailed in Table 14, vectors indicate velocity and direction

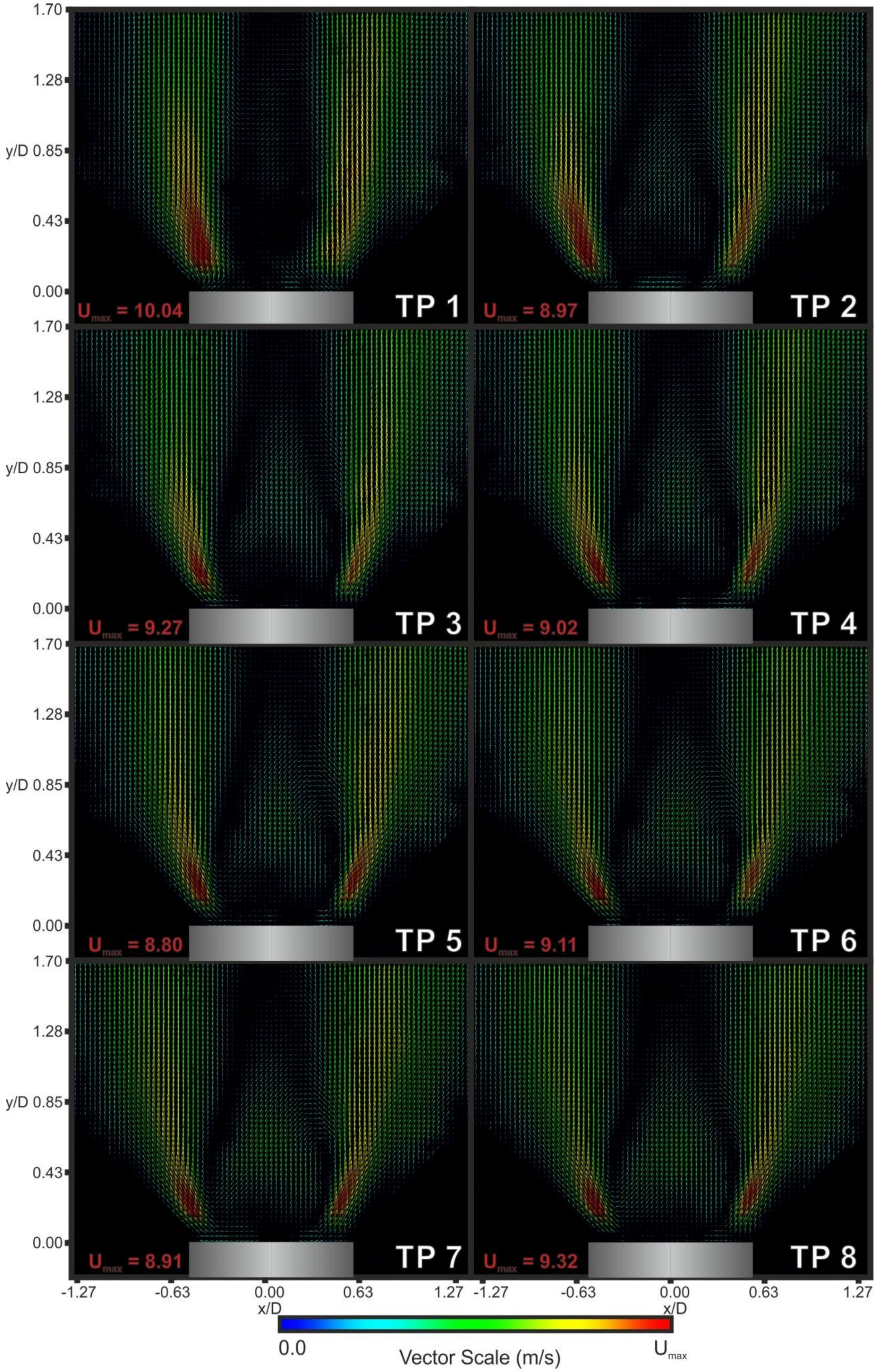

Figure A. 2: Single camera vector plots of TP 1 to TP 8 in the ASBG as detailed in Table 15, vectors indicate velocity and direction

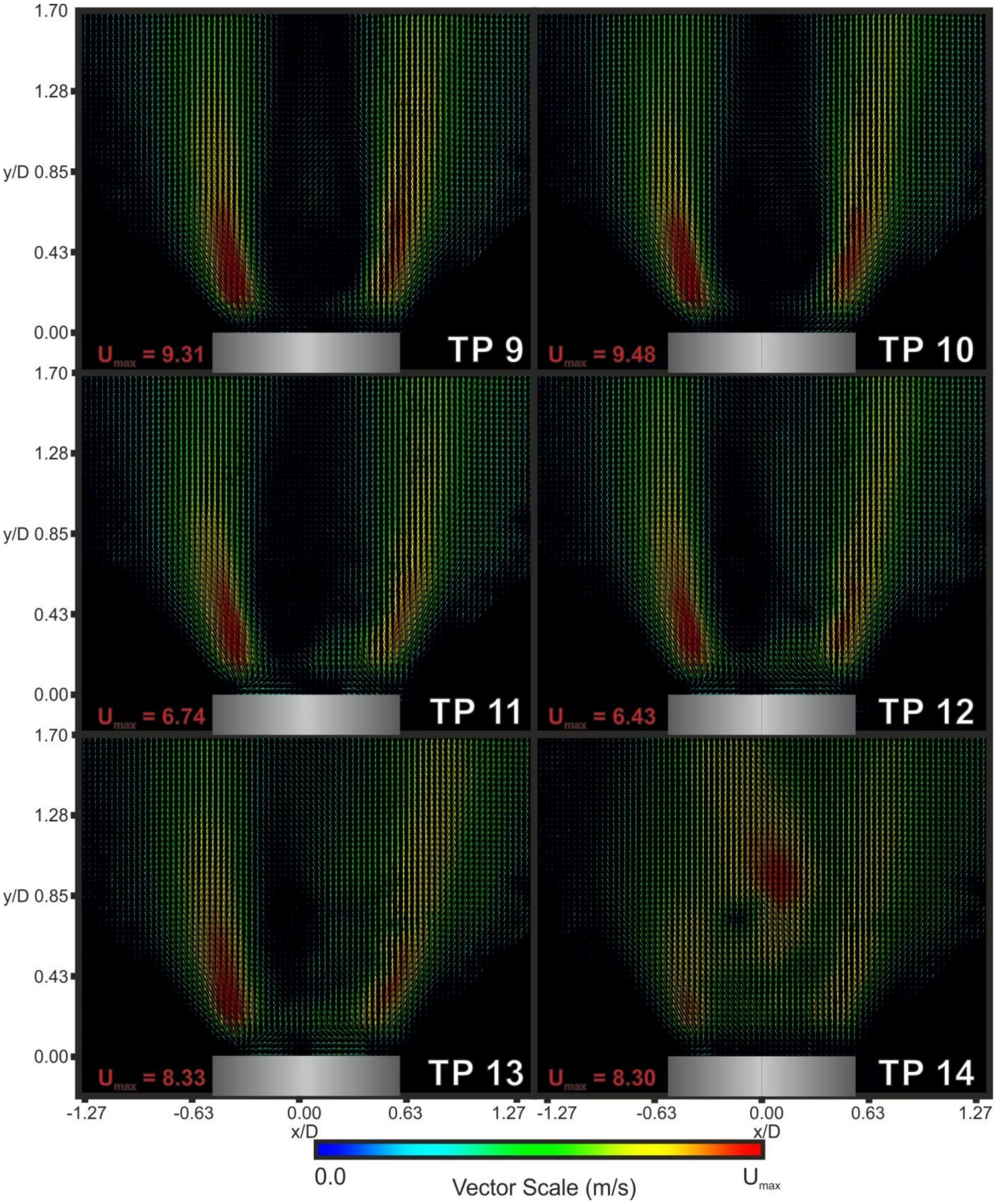

Figure A. 3: Single camera vector plots of TP 9 to TP 14 in the ASBG as detailed in Table 15, vectors indicate velocity and direction

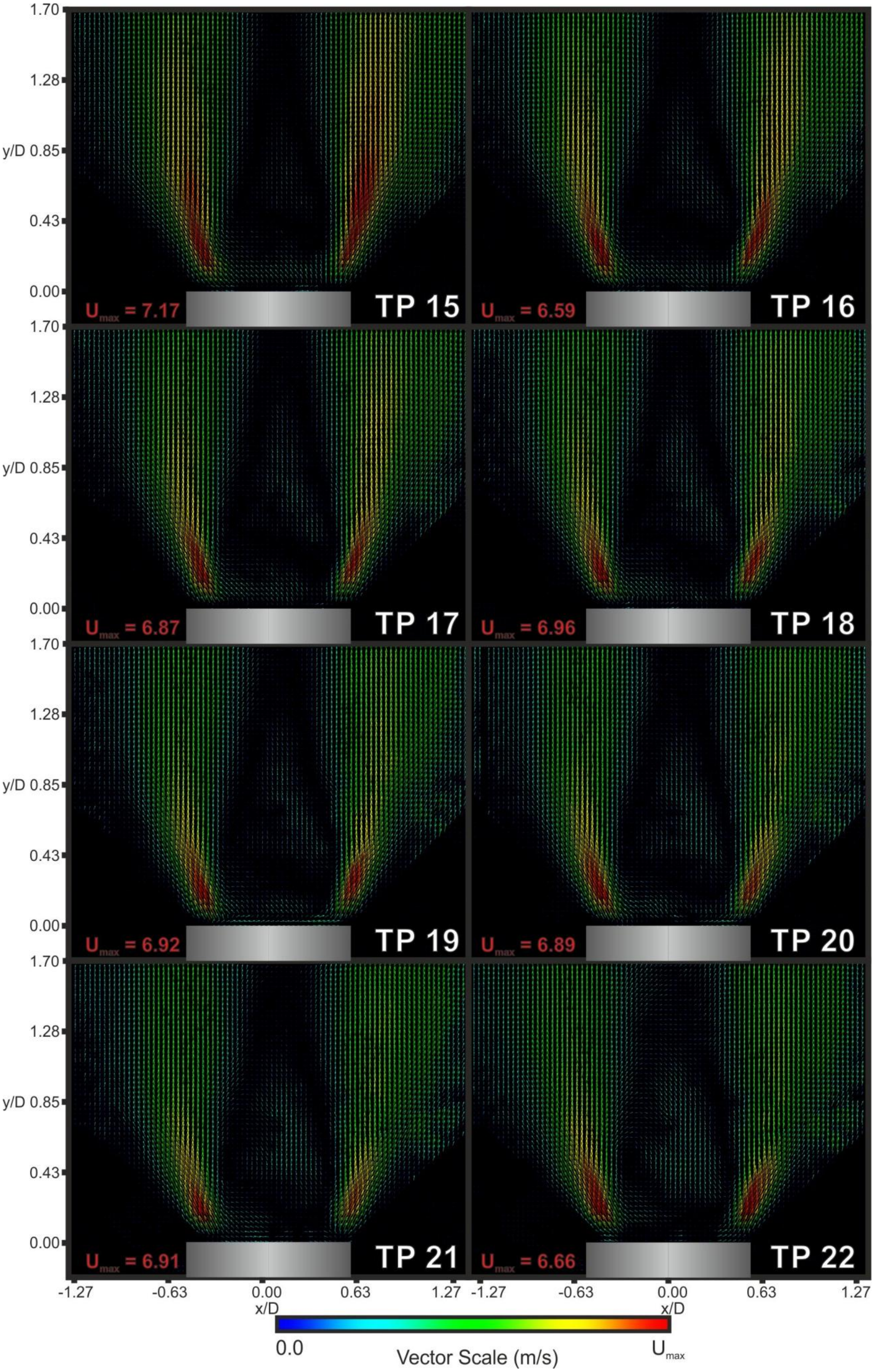

Figure A. 4: Single camera vector plots of TP 15 to TP 22 in the ASBG as detailed in Table 15, vectors indicate velocity and direction

Appendix B - Structure Divisions

The cross sectional area and velocities (U_x) of the structures within the flame were assessed using the exported, numeric PIV data, with different components of the flame designated based on the axial velocity component, as indicated in Figure A. 5 (a).

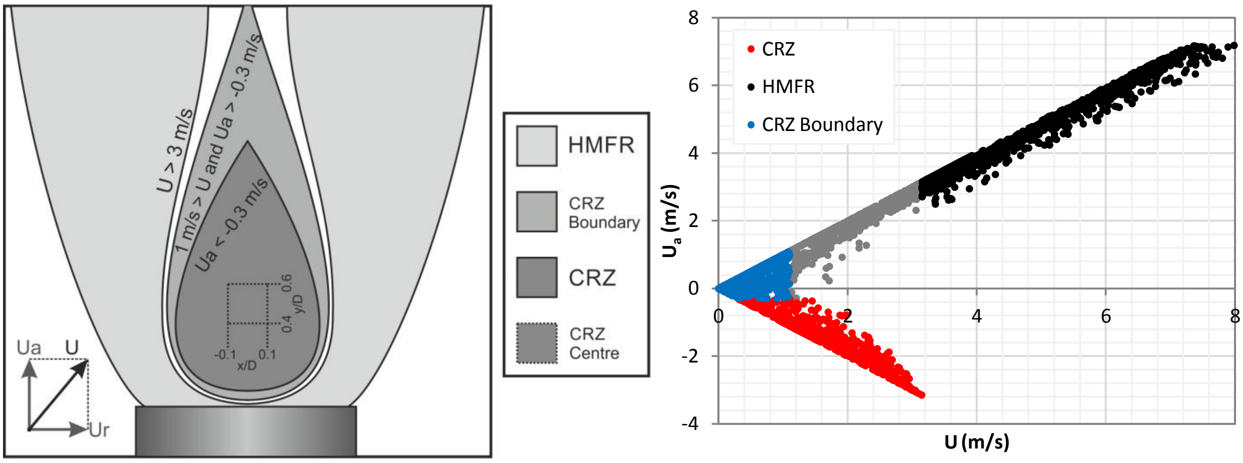

(a) *(b)*

Figure A. 5: (a) Comparison of axial velocity (U_a) and total velocity (U) at each measurement point in TP VI and (b) designation of areas within the flame

The designations were based on the results from TP VI, the total and axial velocities of each measurement point of which are plotted in Figure A. 5 (b), for the following reasons:

- The CRZ is the region where axial velocity exceeds 0.3 m/s in the negative axial direction.

  This value is simply chosen to remove outlying values that occur in the results.
- The HMFR is the region where total velocity exceeds 3 m/s.

  Each measurement point considered to be in the HMFR is denoted by a black circle in Figure A. 5 (b), with the measurement points considered to be in the CRZ denoted by red points. The peak total velocity in the CRZ is slightly greater than 3 m/s, the total velocity of all points in the HMFR exceed this.
- The CRZ boundary is the region where axial velocity is greater than -0.3 m/s and total velocity is less than 1 m/s.

  The -0.3 m/s represents the outer CRZ, and 1 m/s is the highest total velocity that occurs when axial velocity equals 0.

- The CRZ centre is the region bound by the arguments *0.1 > x/D > -0.1* and *0.6 > x/D > -0.4.*
  It is defined geometrically so it is defined independently of velocity.

When each measurement point has been designated to a relevant structure, cross sectional area, radius of centroid, volume, and mean velocity are calculated thus:

$$A_s = n_{mp} \cdot A_{mp} \qquad \text{Eq (A4.1)}$$

$$r_c = \frac{\Sigma|x_{mp}|}{n_{mp}} \qquad \text{Eq (A4.2)}$$

$$V_s = A_s \cdot r_c \cdot \pi \qquad \text{Eq (A4.3)}$$

$$\bar{U} = \frac{U_{mp}}{n_{mp}} \qquad \text{Eq (A4.4)}$$

Where: A_s = Cross sectional area of structure (m^2)

n_{mp} = Number of measurement points in structure (-)

A_{mp} = Area represented by each measurement point (m^2)

X_{mp} = x-coordinate of measurement point (m)

V_s = Volume of structure (m^3)

r_c = Radius of centroid (m)

$\bar{U}$ = Mean velocity (m/s)

u_{mp} = Velocity at measurement point (m/s)

Appendix C - Pressurised Generic Swirl Burner

The pressurised generic swirl burner is a design evolution of the AGSB, with the salient features being scaled up, and modifications made for installation in the HPCR, as shown in Figure A. 6 (a). The principle of operation remains the same as the AGSB, with pilot fuel being fed into a diffusion pilot at (a) in Figure A. 6 (b), and the main fuel entering the assembly at (b). The premixed air and fuel enter a plenum chamber and pass through the swirl vanes, before exiting the burner and entering the combustion chamber. The combustion chamber is a quartz confinement, (c), which protects the steel casing whilst making the assembly more representative of a gas turbine combustor and providing visual access. The combustion zone is visible from (d), (e) and (f); with the product gasses exiting the assembly via the water-cooled exhaust section.

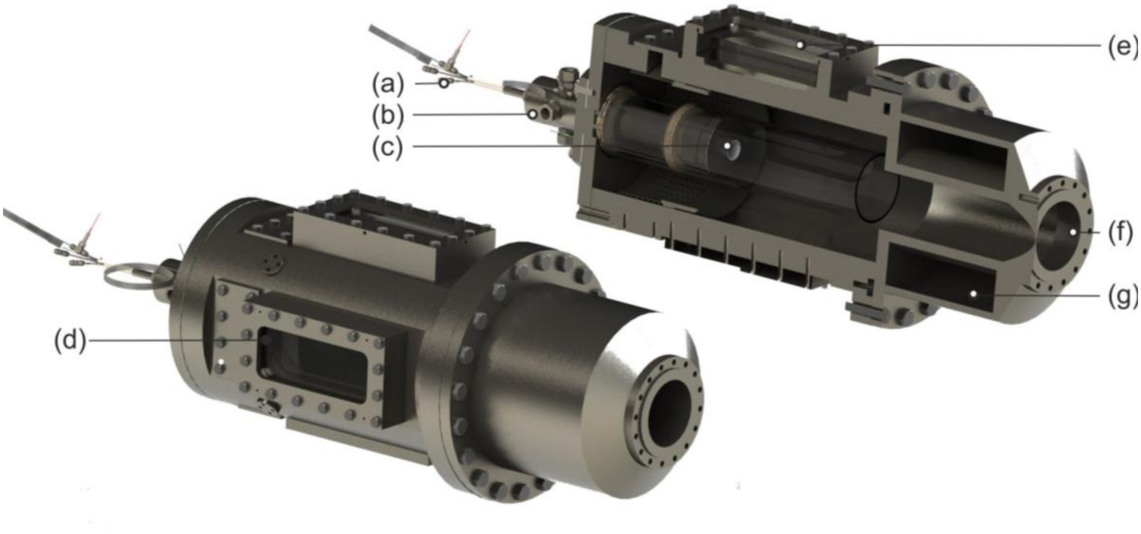

(a) *(b)*

Figure A. 6: External and sectioned views of the HPCR with LCRI burner installed

It is possible to alter the geometric swirl number of the burner by changing the various parameters of the outlet geometry. It is preferable to change as few parameters as possible when trying to achieve different values of C_f. Swirl heads in the PGSB are single pieces that contain the radial swirl vanes and the burner exhaust nozzle; the geometric coefficient of swirl number is altered by changing the width of the nine radial passages. Figure A. 7 demonstrates the different head geometries that are used to impart different intensities of swirl on the flow.

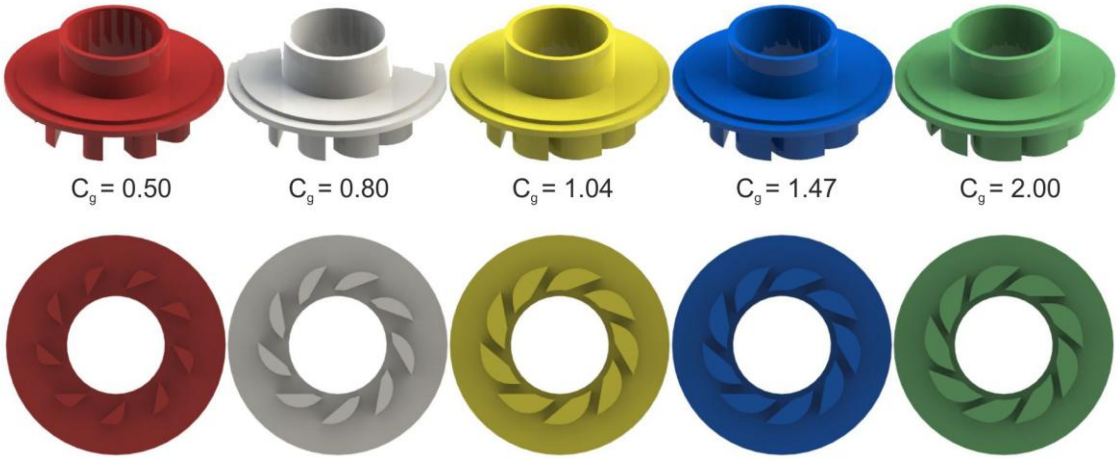

Figure A. 7: Visualisation of the swirl heads used to vary geometric coefficient in the PGSB

The geometry of the swirl vanes is listed in Table 17; all dimensions are constant except for the width of the swirl chamber inlet channels. By changing the area of the channels the tangential velocity of the premixed flow is altered relative to the axial velocity of the flow at the exit.

Table 17: Details of swirl head geometry

Geometry Coefficient (-)	0.5	0.8	1.04	1.47	2.00
Exit radius (mm)	20	20	20	20	20
Injector Radius (mm)	9	9	9	9	9
Inlet Height (mm)	18	18	18	18	18
Number of Inlets (-)	9	9	9	9	9
Inlet Width (mm)	12	7.5	5.8	4.1	3.0